frontiers | Research Topics

Condition monitoring for renewable energy systems

Edited by
Yusen He, Tinghui Ouyang, Xun Shen, Shuang Zhao and Alan Wai Hou Lio

Published in
Frontiers in Energy Research

FRONTIERS EBOOK COPYRIGHT STATEMENT

The copyright in the text of individual articles in this ebook is the property of their respective authors or their respective institutions or funders. The copyright in graphics and images within each article may be subject to copyright of other parties. In both cases this is subject to a license granted to Frontiers.

The compilation of articles constituting this ebook is the property of Frontiers.

Each article within this ebook, and the ebook itself, are published under the most recent version of the Creative Commons CC-BY licence. The version current at the date of publication of this ebook is CC-BY 4.0. If the CC-BY licence is updated, the licence granted by Frontiers is automatically updated to the new version.

When exercising any right under the CC-BY licence, Frontiers must be attributed as the original publisher of the article or ebook, as applicable.

Authors have the responsibility of ensuring that any graphics or other materials which are the property of others may be included in the CC-BY licence, but this should be checked before relying on the CC-BY licence to reproduce those materials. Any copyright notices relating to those materials must be complied with.

Copyright and source acknowledgement notices may not be removed and must be displayed in any copy, derivative work or partial copy which includes the elements in question.

All copyright, and all rights therein, are protected by national and international copyright laws. The above represents a summary only. For further information please read Frontiers' Conditions for Website Use and Copyright Statement, and the applicable CC-BY licence.

ISSN 1664-8714
ISBN 978-2-83250-701-8
DOI 10.3389/978-2-83250-701-8

About Frontiers

Frontiers is more than just an open access publisher of scholarly articles: it is a pioneering approach to the world of academia, radically improving the way scholarly research is managed. The grand vision of Frontiers is a world where all people have an equal opportunity to seek, share and generate knowledge. Frontiers provides immediate and permanent online open access to all its publications, but this alone is not enough to realize our grand goals.

Frontiers journal series

The Frontiers journal series is a multi-tier and interdisciplinary set of open-access, online journals, promising a paradigm shift from the current review, selection and dissemination processes in academic publishing. All Frontiers journals are driven by researchers for researchers; therefore, they constitute a service to the scholarly community. At the same time, the *Frontiers journal series* operates on a revolutionary invention, the tiered publishing system, initially addressing specific communities of scholars, and gradually climbing up to broader public understanding, thus serving the interests of the lay society, too.

Dedication to quality

Each Frontiers article is a landmark of the highest quality, thanks to genuinely collaborative interactions between authors and review editors, who include some of the world's best academicians. Research must be certified by peers before entering a stream of knowledge that may eventually reach the public - and shape society; therefore, Frontiers only applies the most rigorous and unbiased reviews. Frontiers revolutionizes research publishing by freely delivering the most outstanding research, evaluated with no bias from both the academic and social point of view. By applying the most advanced information technologies, Frontiers is catapulting scholarly publishing into a new generation.

What are Frontiers Research Topics?

Frontiers Research Topics are very popular trademarks of the *Frontiers journals series*: they are collections of at least ten articles, all centered on a particular subject. With their unique mix of varied contributions from Original Research to Review Articles, Frontiers Research Topics unify the most influential researchers, the latest key findings and historical advances in a hot research area.

Find out more on how to host your own Frontiers Research Topic or contribute to one as an author by contacting the Frontiers editorial office: frontiersin.org/about/contact

Condition monitoring for renewable energy systems

Topic editors
Yusen He — The University of Iowa, United States
Tinghui Ouyang — National Institute of Advanced Industrial Science and Technology (AIST), Japan
Xun Shen — Tokyo Institute of Technology, Japan
Shuang Zhao — Hefei University of Technology, China
Alan Wai Hou Lio — Technical University of Denmark, Denmark

Citation
He, Y., Ouyang, T., Shen, X., Zhao, S., Lio, A. W. H., eds. (2023). *Condition monitoring for renewable energy systems*. Lausanne: Frontiers Media SA.
doi: 10.3389/978-2-83250-701-8

Table of contents

frontiers | Frontiers in Energy Research

ORIGINAL RESEARCH
published: 27 April 2022
doi: 10.3389/fenrg.2022.887769

Global Exponential Stability of a Class of Memristor-Based RNN and Its Application to Design Stable Voltage Circuits

Zhao Yao[1,2] *and Yingshun Li*[2]*

[1]*Army Academy of Armored Forces, Changchun, China,* [2]*School of Control Science and Engineering, Dalian University of Technology, Dalian, China*

In this article, we study the global exponential stability of the equilibrium point for a class of memristor-based recurrent neural networks (MRNNs). The MRNNs are based on a realistic memristor model and can be implemented by a very large scale of integration circuits. By introducing a proper Lyapunov functional, it is proved that the equilibrium point of the MRNN is globally exponentially stable under two less conservative assumptions. Furthermore, an algorithm is proposed for the design of MRNN-based circuits with stable voltages. Finally, an illustration example is performed to show the validation of the proposed theoretical results; an MRNN-based circuit with stable voltages is designed according to the proposed algorithm.

Keywords: memristor, voltage, circuit, recurrent neural network, stability

Edited by:
Xun Shen,
Tokyo Institute of Technology, Japan

Reviewed by:
Zhou Liqun,
Tianjin Normal University, China
Yi Cheng,
Bohai University, China

****Correspondence:***
Yingshun Li
leeys@dlut.edu.cn

Specialty section:
This article was submitted to Smart Grids, a section of the journal Frontiers in Energy Research

Received: *02 March 2022*
Accepted: *17 March 2022*
Published: *27 April 2022*

Citation:
Yao Z and Li Y (2022) Global Exponential Stability of a Class of Memristor-Based RNN and Its Application to Design Stable Voltage Circuits.
Front. Energy Res. 10:887769.
doi: 10.3389/fenrg.2022.887769

1 INTRODUCTION

Recurrent networks have been one of the necessary tools to character system states since their wide applications in optimization (Li et al., 2021; Ma and Bian, 2021), games (Wu et al., 2019, 2021; Cheng et al., 2021), control (Yang et al., 2015; Jianmin et al., 2021; Toyoda and Wu, 2021), and so on (Wang et al., 2007; Shen et al., 2020; Shen and Raksincharoensak, 2021). In recent years, a new type of recurrent network was proposed based on a new two-terminal circuit element called the memristor (Chua, 1971; Strukov et al., 2008). Note that a memristor works like a biological synapse (Anthes, 2011; Qin et al., 2015) and has the ability of automatic information storage. Thus, memristors replaced resistors as synapses in recurrent neural networks, that is, memristor-based recurrent neural networks (MRNNs) (Anthes, 2011; Wen et al., 2013; Zhang et al., 2013). In recent years, the stability and stabilization of Boolean networks have been extensively investigated (Chen et al., 2018; Guo et al., 2019, 2021).

MRNNs have been a promising architecture in neuromorphic systems by virtue of their non-volatility, high-density, and physical storable feature. According to the realistic structure of MRNNs, several different mathematical models for MRNNs were proposed (Hu and Wang, 2010; Wu et al., 2011; Li et al., 2014; Chen et al., 2015; Jianmin et al., 2019). Meanwhile, notice that the MRNN, a special recurrent network, depends on the stability of its equilibrium points in application scenarios. Therefore, many interesting works were addressed to analyze the stability for the MRNNs (Hu and Wang, 2010; Wu et al., 2011; Li et al., 2014; Chen et al., 2015; Jianmin et al., 2019). A mathematical model of MRNN was proposed, and its global uniform asymptotic stability was investigated in a Lyapunov sense (Hu and Wang, 2010). A simple model of MRNN was introduced by Wu et al. (2011) by means of the typical current–voltage characteristics of memristors. A stochastic MRNN was proposed by Li et al. (2014) based on the work by Wang et al. (2007), in which there was some unavoidable noise in real networks. Furthermore, the global exponential stability for the stochastic MRNN was studied under the framework of Filppov's solution; three sufficient conditions with the form of linear inequalities were provided to determine the global exponential stability of the stochastic MRNN. The global asymptotic stability and synchronization of a class of fractional-order memristor-based delayed neural networks were investigated by Chen et al. (2015). The existence and global exponential stability were discussed by Jianmin et al. (2019) for an uncertain MRNN with mixed time delay under two assumptions.

Motivated by the aforementioned works, the global exponential stability of the equilibrium point is investigated for a class of MRNNs with time-varying delay, and its application to stabilize the voltage in a circuit network is carried out in this study. A sufficient condition is obtained for the global exponential stability of MRNNs. Based on this condition, an algorithm is proposed to stabilize the voltage of the MRNN-based circuit. The time-varying delay was considered in the activation functions of MRNN in this study. In addition, the activation functions in the MRNN are not necessarily non-decreasing, while the activation functions are non-decreasing in the works by Hu and Wang (2010); Wu et al. (2011); Li et al. (2014); Chen et al. (2015); Jianmin et al. (2019). Thus, the MRNN considered in this study is the extension from the view of activation functions compared with those in the works by Hu and Wang (2010); Wu et al. (2011); Li et al. (2014); Chen et al. (2015); Jianmin et al. (2019). Meanwhile, the stable voltage is a necessary prerequisite for obtaining high-quality electric energy in power systems, such as wind power converters (Kobravi et al., 2007). Consequently, the obtained theretical results are successfully applied to design the MRNN-based circuit system with global exponential stability, which makes it possible to apply the MRNN to power converters.

The structure of this article is given as follows: an MRNN with time-varying delay and some notations is introduced in **Section 2**. In **Section 3**, the global exponential stability of the equilibrium point for the MRNN is obtained, and an example is given to show the effectiveness of the obtained results. Then, an algorithm to design the MRNN-based circuit with stable voltage is proposed, and a simple application is carried out in **Section 4**. Finally, the main conclusions are given in **Section 5**.

2 MEMRISTOR-BASED RECURRENT NEURAL NETWORK

In this section, some notations are introduced, and an MRNN is described under two assumptions based on the mathematical models by Wen et al. (2013); Jianmin et al. (2019).

Notation: $\mathbb{R}$ denotes the set of real numbers. $x = (x_1, x_2, \ldots, x_m)^T$ is an $m-$ dimensional column, and the superscript T stands for the transpose operator. $\| x \| := (\sum_{i=1}^{m} x_i^2)^{1/2}$. $A = (a_{ij}) \in \mathbb{R}^{m\times m}$ is a matrix. $\| A \| = \sqrt{\lambda_M(A^T A)}$, where $\lambda_M(A)$ represents the maximum eigenvalue of A. $I \in \mathbb{R}^{m\times m}$ stands for an identity matrix. For a real symmetric matrix A, $A > 0 (A < 0)$ means that A is positive (negative) definite.

Consider the following MRNN, which was originated from Wen et al. (2013),

$$C_i\dot{x}_i(t) = -\left[\sum_{j=1}^{n}\left(\frac{1}{R_{fij}} + \frac{1}{R_{gij}}\right) + W_i\left(x_i(t)\right)\right] x_i(t) + \sum_{j=1}^{n} \frac{\mathrm{sign}_{ij}}{R_{fij}} f_j\left(x_j(t)\right) + \sum_{j=1}^{n} \frac{\mathrm{sign}_{ij}}{R_{gij}} g_j\left(x_j\left(t - \tau_j(t)\right)\right) + I_i. \tag{1}$$

Here, $f_j(\cdot)$ is the activation function, $\tau_j(\cdot)$ is the time-varying delay, C_i is the capacitance of the capacitor, and $x_i(t)$ is the voltage of the capacitor. $R_{f_{ij}}$ is the resistor between the feedback function $f_j(x_j(t))$ and the state $x_i(t)$, and $R_{g_{ij}}$ is the resistor between the feedback function $g_j(x_j(t - \tau_j(t)))$ and the state $x_i(t)$. sign_{ij} is defined as

$$\mathrm{sign}_{ij} = \begin{cases} 1, & \text{if } i \neq j; \\ 0, & \text{if } i = j. \end{cases} \tag{2}$$

$W_i[x_i(t)]$ is the memductance of the $i-$ th memristor satisfying

$$W_i\left(x_i(t)\right) = \begin{cases} W_i', & \text{if } x_i(t) \leq 0; \\ W_i'', & \text{if } x_i(t) > 0. \end{cases} \tag{3}$$

I_i is an external input or bias and $i, j = 1, 2, \ldots, n$. Let

$$\widetilde{W}_i = \frac{W_i'' - W_i'}{2C_i}. \tag{4}$$

From Jianmin et al. (2019), the MRNN (**Eq. 1**) is transformed into:

$$\dot{x}_i(t) = -d_i x_i(t) - \widetilde{W}_i |x_i(t)| + \sum_{j=1}^{n} a_{ij} f_j\left(x_j(t)\right) + \sum_{j=1}^{n} b_{ij} g_j\left(x_j\left(t - \tau_j(t)\right)\right) + U_i. \tag{5}$$

Here,

$$\begin{gathered} d_i = \sum_{j=1}^{n}\left[\frac{1}{C_i R_{f_{ij}}} + \frac{1}{C_i R_{g_{ij}}} + \frac{W_i' + W_i''}{2C_i}\right], \\ a_{ij} = \frac{\mathrm{sign}_{ij}}{C_i R_{f_{ij}}},\ b_{ij} = \frac{\mathrm{sign}_{ij}}{C_i R_{g_{ij}}},\ U_i = \frac{I_i}{C_i}. \end{gathered} \tag{6}$$

Next, let $D = \mathrm{diag}\{d_1, d_2, \ldots, d_n\}$, $\widetilde{W} = \mathrm{diag}\{\widetilde{W_1}, \widetilde{W_2}, \ldots, \widetilde{W_n}\}$, $A = (a_{ij})_{n\times n}$, $B = (b_{ij})_{n\times n}$, $|x(t)| = (|x_1(t)|, |x_2(t)|, \ldots, |x_n(t)|)^T$, $\tau(t) = (\tau_1(t), \tau_2(t), \ldots, \tau_n(t))^T$, and $U = (U_1, U_2, \ldots, U_n)^T$. Then, **Eq. 5** is rewritten as:

$$\dot{x}(t) = -Dx(t) - \widetilde{W}|x(t)| + Af(x(t)) + Bg(x(t - \tau(t))) + U. \tag{7}$$

In addition, there are two assumptions and one lemma, which will be needed in the sequel, for the MRNN (**Eq. 7**). The first assumption about the activation function f_i is from Wen et al. (2013). The second assumption about the time-varying delay τ_j is from Wen et al. (2013).

$\mathbf{S_1}$. For $i \in \{1, 2, \ldots, n\}$, the activation function f_i is bounded continuous, and $\forall r_1, r_2 \in \mathbb{R}$, there exists real number $l_i > 0$ such that

$$0 \le \frac{f_i(r_1) - f_i(r_2)}{r_1 - r_2} \le l_i. \tag{8}$$

Here, we set $L_f = \mathrm{diag}\{l_1, l_2, \ldots, l_n\}$.

For $i \in \{1, 2, \ldots, n\}$, the activation function g_i is bounded continuous, $g_i(0) = 0$, and $\forall r_1, r_2 \in \mathbb{R}$, there exists real number $l_i' > 0$ such that

$$-l_i' \le \frac{g_i(r_1) - g_i(r_2)}{r_1 - r_2} \le l_i'. \tag{9}$$

Here, we set $L_g = \mathrm{diag}\{l_1', l_2', \ldots, l_n'\}$.

$\mathbf{S_2}$. For $i \in \{1, 2, \ldots, n\}$, $\tau_i(t)$ satisfies

$$0 \le \tau_i(t) \le \overline{\tau}_i, \ \dot{\tau}_i(t) \le \mu_i < 1. \tag{10}$$

Here, we let $\overline{\tau} = \max\{\overline{\tau}_1, \ldots, \overline{\tau}_n\}$, and $\mu = \max\{\mu_1, \ldots, \mu_n\}$.

Remark 1. From **Eq. 9**, the activation functions $g_i[x_i(t)]$ are non-monotonic in this study. On the other hand, we notice that the activation functions of MRNNs in the works by Hu and Wang (2010; Wu et al. (2011); Li et al. (2014); Chen et al. (2015); Jianmin et al. (2019) are non-decreasing. Thus, **Eq. 1** is the extension from the view of activation functions compared with those references.

3 GLOBALLY EXPONENTIAL STABILITY

In this section, we will prove that the MRNN (**Eq. 1**) is globally exponentially stable under the assumptions $\mathbf{S_1}$ and $\mathbf{S_2}$. A sufficient condition with the form of linear matrix inequalities can be obtained for globally exponential stability of MRNN by constructing a suitable Lyapunov functional.

Theorem 1. Assume that $\mathbf{S_1}$ and $\mathbf{S_2}$ hold. If there exist a matrix $P = diag\{p_1, p_2, \ldots, p_n\} > 0$, a constant $k > 0$, and small enough constants $\xi > 0$ and $\vartheta > 0$ such that

$$\begin{aligned} \Phi &:= \xi P - 2PD + 2P|\widetilde{W}| + \left(1 + \frac{1}{k}\right) I + 2\vartheta\left(\xi L_f P + L_f P |\widetilde{W}|\right) \\ &\quad + \frac{(1+\vartheta)}{1-\mu} \| PB \|^2 e^{\xi \overline{\tau}} L_g L_g < 0, \\ \Psi &:= -2\vartheta L_f^{-1} PD + \vartheta\left(PA + A^T P\right) + \vartheta I + k \| PA \|^2 I < 0. \end{aligned} \tag{11}$$

Then, the equilibrium point of the MRNN (**Eq. 1**) is globally exponentially stable.

Proof: To simplify the proof, we make the following transformation:

$$z = x - x^*, \tag{12}$$

where x^* is the equilibrium point of the MRNN (**Eq. 1**). Then, the MRNN (**Eq. 1**) can be rewritten equivalently as

$$\begin{aligned} \dot{z}(t) &= -Dz(t) - \widetilde{W}(|z(t) + x^*| - |x^*|) \\ &\quad + A\mathscr{f}(z(t)) + B\mathscr{g}(z(t - \tau(t))), \end{aligned} \tag{13}$$

where $\mathscr{f}(z(t)) = f(z(t) + x^*) - f(x^*)$ and $\mathscr{g}(z(t - \tau(t))) = g(z(t - \tau(t)) + x^*) - g(x^*)$. It is obvious that $\mathscr{f}_i(0) = 0$ and $\mathscr{g}_i(0) = 0$. By the assumption $\mathbf{S_1}$, we get

$$\begin{aligned} &\mathscr{f}^T(z(t))z(t) \ge \mathscr{f}^T(z(t)) L_f^{-1} \mathscr{f}(z(t)), \\ &\mathscr{f}^T(z(t))z(t) \le z^T(t) L_f z(t), \\ &\mathscr{g}(z(t)) \le L_g |z(t)|. \end{aligned} \tag{14}$$

We define a Lyapunov functional as follows:

$$\mathscr{V}(t,z) = \mathscr{V}_0(t,z) + \mathscr{V}_1(t,z) + \mathscr{V}_2(t,z), \tag{15}$$

where

$$\begin{aligned} \mathscr{V}_0(t,z) &= e^{\xi t} z^T P z, \\ \mathscr{V}_1(t,z) &= 2\vartheta e^{\xi t} \sum_{i=1}^{n} p_i \int_0^{z_i} \mathscr{f}_i(s)\, ds, \\ \mathscr{V}_2(t,z) &= \eta \sum_{i=1}^{n} \int_{t-\tau_i(t)}^{t} \mathscr{g}_i^2(z_i(s)) e^{\xi(s+\overline{\tau}_i)} ds. \end{aligned} \tag{16}$$

Here, ξ, ϑ are small positive constants, and η is a positive constant to be determined.

First, calculating the time derivative of $\mathscr{V}_0(t,z)$ along the trajectories of the MRNN (**Eq. 13**), we have

$$\begin{aligned} \frac{d}{dt}\mathscr{V}_0(t, z(t)) &= \xi e^{\xi t} z^T(t) P z(t) + 2e^{\xi t} z^T(t) P \dot{z}(t) \\ &= \xi e^{\xi t} z^T(t) P z(t) - 2e^{\xi t} z^T(t) PDz(t) \\ &\quad - 2e^{\xi t} z^T(t) P\widetilde{W}(|z(t) + x^*| - |x^*|) \\ &\quad + 2e^{\xi t} z^T(t) PA\mathscr{f}(z(t)) \\ &\quad + 2e^{\xi t} z^T(t) PB\mathscr{g}(z(t - \tau(t))). \end{aligned} \tag{17}$$

In addition,

$$\begin{aligned} -2e^{\xi t} z^T(t) P\widetilde{W}(|z(t) + x^*| - |x^*|) &\le 2e^{\xi t} |z(t)|^T P |\widetilde{W}| \\ &\quad \times |(|z(t) + x^*| - |x^*|)| \\ &\le 2e^{\xi t} |z(t)|^T P |\widetilde{W}| \cdot |z(t)| \\ &= 2e^{\xi t} z^T(t) P |\widetilde{W}| z(t), \end{aligned} \tag{18}$$

$$\begin{aligned} &2e^{\xi t} z^T(t) PA\mathscr{f}(z(t)) \\ &\quad \le e^{\xi t}\left[\frac{1}{k} z^T(t) z(t) + \mathscr{f}^T(z(t)) k \| PA \|^2 \mathscr{f}(z(t))\right], \end{aligned} \tag{19}$$

$$\begin{aligned} 2e^{\xi t} z^T(t) PB\mathscr{g}(z(t - \tau(t))) &\le e^{\xi t}\left[z^T(t) z(t) + \mathscr{g}^T(z(t - \tau(t)))\right. \\ &\quad \left. \times \| PB \|^2 \mathscr{g}(z(t - \tau(t)))\right]. \end{aligned} \tag{20}$$

Here, the parameter k is a positive constant. Substituting **Eqs 18–20** into **Eq. 17**, we obtain

$$\begin{aligned} \frac{d}{dt}\mathscr{V}_0(t, z(t)) &\le e^{\xi t} z^T(t)\left[\xi P - 2PD + 2P|\widetilde{W}| + \left(1 + \frac{1}{k}\right) I\right] z(t) \\ &\quad + e^{\xi t} \mathscr{f}^T(z(t)) k \| PA \|^2 \mathscr{f}(z(t)) + e^{\xi t} \mathscr{g}^T(z(t - \tau(t))) \\ &\quad \times \| PB \|^2 \mathscr{g}(z(t - \tau(t))). \end{aligned} \tag{21}$$

Second, by calculating the time derivative of $\mathcal{V}_1(t,z)$ along the trajectories of the MRNN (**Eq. 13**), it follows

$$
\begin{aligned}
\frac{d}{dt}\mathcal{V}_1(t,z(t)) &= 2\xi\vartheta e^{\xi t}\sum_{i=1}^{n}p_i\int_0^{z_i}f_i(s)\,ds + 2\vartheta e^{\xi t}f^T(z(t))P\dot{z}(t)\\
&\le 2\xi\vartheta e^{\xi t}f^T(z(t))Pz(t) - 2\vartheta e^{\xi t}f^T(z(t))PDz(t)\\
&\quad - 2\vartheta e^{\xi t}f^T(z(t))P\widetilde{W}(|z(t)+x^*|-|x^*|)\\
&\quad + 2\vartheta e^{\xi t}f^T(z(t))PAf(z(t)) + 2\vartheta e^{\xi t}f^T(z(t))PB\\
&\quad \times g(z(t-\tau(t))).
\end{aligned}
\tag{22}
$$

By **Eq. 14**, we have

$$
\begin{aligned}
&2\xi\vartheta e^{\xi t}f^T(z(t))Pz(t) \le 2\xi\vartheta e^{\xi t}z^T(t)L_fPz(t),\\
&\quad -2\vartheta e^{\xi t}f^T(z(t))PDz(t) \le -2\vartheta e^{\xi t}f^T(z(t))L_f^{-1}PDf(z(t)),
\end{aligned}
\tag{23}
$$

$$
\begin{aligned}
&-2\vartheta e^{\xi t}f^T(z(t))P\widetilde{W}(|z(t)+x^*|-|x^*|)\\
&\le 2\vartheta e^{\xi t}|z(t)|^TL_fP|\widetilde{W}\parallel z(t)|\\
&= 2\vartheta e^{\xi t}z^T(t)L_fP|\widetilde{W}|z(t).
\end{aligned}
\tag{24}
$$

Notice that

$$
\begin{aligned}
&2\vartheta e^{\xi t}f^T(z(t))PBg(z(t-\tau(t)))\\
&\quad\le \vartheta e^{\xi t}f^T(z(t))f(z(t)) + e^{\xi t}g^T(z(t-\tau(t)))\vartheta\parallel PB\parallel^2\\
&\quad\quad\times g(z(t-\tau(t))).
\end{aligned}
\tag{25}
$$

Substituting **Eqs 23–25** into **Eq. 22**, we have

$$
\begin{aligned}
&\frac{d}{dt}\mathcal{V}_1(t,z(t))\\
&\quad\le 2\xi\vartheta e^{\xi t}z^T(t)L_fPz(t) - 2e^{\xi t}f^T(z(t))\vartheta L_f^{-1}PDf(z(t))\\
&\quad\quad + 2\vartheta e^{\xi t}z^T(t)L_fP|\widetilde{W}|z(t) + 2\vartheta e^{\xi t}f^T(z(t))PAf(z(t))\\
&\quad\quad + \vartheta e^{\xi t}f^T(z(t))f(z(t)) + e^{\xi t}g^T(z(t-\tau(t)))\vartheta\parallel PB\parallel^2\\
&\quad\quad\times g(z(t-\tau(t)))\\
&\quad= 2\vartheta e^{\xi t}z^T(t)\left[\xi L_fP + L_fP|\widetilde{W}|\right]z(t) + 2e^{\xi t}f^T(z(t))\\
&\quad\quad\times\left[-\vartheta L_f^{-1}PD + \vartheta PA + \frac{1}{2}\vartheta I\right]f(z(t))\\
&\quad\quad + e^{\xi t}g^T(z(t-\tau(t)))\vartheta\parallel PB\parallel^2 g(z(t-\tau(t))).
\end{aligned}
\tag{26}
$$

Third, calculating the time derivative of $\mathcal{V}_2(t,z)$ along the trajectories of the MRNN (**Eq. 13**), we have

$$
\begin{aligned}
&\frac{d}{dt}\mathcal{V}_2(t,z(t))\\
&\quad= \eta\sum_{i=1}^{n}e^{\xi(t+\overline{\tau}_i)}g_i^2(z_i(t)) - \eta\sum_{i=1}^{n}\left(1-\dot{\tau}_i(t)\right)e^{\xi(t-\tau_i(t)+\overline{\tau}_i)}\\
&\quad\quad\times g_i^2\left(z_i\left(t-\tau_i(t)\right)\right)\\
&\quad\le \eta e^{\xi(t+\overline{\tau})}g^T(z(t))g(z(t)) - \eta\left(1-\mu\right)e^{\xi t}g^T(z(t-\tau(t)))\\
&\quad\quad\times g(z(t-\tau(t)))\\
&\quad\le e^{\xi t}z(t)^T\left[\eta e^{\xi\overline{\tau}}L_gL_g\right]z(t) - \eta\left(1-\mu\right)e^{\xi t}g^T(z(t-\tau(t)))\\
&\quad\quad\times g(z(t-\tau(t))).
\end{aligned}
\tag{27}
$$

Hence, by **Eqs 21**, **26**, **27**, we have

$$
\begin{aligned}
&\frac{d}{dt}\mathcal{V}(t,z(t))\\
&\quad= \frac{d}{dt}\mathcal{V}_0(t,z(t)) + \frac{d}{dt}\mathcal{V}_1(t,z(t)) + \frac{d}{dt}\mathcal{V}_2(t,z(t))\\
&\quad\le e^{\xi t}z^T(t)\Big[\xi P - 2PD + 2P|\widetilde{W}| + \left(1+\frac{1}{k}\right)I\\
&\quad\quad +2\vartheta\left(\xi L_fP + L_fP|\widetilde{W}|\right) + \eta e^{\xi\overline{\tau}}L_gL_g\Big]z(t)\\
&\quad\quad +e^{\xi t}f^T(z(t))\left[-2\vartheta L_f^{-1}PD+\vartheta\left(PA+A^TP\right)+\vartheta I+k\parallel PA\parallel^2 I\right]\\
&\quad\quad\times f(z(t)) + e^{\xi t}g^T(z(t-\tau(t)))\left[(1+\vartheta)\parallel PB\parallel^2 - \eta\left(1-\mu\right)\right]\\
&\quad\quad\times g(z(t-\tau(t))).
\end{aligned}
\tag{28}
$$

Let $\eta = \frac{(1+\vartheta)}{1-\mu}\parallel PB\parallel^2$ in **Eq. 28**. It means that

$$
\begin{aligned}
&\frac{d}{dt}\mathcal{V}(t,z(t))\\
&\quad\le e^{\xi t}z^T(t)\Big[\xi P - 2PD + 2P|\widetilde{W}| + \left(1+\frac{1}{k}\right)I\\
&\quad\quad +2\vartheta\left(\xi L_fP + L_fP|\widetilde{W}|\right) + \frac{(1+\vartheta)}{1-\mu}\parallel PB\parallel^2 e^{\xi\overline{\tau}}L_gL_g\Big]z(t)\\
&\quad\quad + e^{\xi t}f^T(z(t))\left[-2\vartheta L_f^{-1}PD + \vartheta\left(PA+A^TP\right) + \vartheta I\right.\\
&\quad\quad \left.+ k\parallel PA\parallel^2 I\right]f(z(t))\\
&\quad= e^{\xi t}z^T(t)\Phi z(t) + e^{\xi t}f^T(z(t))\Psi f(z(t)).
\end{aligned}
\tag{29}
$$

Since $\Phi < 0$, $\Psi < 0$, and by **Eq. 29**, we have

$$
\frac{d}{dt}\mathcal{V}(t,z(t)) \le 0,
\tag{30}
$$

which means that $e^{\xi t}z^T(t)Pz(t) = \mathcal{V}_0(t,z(t)) \le \mathcal{V}(t,z(t)) \le \mathcal{V}(0,z(0))$. More precisely,

$$
\parallel x(t)-x^*\parallel=\parallel z(t)\parallel\le Me^{-\frac{\xi}{2}t},
\tag{31}
$$

where $M = [p\mathcal{V}(0,z(0))]^{\frac{1}{2}}$ and $p = \max\{p_i : i = 1,\ldots,n\}$, that is, the unique equilibrium point x^* of the MRNN (**Eq. 1**) is globally exponentially stable.

Remark 2. Motivated by the representation of the Lyapunov functional in the work by Jianmin et al. (2019), we construct a new Lyapunov functional $\mathcal{V}(t,x(t))$, in order to overcome the difficulty brought by the nonmonotone activation functions in MRNN (**Eq. 1**) in the proof of Theorem 1.

Now, we give an example to illustrate that the equilibrium point of the MRNN is globally exponentially stable when the conditions in Theorem 1 are satisfied.

Example 1. Consider an MRNN (**Eq. 1**) with four state voltages, for which the parameter values of MRNN (**Eq. 1**) are originated from the work by Jianmin et al. (2019), especially the capacitors $C_1 = 2$, $C_2 = 3$, $C_3 = 2$, and $C_4 = 7$; the external inputs $I_1 = 9$, $I_2 = 3$, $I_3 = 9.5$, and $I_4 = 6$; the memductances $W_1' = 1$, $W_2' = 3$, $W_3' = 9.5$, and $W_4' = 1$ for $x_i(t) \le 0$; the memductances $W_1'' = 4$, $W_2'' = 1.5$, $W_3'' = 2$, and $W_4'' = 3.5$ for $x_i(t) \ge 0$; and the resistors $R_f := (R_{f_{ij}})$ and $R_g := (R_{g_{ij}})$ are given as follows:

$$
R_f = \begin{bmatrix} 1 & 3 & 1.5 & 2\\ 2 & 4 & 6 & 12\\ 1.8 & 2.6 & 3.5 & 4\\ 7 & 3 & 4 & 3 \end{bmatrix},
$$

$$R_g = \begin{bmatrix} 1 & 3 & 1.5 & 2 \\ 2 & 2 & 2 & 2 \\ 1.8 & 2.6 & 3.5 & 4 \\ 7 & 3 & 4 & 3 \end{bmatrix}.$$

Next, by the aforementioned parameters and **Eqs 2–6**, it follows that D, $\widetilde{W}$, U, A, and B. Let the activation functions

$$f_i(x_i(t)) = \frac{1}{2}\left(|x_i(t)+1| - |x_i(t)-1|\right),$$

$$g_i(x_i(t)) = \sin(x_i(t)),$$

and the time-varying delays

$$\tau_i(t) = 1.8 + 0.5\sin t,$$

for $i = 1,2,3,4$. It is obvious that the assumptions $\mathbf{S}_1$ and $\mathbf{S}_2$ are satisfied. Then, by assumptions $\mathbf{S}_1$ and $\mathbf{S}_2$, we have $L = \mathrm{diag}\{1,1,1,1\}$, $\overline{\tau} = 2.3$, and $\mu = 0.5$.

Now, by fixing the parameters $k = 1000$, $\xi = 0.001$, and $\vartheta = 0.001$ in Theorem 1 and substituting the matrices $A, B, D, \widetilde{W}$ into the linear matrix inequalities (**Eq. 11**), we get a positive definite diagonal matrix

$$P = diag\{0.0499, 0.0499, 0.0499, 0.0499\},$$

namely, by Theorem 1, the equilibrium point of the MRNN (**Eq. 1**) is globally exponentially stable.

The initial values of the neural network (**Eq. 1**) are set at $(0.1,0.1,0.1,0.1)^{\mathrm{T}}$, $(0.5,0.5,0.5,0.5)^{\mathrm{T}}$, and $(0.9,0.9,0.9,0.9)^{\mathrm{T}}$. The solution trajectories of **Eq. 1** are illustrated in **Figure 1**. From **Figure 1**, we see that the equilibrium point of the MRNN is globally exponentially stable, which shows the validation of the obtained result from Theorem 1.

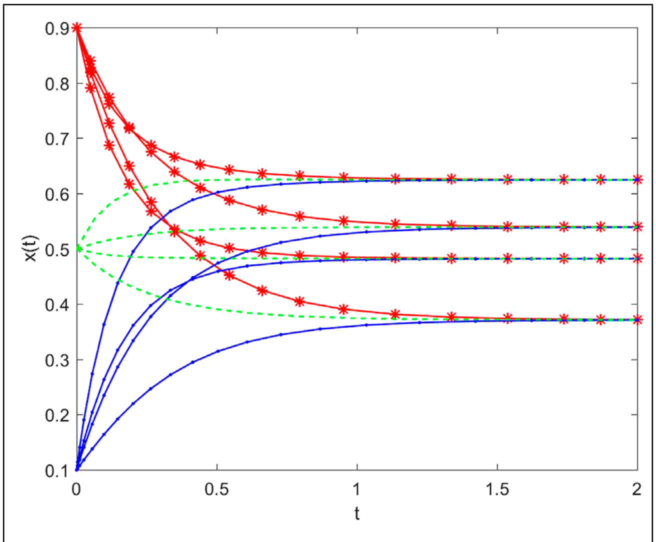

FIGURE 1 | Solution trajectories of the MRNN (1).

4 AN ALGORITHM TO DESIGN THE MRNN-BASED CIRCUIT WITH STABLE VOLTAGES

Note that the stable voltage is a necessary prerequisite for obtaining high-quality electric energy in power systems. In this section, the two linear inequalities in Theorem 1 are used to design the MRNN-based circuit with globally exponentially stable voltages, which make it possible to apply the MRNN to power converters. The design process is described by the following four steps:

Step 1: Fix the values of capacitor C_i, external input I_i, and the resistors $R_{f_{ij}}$ and $R_{g_{ij}}$ in **Eq. 1** for $i,j = 1,2,\ldots,n$.

Step 2: For the given time-varying delay $\tau_i(t)$ and the activation functions f_i, g_i, calculate the matrices L_f, L_g in the assumption $\mathbf{S}_1$ and the parameters $\overline{\tau}$ and μ in the assumption $\mathbf{S}_2$.

Step 3: Determine the parameters W_i' and W_i'' in the memductance $W_i(x_i(t))$ of the $i-$ th memristor in **Eq. 1** for $i = 1,2,\ldots,n$.

- Fix a matrix $P > 0$ and the parameters k, ξ, and ϑ in Theorem 1.
- Substitute C_i, I_i, $R_{f_{ij}}$, and $R_{g_{ij}}$ into a_{ij}, b_{ij}, and U_i in **Eq. 6** to obtain matrices A, B, D, and U.
- Substitute the matrices P, D, A, B, and U into the linear matrix inequalities (11).
- Solve **Eq. 11** to obtain the matrix $\widetilde{W}$.
- Calculate W_i' and W_i'' by the d_i and $\widetilde{W}_i$ in **Eq. 5**.

Step 4: By substituting $C_i, I_i, R_{f_{ij}}, R_{g_{ij}}, W_i'$, and W_i'' into **Eq. 1**, the MRNN-based circuit with stable voltages is obtained.

Remark 3. From Step 3, the parameters W_i' and W_i'' in the MRNN (**Eq. 1**) can be determined at the same time by the parameter $\mathrm{d_i}$ and $\widetilde{W}_i$ for $i = 1,2,\ldots,n$ in (6). Consequently, we can select or make the memristor guarantee the MRNN-based circuit with stable voltage when the other elements are given beforehand by means of the proposed algorithm.

Next, we will design an MRNN-based circuit with four stable voltages by the proposed algorithm, where the activation functions and some of the parameters in the MRNN-based circuit in this example are the same as those in the first example.

Example 2. It is declared that the activation functions $f_i(x_i(t))$, $g_i(x_i(t))$, the time-varying delay $\tau_i(\mathrm{t})$, and the values of parameters $\mathrm{C_i}$, $\mathrm{I_i}$, $R_{f_{ij}}$, and $R_{g_{ij}}$ for the MRNN-based circuit are the same as those in the first example. Next, by Step 3, we determine the values of W_i' and W_i'' in the memductance $W_i[x_i(t)]$ *of the* $i-$ th memristor in **Eq. 1** for $i,j = 1,2,3,4$.

- Fix the values of parameters $k = 1000$, $\xi = 0.001$, and $\vartheta = 0.001$ in Theorem 1 and a matrix $P = diag\{5,5,5,5\} > 0$ and $D = diag\{30,20,25,10\}$. Substitute the matrices P, D, B, and U into the linear matrix inequalities (11). Then, solve **Eq. 11** to obtain the matrix $\widetilde{W}$:

$$\widetilde{W} = \{25.5148, 15.9082, 20.7115, 6.3017\}.$$

- Calculate W_i' and W_i'' by d_i and $\widetilde{W}_i$ in **Eq. 6**, especially $W_1'' = 60.9574$, $W_2'' = 56.3541$, $W_3'' = 47.3558$,

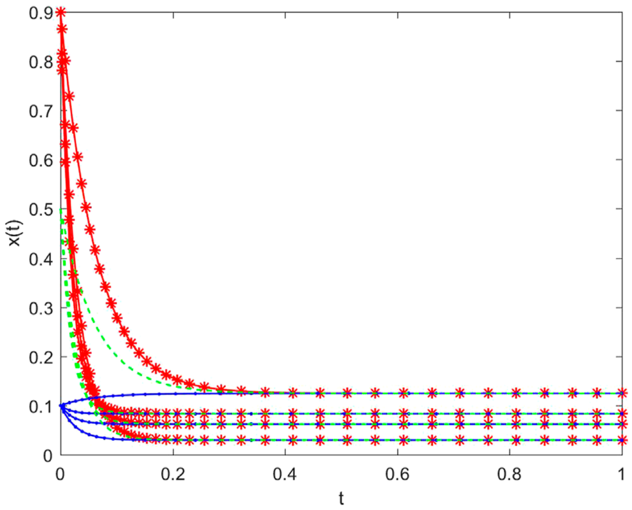

FIGURE 2 | Solution trajectories of the designed MRNN-based circuit.

$W_4'' = 17.1508$; $W_1' = 35.4426$, $W_2' = 40.4459$, $W_3' = 26.6443$, and $W_4' = 10.8492$.

By Step 4, substituting C_i, I_i, $R_{f_{ij}}$, $R_{g_{ij}}$, W_i', and W_i'' into **Eq. 1**, we obtain the MRNN-based circuit with stable voltages. The initial values of **Eq. 1** are given as same as those in Example 1. The solution trajectories of the designed MRNN-based circuit are depicted in **Figure 2**, which means that we obtain a MRNN-based circuit with stable voltages through selecting the suitable parameter values in the memductance of the memristor.

5 CONCLUSION

In this study, the global exponential stability of the equilibrium point of the MRNN is investigated for a class of general activation functions. A sufficient condition with the form of linear matrix inequalities is obtained for the global exponential stability. Furthermore, the proposed results are applied to design the MRNN-based circuits with stable voltages. From the view of the MRNN-based circuit, some elements of the MRNN-based circuit with stable voltages can be determined by the proposed algorithm. Note that the earth's environmental pollution and the lack of energy restrict the survival and development of the human society. Wind energy, an environment-friendly renewable resource, has become one of the effective ways to solve these two difficulties. The conversion of wind energy into electric energy can rely on wind power converters. The mathematical model of the power system of new wind turbines was described by a recurrent network. Thus, further research will focus on transforming the output voltage of the wind power converter to ensure the stable amplitude of its output voltage based on MRNN with stability.

DATA AVAILABILITY STATEMENT

The original contributions presented in the study are included in the article/Supplementary Material, further inquiries can be directed to the corresponding author.

AUTHOR CONTRIBUTIONS

ZY contributed to the globally exponential stability of MRNN by considering the proper assumptions and constructing a suitable Lyapunov functional. YL drafted the manuscript and contributed to the algorithm of design of the MRNN-based circuit with stable voltages, experiments, and conclusions. All authors agree to be accountable for the content of the work.

FUNDING

This work was financially supported by the China Postdoctoral Science Foundation (Grant No. 2020M670785).

REFERENCES

Anthes, G. (2011). Memristors. *Commun. ACM* 54, 22–24. doi:10.1145/1897852.1897859

Chen, L., Wu, R., Cao, J., and Liu, J.-B. (2015). Stability and Synchronization of Memristor-Based Fractional-Order Delayed Neural Networks. *Neural Networks* 71, 37–44. doi:10.1016/j.neunet.2015.07.012

Chen, S., Wu, Y., Macauley, M., and Sun, X.-M. (2018). Monostability and Bistability of Boolean Networks Using Semitensor Products. *IEEE Trans. Control. Netw. Syst.* 6, 1379.

Cheng, D., Wu, Y., Zhao, G., and Fu, S. (2021). A Comprehensive Survey on STP Approach to Finite Games. *J. Syst. Sci. Complex* 34, 1666–1680. doi:10.1007/s11424-021-1232-8

Chua, L. (1971). Memristor-the Missing Circuit Element. *IEEE Trans. Circuit Theor.* 18, 507–519. doi:10.1109/tct.1971.1083337

Guo, Y., Wu, Y., and Gui, W. (2021). Stability of Discrete-Time Systems under Restricted Switching via Logic Dynamical Generator and Stp-Based Mergence of Hybrid States. *IEEE Trans. Automatic Control.* doi:10.1109/tac.2021.3105319

Guo, Y., Zhou, R., Wu, Y., Gui, W., and Yang, C. (2019). Stability and Set Stability in Distribution of Probabilistic Boolean Networks. *IEEE Trans. Automatic Control.* 64, 736–742. doi:10.1109/TAC.2018.2833170

Hu, J., and Wang, J. (2010). "Global Uniform Asymptotic Stability of Memristor-Based Recurrent Neural Networks with Time Delays," in *IEEE Congress on Cumputational Intelligence* (Spain): Barcelona), 2127–2134. doi:10.1109/ijcnn.2010.5596359

Jianmin, W., Fengqiu, L., and Sitian, Q. (2021). Exponential Stabilization of Memristor-Based Recurrent Neural Networks with Disturbance and Mixed Time Delays via Periodically Intermittent Control. *Int. J. Control Automation Syst.* 19, 2284–2296. doi:10.1007/s12555-020-0083-8

Jianmin, W., Fengqiu, L., and Sitian, Q. (2019). Global Exponential Stability of Uncertain Memristor-Based Recurrent Neural Networks with Mixed Time Delays. *Int. J. Machine Learn. Cybernetics* 10, 743–755. doi:10.1007/s13042-017-0759-4

Kobravi, K., Kinsner, W., and Filizadeh, S. (2007). Analysis of Bifurcation and Stability in a Simple Power System Using Matcont. *Can. Conf. Electr. Comput. Eng.*, 1150–1154. doi:10.1109/ccece.2007.292

Li, H., Shao, S., Qin, S., and Yang, Y. (2021). Neural Networks with Finite-Time Convergence for Solving Time-Varying Linear Complementarity

Problem. *Neurocomputing* 439, 146–158. doi:10.1016/j.neucom.2021.01.015

Li, J., Hu, M., and Guo, L. (2014). Exponential Stability of Stochastic Memristor-Based Recurrent Neural Networks with Time-Varying Delays. *Neurocomputing* 138, 92–98. doi:10.1016/j.neucom.2014.02.042

Ma, L., and Bian, W. (2021). A Novel Multiagent Neurodynamic Approach to Constrained Distributed Convex Optimization. *IEEE Trans. Cybern.* 51, 1322–1333. doi:10.1109/TCYB.2019.2895885

Qin, S., Wang, J., and Xue, X. (2015). Convergence and Attractivity of Memristor-Based Cellular Neural Networks with Time Delays. *Neural Networks* 63, 223–233. doi:10.1016/j.neunet.2014.12.002

Shen, X., and Raksincharoensak, P. (2021). Pedestrian-aware Statistical Risk Assessment. *IEEE Trans. Intell. Transport. Syst.*, 1–9. doi:10.1109/TITS.2021.3074522

Shen, X., Zhang, X., and Raksincharoensak, P. (2020). Probabilistic Bounds on Vehicle Trajectory Prediction Using Scenario Approach. *IFAC-PapersOnLine* 53, 2385–2390. doi:10.1016/j.ifacol.2020.12.038

Strukov, D. B., Snider, G. S., Stewart, D. R., and Williams, R. S. (2008). The Missing Memristor Found. *Nature* 453, 80–83. doi:10.1038/nature06932

Toyoda, M., and Wu, Y. (2021). Mayer-type Optimal Control of Probabilistic Boolean Control Network with Uncertain Selection Probabilities. *IEEE Trans. Cybern.* 51, 3079–3092. doi:10.1109/tcyb.2019.2954849

Wang, Z., Lauria, S., Fang, J. a., and Liu, X. (2007). Exponential Stability of Uncertain Stochastic Neural Networks with Mixed Time-Delays. *Chaos, Solitons & Fractals* 32, 62–72. doi:10.1016/j.chaos.2005.10.061

Wen, S., Bao, G., Zeng, Z., Chen, Y., and Huang, T. (2013). Global Exponential Synchronization of Memristor-Based Recurrent Neural Networks with Time-Varying Delays. *Neural Networks* 48, 195–203. doi:10.1016/j.neunet.2013.10.001

Wu, A., Zeng, Z., Zhu, X., and Zhang, J. (2011). Exponential Synchronization of Memristor-Based Recurrent Neural Networks with Time Delays. *Neurocomputing* 74, 3043–3050. doi:10.1016/j.neucom.2011.04.016

Wu, Y., Cheng, D., Ghosh, B. K., and Shen, T. (2019). Recent Advances in Optimization and Game Theoretic Control for Networked Systems. *Asian J. Control.* 21, 2493–2512. doi:10.1002/asjc.2303

Wu, Y., Guo, Y., and Toyoda, M. (2021). Policy Iteration Approach to the Infinite Horizon Average Optimal Control of Probabilistic Boolean Networks. *IEEE Trans. Neural Netw. Learn. Syst.* 32, 2910–2924. doi:10.1109/tnnls.2020.3008960

Yang, S., Guo, Z., and Wang, J. (2015). Robust Synchronization of Multiple Memristive Neural Networks with Uncertain Parameters via Nonlinear Coupling. *IEEE Trans. Syst. Man. Cybern, Syst.* 45, 1077–1086. doi:10.1109/tsmc.2014.2388199

Zhang, G., Shen, Y., Yin, Q., and Sun, J. (2013). Global Exponential Periodicity and Stability of a Class of Memristor-Based Recurrent Neural Networks with Multiple Delays. *Inf. Sci.* 232, 386–396. doi:10.1016/j.ins.2012.11.023

Conflict of Interest: The authors declare that the research was conducted in the absence of any commercial or financial relationships that could be construed as a potential conflict of interest.

frontiers | Frontiers in Energy Research

BRIEF RESEARCH REPORT
published: 09 May 2022
doi: 10.3389/fenrg.2022.920407

Short-Term Wind Power Prediction *via* Spatial Temporal Analysis and Deep Residual Networks

Huajin Li *

School of Architecture and Civil Engineering, Chengdu University, Chengdu, China

Wind power is a rapidly growing source of clean energy. Accurate short-term forecasting of wind power is essential for reliable energy generation. In this study, we propose a novel wind power forecasting approach using spatiotemporal analysis to enhance forecasting performance. First, the wind power time-series data from the target turbine and adjacent neighboring turbines were utilized to form a graph structure using graph neural networks (GNN). The graph structure was used to compute the spatiotemporal correlation between the target turbine and adjacent turbines. Then, the prediction models were trained using a deep residual network (DRN) for short-term wind power prediction. Considering the wind speed, the historic wind power, air density, and historic wind power in adjacent wind turbines within the supervisory control and data acquisition (SCADA) system were utilized. A comparative analysis was performed using conventional machine-learning approaches. Industrial data collected from Hami County, Xinjiang, China, were used for the case study. The computational results validate the superiority of the proposed approach for short-term wind-power forecasting.

Keywords: wind power forecasting, spatial temporal analysis, graph neural networks, deep residual network, SCADA

Edited by:
Tinghui Ouyang,
National Institute of Advanced Industrial Science and Technology (AIST), Japan

Reviewed by:
Zhiyu Sun,
The University of Iowa, United States
Heming Huang,
Wuhan University, China

***Correspondence:**
Huajin Li
lihuajin@cdu.edu.cn

Specialty section:
This article was submitted to Smart Grids,
a section of the journal Frontiers in Energy Research

Received: *14 April 2022*
Accepted: *25 April 2022*
Published: *09 May 2022*

Citation:
Li H (2022) Short-Term Wind Power Prediction via Spatial Temporal Analysis and Deep Residual Networks. Front. Energy Res. 10:920407. doi: 10.3389/fenrg.2022.920407

1 INTRODUCTION

To a large extent, wind energy can curb energy crises and global warming (Kumar et al., 2016). This renewable energy resource is valuable to both humans and the environment. However, its natural dynamics and uncertainty can deteriorate the system reliability of grid networks (Li et al., 2021a; Li et al., 2021b). Therefore, high-quality forecasting of short-term wind power is of great significance and practicability for optimal power system planning and reasonable arrangement of system reserves (He and Kusiak 2017; Onyang et al., 2019a; Onyang et al., 2019b).

According to the literature, wind power forecasting models can be primarily categorized as conventional statistical and artificial intelligence (AI) models. Conventional statistical models are usually time-series models that are capable of characterizing the linear fluctuations of wind power series. Han et al. (2017) utilized autoregressive moving average (ARMA) to fit a time-series wind power dataset. Yunus et al. (2015) employed an autoregressive integrated moving average (ARIMA) to forecast short-term wind speed data, and then integrated a physics model to forecast short-term wind power. Kavasseri and Seetharaman (2009) adopted the fractional ARIMA model to forecast the day-ahead wind power generation. Maatallah et al. (2015) recursively forecasted short-term wind power using the Hammerstein autoregressive model. In general, statistical models have exhibited good forecasting performance in very short-term wind-power forecasting tasks.

With advances in technology (Ouyang et al., 2017; Ouyang et al. 2019c; Ouyang et al. 2019d; Long et al., 2021; Li et al., 2022; Long et al., 2022), AI-based models are now being widely utilized in wind-power forecasting tasks (Tang et al., 2020; Shen et al., 2021). Wang et al. (2019) trained a support vector machine (SVM) as a regression model to forecast short-term wind power. Wang et al. (2015) used an improved version of the SVM, namely the least square support vector machine (LSSVM), to forecast wind power using the data collected from a wind farm in northern China. Yin et al. (2017) employed a single hidden feedforward neural network called an extreme learning machine (ELM) to forecast the wind power. Crisscross optimization was used to optimize the ELM model. Mezaache et al. (2016) proposed using the kernel ELM (KELM) to predict wind power in wind farms. Deo et al. (2018) developed a multi-layer perceptron (MLP), whose parameters were optimized by the firefly algorithm, to predict wind. Chen et al. (2020) trained a back-propagation neural network (BPNN) to forecast short-term wind power. Liu et al. (2018) integrated a long short-term memory recurrent neural network (LSTM-RNN) with variational model decomposition to construct a short-term wind-power prediction approach. Wan et al. (2016) performed day-ahead wind power forecasting using a deep belief network (DBN) and deep features were learned from the power data. In summary, the AI-based models are superior in terms of forecasting accuracy and efficiency (Shen et al., 2020).

Most wind power forecasting models are applied to single wind turbines, and the data include wind speed, air density, and other related variables (Lee et al., 2015; Huang et al., 2018; Ulazia et al., 2019; Long et al., 2020). Nevertheless, the power output from adjacent wind turbines in the neighborhood can also improve the wind power forecasting performance. In recent years, there has been an increasing interest in using graphs to solve time-series forecasting problems. The graph structure can handle non-Euclidean data structures (Scarselli et al., 2009). The graph neural network (GNN) (Gori et al., 2005) which learns graph structures, has become a new actively-studied topic of research. It has been successfully applied in many fields, including recommendation systems (Han et al., 2020), traffic volume prediction (Chen et al., 2019), and surface water quality prediction (Bi et al., 2020).

In this study, we propose a combinatory framework that integrates the GNN and Deep Residual Network (DRN) for short-term wind power prediction. First, the wind power from a single turbine is defined as the outtarget output. The historical wind power data from the target turbine and adjacent turbines are learned by the GNN and a graph structure with correlations of the wind power among the selected turbines is obtained. The DRN can then serve as a regression model to predict the wind power of the target turbine in the near future. The DRN considers the supervisory control and data acquisition (SCADA) variables and historic wind power from adjacent turbines as the input and the future wind power of the target turbine as the output. The computational experiments validated the superiority of the proposed approach.

The main contributions of this study are summarized below:

- This paper used graph neural network (GNN) to produce a graph structure between the target turbine power and power generated by adjacent turbines. The graph structure indicates correlation among the power outputs and enhanced power prediction outcome.
- The deep residual network (DRN) is introduced to reinforce the short-term wind power prediction performance. The impact of filter size on the prediction performance are thoroughly investigated.

The remainder of this study is organized as follows. **Section 2** provides a detailed introduction to the methods used in this study. **Section 3** presents experimental results. **Section 4** summarizes the results of this study.

2 METHODOLOGY

2.1 Graph Neural Network

As we all know, a graph is a kind of structured data, which comprises a series of objects (nodes) and relationship types (edges) (Scarselli et al., 2008). As a type of non-Euclidean data, graph analysis applied to node classification, link prediction, and clustering. Recently, GNN, a neural network model, has been used for fire detection because of its powerful ability for data processing in graph structures. They resemble convolutional neural networks (CNN) in terms of local connections, weight sharing, and multilayer networks. A GNN can generate reasoning graphs from unstructured data, which makes it advantageous over CNN.

The basic idea of a GNN is to embed nodes based on their local neighbor information (Luo et al., 2020). Intuitively, it aggregates the information of each node and its neighbors using a neural network. To obtain information about its neighbor nodes, the average method, which utilizes the neural network for aggregation, is used to aggregate the neighbor node information of a node.

As shown in **Figure 1**, the prediction task can be defined as follows: a GNN is built, the historical wind power data $X \in R^{N \times T_{in} \times D}$ (where N denotes the number of wind power generators, T_{in} denotes the length of the time window, D denotes the feature dimension of inputs) is set as the input, the spatial connectivity between each wind power generator, and the output of wind power for a prediction period $Y \in R^{N \times T_{out}}$ (where T_{out} denotes the forecast step). Based on the spatial-temporal dependencies between wind power generators, more positive deep features can be obtained for the next step.

2.2 Deep Residual Network

In the practice of deep learning, there are problems in which the learning efficiency is lowered, and accuracy cannot be effectively improved owing to the deepening of the network. The essence of this problem is the loss of effective information caused by the deepening of the training process, commonly known as the network-degradation problem. In contrast to overfitting, this problem causes an overall decline in the training and testing accuracy.

He et al. (2016) proposed the DRN, a new network which provides an idea for effectively solving the problem of gradient disappearance when the network depth increases. A DRN can

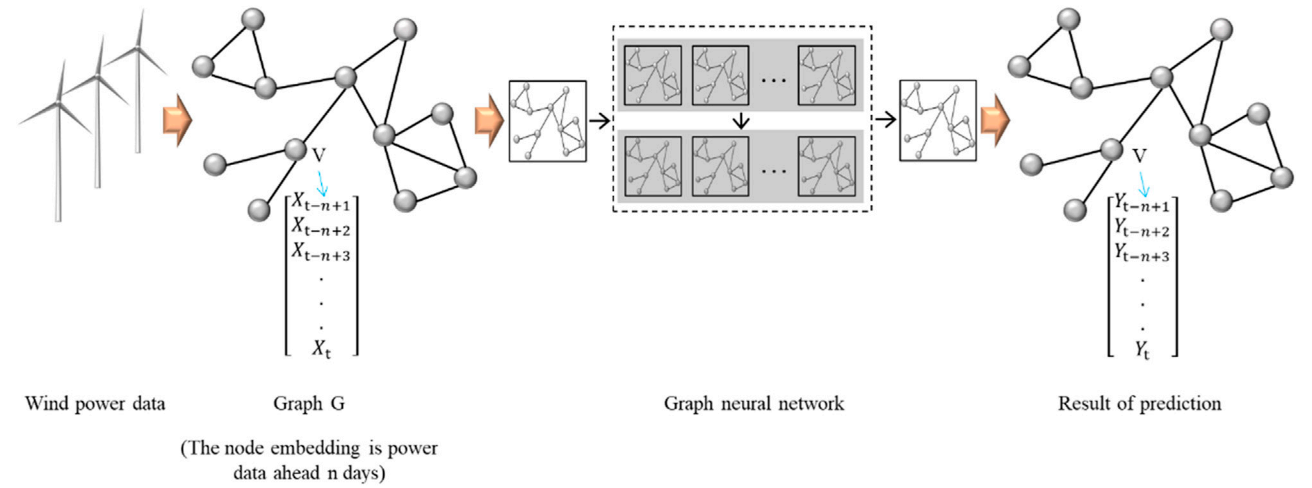

FIGURE 1 | Schematic diagram of the graph neural network.

solve this problem in two ways, namely, identity mapping and residual mapping (Sun et al., 2020a; Sun et al., 2020b). If the network has reached the optimum and continues to deepen, the residual mapping will be pushed to 0, leaving only identity mapping. Thus, the network is in the optimal state, and its performance will not decrease with the deepening of the network.

During residual learning, input x passes through a few stacked nonlinear layers (Boroumand et al., 2018). Any desired mapping can be expressed as h(x), which can directly use a shortcut connection named identity mapping x, while the stacked nonlinear layers can be used to fit a residual mapping function F(x) = h(x) − x. Therefore, assuming that the two weight layers fit the residual function F(x), let h(x) = F(x) + x. In practice, the residual mapping F(x) are found to be easier to optimize than h(x). The details of the residual block are expressed as follows:

$$\boldsymbol{y}_l = \boldsymbol{h}(\boldsymbol{x}_l) + \boldsymbol{F}(\boldsymbol{x}_l, \boldsymbol{W}_l) \tag{1}$$

$$\boldsymbol{x}_{l+1} = \boldsymbol{f}(\boldsymbol{y}_l) \tag{2}$$

where x_l is the input of the lth block of the residual network and x_{l+1} is the output. $h(x_l) = x_l$ denotes identity mapping and $f()$ denotes the activation function.

Eq. 3 can be obtained recursively:

$$\boldsymbol{x}_L = \boldsymbol{x}_l + \sum_{i=l}^{L-1} \boldsymbol{F}(\boldsymbol{x}_i, \boldsymbol{W}_i) \tag{3}$$

The input of the Lth residual block can be expressed as the sum of the input of a shallow residual block and all the complex identity mappings. Introducing a loss function ε, the parameter learning can be described as

$$\frac{\delta \varepsilon}{\delta \boldsymbol{x}_l} = \frac{\delta \varepsilon}{\delta \boldsymbol{x}_L}\left(1 + \frac{\delta}{\delta \boldsymbol{x}_l}\sum_{i=l}^{L-1} \boldsymbol{F}(\boldsymbol{x}_i, \boldsymbol{W}_i)\right) \tag{4}$$

Explicit modification of the network structure and residual mapping make it easier for the network to learn the optimal solution. In this study, the filter size and filter number were selected to optimize the computational performance.

2.3 Benchmark

In this study, three benchmarking machine learning algorithms, namely, neural network, support vector regression, and extreme learning machine, were compared with the proposed method in power prediction.

Neural networks (NN) are the underlying models of AI that have a wide range of applications in many fields (Ouyang et al., 2019a). The NN model with the backpropagation optimization mode was selected in this work. The number of hidden layers with values of 3, 4, and five and the number of hidden neurons in each hidden layer with values of 10, 20, 30, 40, and 50 were all evaluated in the training process via 10-fold cross validation. The activation function used in NN is the sigmoid function.

The (SVR) algorithm is used to find a regression plane and position all the data in a set closest to the plane (Li et al., 2020). The SVR parameters included the capacity factor C and $\gamma = 1/2\sigma^2$. The values of C (1, 10, 100, 1,000, 10,000), and σ (0.0001, 0.001, 0.01, 0.1, 1) were all evaluated in the training process via 10-fold cross-validation. The kernel function used in SVR is the RBF function.

An extreme learning machine (ELM) is a type of machine learning algorithm based on a single hidden layer feedforward neural network that is suitable for both supervised and unsupervised learning. The number of hidden neurons with values of 5, 10, 15, . . ., 100 were evaluated during the training process via 10-fold cross-validation. The activation function used in ELM is the sigmoid function (Li et al., 2018).

2.4 Evaluation Metrics

In this study, the mean square error (MSE) and coefficient of determination (R^2) were used to assess the prediction accuracy of the proposed framework. Here, R^2 measures the percentage of the variance explained by the prediction outcome. It basically interprets what percentage of variance of the actual outcome are explained by the prediction outputs.

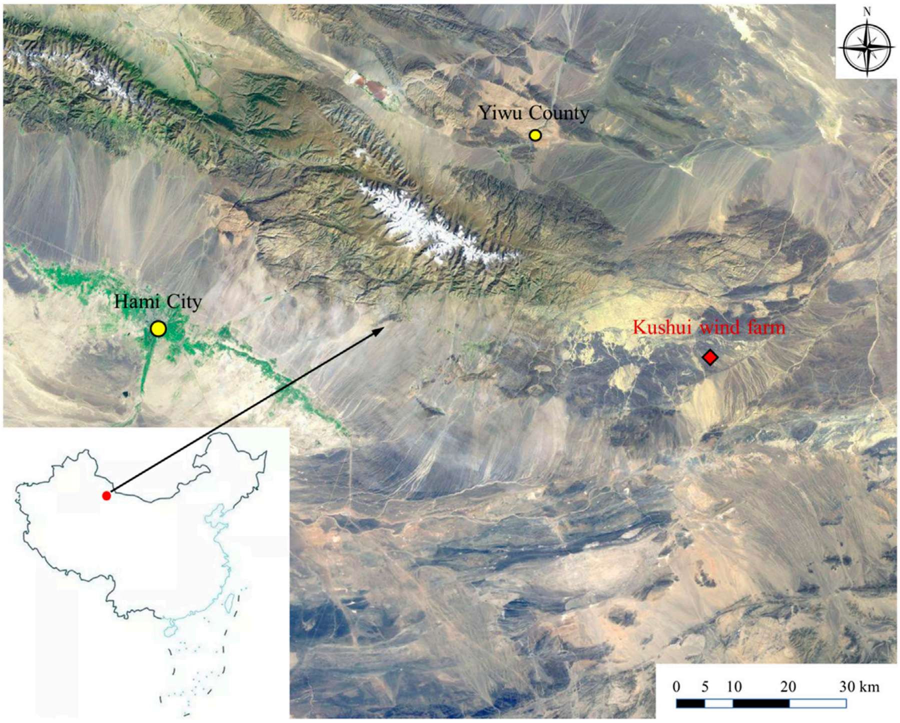

FIGURE 2 | Location of the case study wind farm in Hami County, Xinjiang, China.

TABLE 1 | Summary of the dataset in the case study.

Variable name	Unit	Description
Wind speed	m/s	The rate at which air moves relative to a fixed location on the earth
Wind direction	Rad	Refers to the direction of the wind
Temperature	°C	A numerical value used to measure the temperature of an object
Barometric pressure	kPa	The atmospheric pressure acting on a unit area
Humidity	%	Meteorological elements indicating moisture content and moisture content in the air
Historic wind power from adjacent wind turbines	kW	The generated wind power from adjacent wind turbines

$$MSE = \frac{1}{n}\sum\nolimits_{i=1}^{n}\left|\frac{y_i - \overline{y_i}}{y_i}\right| \tag{5}$$

$$R^2 = \frac{\sum\left(\bar{y} - \overline{y_i}\right)^2}{\sum\left(\bar{y} - y_i\right)^2} \tag{6}$$

where y_i, $\overline{y_i}$, $\bar{y}$, *and* n represent the actual power, predicted power, average value of y_i, and number of test datasets, respectively.

3 CASE STUDY AND DATA COLLECTION

The SCADA dataset used in this study was recorded at a wind farm named Kushui Wind Farm, which is located in the Gobi Desert in the east of the camel circle, approximately 120 km away from Hami City, Xinjiang, China. The wind farm is located in an alpine area at an altitude of 1,135—1,395 m that is rich in wind energy potential. The entire wind farm has many wind turbines distributed on open and flat terrain. Detailed information about the location is presented in **Figure 2**.

According to **Table 1**, the SCADA system collected datasets of individual wind turbines, usually including the wind speed (unit: m/s), wind direction (unit: rad), temperature (unit: °C), barometric pressure (unit: kPa), humidity (unit: %), and wind power (unit: kW). In this case, to predict the wind power, the inputs based on domain knowledge included the first five parameters above.

4 RESULTS

4.1 GNN

In this section, extensive experiments are presented to validate the effectiveness of the proposed approach. The dataset utilized for the experiments was collected from a wind farm

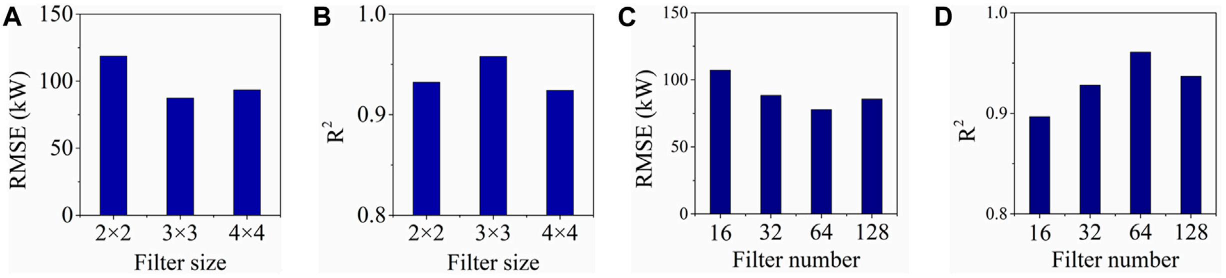

MSE changes with filter size

R^2 changes with filter size

MSE changes with filter number

R^2 changes with filter number

FIGURE 3 | Tuning the filter size and filter number for DRN.

located in Hami, Xinjiang, China, and the data collected were obtained using the SCADA system. We select only the power-related SCADA variables, as listed in **Table 1**. In this study, we collected the SCADA variables from a single target turbine and the historic wind power from its adjacent turbines, which are the neighbors of the target turbine.

A heterogeneous graph was constructed among the six turbines to learn the unified representation power time series of the target turbine. In the graph, the measured real-time power from the target turbine was treated as the target node, and the historical power series from adjacent turbines were defined as the source nodes. Inner-modality attention and inter-modality attention were used to learn the different contributions of graph-structured sources to the target node. Weight values denote the correlation between the source and target nodes. After computing all the weights, a threshold of 0.5 was implemented to determine whether the link between the two nodes was worth retaining. In the final step, a learned graph structure was utilized to determine the number of inputs of wind power generated in adjacent turbines into the prediction model to forecast the power of the target turbine in the short term.

4.2 Hyper-Parameters of DRN

In this section, the hyper-parameters of DRN are studied. Three experiments were designed to evaluate the effect of the filter size on the computation, as well as four experiments for filter number. Owing to the limitations of the hardware, the filter sizes were set as 2 × 2, 3 × 3, and 4 × 4, while the filter numbers were set as 16, 32, 64, and 128.

For the filter size, the DRN is trained with a filter number of 16, which indicates that three reference computational results can be obtained during the validation set. **Figure 3A** shows that the maximum and minimum RMSE appear at the first and second filter sizes, respectively. The RMSE increases with the filter size. As shown in **Figure 3B**, the best R^2 of 0.958 is obtained when the filter size is 3 × 3.

Next, a computation was conducted using a filter size of 3 × 3 and various values of the filter number, as mentioned above. **Figure 3C** shows that the RMSE decreases when filter number increases, and the optimal solution occurs when the filter number is 64, possibly owing to the overfitting of the model with continuously increasing filter numbers. **Figure 3D** provides the same evidence for the computation. Therefore, the best performance is achieved when the filter size and number are 3 × 3 and 64, respectively.

4.3 Wind Power Prediction

Experiments were performed with three selected algorithms were performed using two measurement metrics (RMSE and R^2) to comprehensively evaluate the prediction performance of the proposed method. The hyperparameters of all the algorithms were tuned. In each training-validation experiment, the steps of input time and output time range were 1, 2, . . ., 20. In all the experiments conducted, the wind power was predicted for different input and output time steps. The relevant computational behavior is shown in **Figure 4**, which shows the correspondence between the predicted power obtained numerically and experimentally.

According to **Figure 4**, the RMSE from all the algorithms decreases when the input time step increases, whereas it increases when the output time step increases. When the same length of historical data is input, longer the output steps yield larger prediction errors. Furthermore, a deeper analysis of the results for R^2 indicated good linearity between the predicted and measured wind power values and the error occurring in the long-term horizon of the output time step. The two measurement metrics yielded similar results. Overall, the computational results demonstrated that the proposed method based on DRN significantly outperformed the other three benchmarking machine learning algorithms, exhibiting the lowest RMSE and maximal R^2 with increasing input time step and output time step. The DRN exhibited its outperformance in terms of prediction in the temporal domain owing to its ability to handle redundant information.

Moreover, this study also investigated the influence of the size of the training samples on the prediction results. Three approaches based on NN, SVR, and ELM were adopted to demonstrate the superiority of the DRN model. The hyperparameters of all the algorithms were selected from previous results, and the data samples ranged from 400—4,000, at intervals of 200.

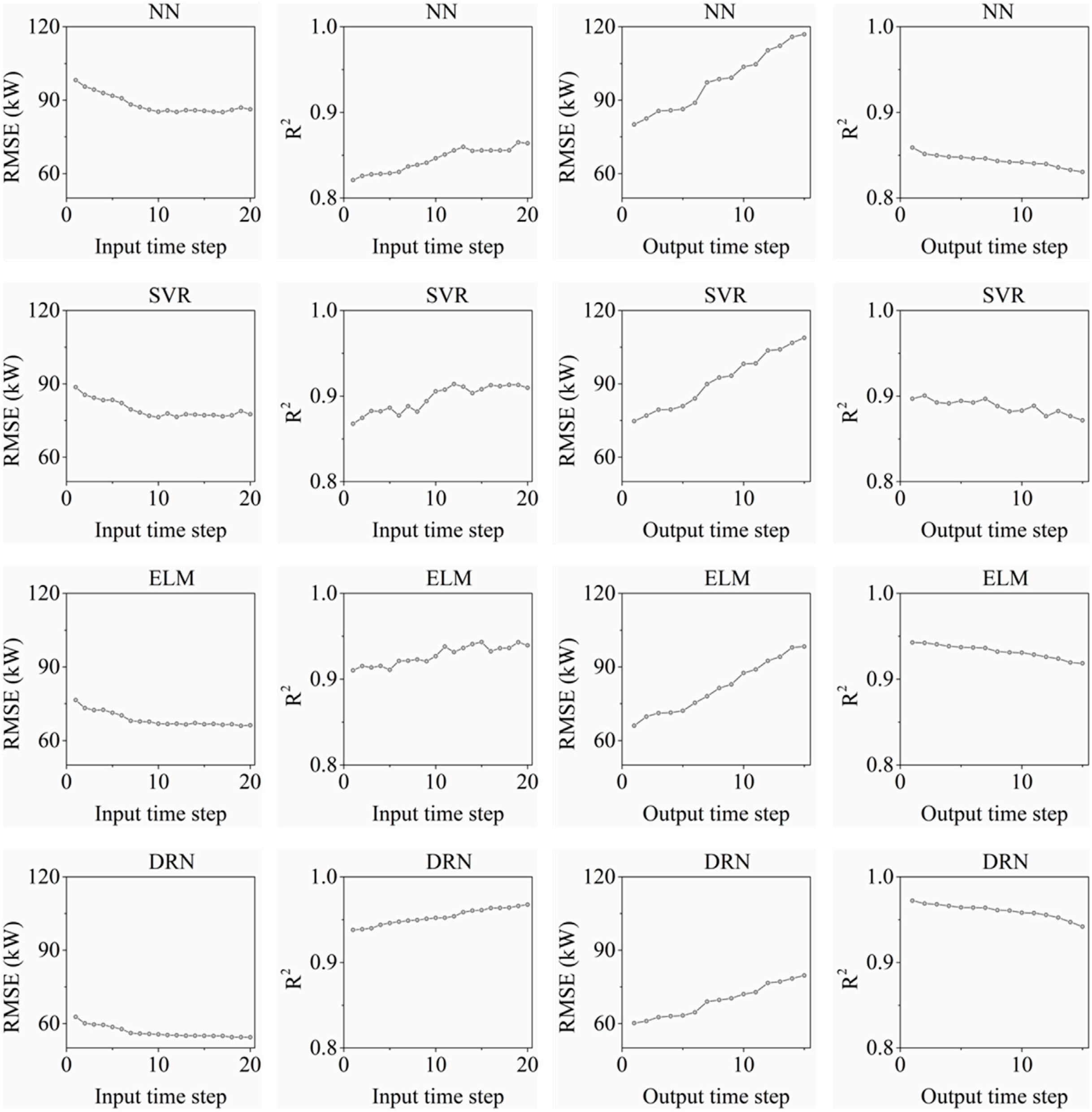

FIGURE 4 | Impact of input/output size on the prediction performance.

From **Figure 5**, it can be observed that the prediction performance varies with the training data size. As the training data size increases, the RMSE of NN decreases from 116.61 to 80.07 kW. The smallest RMSE values of SVR, ELM, and DRN were 74.74, 66.25 and 60.28 kW, respectively. The R^2 of the DRN increases from 0.941 to 0.976, and the maximal R^2 values of the other three algorithms were 0.862, 0.908, and 0.943, respectively. The computational results imply that the worst case result from DRN surpasses the other best cases. This phenomenon provides strong evidence for DRN optimization.

Table 2 shows that the proposed DRN-based method produces the lowest prediction error and best prediction performance based on the case study presented. The mean values of the RMSE from NN, SVR, ELM, and DRN were 99.32, 88.26, 80.53, and 70.19, respectively. The Std. for the four methods are 10.79, 12.36, 10.46, and 5.93, respectively. For R^2, the mean value from DRN is 0.96, which possesses the most advantages compared to NN, SVR, and ELM. This phenomenon indicates that the proposed method for wind-power prediction is a statistical outlier and can be utilized to further improve related prediction tasks.

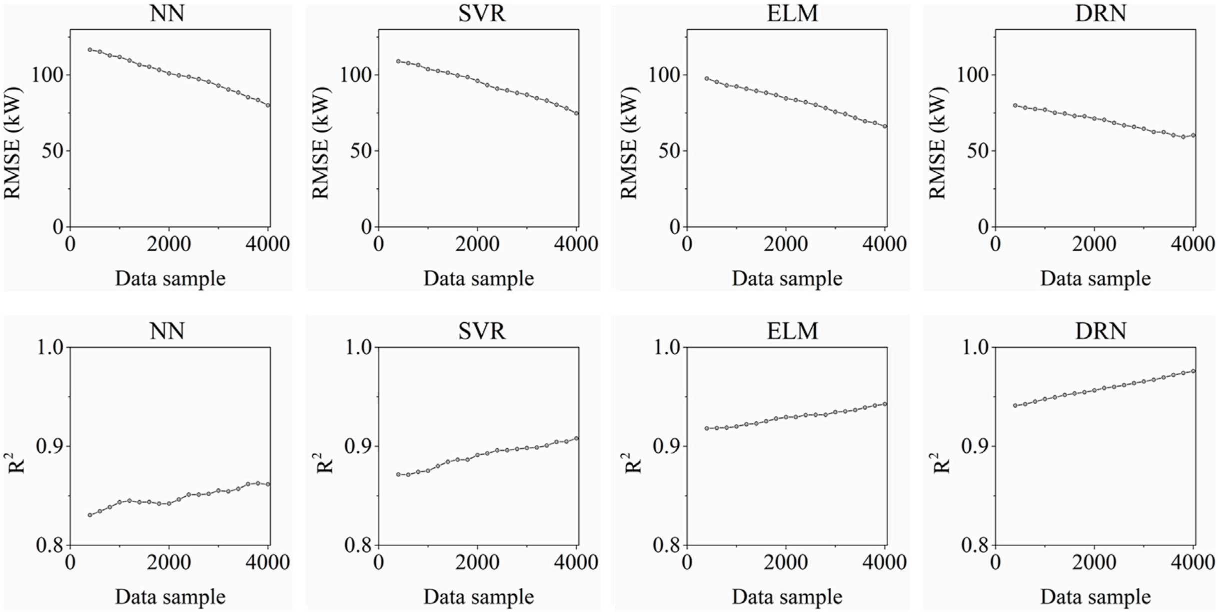

FIGURE 5 | Impact of training sample size on the prediction performance.

TABLE 2 | Summary of the wind power forecasting performance.

		NN	SVR	ELM	DRN
RMSE (kW)	Mean	99.32	88.26	80.53	70.19
	Std	10.79	12.36	10.46	5.93
R^2	Mean	0.85	0.89	0.93	0.96
	Std	0.82%	1.10%	0.71%	1.13%

5 CONCLUSION

In this study, we present a data-driven short-term wind power prediction framework that integrates GNN and DRN. GNN was used to obtain a graph structure to describe the correlation between the power of the target turbine and that generated by adjacent turbines. The DRN was trained to predict the short-term wind power. The SCADA variables, along with the power generation of adjacent turbines, were all considered as inputs of the forecasting model. A comparative analysis was conducted against other benchmark forecasting algorithms.

Computational results demonstrated that the graph structure can effectively capture the spatial-temporal relationships among adjacent turbines. Comparative analysis demonstrated that the DRN has superior power in short-term wind power forecasting. The proposed approach is expected to be useful to field engineers at wind farms. Ouyang et al., 2019c.

DATA AVAILABILITY STATEMENT

The original contributions presented in the study are included in the article/Supplementary Material, further inquiries can be directed to the corresponding author.

AUTHOR CONTRIBUTIONS

HL conceptualized the study, contributed to the study methodology, data curation, software and formal analysis, and wrote the original draft.

FUNDING

This research is supported by the “Miaozi project” of scientific and technological innovation in Sichuan Province, China (Grant No. 2021090) and the Opening fund of State Key Laboratory of Geohazard Prevention and Geoenvironment Protection (Chengdu University of Technology) (Grant No. SKLGP 2021K014).

REFERENCES

Ait Maatallah, O., Achuthan, A., Janoyan, K., and Marzocca, P. (2015). Recursive Wind Speed Forecasting Based on Hammerstein Auto-Regressive Model. *Appl. Energy* 145, 191–197. doi:10.1016/j.apenergy.2015.02.032

Bi, X., Liu, Z., He, Y., Zhao, X., Sun, Y., and Liu, H. (2020). GNEA: a Graph Neural Network with ELM Aggregator for Brain Network Classification. *Complexity* 2020. doi:10.1155/2020/8813738

Boroumand, M., Chen, M., and Fridrich, J. (2018). Deep Residual Network for Steganalysis of Digital Images. *IEEE Trans. Inf. Forensics Secur.* 14 (5), 1181–1193. doi:10.1109/TIFS.2018.2871749

Chen, C., Li, K., Teo, S. G., Zou, X., Wang, K., Wang, J., et al. (2019). Gated Residual Recurrent Graph Neural Networks for Traffic Prediction. *Aaai* 33 (1), 485–492. doi:10.1609/aaai.v33i01.3301485

Chen, G., Li, L., Zhang, Z., and Li, S. (2020). Short-term Wind Speed Forecasting with Principle-Subordinate Predictor Based on Conv-Lstm and Improved Bpnn. *IEEE Access* 8, 67955–67973. doi:10.1109/access.2020.2982839

Deo, R. C., Ghorbani, M. A., Samadianfard, S., Maraseni, T., Bilgili, M., and Biazar, M. (2018). Multi-layer Perceptron Hybrid Model Integrated with the Firefly Optimizer Algorithm for Windspeed Prediction of Target Site Using a Limited Set of Neighboring Reference Station Data. *Renew. energy* 116, 309–323. doi:10.1016/j.renene.2017.09.078

Gori, M., Monfardini, G., and Scarselli, F. (2005). "A New Model for Learning in Graph Domainsconf," in Proceedings. 2005 IEEE International Joint Conference on Neural Networks, 2005, 31 July-4 Aug. 2005, Montreal, QC, Canada 2 (2005), 729–734. doi:10.1109/IJCNN.2005.1555942

Han, P., Li, Z., Liu, Y., Zhao, P., Li, J., Wang, H., et al. (2020). "Contextualized Point-Of-Interest Recommendation," in Proceedings of the International Joint Conferences on Artificial Intelligence Organization, Yokohama Yokohama, Japan, January 2020. doi:10.24963/ijcai.2020/344

Han, Q., Meng, F., Hu, T., and Chu, F. (2017). Non-parametric Hybrid Models for Wind Speed Forecasting. *Energy Convers. Manag.* 148, 554–568. doi:10.1016/j.enconman.2017.06.021

He, K., Zhang, X., Ren, S., and Sun, J. (2016). "Deep Residual Learning for Image Recognition," in Proceedings of the IEEE conference on computer vision and pattern recognition, Las Vegas, NV, USA, June 2016, 770–778. doi:10.1109/cvpr.2016.90

He, Y., and Kusiak, A. (2017). Performance Assessment of Wind Turbines: Data-Derived Quantitative Metrics. *IEEE Trans. Sustain. Energy* 9 (1), 65–73. doi:10.1109/TSTE.2017.2715061

Huang, H., Liu, F., Zha, X., Xiong, X., Ouyang, T., Liu, W., et al. (2018). Robust Bad Data Detection Method for Microgrid Using Improved ELM and DBSCAN Algorithm. *J. Energy Eng.* 144 (3), 04018026. doi:10.1061/(asce)ey.1943-7897.0000544

Kavasseri, R. G., and Seetharaman, K. (2009). Day-ahead Wind Speed Forecasting Using F-ARIMA Models. *Renew. Energy* 34 (5), 1388–1393. doi:10.1016/j.renene.2008.09.006

Kumar, Y., Ringenberg, J., Depuru, S. S., Devabhaktuni, V. K., Lee, J. W., Nikolaidis, E., Andersen, B., and Afjeh, A. (2016). Wind Energy: Trends and Enabling Technologies. *Renew. Sustain. Energy Rev.* 53, 209–224. doi:10.1016/j.rser.2015.07.200

Lee, G., Ding, Y., Genton, M. G., and Xie, L. (2015). Power Curve Estimation with Multivariate Environmental Factors for Inland and Offshore Wind Farms. *J. Am. Stat. Assoc.* 110 (509), 56–67. doi:10.1080/01621459.2014.977385

Li, H., Deng, J., Feng, P., Pu, C., Arachchige, D. D. K., and Cheng, Q. (2021a). Short-Term Nacelle Orientation Forecasting Using Bilinear Transformation and ICEEMDAN Framework. *Front. Energy Res.* 9, 780928. doi:10.3389/fenrg.2021.780928

Li, H., Deng, J., Yuan, S., Feng, P., and Arachchige, D. D. K. (2021b). Monitoring and Identifying Wind Turbine Generator Bearing Faults Using Deep Belief Network and EWMA Control Charts. *Front. Energy Res.* 9, 799039. doi:10.3389/fenrg.2021.799039

Li, H., He, Y., Xu, Q., Deng, j., Li, W., and Wei, Y. (2022). Detection and Segmentation of Loess Landslides via Satellite Images: a Two-phase Framework. *Landslides* 19, 673–686. doi:10.1007/s10346-021-01789-0

Li, H., Xu, Q., He, Y., and Deng, J. (2018). Prediction of Landslide Displacement with an Ensemble-Based Extreme Learning Machine and Copula Models. *Landslides* 15 (10), 2047–2059. doi:10.1007/s10346-018-1020-2

Li, H., Xu, Q., He, Y., Fan, X., and Li, S. (2020). Modeling and Predicting Reservoir Landslide Displacement with Deep Belief Network and EWMA Control Charts: a Case Study in Three Gorges Reservoir. *Landslides* 17 (3), 693–707. doi:10.1007/s10346-019-01312-6

Liu, H., Mi, X., and Li, Y. (2018). Smart Multi-step Deep Learning Model for Wind Speed Forecasting Based on Variational Mode Decomposition, Singular Spectrum Analysis, LSTM Network and ELM. *Energy Convers. Manag.* 159, 54–64. doi:10.1016/j.enconman.2018.01.010

Long, H., Li, P., and Gu, W. (2020). A Data-Driven Evolutionary Algorithm for Wind Farm Layout Optimization. *Energy* 208, 118310. doi:10.1016/j.energy.2020.118310

Long, H., Xu, S., and Gu, W. (2022). An Abnormal Wind Turbine Data Cleaning Algorithm Based on Color Space Conversion and Image Feature Detection. *Appl. Energy* 311, 118594. doi:10.1016/j.apenergy.2022.118594

Long, H., Zhang, C., Geng, R., Wu, Z., and Gu, W. (2021). A Combination Interval Prediction Model Based on Biased Convex Cost Function and Auto-Encoder in Solar Power Prediction. *IEEE Trans. Sustain. Energy* 12 (3), 1561–1570. doi:10.1109/tste.2021.3054125

Luo, D., Cheng, W., Xu, D., Yu, W., Zong, B., Chen, H., et al. (2020). Parameterized Explainer for Graph Neural Network. *Adv. neural Inf. Process. Syst.* 33, 19620–19631. doi:10.48550/arXiv.2011.04573

Mezaache, H., Bouzgou, H., and Raymond, C. (2016). "Kernel Principal Components Analysis with Extreme Learning Machines for Wind Speed Prediction," in Proceedings of the Seventh International Renewable Energy Congress, IREC2016, March 2016, Hammamet, Tunisia.

Ouyang, T., Zha, X., Qin, L., He, Y., and Tang, Z. (2019a). Prediction of Wind Power Ramp Events Based on Residual Correction. *Renew. Energy* 136, 781–792. doi:10.1016/j.renene.2019.01.049

Ouyang, T., He, Y., Li, H., Sun, Z., and Baek, S. (2019b). Modeling and Forecasting Short-Term Power Load with Copula Model and Deep Belief Network. *IEEE Trans. Emerg. Top. Comput. Intell.* 3 (2), 127–136. doi:10.1109/tetci.2018.2880511

Ouyang, T., Pedrycz, W., Reyes-Galaviz, O. F., and Pizzi, N. J. (2019c). Granular Description of Data Structures: A Two-phase Design. *IEEE Trans. Cybern.* 51 (4), 1902–1912. doi:10.1109/TCYB.2018.2887115

Ouyang, T., Pedrycz, W., and Pizzi, N. J. (2019d). Rule-based Modeling with DBSCAN-Based Information Granules. *IEEE Trans. Cybern.* 51 (7), 3653–3663. doi:10.1109/TCYB.2019.2902603

Ouyang, T., Kusiak, A., and He, Y. (2017). Modeling Wind-Turbine Power Curve: A Data Partitioning and Mining Approach. *Renew. Energy* 102, 1–8. doi:10.1016/j.renene.2016.10.032

Scarselli, F., Gori, M., Tsoi, A. C., Hagenbuchner, M., and Monfardini, G. (2008). The Graph Neural Network Model. *IEEE Trans. Neural Netw.* 20 (1), 61–80. doi:10.1109/TNN.2008.2005605

Shen, X., Ouyang, T., Yang, N., and Zhuang, J. (2021). Sample-Based Neural Approximation Approach for Probabilistic Constrained Programs. *IEEE Trans. Neural Netw. Learn. Syst.* 1-8. doi:10.1109/tnnls.2021.3102323

Shen, X., Zhang, Y., Sata, K., and Shen, T. (2020). Gaussian Mixture Model Clustering-Based Knock Threshold Learning in Automotive Engines. *IEEE/ASME Trans. Mechatron.* 25 (6), 2981–2991. doi:10.1109/tmech.2020.3000732

Sun, Z., He, Y., Gritsenko, A., Lendasse, A., and Baek, S. (2020a). Embedded Spectral Descriptors: Learning the Point-wise Correspondence Metric via Siamese Neural Networks. *J. Comput. Des. Eng.* 7 (1), 18–29. doi:10.1093/jcde/qwaa003

Sun, Z., Rooke, E., Charton, J., He, Y., Lu, J., and Baek, S. (2020b). Zernet: Convolutional Neural Networks on Arbitrary Surfaces via Zernike Local Tangent Space Estimation. *Comput. Graph. Forum* 39 (6), 204–216. doi:10.1111/cgf.14012

Tang, Z., Li, Y., Chai, X., Zhang, H., and Cao, S. (2020). Adaptive Nonlinear Model Predictive Control of Nox Emissions under Load Constraints in Power Plant Boilers. *J. Chem. Eng. Jpn.* 53 (1), 36–44. doi:10.1252/jcej.19we142

Ulazia, A., Sáenz, J., Ibarra-Berastegi, G., González-Rojí, S. J., and Carreno-Madinabeitia, S. (2019). Global Estimations of Wind Energy Potential Considering Seasonal Air Density Changes. *Energy* 187, 115938. doi:10.1016/j.energy.2019.115938

Wan, J., Liu, J., Ren, G., Guo, Y., Yu, D., and Hu, Q. (2016). Day-ahead Prediction of Wind Speed with Deep Feature Learning. *Int. J. Pattern Recognit. Artif. Intell.* 30 (5), 1650011. doi:10.1142/s0218001416500117

Wang, J., Wang, S., and Yang, W. (2019). A Novel Non-linear Combination System for Short-Term Wind Speed Forecast. *Renew. Energy* 143, 1172–1192. doi:10.1016/j.renene.2019.04.154

Wang, Y., Wang, J., and Wei, X. (2015). A Hybrid Wind Speed Forecasting Model Based on Phase Space Reconstruction Theory and Markov Model: A Case Study of Wind Farms in Northwest China. *Energy* 91, 556–572. doi:10.1016/j.energy.2015.08.039

Yin, H., Dong, Z., Chen, Y., Ge, J., Lai, L. L., Vaccaro, A., et al. (2017). An Effective Secondary Decomposition Approach for Wind Power Forecasting Using Extreme Learning Machine Trained by Crisscross Optimization. *Energy Convers. Manag.* 150, 108–121. doi:10.1016/j.enconman.2017.08.014

Yunus, K., Thiringer, T., and Chen, P. (2015). ARIMA-based Frequency-Decomposed Modeling of Wind Speed Time Series. *IEEE Trans. Power Syst.* 31 (4), 2546–2556.

Conflict of Interest: The author declares that the research was conducted in the absence of any commercial or financial relationships that could be construed as a potential conflict of interest.

frontiers | Frontiers in Energy Research

BRIEF RESEARCH REPORT
published: 12 May 2022
doi: 10.3389/fenrg.2022.920837

SCADA Data Based Wind Power Interval Prediction Using LUBE-Based Deep Residual Networks

Huajin Li*

School of Architecture and Civil Engineering, Chengdu University, Chengdu, China

Wind is a pollution-free renewable energy source. It has attracted increasing attention owing to the decarbonization of electricity generation. However, owing to the dynamic nature of wind speed, ensuring a stable supply of wind energy to electric grid networks is challenging. Therefore, accurate short-term forecasting of wind power prediction plays a key role for wind farm engineers. With the boom in AI technologies, deep-learning-based forecasting models have demonstrated superior performance in wind power forecasting. This paper proposes a short-term deep-learning-based interval prediction algorithm for forecasting short-term wind power generation in wind farms. The proposed approach combines the lower upper bound estimation (LUBE) method and a deep residual network (DRN). Wind farm data collected in northwestern China are selected for this empirical study. The proposed approach is compared with three benchmark short-term forecasting approaches. Extensive experiments conducted on the data collected from five wind turbines in 2021 indicate that the proposed algorithm is efficient, stable, and reliable.

Keywords: SCADA data, wind power, deep residual networks, LUBE approach, interval prediction

Edited by:
Xun Shen,
Tokyo Institute of Technology, Japan

Reviewed by:
Huan Long,
Southeast University, China
Zhenhao Tang,
School of Automatic Engineering.Northeast Electric Power University, China

***Correspondence:**
Huajin Li
lihuajin@cdu.edu.cn

Specialty section:
This article was submitted to Smart Grids, a section of the journal Frontiers in Energy Research

Received: *15 April 2022*
Accepted: *27 April 2022*
Published: *12 May 2022*

Citation:
Li H (2022) SCADA Data Based Wind Power Interval Prediction Using LUBE-Based Deep Residual Networks. Front. Energy Res. 10:920837. doi: 10.3389/fenrg.2022.920837

1 INTRODUCTION

Wind power, a major source of renewable energy, has been widely developed worldwide to supplement and replace traditional fossil fuels (He and Kusiak 2017; Javed et al., 2020). Owing to the intermittent and stochastic nature of wind, wind power systems face challenges in terms of reliability and stability. Thus, high-quality wind power predictions are expected in practice (Long et al., 2020; Long et al., 2021).

According to a literature review, point estimation plays a dominant role in wind power prediction. Haykin (1994) experimented with multiple architectures of neural networks to explore the power of wind-turbine energy prediction. Kelouwani et al. (2004) first used a neural network and wind speed to forecast wind power based on power curves. Tascikaraoglu and Uzunoglu (2014) proposed the use of an autoregressive integrated moving average model to forecast short-term wind power. Ren et al. (2014) applied adaboost-backpropagation to improve the neural network algorithm and achieved an improved wind power prediction performance. Wu and Peng, (2017) performed short-term wind power prediction using k-means clustering with a bagging neural network. Zhang et al. (2016) adopted a probabilistic support vector machine to predict short-term wind power. Deng et al. (2020) trained deep neural networks (DNNs) to forecast short-term wind power. Li et al. (2021a) introduced a framework called ICEEMDAN to decompose wind power time-series data and discovered that the prediction performance was enhanced. Li et al. (2021b) trained a deep belief network to forecast short-term wind power and used EWMA control charts to monitor abnormal wind power prediction errors.

In summary, the point-based prediction of wind power has already achieved promising performance in practice (Long et al., 2022).

High-quality wind power forecasting is expected to reduce uncertainty at various time scales (Ouyang et al., 2017; Huang et al., 2018; Tang et al., 2020). However, point estimation, which outputs a deterministic value, fails to provide sufficient consideration of the prediction uncertainty (Shen and Shen 2018; Ouyang et al., 2020). In comparison, interval prediction with a certain confidence level is gaining popularity among scholars and engineers (Shen et al., 2020). Unlike the point estimation approach, interval prediction quantifies the uncertainty of wind power and provides probabilistic estimation in the temporal domain.

Among various interval prediction methods, the interval prediction model based on the lower and upper bound estimation (LUBE) (Khosravi et al., 2010) approach has become the most popular and has attracted considerable attention. Following the LUBE architecture, a prediction algorithm with two outputs instead of a single output was utilized. The two outputs, which represent the upper and lower bounds, share the same input data vector and hidden layer. Both the loss function and training strategy are identical for both outputs (Sun et al., 2020a).

In this paper, we propose a combination of the LUBE approach with a deep residual network (DRN) for short-term wind power prediction. The DRN is first modified with two outputs that represent the upper and lower bounds of the prediction interval. The LUBE approach was then utilized to train the DRN algorithm. Here, the coverage width-based criterion (CWC) was selected as the objective function to optimize the DRN, and the Adam optimizer was adopted to optimize the CWC. Field data collected from a wind farm located in northwest China were used for the case study.

The main contributions of this paper can be concluded as follows:

- A new approach combining a DRN and the LUBE method is proposed for wind power interval prediction.
- Supervisory control and data acquisition (SCADA) data considering wind speed, wind direction, ambient temperature, air density, historic power output, gearbox bearing temperature, rotor speed, and pitch angle are utilized as inputs for power interval prediction.

The remainder of this paper is organized as follows. **Section 2** introduces the DRN structure, the LUBE approach, other popular interval prediction algorithms, and evaluation metrics. **Section 3** introduces the dataset and the variables used for interval prediction. **Section 4** presents the computational results. **Section 5** concludes the paper.

2 METHODOLOGY

2.1 Deep Residual Network

DNNs have achieved promising performances in both classification and regression tasks (Li et al., 2020; Li et al., 2022). However, in practice, gradient vanishing or explosion during the training process presents a challenge. The DRN, which incorporates the residual unit into the DNNs, is capable of offering superior performance in supervised learning tasks, such as image classification, target detection, and statistical anomaly detection (Sun et al., 2020b; Shen et al., 2021; Shen and Raksincharoensak, 2021).

According to a literature review (He et al., 2016), a single residual unit can be expressed as follows:

$$X_{l+1} = f\left(X_l + F\left(X_l\right)\right) \tag{1}$$

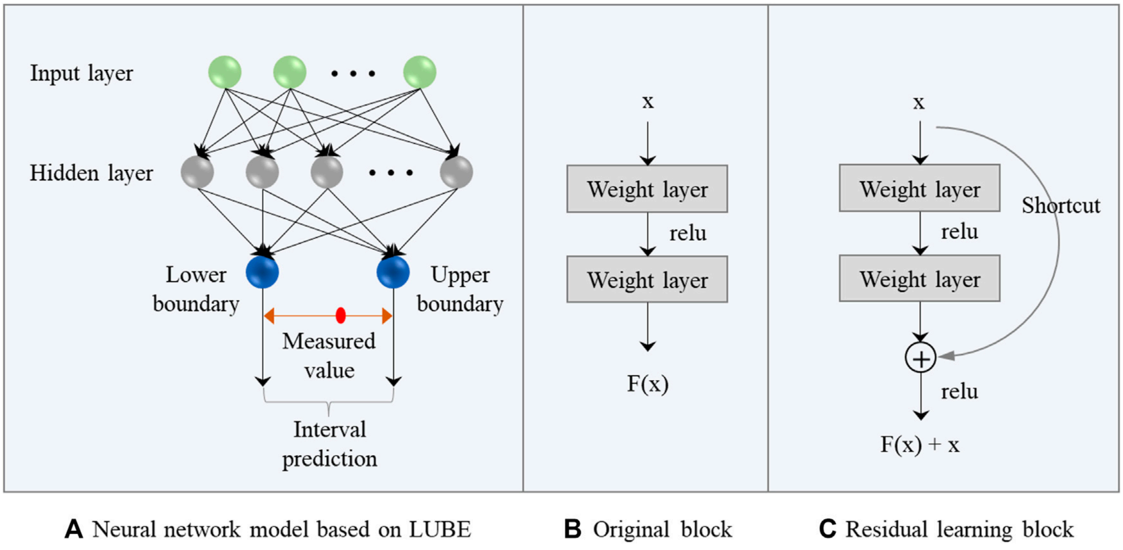

FIGURE 1 | Deep residual network integrated with LUBE approach.

TABLE 1 | SCADA variables utilized in this study.

Environmental	Unit	Electrical	Unit	Mechanical	Unit	Control	Unit
Wind speed	m/s	Historic wind power	MW	Gearbox bearing temperature	°F	Pitch angle	°
Wind direction	°			Rotor speed	rpm		
Ambient temperature	°F						
Air density	kg/m^3						

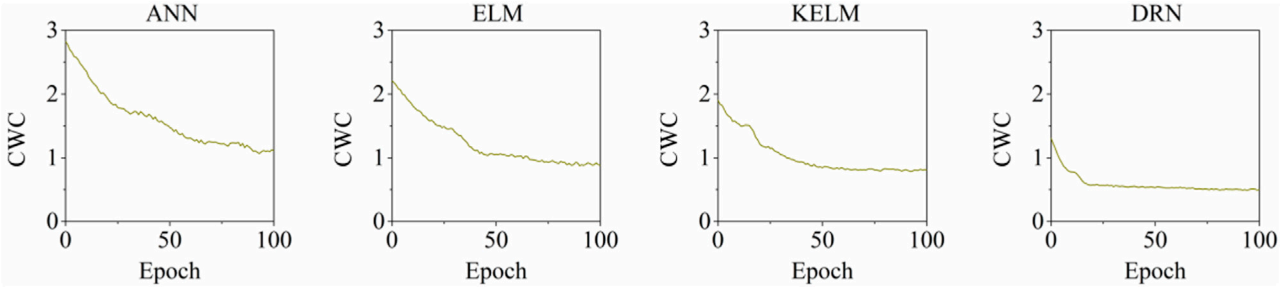

FIGURE 2 | Changes of CWC at different training epochs.

where X_l and X_{l+1} represent the input and output of the residual unit, respectively; $F()$ denotes the residual function that contains a convolution operator, batch normalization, and rectified linear unit (ReLU); and $f()$ represents a ReLU activation function. The output of the residual function is added to the input and passed through the ReLU activation function. During the training process, the gradient of the loss function with respect to any hidden layer can be derived using the chain rule used in backpropagation.

Compared with the conventional DNN architecture, the DRN has two major advantages: first, it does not experience the problem of gradient vanishing or explosion during the training process; second, the backpropagation step enables gradient progression from the deeper layer to the shallow layer. Thus, the residual characteristics enable a smooth transfer of information between the deeper and shallow layers. This guarantees successful training of the DRN in practice.

2.2 Lower Upper Bound Estimation Approach With Deep Residual Network

A common misconception in practice during interval prediction is that data follow a certain distribution (Shen et al., 2019). Although such an assumption can simplify the construction of prediction intervals (PIs), it can cause other problems concerning the possible deviation of the data from the pre-assumed distribution (Ouyang et al., 2019b; Ouyang et al., 2019c).

Khosravi et al. (2010) first proposed the LUBE approach for interval prediction in 2011. The proposed approach is based on the PI of neural networks and aims to train neural networks by minimizing the objective function of the PI. Instead of a single output for point-based estimation, the LUBE approach involves two outputs: the upper and lower boundaries of the PI. Here, the PI includes the predicted values within a certain range, along with a computed probability as the confidence level, which is based on historical data. Generally, high-quality interval prediction refers

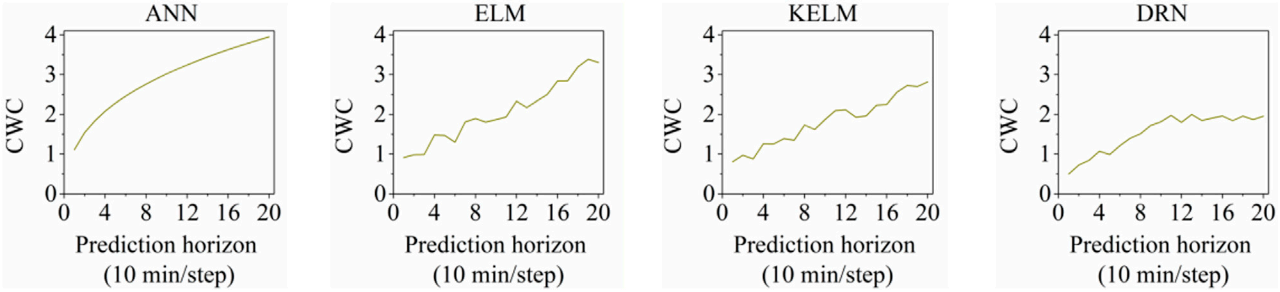

FIGURE 3 | Changes of CWC at different prediction horizons.

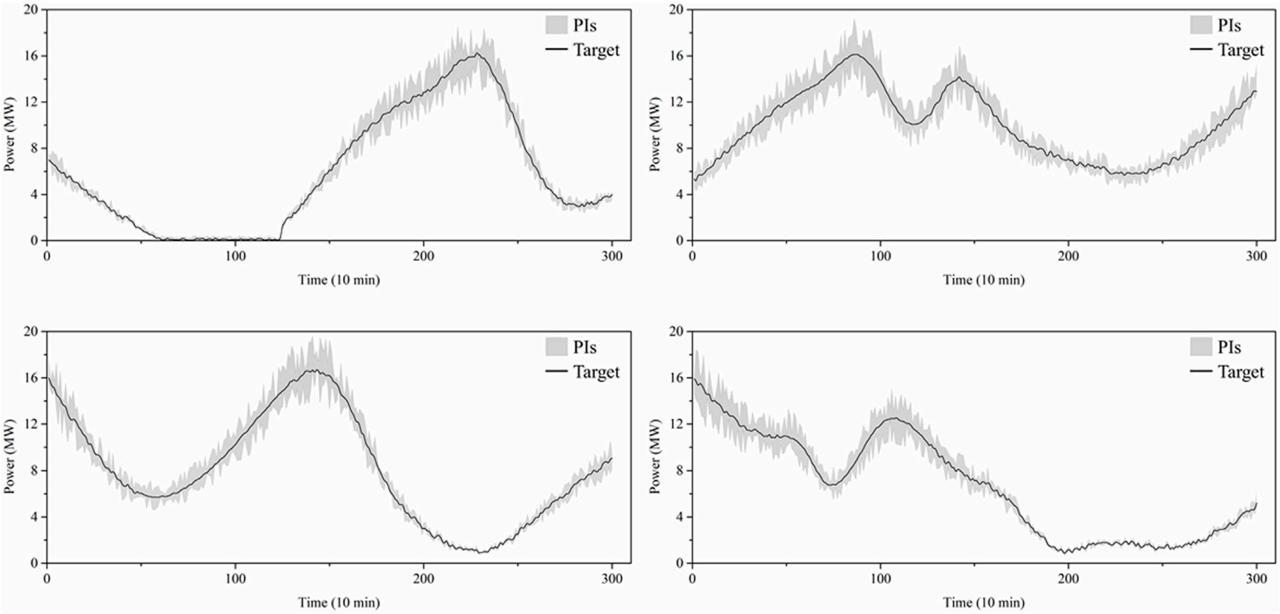

FIGURE 4 | Constructed PIs and actual target wind power of the test dataset.

TABLE 2 | Summary of the interval prediction performance.

Algorithm	Evaluation metrics					
	PICP(%)	Std (%)	PINAW (%)	Std (%)	CWC	Std
ANN	91.37	5.82	16.83	3.71	0.24	0.03
ELM	89.76	4.97	23.97	5.82	0.27	0.06
KELM	92.01	4.64	15.88	3.13	0.19	0.04
DRN	92.45	5.24	13.23	4.29	0.18	0.03

to the actual measured values that fall within the PI as much as possible, whereas the PI is as narrow as possible.

In this study, the LUBE approach was incorporated with a DRN to provide PIs for short-term wind energy. **Figure 1** shows the revised version of the DRN that was applied using the LUBE approach. **Figure 1A** shows the general neural network architecture using the LUBE approach for interval prediction. It contains an input layer, hidden layer, and two output layers that represent both the lower and upper boundaries of the PIs. The PI denotes the interval between the two boundaries, and a correct prediction implies that the actual value falls within the PI. The hidden layers of the DRN differ from those in conventional neural networks. Instead of a layer with hidden nodes (see **Figure 1B**), the DRN contains residual blocks as hidden layers. As shown in **Figure 1C**, each residual block inputs the data into a residual function, and the output of the residual function is concatenated with the original input. It then passes through the ReLU activation function, as described in **Section 2.1**.

According to **Figure 1**, the main advantage of the proposed method that uses a DRN and the LUBE approach for short-term wind power forecasting is evident: it simplifies the process of PI construction. The LUBE approach uses a feed-forward strategy to estimate the lower and upper boundaries of the PI. By outputting two point forests that represent the two boundaries, the actual short-term wind power is expected to fall within the PI.

2.3 Other Interval Prediction Algorithms

Besides the DRN, there are other popular benchmark interval prediction algorithms, such as artificial neural networks (ANN), extreme learning machines (ELM), and kernel extreme learning machines (KELM). They achieved promising results in other time-series interval prediction tasks and were also selected and trained in this study for comparative analysis against the proposed DRN using the same LUBE approach.

The ANN is a nonparametric supervised learning analytic algorithm, that is, widely used for classification and regression tasks (Li et al., 2018). It is capable of performing high-quality predictions, as it is modeled after the processes of learning in a cognitive system. The ANN can accurately and effectively extract patterns from the dataset and construct mapping relationships between inputs and outputs. A typical ANN architecture contains an input layer, one or more hidden layers, and an output layer. The output of each neuron inside the layers is based on the neuron of the previous layer and its associated weights, which can be expressed by **Eq. 2**:

$$\alpha_{ij} = f_j\left(\sum_{k=1}^{n_{(j-1)}} \left(\alpha_{k(j-1)} * \omega_{ki(j-1)} \right) + b_{ij} \right) \tag{2}$$

where α_{ij} and b_{ij} are the output and bias of the ith neuron in the jth hidden layer, respectively; $\alpha_{k(j-1)}$ and $\omega_{ki(j-1)}$ represent the output and weight of the neuron from the previous layer, respectively; $n_{(j-1)}$ is the total number of neurons in layer $(j-1)$ and $f_j()$ is the activation function of the *j*th layer.

An ELM is a novel single-hidden-layer feedforward neural network (SLFN) proposed by Huang et al. (2018). It randomly initializes the linking weights and biases, and contains a limited number of hidden neurons defined by the users. With only one hidden layer, the ELM is capable of obtaining unique optimal output weights using only a one-step calculation, and thus obtains a high training speed. For a given dataset with input $\mathbf{x_j}$ and target output $\boldsymbol{t_j}$, the ELM in a regression task can be expressed by **Eq. 3** and the optimization task can be expressed by **Eq. 4**:

$$\boldsymbol{o_j} = \sum\nolimits_{i=1}^{n} \beta_i G\left(\mathbf{x_j}, \omega_i, b_i\right) \tag{3}$$

$$\min_{\beta} \left\| \boldsymbol{o_j} - \boldsymbol{t_j} \right\| \tag{4}$$

where ω_i and b_i are the weights and bias for the connection between the *i*th node in the hidden layer and the input vector $\mathbf{x_j}$, respectively; β_i is the weight vector between the *i*th node in the hidden layer and the output; and $\boldsymbol{o_j}$ is the prediction output from the ELM. Here, **Eq. 3** can be written as $\mathbf{H}\beta = \mathbf{T}$, where $\mathbf{H}$ is the hidden layer output matrix and $\mathbf{T}$ is the target output matrix. The solution is expressed in **Eq. 5** as follows:

$$\hat{\beta} = \mathbf{H}^{\dagger}\mathbf{T} \tag{5}$$

where $\mathbf{H}^{\dagger}$ is the Moore–Penrose pseudoinverse of the hidden layer output matrix of $\mathbf{H}$.

KELM is an improved version of the ELM and has a higher generalization capacity and less chance of overfitting (Iosifidis et al., 2015). Compared with the vanilla ELM, it introduces a kernel function $k(x_i, x_j)$ when the feature mapping $\mathbf{H}$ is unknown. Here, the kernel function $k(x_i, x_j)$ is a substitution of the ELM's arbitrary feature mapping, and the output weight becomes robust. The kernel serves as a function to describe the relationship between data points which enhances the performance of feature mapping for ELM. The generalization capacity on both regression and classification problem is improved by introducing the kernel function in ELM. Various kernel functions can be utilized for KELM, such as polynomial, linear, and radial basis function (RBF) kernels. In practice, the RBF kernel demonstrates considerable learning capacity in interval prediction tasks with fewer hyperparameters. Thus, the RBF kernel was considered in this task, and it can be expressed by **Eq. 6**:

$$k\left(x_i, x_j\right) = \exp\left(-g\left\|x_i - xj\right\|^2\right) \tag{6}$$

where g is the kernel parameter.

2.4 Objective Function and Evaluation Metrics

Once the PIs are constructed, it is essential to evaluate the quality of their output from interval prediction algorithms. In general, interval prediction algorithms aim to predict an interval that encompasses predicted points under a certain confidence level (Ouyang et al., 2019a). Thus, the prevailing two dimensions, i.e., the coverage rate and interval width, are key quantitative metrics for the quality evaluation of the constructed PIs.

First, the PI coverage probability (PICP) (Khosravi et al., 2011) was utilized to measure the coverage rate. The PICP can be computed using **Eq. 7**:

$$PICP = \frac{1}{N}\sum\nolimits_{i=1}^{N} c_i \tag{7}$$

where N is the total number of samples measured and c_i is the number of samples that fall into the PI. The value of c_i is binary and is either 0 or 1.

Second, the PI normalized average width (PINAW) (Kavousi-Fard et al., 2015) was introduced in this study to evaluate the PI width. The PINAW can be computed as follows:

$$PINAW = \frac{1}{RN}\sum\nolimits_{i=1}^{N} (u_i - l_i) \tag{8}$$

where N is the total number of samples measured, u_i and l_i are the upper and lower bounds of the *i*th sample, respectively, and R is the total range of the prediction target.

In addition, the coverage width-based criterion (CWC) (Taormina and Chau, 2015), which considers both the PI width and coverage, was computed in this study. The computation of the CWC can be achieved using **Eq. 9**.

$$CWC = PINAW\left(1 + \gamma(PICP)e^{-\eta\left(PICP-\mu\right)}\right) \tag{9}$$

where the parameters η and μ are used to define the penalty term $e^{-\eta(PICP-\mu)}$ to maintain the balance between $PINAW$ and $PICP$; and $\gamma()$ is used to reduce the risk of the PI constraint violation during the training process. The CWC is utilized as the objective function in this study.

3 DATASET SUMMARY

Field data were collected from a wind farm located in northwestern China in 2021. The wind farm contains more than 200 wind turbines, all of which have a rated power of 16 MW. To manage the wind turbines, the wind farm installed a standard SCADA system, which is principally used for performance monitoring. The SCADA system provides a considerable amount of data collected at a 10-min resolution. In total, more than 100 variables were collected by the SCADA system in real time, and they varied widely in terms of scale and type. The top eight SCADA variables related to wind power were selected in this study and are summarized in **Table 1**.

According to **Table 1**, eight prevailing SCADA variables were utilized as inputs for the interval prediction task in this study. Half of the selected variables were environmental factors and the others were either the electrical or mechanical characteristics of the wind turbine measured. The selected variables overlap with those used by the majority of related studies, confirming the validity of the selection.

4 EXPERIMENTAL RESULTS

To perform short-term wind power forecasting, experiments were conducted to train the DRN following the LUBE approach. In this study, the entire day dataset was utilized as the training dataset and the 10-min following wind power as the target output. The CWC was selected as the objective function, and the Adam optimizer tuned the hyperparameters of the DRN.

Figure 2 displays the training process of the DRN together with those of three other benchmark interval forecasting algorithms: ANN, ELM, and KELM. All the tested interval forecasting algorithms were trained using the LUBE approach, as described in **Section 2.2**. In total, 100 training epochs were set for all the interval forecasting algorithms. It can be observed that using DRN, the CWC converges around the first 20 epochs, which is significantly higher than the CWC from other interval prediction algorithms. This demonstrates the superiority of the proposed interval prediction approach using the DRN.

In addition, this study also explored the relationship between the prediction horizon and CWC. Here, as see **Figure 3**, instead of single 10-min ahead power forecasting, we also tested the interval prediction performance of multiple horizons from 20-min ahead to 200-min ahead. Intuitively, the CWC for all the algorithms escalates as the prediction horizon increases. Comparatively, the CWC values of DRN escalate slower than those of the other algorithms, which confirms its outperformance in interval prediction tasks in longer prediction horizons.

Finally, 10-min ahead short-term wind power forecasting was performed on the test dataset, as presented in **Figure 4**, which includes the interval forecasting outcome from a whole day in four different seasons. The PIs denote the 95% confidence interval within which the actual power falls, and the target represents the measured wind power according to the SCADA system. A summary of interval forecasting on the test data is provided in **Table 2**.

As summarized in **Table 2**, all the tested algorithms in this study were trained using the LUBE approach and examined using the same test dataset. The proposed DRN produced the highest PICP and the lowest PINAW and CWC values. All evaluation metrics were computed as mean and standard deviation. The computational results confirmed the superiority of the proposed approach.

5 CONCLUSION

In this paper, we propose an interval prediction approach that provides probabilistic short-term wind turbine power generation. SCADA data at 10-min resolution were collected from a wind farm in northwestern China for the case studies. A DRN integrated with the LUBE approach was proposed in a short-term interval forecasting framework. A comparative analysis was performed with three other popular interval prediction algorithms. The computational results confirmed that the interval prediction error of the short-term wind power increased as the prediction horizon became more distant. The proposed approach using a DRN produced the best results for power interval prediction. The application of this model requires the development of new wind turbine control approaches.

DATA AVAILABILITY STATEMENT

The original contributions presented in the study are included in the article/Supplementary Material, further inquiries can be directed to the corresponding author.

AUTHOR CONTRIBUTIONS

HL conceptualized the study, contributed to the study methodology, data curation, software and formal analysis, and wrote the manuscript.

FUNDING

This research is supported by the “Miaozi project” of scientific and technological innovation in Sichuan Province, China (Grant No. 2021090) and the Opening fund of State Key Laboratory of Geohazard Prevention and Geoenvironment Protection (Chengdu University of Technology) (Grant No. SKLGP 2021K014).

REFERENCE

Deng, X., Shao, H., Hu, C., Jiang, D., and Jiang, Y. (2020). Wind Power Forecasting Methods Based on Deep Learning: A Survey. *Comput. Model. Eng. Sci.* 122 (1), 273–301. doi:10.32604/cmes.2020.08768

Haykin, S. (1994). *Neural Networks: A Comprehensive Foundation*, 2. Prentice Hall PTR: United States, 41.

He, K., Zhang, X., Ren, S., and Sun, J. (2016). “Deep Residual Learning for Image Recognition,” in Proceedings of the IEEE Conference on Computer Vision and Pattern Recognition, Las Vegas, NV, United States, June 27–June 30, 2016 (IEEE), 770–778. doi:10.1109/cvpr.2016.90

He, Y., and Kusiak, A. (2017). Performance Assessment of Wind Turbines: Data-Derived Quantitative Metrics. *IEEE Trans. Sustain. Energy* 9 (1), 65–73. doi:10.1109/TSTE.2017.2715061

Huang, H., Liu, F., Zha, X., Xiong, X., Ouyang, T., Liu, W., et al. (2018). Robust Bad Data Detection Method for Microgrid Using Improved ELM and DBSCAN Algorithm. *J. Energy Eng.* 144 (3), 04018026. doi:10.1061/(asce)ey.1943-7897.0000544

Iosifidis, A., Tefas, A., and Pitas, I. (2015). On the Kernel Extreme Learning Machine Classifier. *Pattern Recognit. Lett.* 54, 11–17. doi:10.1016/j.patrec.2014.12.003

Javed, M. S., Ma, T., Jurasz, J., and Amin, M. Y. (2020). Solar and Wind Power Generation Systems with Pumped Hydro Storage: Review and Future Perspectives. *Renew. Energy* 148, 176–192. doi:10.1016/j.renene.2019.11.157

Kelouwani, S., and Agbossou, K. (2004). Nonlinear Model Identification of Wind Turbine With a Neural Network. *IEEE Trans. Energy Convers.* 19 (3), 607–612.

Kavousi-Fard, A., Khosravi, A., and Nahavandi, S. (2015). A New Fuzzy-Based Combined Prediction Interval for Wind Power Forecasting. *IEEE Trans. Power Syst.* 31 (1), 18–26.doi:10.1109/TPWRS.2015.2393880

Khosravi, A., Nahavandi, S., Creighton, D., and Atiya, A. F. (2010). Lower Upper Bound Estimation Method for Construction of Neural Network-

Based Prediction Intervals. *IEEE Trans. Neural Netw.* 22 (3), 337–346. doi:10.1109/TNN.2010.2096824

Khosravi, A., Mazloumi, E., Nahavandi, S., Creighton, D., and Van Lint, J. W. C. (2011). Prediction Intervals to Account for Uncertainties in Travel Time Prediction. *IEEE Trans. Intell. Transp. Syst.* 12 (2), 537–547. doi:10.1109/tits.2011.2106209

Li, H., Deng, J., Feng, P., Pu, C., Arachchige, D. D. K., and Cheng, Q. (2021a). Short-Term Nacelle Orientation Forecasting Using Bilinear Transformation and ICEEMDAN Framework. *Front. Energy Res.* 9, 780928. doi:10.3389/fenrg.2021.780928

Li, H., Deng, J., Yuan, S., Feng, P., and Arachchige, D. D. K. (2021b). Monitoring and Identifying Wind Turbine Generator Bearing Faults Using Deep Belief Network and EWMA Control Charts. *Front. Energy Res.* 9, 799039. doi:10.3389/fenrg.2021.799039

Li, H., He, Y., Xu, Q., Deng, j., Li, W., and Wei, Y. (2022). Detection and Segmentation of Loess Landslides via Satellite Images: a Two-phase Framework. *Landslides* 19, 673–686. doi:10.1007/s10346-021-01789-0

Li, H., Xu, Q., He, Y., and Deng, J. (2018). Prediction of Landslide Displacement with an Ensemble-Based Extreme Learning Machine and Copula Models. *Landslides* 15 (10), 2047–2059. doi:10.1007/s10346-018-1020-2

Li, H., Xu, Q., He, Y., Fan, X., and Li, S. (2020). Modeling and Predicting Reservoir Landslide Displacement with Deep Belief Network and EWMA Control Charts: a Case Study in Three Gorges Reservoir. *Landslides* 17 (3), 693–707. doi:10.1007/s10346-019-01312-6

Long, H., Li, P., and Gu, W. (2020). A Data-Driven Evolutionary Algorithm for Wind Farm Layout Optimization. *Energy* 208, 118310. doi:10.1016/j.energy.2020.118310

Long, H., Xu, S., and Gu, W. (2022). An Abnormal Wind Turbine Data Cleaning Algorithm Based on Color Space Conversion and Image Feature Detection. *Appl. Energy* 311, 118594. doi:10.1016/j.apenergy.2022.118594

Long, H., Zhang, C., Geng, R., Wu, Z., and Gu, W. (2021). A Combination Interval Prediction Model Based on Biased Convex Cost Function and Auto-Encoder in Solar Power Prediction. *IEEE Trans. Sustain. Energy* 12 (3), 1561–1570. doi:10.1109/tste.2021.3054125

Ouyang, T., Pedrycz, W., and Pizzi, N. J. (2019c). Rule-based Modeling with DBSCAN-Based Information Granules. *IEEE Trans. Cybern.* 51 (7), 3653–3663. doi:10.1109/TCYB.2019.2902603

Ouyang, T., Pedrycz, W., Reyes-Galaviz, O. F., and Pizzi, N. J. (2019b). Granular Description of Data Structures: A Two-phase Design. *IEEE Trans. Cybern.* 51 (4), 1902–1912. doi:10.1109/TCYB.2018.2887115

Ouyang, T., He, Y., Li, H., Sun, Z., and Baek, S. (2019a). Modeling and Forecasting Short-Term Power Load with Copula Model and Deep Belief Network. *IEEE Trans. Emerg. Top. Comput. Intell.* 3 (2), 127–136. doi:10.1109/tetci.2018.2880511

Ouyang, T., Huang, H., He, Y., and Tang, Z. (2020). Chaotic Wind Power Time Series Prediction via Switching Data-Driven Modes. *Renew. Energy* 145, 270–281. doi:10.1016/j.renene.2019.06.047

Ouyang, T., Kusiak, A., and He, Y. (2017). Modeling Wind-Turbine Power Curve: A Data Partitioning and Mining Approach. *Renew. Energy* 102, 1–8. doi:10.1016/j.renene.2016.10.032

Ren, Y., Qiu, X., and Suganthan, P. N. (2014). “Empirical Mode Decomposition Based Adaboost-Backpropagation Neural Network Method for Wind Speed Forecasting,” in 2014 IEEE Symposium on Computational Intelligence in Ensemble Learning (CIEL), Orlando, FL, United States, December 09–December 12, 2014 (IEEE), 1–6.

Shen, X., Ouyang, T., Yang, N., and Zhuang, J. (2021). Sample-Based Neural Approximation Approach for Probabilistic Constrained Programs. *IEEE Trans. Neural Netw. Learn. Syst.*. doi:10.1109/tnnls.2021.3102323

Shen, X., Ouyang, T., Zhang, Y., and Zhang, X. (2020). Computing Probabilistic Bounds on State Trajectories for Uncertain Systems. *IEEE Trans. Emerg. Top. Comput. Intell.*. doi:10.1109/tetci.2020.3019040

Shen, X., and Raksincharoensak, P. (2021). Pedestrian-aware Statistical Risk Assessment. *IEEE Trans. Intelligent Transp. Syst.*. doi:10.1109/tits.2021.3074522

Shen, X., and Shen, T. (2018). Chance-constrained Optimization for Torque Tracking Control with Improving Fuel Economy in Spark-Ignition Engines. *SICE J. Control, Meas. Syst. Integration* 11 (4), 365–371. doi:10.9746/jcmsi.11.365

Shen, X., Zhuang, J., and Zhang, X. (2019). Approximate Uncertain Program. *IEEE Access* 7, 182357–182365. doi:10.1109/access.2019.2958621

Sun, Z., He, Y., Gritsenko, A., Lendasse, A., and Baek, S. (2020a). Embedded Spectral Descriptors: Learning the Point-wise Correspondence Metric via Siamese Neural Networks. *J. Comput. Des. Eng.* 7 (1), 18–29. doi:10.1093/jcde/qwaa003

Sun, Z., Rooke, E., Charton, J., He, Y., Lu, J., and Baek, S. (2020b). Zernet: Convolutional Neural Networks on Arbitrary Surfaces via Zernike Local Tangent Space Estimation. *Comput. Graph. Forum* 39 (6), 204–216. doi:10.1111/cgf.14012

Tang, Z., Li, Y., Chai, X., Zhang, H., and Cao, S. (2020). Adaptive Nonlinear Model Predictive Control of Nox Emissions under Load Constraints in Power Plant Boilers. *J. Chem. Eng. Jpn.* 53 (1), 36–44. doi:10.1252/jcej.19we142

Taormina, R., and Chau, K.-W. (2015). ANN-based Interval Forecasting of Streamflow Discharges Using the LUBE Method and MOFIPS. *Eng. Appl. Artif. Intell.* 45, 429–440. doi:10.1016/j.engappai.2015.07.019

Tascikaraoglu, A., and Uzunoglu, M. (2014). A Review of Combined Approaches for Prediction of Short-Term Wind Speed and Power. *Renew. Sustain. Energy Rev.* 34, 243–254. doi:10.1016/j.rser.2014.03.033

Wu, W., and Peng, M. (2017). A Data Mining Approach Combining K -Means Clustering with Bagging Neural Network for Short-Term Wind Power Forecasting. *IEEE Internet Things J.* 4 (4), 979–986. doi:10.1109/jiot.2017.2677578

Zhang, X.-D., Li, A., and Pan, R. (2016). Stock Trend Prediction Based on a New Status Box Method and AdaBoost Probabilistic Support Vector Machine. *Appl. Soft Comput.* 49, 385–398. doi:10.1016/j.asoc.2016.08.026

Conflict of Interest: The author declares that the research was conducted in the absence of any commercial or financial relationships that could be construed as a potential conflict of interest.

frontiers | Frontiers in Energy Research

BRIEF RESEARCH REPORT
published: 19 May 2022
doi: 10.3389/fenrg.2022.900298

Assisting Smart Construction With Reliable Edge Computing Technology

Qiang Yue[1]*, *Song Mu*[2], *Longguan Zhang*[2], *Zhun Wang*[1,3], *Zhonghua Zhang*[2], *Xing Zhang*[2], *Yongge Wang*[1,3] *and Zhuang Miao*[1,3]

[1]*Institute of Artificial Intelligence, Hebi, China,* [2]*China Railway Engineering Equipment Group Mechanical and Electrical Engineering Co., Ltd, Chengdu, China,* [3]*Zhongke Xingyun (Hebi) Digital Technology Innovation Co., Ltd, Hebi, China*

Although smart construction tools are already assisting the construction sector, still major reforms are considerably seen in the coming years with Artificial Intelligence of Things (AIoT). The purpose of this work was to develop a down-to-earth reliable edge-computing design and plan, which can be utilized to bolster savvy development situations with high quality of service. The number of devices connected to industrial processes is growing in tandem with the advancement of sophisticated technologies and the use of the AIoT. Big data are created as gadgets grow more integrated and need more computing power. However, as the amount of big data generated grows, processing and analytical issues arise. Cloud computing technologies are now being used to solve processing and analytical challenges. However, by using edge computing technologies, greater emphasis is placed on executing calculations as near to the device as feasible. As a result of these facts, this article suggests the arrangement plan, which depends on the most recent cloud and computer program designing approaches and advances, and gives flexibility, interoperability, and adjustment to construction companies' particular needs.

Keywords: smart construction, artificial intelligence of things, reliable edge computing, quality of service, qos, big data

Edited by:
Xun Shen,
Tokyo Institute of Technology, Japan

Reviewed by:
Sandeep Kumar Duran,
Lovely Professional University, India
Bhagwan Shree Ram,
Saharsa College of Engineering, India

Correspondence:
Qiang Yue
yueqiang@sugonsc.com

Specialty section:
This article was submitted to Smart Grids, a section of the journal Frontiers in Energy Research

Received: *20 March 2022*
Accepted: *12 April 2022*
Published: *19 May 2022*

Citation:
Yue Q, Mu S, Zhang L, Wang Z, Zhang Z, Zhang X, Wang Y and Miao Z (2022) Assisting Smart Construction With Reliable Edge Computing Technology. Front. Energy Res. 10:900298. doi: 10.3389/fenrg.2022.900298

INTRODUCTION

Fundamental aspects influencing the uninterrupted functionality of the Internet within the future era of the internet, with millions and billions of tools, will be: 1) the big, rapid, and diversified information obtained by them and their consumers, 2) the population boom of tools and their expert systems, and 3) need for huge, flexible infrastructure, and services to access and extract knowledge from these huge datasets to aid in making critical, data-driven judgments. Now, a key roadblock to the adoption of sophisticated AIoT applications in the construction industry is their unacceptably low quality of service, which limits real-time processing capabilities. Several reviews of past AIoT implementations in the construction industry have been published in recent years (Avizienis et al., 2004; Braun et al., 2015).

Within the last 5 years, artificial intelligence (AI) has made great progress, and it has managed to establish a footing within construction firms, from concept to construction. The use of constructively alternative analyses to enhance the precision of estimated costs, precise deadlines, and decrease on-site risks is the possible use of AI in the design and planning stage (Bonomi et al., 2012; Kim et al., 2013; and Khodadadi et al., 2015). Furthermore, better productivity, enhanced work procedures, and a lower risk of accidents on construction sites are also advantages of AI in the construction stage.

Indeed, stringent quality of service criteria, i.e., dependability requirements, are required for such applications to realize their commercial value. To continuously analyze data from cameras, sensors, robotics, smartphones, and smart apps, for example, requires extensive networking, processing, and memory resources; in addition, control loops and feedback for signage and actuators are available. Our strategy will be based on the existing cloud service design along with reliability of solutions in general. Cloud computing, according to Mell et al (Dave et al., 2016) is an architecture that allows universally requisite accessibility to a group of computing resources over the internet that is shared, such as servers, networks, applications, storing, and services, those can be established and maintained with no difficulty.

In response to slowing growth, the need for investment and research in AI technology is being investigated (Avizienis et al., 2004; Braun et al., 2015; and Dave et al., 2016). The goal was to simplify operations and boost efficiency. Avoiding cost overruns, enhancing site security, and effectively managing projects are all advantages of AI for the construction sector (Foster et al., 2008; Bai et al., 2012; Jin et al., 2014; Prasad et al., 2015; Chen et al., 2016). The following AI sectors of big data and analytics, robotics, automation, data integration, and wearable technology have already experienced significant growth (Wang et al., 2007; Golparvar-Fard et al., 2012).

RELATED WORKS—SMART CONSTRUCTION AND EDGE COMPUTING

A collection of cyber-physical systems (CPSs) uses real-time monitoring to prevent the breakdown of temporary (Bonomi et al., 2012) structures. A cloud-premised dataset and mobile app are part of their approach. It has an impact on the issue of crane-to-immobile-object collisions, which they are attempting to reduce (Khodadadi et al., 2015). A natural-world computation, a network of anti-collision systems that cautions of an impending collision and applies appropriate precautionary methods, might be their answer. The works show methods for construction site safety that use various monitoring technologies to prevent accidents between construction equipment and pedestrians. Their approach is based on the premise of tags and warning devices that use radio frequency identification as well as communication protocol and interfaces.

AI is increasingly used at construction sites, and the future success of the project depends heavily on the efficient use of these technologies. Several communication software models and supply management availabilities are presented to help with the development process (Wang et al., 2007; Bai et al., 2012). Golparvar-Fard et al (2012) state that material handling has a substantial impact on the development process; as a result, they may provide a software model prototype for efficiently handling building materials with minimal human participation Villari et al (2016) provide web-premised offerings that may combine radiofrequency identification technology with smart devices to boost the efficiency of information and knowledge exchange on building sites. Mell and Grance (2012), Swain et al (2015), Jegen -Perrin et al (2016), Li et al (2021a), and Li et al (2021b) looked at methods for real-time data, task management, site and monitoring, and exchange using a multi-tier computer architecture in their research.

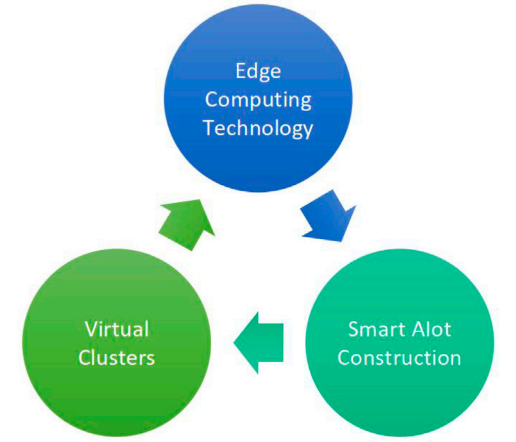

FIGURE 1 | Reliable edge-computing technology and smart AIoT construction.

Next, NVivo was used to perform content analysis to analyze word frequency, concepts, and technology to identify the main topics of tweets about AI applications in the construction industry. The reasons for this choice are:

i. AI is beginning to be recognized by some of Australia's top construction businesses. These businesses are effectively utilizing AI in their initiatives to save money and time.
ii. A national AI strategy and roadmap are being developed in Australia. To summarize, the development of AI in cities and industries is being carefully planned to prevent becoming simply organic.
iii. In Australia, social media is widely used and has evolved into a source of information for conveying the common view of AI in the construction business.

The lack of communication on construction sites is a common source of accidents, and it should also create a slew of serious on-site issues and delays.

Several studies specialize in the utilization of varied AIoT devices in construction. Avizienis et al (2004) discussed how the Internet of Things (IoT) and associated protocols can help to improve the development management system. Le et al (2014) and Roman et al (2018) described a tower crane safety monitoring system powered by AIoT that successfully monitors the safety of the tower production process. The majority of AIoT apps developed so far have been built to operate natively or on Web browsers, with no measures in place to reduce application/system downtime or data loss.

APPLIED METHODOLOGY

Methodology

The recognized test is to characterize a bunch of edge computing technologies as shown in **Figure 1** that can be utilized to oversee smart AIoT construction. Inside the shrewd conditions, different savvy applications are sent to help computerization. The essential objective of the services for edge management was to add to higher quality of service, in contrast, with existing cloud frameworks and hence likewise to have the option to meet rigid trustworthiness necessities of each expected brilliant application.

The current work adopts a hierarchical strategy. In light of edge and haze figuring definitions (Chae, 2009), leaving innovation surveys (Chae and Yoshida, 2010; Yi et al., 2015), the distinguished specialized necessities of the possible applications, and experience acquired over cutting edge-distributed computing and programming projects, a sufficient calculated methodology for edge registering in development is ready. It characterizes the vital administrations that can be utilized to acquire high quality of service. Following the engineering and plan, two praiseworthy edge-processing applications were created to show the feasibility of the methodology and the potential advantages while meeting the expected quality of service. The applications that have been chosen to show the methodology are connected with video correspondences and documents of the executives, which are agents for different functionalities required inside well-informed development conditions.

Necessities

Brilliant frameworks in the development area must be planned as dependable. Framework reliability addresses the framework's capacity to convey administration that can be sensibly trusted. From a framework disappointment viewpoint, the reliability can be additionally characterized as the frameworks capacity to stay away from disappointments that are successive or serious, and longer blackout lengths than it is ok with the client (Beach et al., 2013; Datta et al., 2016), for instance, to perform security and business basic activities.

At the point when the key trustworthiness prerequisites are not fulfilled, extreme results are inescapable. For example, this can cause extra monetary expenses, compromised well-being at the building site, development process delays, loss of notoriety, and numerous different repercussions. Overall, giving the necessary steadfastness to AIoT building locales, where time-basic applications are utilized, certain trustworthiness credits must be tended to and fulfilled consistently.

Approaches and Methods for Cloud and Edge Computing

Cloud computing is widely utilized today owing to features like seamless scalability, configuration, and pay-per-use (Stankovski and Petcu, 2014). In the recent decade, it has been extensively explored, developed, and utilized in a variety of fields. Past initiatives have been supplemented by the new generation of edges and cloud computing projects, including SWITCH, which focuses on system software for ENTICE, AIoT, and Big Data that focuses on innovative cloud computing storage solutions. Advanced novel techniques have evolved, such as osmotic computing (Shi et al., 2016a). They recommend building apps out of microservices, and they are carried out at the edge network systems. Contrary to popular belief, cloud computing is still a centralized computing architecture; new computing concepts decentralize computing by extending processing capability to the network edge. Cloud computing concentrates on processing operations inside this network, among end devices and cloud computing data centers (Prasad et al., 2015). Edge computing, on the other hand, brings processes even nearer to data resources, allowing any devices on to the edge to process data (Kim et al., 2013). Although edge and cloud computing are distinct computer tactics, they have comparable aims, and hence edge and cloud computing may be thought of as the two sides of a single coin.

There are currently data-centric technologies (Chae, 2009; Chae and Yoshida, 2010) available that enable near-data computing and significant AIoT compatibility. At the network edge, decentralized computing technologies bring services closer to users. Their objectives include reducing delays, lowering data transport and processing costs, and increasing scalability. Additionally, it is feasible to turn edge devices into virtualization platforms (Ren and Wu, 2014; Shi et al., 2016b). Container-based virtualization, for example, may be utilized to create edge-computing architectures. A container, in general, includes the application data code, all essential info libraries, and, if necessary, the data code. As a result, both functionality and data are included in a container instance.

Modern Software Tools and Techniques

Parallel to the advancement of virtualization technology, software engineering methodologies and tools have also made significant strides in recent years. Rapid extreme programming, application development, behavior-driven development, test-driven development, and other modern software development and engineering approaches are only a few examples. Component-based software engineering, in general, facilitates such advancement. It encourages closer collaboration among development, business, and IT operations teams.

Modifying the Edge Computing Technology

Edge compute clusters (Raspberry PIs, microservers, routers, and more computational capabilities close to the environment that is smart) as well as public and private clouds are two types of infrastructure for computation that might be utilized to execute AIoT applications (that is, data center computing capacity). The initial stage in this procedure is for a smart application administrator to examine their edge-computing requirements.

Figure 2 shows a layered edge-computing architecture that divides services into three levels. Because apps are built up of software modules, they may be used at any stage of development. The first stage of the first would operate on AIoT devices in the field, while the second would run on edge-computing nodes, and the third on the most suited public cloud from the virtual bunches indefinitely. Various AIoT devices, such as video-camera-fitted headsets, might function on batteries and send data to the cloud regularly.

Due to their high networking resource requirements, edge computing must be used for time-critical software applications. Relying on the circumstance, the intelligent environment

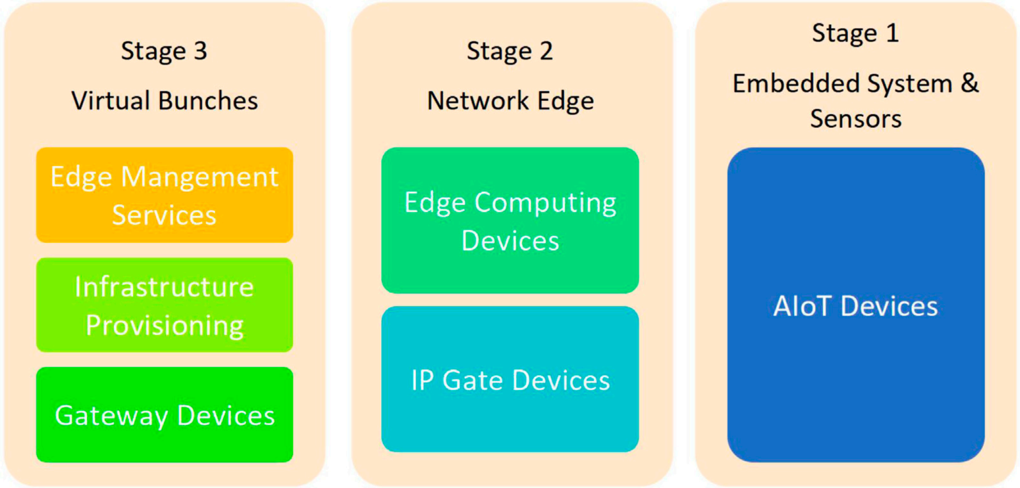

FIGURE 2 | Layered architecture for reliable edge-computing technology and smart AIoT construction.

TABLE 1 | Open-source Web communication applications.

<! --Col Count:5-->	Google Meet	Microsoft Teams	Jio Meet	Zoom
Chat	Y	N	N	Y
Videoconference	Y	Y	Y	Y
Screen-sharing	N	Y	Y	Y
Encryption	Y	Y	N	Y
Record	N	N	Y	Y

operator can determine how many edge-computing devices are required to ensure that smart applications run reliably. In total, three high-performance microservers, for example, located near a medium-sized intelligent construction atmospheric environment, may be sufficient to provide good quality of service and dependency. Furthermore, sections of the applications with no time-critical needs can be placed in a dataset center, lowering operational expenses.

The infrastructure of high standard flexibility enabled by the ENTICE and SWITCH services fundamentally implies that the system may operate AIoT applications without the requirement for ongoing management. The Kubernetes-premised orchestrator can swiftly stop and start containers servicing specific AIoT units throughout the entire range of computing, such as in the dataset center, at the edge, and even in transportable AIoT device-integrated computer systems (on which an operating system and an orchestrator are installed and running). As a result, this is a fully complete system capable of running, updating, extending, building, deleting, and managing software services in real-time.

The orchestrator that has been built may be utilized to effectively expand containers horizontally as consumption grows, allowing for excellent service availability. Of course, this translates to increased operation safety near the smart construction environment. To guarantee dependable operation, an availability parameter can be used that specifies how many service copies should be operating at the same time. Furthermore, as a result of the applications' rapid recovery process, the orchestrator ensures a more stable continuous delivery of services—applications are monitored closely by a collection of assets that are able to monitor elements, and an alerting trigger creates warnings so when service quality thresholds (e.g., jitter, latency, and bandwidth) are exceeded.

Edge Computing

Edge computing can be made up of a variety of gateway routers, devices, tiny servers, and small data centers with energy consumption ranging from 1–5 kW. All of these computer systems have an operating system in common. Core OS, RancherOS, and nearly any Linux-based systems are examples of operating systems that can effortlessly handle Docker containers. An IP gateway is a specialized device that connects AIoT devices to the Internet. IP gateways such as the TA900e or Cisco-ASA are examples of IP gateways, whereas AIoT devices and sensors include video communications, cellphones, temperature, air quality, and humidity transmitters, among others. Naturally, a system operator would be required to set up such a system and regularly monitor it using the monitoring components. The study did not focus on the forms of communication (wired and wireless) between the AIoT and the software services running at the network edge. This is an aspect about which the intended architecture is agnostic.

The AIoT devices that have been deployed can broadcast video, sensor data, and audio in real-time. Computing devices that run container-based services then interact and analyze their data directly.

In time-critical scenarios, such as probable collisions or accidents, when an immediate response to events is required, on-site data processing may be required. Furthermore, edge processing enables more efficient data processing in the cloud at reduced prices. The edge-processed data is then forwarded to network gateways, which transfer it to the most appropriate virtual data center entity (bunches).

Communication

Efficient communication and a range of signal solutions are necessitated for the success of any construction operation on one or many constructional projects. Communication through video may require for every construction project's success to be enhanced with several time-consuming functions, such as real-time video analysis to detect security and safety issues, augmented reality environments to increase cooperation and project collaboration, and construction site delays and blunders.

Construction businesses, site teams, surveyors, architects, engineers, and other site employees need to communicate often; therefore, videoconferencing eliminates the need for face-to-face meetings. As a result, face-to-face discussions may be held at any moment at a lower cost, and interaction across office-to-office, site-to-site, and project work-to-project work teams is easier. In addition to meetings, videoconferencing participants can use to discuss a video from the worksite and resolve potential on-site issues, regardless of their geographic location. This type of communication might lead to improved cooperation, faster delivery of solutions, and lower manufacturing costs. As a result, it serves as an example of a critical application.

Open-source software can be utilized to create an edge-computing application. Google Meet, Microsoft Teams, Jio Meet, and Zoom were all viewed as open-source video conferencing apps. **Table 1** compares and contrasts their functions.

The Construction Process Is Being Documented

Documentation is a regular problem in various sectors, and it also performs an important role in the building phase. Although this is not a significant issue for minor building projects, some recent firms are attempting to solve it. Delays and data loss are likely in larger projects; thus, documentation is vital. New AIoT devices, such as radiofrequency identification sensor data, video surveillance, and tags, may assist record the entire process using new formats and methodologies, all of which are Big Data problems (veracity of data, variety, volume, and velocity). In such circumstances, using cloud-premised solutions may be able to overcome the obstacles.

This application is time-critical because it must run to avoid any delays, and everything is performed in real-time. The overall purpose of this application was to provide a file-sharing mechanism among building process participants with a high level of service quality.

CONCLUSION

The innovation of this study, in comparison to other current methods used for construction automation outlined in **Section 2**, is the innovative edge-computing architecture and creation of a reliable AIoT construction system. Artificial intelligence (AI) is a powerful instrument with the potential to transform and disrupt the construction sector. In total, two AIoT applications with strong quality of service requirements are used to showcase the methodology, which is based on the created design. This revolutionary design can accommodate a variety of smart applications for a variety of building project demands and sizes. Furthermore, software services, such as analytic services like data mining, machine learning, and simulations, may be created using containers and used successfully in the current edge-computing architecture. As a result, deploying cloud environments adjacent to construction sites might provide seamless construction site administration and communication, reducing costs and increasing dependability. The current state of knowledge about emerging construction technologies and their application areas is insufficient.

DATA AVAILABILITY STATEMENT

The original contributions presented in the study are included in the article/Supplementary Material, further inquiries can be directed to the corresponding author.

AUTHOR CONTRIBUTIONS

All authors listed have made a substantial, direct, and intellectual contribution to the work and approved it for publication.

REFERENCES

Avizienis, A., Laprie, J.-C., Randell, B., and Landwehr, C. (2004). Basic Concepts and Taxonomy of Dependable and Secure Computing. *IEEE Trans.Dependable Secure Comput.* 1 (1), 11–33. doi:10.1109/tdsc.2004.2

Bai, L., Sun, Y., and Guo, X. (2012). *Applied Research on tower crane Safety Supervising System Based on Internet of Things, Business, Economics, Financial Sciences, and Management*. Palo Alto, CA: Springer, 549–556. doi:10.1007/978-3-642-27966-9_74

Beach, T. H., Rana, O. F., Rezgui, Y., and Parashar, M. (2013). Cloud Computing for the Architecture, Engineering & Construction Sector: Requirements, Prototype & Experience. *J. Cloud Comput. Adv. Syst. Appl.* 2 (1), 8. doi:10.1186/2192-113x-2-8

Bonomi, F., Milito, R., Zhu, J., and Addepalli, S. (2012). “Fog Computing and its Role in the Internet of Things,” in *Proceedings of the First Edition of the MCC*

Workshop on Mobile Cloud Computing (Palo Alto, CA: ACM), 13–16. doi:10.1145/2342509.2342513

Braun, A., Tuttas, S., Borrmann, A., and Stilla, U. (2015). A Concept for Automated Construction Progress Monitoring Using BIM-Based Geometric Constraints and Photogrammetric point Clouds. *Electron. J. Inf. Technol. Constr. (Itcon)* 20 (5), 68–79.

Chae, S. (2009). "Development of Warning System for Preventing Collision Accident on Construction Site," in *Proceedings of the 26th International Symposium on Automation and Robotics in Construction* (Palo Alto, CA: ISARC). doi:10.22260/isarc2009/0035

Chae, S., and Yoshida, T. (2010). Application of RFID Technology to Prevention of Collision Accident with Heavy Equipment. *Automation in Construction* 19 (3), 368–374. doi:10.1016/j.autcon.2009.12.008

Chen, H.-M., Chang, K.-C., and Lin, T.-H. (2016). A Cloud-Based System Framework for Performing Online Viewing, Storage, and Analysis on Big Data of Massive BIMs. *Automation in Construction* 71, 34–48. doi:10.1016/j.autcon.2016.03.002

Datta, S. K., Bonnet, C., Da Costa, R. P. F., and Härri, J. (2016). "DataTweet: An Architecture Enabling Data-Centric IoT Services," in 2016 IEEE Region 10 Symposium (TENSYMP), Bali, Indonesia, 9-11 May 2016 (Palo Alto, CA: IEEE), 343–348.

Dave, B., Kubler, S., Främling, K., and Koskela, L. (2016). Opportunities for Enhanced Lean Construction Management Using Internet of Things Standards. *Automation in Construction* 61, 86–97. doi:10.1016/j.autcon.2015.10.009

Foster, I., Zhao, Y., Raicu, I., and Lu, S. (2008). "Cloud Computing and Grid Computing 360-degree Compared," in 2008 Grid Computing Environments Workshop, Austin, TX, USA, 12-16 Nov. 2008(Palo Alto, CA: IEEE), 1–10. GCE'08.

Golparvar-Fard, M., Pe na-Mora, F., and Savarese, S. (2012). Automated Progress Monitoring Using Unordered Daily Construction Photographs and IFC-Based Building Information Models. *J. Comput. Civ. Eng.* 29 (1), 04014025. doi:10.1061/(asce)cp.1943-5487.0000205

Jegen-Perrin, N., Lux, A., Wild, P., and Marsot, J. (2016). Preventing Plant-Pedestrian Collisions: Camera & Screen Systems and Visibility from the Driving Position. *Int. J. Ind. Ergon.* 53, 284–290. doi:10.1016/j.ergon.2016.02.003

Jin, J., Gubbi, J., Marusic, S., and Palaniswami, M. (2014). An Information Framework for Creating a Smart City through Internet of Things. *IEEE Internet Things J.* 1 (2), 112–121. doi:10.1109/jiot.2013.2296516

Khodadadi, F., Calheiros, R. N., and Buyya, R. (2015). "A Data-Centric Framework for Development and Deployment of Internet of Things Applications in Clouds," in 2015 IEEE Tenth International Conference on Intelligent Sensors, Sensor Networks and Information Processing (ISSNIP) (Palo Alto, CA: IEEE), 1–6. doi:10.1109/issnip.2015.7106952

Kim, C., Park, T., Lim, H., and Kim, H. (2013). On-site Construction Management Using mobile Computing Technology. *Automation in Construction* 35, 415–423. doi:10.1016/j.autcon.2013.05.027

Le, Q. T., Lee, D. Y., and Park, C. S. (2014). Corrigendum to "A Social Network System for Sharing Construction Safety and Health Knowledge" [Autom. Constr. 46 (2014) Pages 30-37]. *Automation in Construction* 43, 30–37. doi:10.1016/j.autcon.2014.03.001

Li, H., Deng, J., Feng, P., Pu, C., Arachchige, D. D. K., and Cheng, Q. (2021). Short-Term Nacelle Orientation Forecasting Using Bilinear Transformation and ICEEMDAN Framework. *Front. Energ. Res.* 9, 780928. doi:10.3389/fenrg.2021.780928

Li, H., Deng, J., Yuan, S., Feng, P., and Arachchige, D. D. K. (2021). Monitoring and Identifying Wind Turbine Generator Bearing Faults Using Deep Belief Network and EWMA Control Charts. *Front. Energ. Res.* 9, 799039. doi:10.3389/fenrg.2021.799039

Mell, P., and Grance, T. (2012). *The NIST Definition of Cloud Computing: Recommendations of the National Institute of Standards and Technology*. Palo Alto, CA: NIST Special Publication, 800145.

Prasad, K., Zavadskas, E. K., and Chakraborty, S. (2015). A Software Prototype for Material Handling Equipment Selection for Construction Sites. *Automation in Construction* 57, 120–131. doi:10.1016/j.autcon.2015.06.001

Ren, W., and Wu, Z. (2014). Real-time Anticollision System for mobile Cranes during Lift Operations. *J. Comput. Civ. Eng.* 29 (6), 04014100. doi:10.1061/(asce)cp.1943-5487.0000438

Roman, R., Lopez, J., and Mambo, M. (2018). Mobile edge computing, fog et al.: a survey and analysis of security threats and challenges. *Futur. Gener. Comput. Syst.* 78, 680–698. doi:10.1016/j.future.2016.11.009

Shi, Q., Ding, X., Zuo, J., and Zillante, G. (2016). Mobile Internet Based Construction Supply Chain Management: A Critical Review. *Automation in Construction* 72, 143–154. doi:10.1016/j.autcon.2016.08.020

Shi, W., Cao, J., Zhang, Q., Li, Y., and Xu, L. (2016). Edge Computing: Vision and Challenges. *IEEE Internet Things J.* 3 (5), 637–646. doi:10.1109/jiot.2016.2579198

Stankovski, V., and Petcu, D. (2014). Developing a Model Driven Approach for Engineering Applications Based on mOSAIC. *Cluster Comput.* 17 (1), 101–110. doi:10.1007/s10586-013-0263-x

Swain, N. R., Latu, K., Christensen, S. D., Jones, N. L., Nelson, E. J., Ames, D. P., et al. (2015). A Review of Open Source Software Solutions for Developing Water Resources Web Applications. *Environ. Model. Softw.* 67, 108–117. doi:10.1016/j.envsoft.2015.01.014

Villari, M., Fazio, M., Dustdar, S., Rana, O., and Ranjan, R. (2016). Osmotic Computing: a New Paradigm for Edge/cloud Integration. *IEEE Cloud Comput.* 3 (6), 76–83. doi:10.1109/mcc.2016.124

Wang, L.-C., Lin, Y.-C., and Lin, P. H. (2007). Dynamic mobile RFID-Based Supply Chain Control and Management System in Construction. *Adv. Eng. Inform.* 21 (4), 377–390. doi:10.1016/j.aei.2006.09.003

Yi, S., Li, C., and Li, Q. (2015). "A Survey of Fog Computing: Concepts, Applications, and Issues," in *Proceedings of the 2015 Workshop on Mobile Big Data* (Palo Alto, CA: ACM), 37–42.

Conflict of Interest: Authors SM, LZ, ZZ, and XZ were employed by the company China Railway Engineering Equipment Group Mechanical and Electrical Engineering Co., Ltd. Authors ZW, YW, and ZM were employed by the company Zhongke Xingyun (Hebi) Digital Technology Innovation Co., Ltd.

The remaining author declares that the research was conducted in the absence of any commercial or financial relationships that could be construed as a potential conflict of interest.

frontiers | Frontiers in Energy Research

BRIEF RESEARCH REPORT
published: 23 May 2022
doi: 10.3389/fenrg.2022.914026

Design and Validation of Reversing Assistant Based on Extreme Learning Machine

Huanyu Di[1], *Yipeng Yan*[1], *Mingxin Zhao*[1] *and Mingxin Kang*[2]*

[1]Automotive Engineering Institute, Guangzhou Automobile Group Co., Ltd, Guangzhou, China, [2]State Key Laboratory of Synthetical Automation for Process Industries, Northeastern University, Shenyang, China

As an important function of the advanced driver assistance system (ADAS), the reversing assistant (RA) achieves trajectory retracing by applying accurate position estimation and tracking control. To overcome the problem of the modeling complexity in dead reckoning for the reversing assistant function, the heading angular rate is compensated by using the extreme learning machine (ELM) to improve the positioning accuracy. In addition, considering the time delay of the steering system, a tracking controller with a feed-forward of the recorded steering angle and a self-tuning PID feedback controller is designed based on the preview-and-following scheme. Vehicle experiments under various reversing scenarios prove that the proposed positioning method and tracking control scheme are effective, the overall lateral error is less than 10 cm, and the heading angle error is less than 1°, which meets the requirements of performance indicators.

Keywords: reversing assistant, extreme learning machine, dead reckoning, tracking control, self-tuning PID

Edited by:
Xun ShenXun Shen,
Tokyo Institute of Technology, Japan

Reviewed by:
Fengqiu Liu,
Ningbo University of Technology, China
Zhu Junjun,
Yanshan University, China

***Correspondence:**
Mingxin Kang
kangmx@mail.neu.edu.cn

Specialty section:
This article was submitted to Smart Grids,
a section of the journal Frontiers in Energy Research

Received: *06 April 2022*
Accepted: *19 April 2022*
Published: *23 May 2022*

Citation:
Di H, Yan Y, Zhao M and Kang M (2022) Design and Validation of Reversing Assistant Based on Extreme Learning Machine. Front. Energy Res. 10:914026. doi: 10.3389/fenrg.2022.914026

1 INTRODUCTION

In order to improve driving safety and comfort, a fully autonomous reversing assistant (RA) function is developed and designed by automotive engineers. The merit of the RA function can make the vehicle automatically reverse back to the starting position of the original route with a maximum support of 50 m, and therefore, it is quite helpful for unskilled drivers, especially under some complicated driving scenarios such as narrow roads.

The core techniques of the RA function include vehicle position estimation and trajectory tracking control. Currently, commonly used vehicle positioning technologies include dead reckoning (Skog and Handel, 2009; Alvarez et al., 2012; Wang et al., 2014), inertial navigation (Woodman, 2007; Leppäkoski et al., 2013), satellite positioning (Leppäkoski et al., 2013; Jiménez et al., 2014; Li et al., 2022), visual positioning (Woodman, 2007; Beauregard, 2009), and lidar-based positioning (Shin et al., 2010; Hess et al., 2016). Each method has its own advantages and shortage and can be selected according to the specific application scenario. Among them, dead reckoning is favored because of its advantages such as no external sensor, low cost, fast sampling frequency, and high short-time positioning accuracy. However, its long-distance positioning deviation is large due to the accumulation of systematic and non-systematic errors. To overcome the aforementioned problems, the mainstream approach is to use multi-source and multi-sensor information fusion technology to integrate other positioning information and dead reckoning information, to achieve the overall positioning accuracy (Alvarez et al., 2012; Wang et al., 2014; Zhang et al., 2015; Jian et al., 2020). In addition, there are also attempts to improve positioning accuracy by compensating and optimizing the angle information in dead reckoning (Tian et al., 2014; Chen et al., 2016; Ho et al., 2016). For tracking control, geometric relation-based control methods (Coulter, 1992; Thrun et al., 2006; Li et al., 2021a; Le et al., 2021), model-based control methods (Guo and Fancher, 1983; Ziegler et al., 2014; Bayuwindra et al., 2016), and preview-and-following theory-based control methods (Guo and Guan, 1993; Falcone et al., 2007; Marino et al., 2011; Shen et al., 2020) are commonly used at present.

Recently, machine learning techniques have attained much attention in many research fields, such as data-driven modeling (Ourmazd, 2020; Cui et al., 2021), prediction (Huang et al., 2006; Liu et al., 2019; Zhou et al., 2021), control (Kang and Gao, 2020; Zhou et al., 2021; Wu et al., 2022), and fault diagnosis (He and Kusiak, 2017; Li et al., 2021b). Machine learning allows a controller to improve its performance by learning from previous events, in the same way humans learn from experiences. Due to the system complexity of the ADAS, the traditional designs based on the mechanism analysis become more difficult, and then the machine learning techniques have been well studied and gradually adopted (Moujahid et al., 2018). As an efficient learning algorithm with lower computational burden, an extreme learning machine (ELM) has gained much attention in ADAS. The ELM is mainly designed for training single hidden layer feed-forward neural networks, and its hidden nodes are randomly initiated, and then determined without time-consuming iteratively tuning (Huang et al., 2006, 2015).

Based on the aforementioned analysis, in view of the requirement of low cost and high precision of RA positioning scheme, a dead reckoning method with a redundant design based on vehicle signals such as wheel speed and front-wheel angle is proposed; at the same time, in order to compensate the accumulated errors caused by the internal and external errors of the system, the ELM is introduced to correct the heading angle and improve the overall positioning accuracy. In terms of tracking control, considering the characteristics of the RA function and engineering needs, the preview-and-following control scheme is used to realize tracking, namely, using the current vehicle position and vehicle motion to calculate the vehicle position at a certain amount of preview time, and the target tracking point of the desired trajectory is determined based on the vehicle position at the preview point, which can deal with time delay greatly; on the basis of the preview, the following controller is designed by using a feed-forward plus self-tuning PID feedback control algorithm. Finally, functional verification is carried out in different scenarios. Experimental results demonstrate that the positioning and control method designed in this study is effective, and the key performance indexes such as lateral error and heading angle error meet the design requirements.

2 DEAD RECKONING AND COMPENSATION

Dead reckoning calculates the location and the heading of the vehicle's center of gravity (CG) based on vehicle signals such as four-wheel speeds and steering wheel angle. Also a confidence evaluation method of the CG position was designed to avoid the increase in positioning error due to the slip of individual wheels. At the same time, considering the unpredictable disturbance such as the change of wheel diameter caused by load and the uneven ground, the accurate position estimation model is difficult to be established. Then, an extreme learning machine is adopted to compensate for the model error to improve the positioning accuracy.

2.1 Dead Reckoning Based on Yaw Angle

The schematic diagram of the vehicle coordinates is illustrated in **Figure 1**. The CG of the vehicle starting time is taken as the origin of coordinates. At low speed, the sideslip angle of the CG is ignored; the yaw rate of the body is calculated according to the Ackerman steering relation and the average yaw rate of the four wheels:

$$R = \frac{L}{2}\left(\frac{1}{\tan\delta_{\mathrm{fr}}} + \frac{1}{\tan\delta_{\mathrm{fl}}}\right), \tag{1}$$

$$\begin{bmatrix} \omega_{\mathrm{fl}} \\ \omega_{\mathrm{fr}} \\ \omega_{\mathrm{rr}} \\ \omega_{\mathrm{rl}} \end{bmatrix} = \begin{bmatrix} \dfrac{v_{\mathrm{fl}}\mathrm{d}t}{\mathrm{sign}\left(R+\dfrac{W}{2}\right)\sqrt{\left(R+\dfrac{W}{2}\right)^2+L^2}} \\ \dfrac{v_{\mathrm{fr}}\mathrm{d}t}{\mathrm{sign}\left(R-\dfrac{W}{2}\right)\sqrt{\left(R-\dfrac{W}{2}\right)^2+L^2}} \\ \dfrac{v_{\mathrm{rr}}\mathrm{d}t}{\mathrm{sign}\left(R-\dfrac{W}{2}\right)} \\ \dfrac{v_{\mathrm{rl}}\mathrm{d}t}{\mathrm{sign}\left(R+\dfrac{W}{2}\right)} \end{bmatrix}, \tag{2}$$

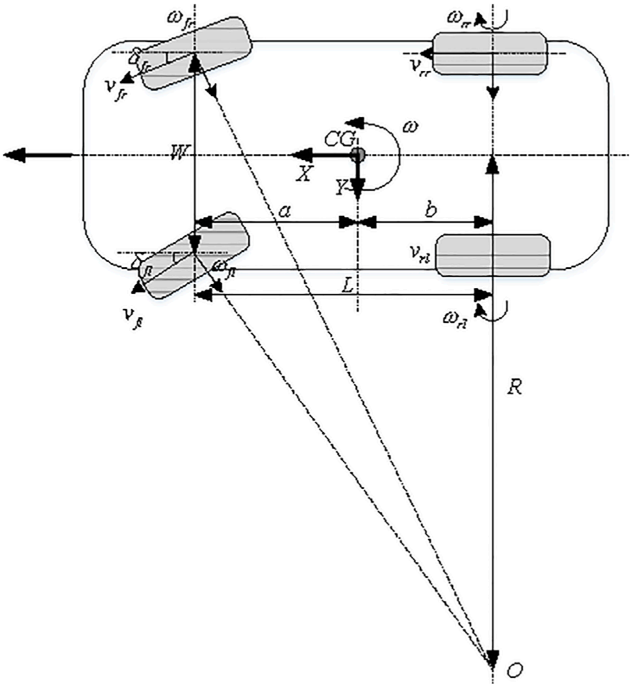

FIGURE 1 | Diagram of the vehicle coordinates.

$$\omega = \frac{1}{4}\left(\omega_{\mathrm{fl}} + \omega_{\mathrm{fr}} + \omega_{\mathrm{rr}} + \omega_{\mathrm{rl}}\right), \tag{3}$$

where L and W denote the wheel base and the wheel track, respectively; δ denotes the steering angle of the wheel, R and v are the turning radius and the wheel speed, respectively; ω with and without subscripts are the yaw rate of the specified wheel and the vehicle body, respectively; $\mathrm{d}t$ is the sampling time; and the subscripts of the notations such as $\mathrm{fl}, \mathrm{fr}, \mathrm{rl}, \mathrm{and\,rr}$ throughout the article denote the front-left, front-right, rear-left, and rear-right wheels, respectively.

Based on the CG position at the last moment, the initial position of the four wheels was calculated:

$$\begin{bmatrix} x_N(i-1) \\ y_N(i-1) \end{bmatrix} = \begin{bmatrix} x_{\mathrm{CG}}(i-1) \\ y_{\mathrm{CG}}(i-1) \end{bmatrix} + \begin{bmatrix} \cos\psi(i-1) & \sin\psi(i-1) \\ -\sin\psi(i-1) & \cos\psi(i-1) \end{bmatrix} \begin{bmatrix} \frac{k_1 W}{2} \\ k_2 L \end{bmatrix}, \tag{4}$$

where (x, y) denote the coordinate positions and ψ is the yaw angle, the subscript $N = 1, 2, 3, \text{and } 4$ represents the front-left, front-right, rear-right, and rear-left wheel, respectively; and

$$\begin{cases} k_1 = -1, & k_2 = 1, \text{ if } N = 1 \\ k_1 = 1, & k_2 = 1, \text{ if } N = 2 \\ k_1 = 1, & k_2 = -1, \text{if } N = 3 \\ k_1 = -1, & k_2 = -1, \text{if } N = 4. \end{cases} \tag{5}$$

Furthermore, the four-wheel positions at the current time can be calculated on the basis of no slip assumption, that is,

$$\begin{bmatrix} x_1(i) \\ y_1(i) \end{bmatrix} = \begin{bmatrix} x_1(i-1) \\ y_1(i-1) \end{bmatrix} + \begin{bmatrix} \sin(\psi(i-1)+\delta_{\mathrm{fl}}) \\ \cos(\psi(i-1)+\delta_{\mathrm{fl}}) \end{bmatrix} v_{\mathrm{fl}}\mathrm{d}t, \tag{6a}$$

$$\begin{bmatrix} x_2(i) \\ y_2(i) \end{bmatrix} = \begin{bmatrix} x_2(i-1) \\ y_2(i-1) \end{bmatrix} + \begin{bmatrix} \sin(\psi(i-1)+\delta_{\mathrm{fr}}) \\ \cos(\psi(i-1)+\delta_{\mathrm{fr}}) \end{bmatrix} v_{\mathrm{fr}}\mathrm{d}t, \tag{6b}$$

$$\begin{bmatrix} x_3(i) \\ y_3(i) \end{bmatrix} = \begin{bmatrix} x_3(i-1) \\ y_3(i-1) \end{bmatrix} + \begin{bmatrix} \sin\psi(i-1) \\ \cos\psi(i-1) \end{bmatrix} v_{\mathrm{rr}}\mathrm{d}t, \tag{6c}$$

$$\begin{bmatrix} x_4(i) \\ y_4(i) \end{bmatrix} = \begin{bmatrix} x_4(i-1) \\ y_4(i-1) \end{bmatrix} + \begin{bmatrix} \sin\psi(i-1) \\ \cos\psi(i-1) \end{bmatrix} v_{\mathrm{rl}}\mathrm{d}t, \tag{6d}$$

$$\psi(i) = \psi(i-1) + \omega\mathrm{d}t. \tag{6e}$$

The four virtual vehicle CG positions $(x_{\mathrm{CG,N}}, y_{\mathrm{CG,N}})$ are calculated according to the four-wheel positions with the geometric relationship and the body direction:

$$\begin{bmatrix} x_{\mathrm{CG,N}}(i) \\ y_{\mathrm{CG,N}}(i) \end{bmatrix} = \begin{bmatrix} x_N(i) \\ y_N(i) \end{bmatrix} + \begin{bmatrix} \cos\psi(i) & \sin\psi(i) \\ -\sin\psi(i) & \cos\psi(i) \end{bmatrix} \begin{bmatrix} \frac{k_1 W}{2} \\ k_2 L \end{bmatrix}, \tag{7}$$

where k_1 and k_2 are defined in **Equation 5**. Finally, the CG position can be obtained by the following relations:

$$\begin{bmatrix} x_{\mathrm{CG}}(i) \\ y_{\mathrm{CG}}(i) \\ \psi_{\mathrm{CG}}(i) \end{bmatrix} = \begin{bmatrix} \frac{1}{4}\sum_{N=1}^{4} x_{\mathrm{CG,N}}(i) \\ \frac{1}{4}\sum_{N=1}^{4} y_{\mathrm{CG,N}}(i) \\ \psi(i) \end{bmatrix}. \tag{8}$$

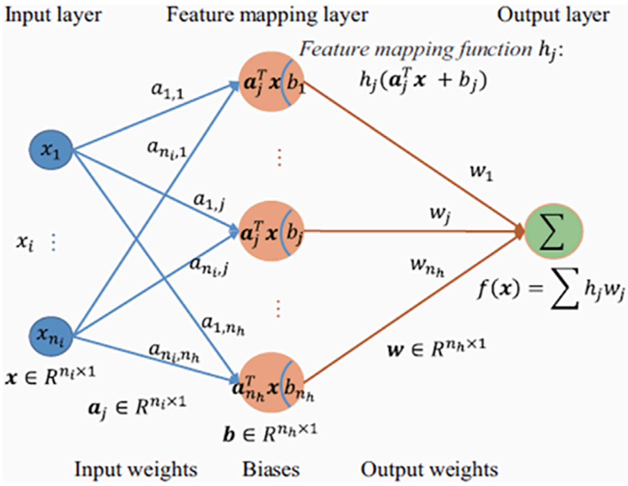

FIGURE 2 | General structure of the ELM.

At the same time, the redundant design is considered to avoid large slips of the individual wheel or large positioning deviations caused by the low tire pressure and the signal disturbance. The evaluation index $d_{\mathrm{C,N}}$ is defined as follows:

$$d_{\mathrm{C,N}} = \sqrt{(x_N - x_{\mathrm{CG}})^2 + (y_N - y_{\mathrm{CG}})^2}, \quad N = 1, 2, 3, 4, \tag{9}$$

and take the front-left wheel (i.e., $N = 1$), for example (same with other wheels), if $d_{\mathrm{C,1}} > (d_{\mathrm{C,2}} + d_{\mathrm{C,3}} + d_{\mathrm{C,4}})/3$, then this value will be regarded as poor confidence and it will be removed. The final CG position with redundant design will use the following calculation:

$$\begin{cases} x_{\mathrm{CG}} = \frac{1}{3}(x_2 + x_3 + x_4) \\ y_{\mathrm{CG}} = \frac{1}{3}(y_2 + y_3 + y_4). \end{cases} \tag{10}$$

2.2 Compensation Scheme Design-Based on ELM

For long-distance dead reckoning, the estimation of the heading angle determines the overall positioning accuracy. In some actual testing scenarios, it is found that due to the mechanical structure of the steering system gap, left and right asymmetry, positioning angle changes, and other factors, the left and right front wheel angle mapping from the steering wheel angle has errors, which leads to inaccurate heading angular rate and indirectly leads to the large cumulative errors in position estimation. Considering the internal parameters of the system affecting the accuracy of heading angular rate cannot be obtained and the compensation model is difficult to be established, an extreme learning machine (ELM) based estimation algorithm is introduced in this study to improve the estimation accuracy of the heading angular rate. The general structure of the ELM can be found in **Figure 2**.

ELM is also referred to as generalized single-hidden layer feed-forward neural networks (FNN) where the hidden layer need not be neuron alike (Huang et al., 2015). Compared to conventional FNN learning methods, ELM adopts Moore–Penrose generalized inverse to set its weights instead of the gradient-based backpropagation strategy. Essentially, the learning process can be implemented without iteratively tuning hidden nodes, and it achieves better generalization performance by minimizing both the training error and the norm of output weights. Therefore, ELM has higher efficiency and generalization ability than other learning methods. Typically, the output function of the ELM is defined as follows:

$$\mathbf{y} = f_{n_h}(\mathbf{x}) = \sum_{j=1}^{n_h} \mathrm{w}_j h_j(\mathbf{x}) = \mathbf{h}(\mathbf{x})\mathbf{w}, \tag{11}$$

where $\mathbf{w} = [\mathrm{w}_1, \ldots, \mathrm{w}_{n_h}]^T$ denotes the output weight vector between the hidden layer of n_h nodes and the m output nodes, $\mathbf{h}(\mathbf{x}) = [h_1(\mathbf{x}), \ldots, h_{n_h}(\mathbf{x})]$ is the feature mapping function. In this study, the training dataset is selected with $\mathbf{x} = \begin{bmatrix} v_{\mathrm{rl}} & v_{\mathrm{rr}} & \theta & \dot{\theta} \end{bmatrix}^T$, where input states include rear-left and rear-right wheel speed, steering wheel angle, and their difference, respectively; the output $\mathbf{y}$ is the error between the calculated yaw rate and the measured yaw rate based on the high-precision inertial navigation. The optimal weights $\mathbf{w}^*$ between the hidden layer and the output layer are calculated by solving the following cost:

$$\min_{\mathbf{w} \in \mathrm{R}^{n_h \times m}} \frac{1}{2} \| \mathbf{w} \|^2 + \frac{C}{2} \| H\mathbf{w} - T \|^2, \tag{12}$$

where H denotes the hidden layer output matrix, T is the training goal matrix, and C is regularization coefficient; the solution is as follows:

$$\mathbf{w}^* = \left(H^T H + \frac{I}{C} \right)^{-1} H^T T, \tag{13}$$

where I is an identity matrix of n_h dimension. Thus, the final ELM-based output for the heading angular rate is

$$\hat{\mathbf{y}} = f_{n_h}(\mathbf{x}) = \mathbf{h}(\mathbf{x})\mathbf{w}^*. \tag{14}$$

The final vehicle yaw rate estimation is the combination of the calculated yaw rate and the heading angular rate calculation error output by ELM.

2.3 Real Vehicle Validation for Dead Reckoning

In order to verify the effectiveness of the ELM-based compensation strategy, vehicle experiments have been carried out under different conditions including straight line, S-shaped, and right-angle bending. The on-board measurement based on a high-precision global position system (GPS) is used for the baseline benchmark, and the positioning effects with and without ELM compensation have been evaluated, as shown in **Figures 3–5**.

It is obvious from **Figures 3–5** that the error accumulation of the dead reckoning is small and the compensation effect is not obvious in the initial short distance. However, as the distance goes far, the dead reckoning without compensation deviates from the GPS measured value, the cumulative error gradually increases, and the positioning accuracy decreases. Even the error becomes more obvious when encountering a large corner. Moreover,

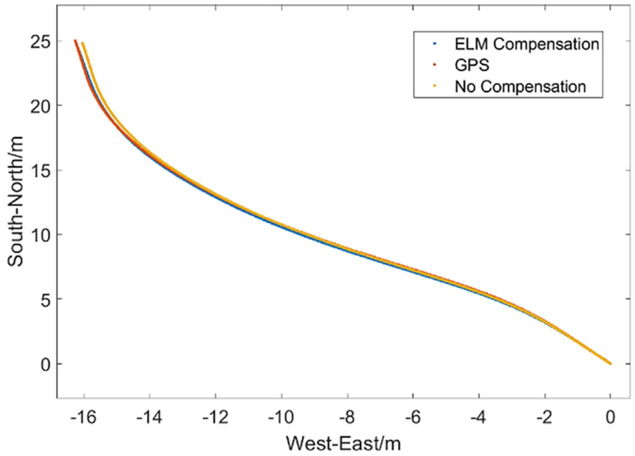

FIGURE 3 | Comparison result of the dead reckoning test under straight line conditions.

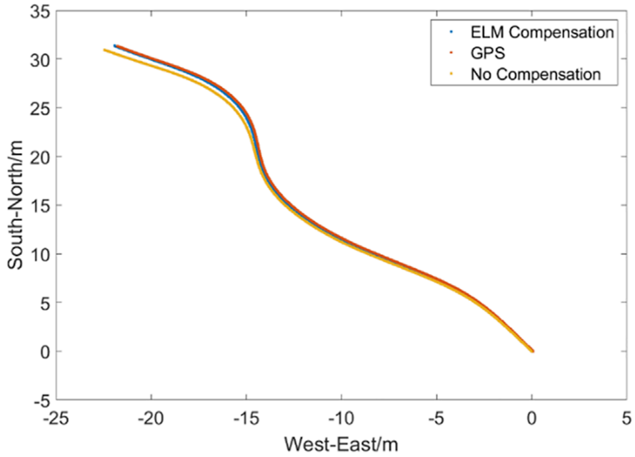

FIGURE 4 | Comparison result of the dead reckoning test under S-shaped condition.

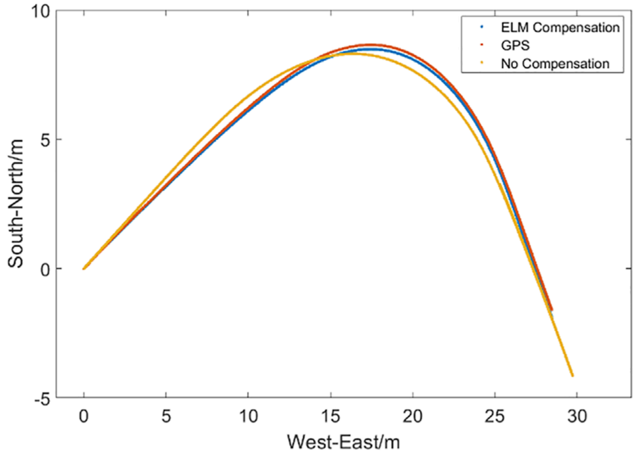

FIGURE 5 | Comparison result of the dead reckoning test under right-angle bending condition.

the dead reckoning with ELM compensation can always be stable near the measured value with a small error. Although the error increases after a large corner, it can quickly return to the true value after the corner, which improves stability and reliability.

3 REVERSING ASSISTANT CONTROLLER DESIGN

RA can record the vehicle's forward track point when the recording condition is satisfied. If the RA function is activated, the system controls the vehicle to follow the recorded track automatically and completes the reverse drive.

3.1 Preview Point Determination

The existence of time delay and external disturbance in the steering system will lead to lag effects in vehicle reversing tracking control, especially when requiring a large turning angle, and therefore leads to the large following error. The preview strategy is used in this study to solve this problem and, based on the vehicle's current position and state, to calculate its position after a certain previewing time.

As shown in **Figure 6**, the current position of the vehicle is $PntV\left(x,y,\varphi\right)$, its position at the preview point is $PntV_p\left(x_p,y_p,\varphi_p\right)$, and if $|\omega| < 0.001\text{rad}$, then the vehicle is identified to be driving in a straight line:

$$x_p = x - vt_p\sin\psi, \tag{15a}$$

$$y_p = y - vt_p\cos\psi, \tag{15b}$$

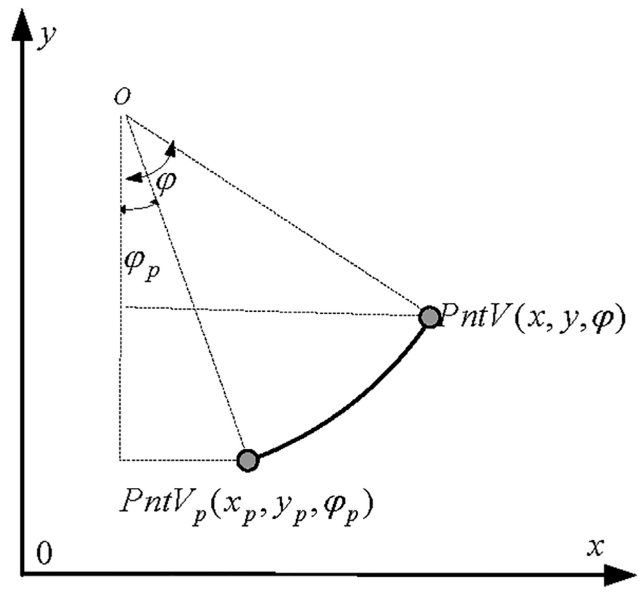

FIGURE 6 | Position calculation diagram at preview point.

$$\psi_p = \psi. \tag{15c}$$

On the contrary, if $|\omega| \geq 0.001\text{rad}$, vehicle position at the preview point is

$$x_p = x + v\left(\sin\left(\psi + \omega t_p\right) - \sin\psi\right)/\omega, \tag{16a}$$

$$y_p = y - v\left(\cos\left(\psi + \omega t_p\right) - \cos\psi\right)/\omega, \tag{16b}$$

$$\psi_p = \psi + \omega t_p, \tag{16c}$$

where t_p is preview time.

3.2 Target Track Point Selection

The closest tracking point to the vehicle preview point, denoted by *PntN*, is determined via the recorded forward tracking point sequence and vehicle preview position. According to the relative position relationship between the vehicle preview point and the closest point, the front point *PntF* and the rear point *PntR* can be determined, and then the target tracking point *PntM* is finally obtained. The decision procedure of the target tracking point is illustrated in **Figure 7**.

3.3 Calculation of Lateral and Heading Deviation

Once the target tracking point is determined, the lateral error Δy and heading angle error $\Delta\psi$ of the target tracking point and the vehicle preview point can be calculated. As shown in **Figure 8**, denote the coordinate of the target point *PntM* as $\left(x_r,y_r,\varphi_r\right)$ and the vehicle preview point $PntV_p$ as $\left(x_v,y_v,\varphi_v\right)$, there exists the following relations:

$$\begin{cases}\Delta y = \left(y_r - y_v\right)\cos\psi_r - \left(x_r - x_v\right)\sin\psi_v \\ \Delta\psi = \psi_r - \psi_v,\end{cases} \tag{17}$$

where the heading angle error is normalized to $[-\pi,\pi]$.

3.4 RA Controller Design

The implementation of the RA function mainly depends on the accuracy of the tracking control by adjusting the steering angle. The recorded steering angle when driving forward, denoted as sw_e, is used as a reference steering wheel angle at the corresponding position, which provides the feed-forward control input. In addition, considering the external interference and other factors, a parameter adaptive PID feedback control scheme is designed for correction and compensation. The feed-forward and the feedback control variables are given as follows:

$$\begin{cases}u_{\text{ff}} = sw_e \\ u_{\text{fb}} = \left(\dfrac{k_{pd}\Delta y}{\cos\Delta\psi} + \dfrac{k_{p\psi}\Delta\psi}{\cos\Delta\psi}\right) + k_i\int\Delta y dt + k_d\Delta y\end{cases} \tag{18}$$

where the continuous smooth self-tuning of the proportion parameter is determined by the heading angle error, namely, when the heading angle error is small, the following effect is

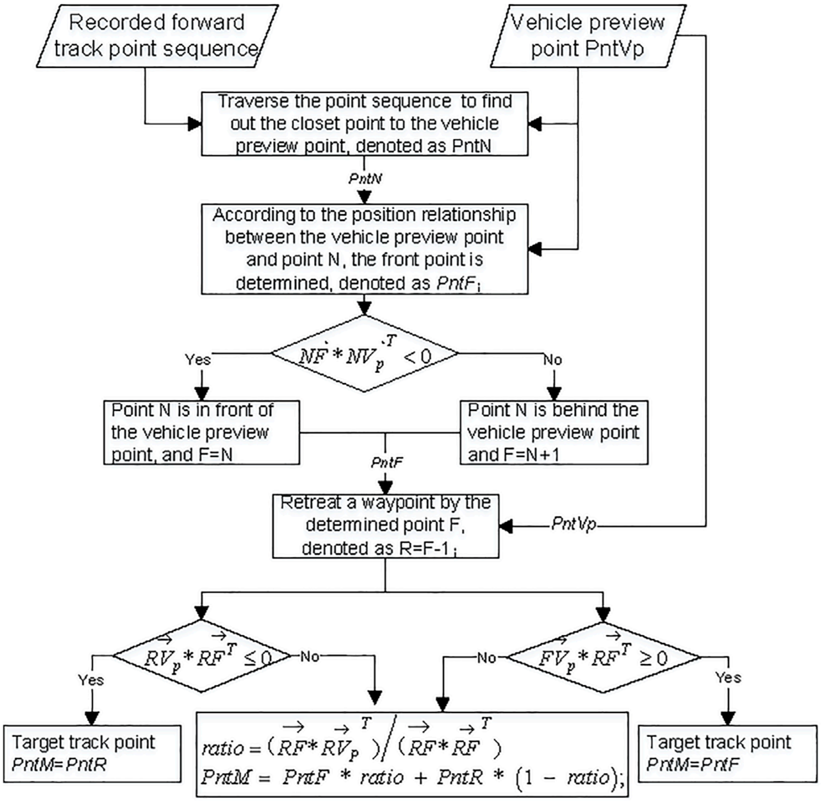

FIGURE 7 | Calculation process of the target tracking point.

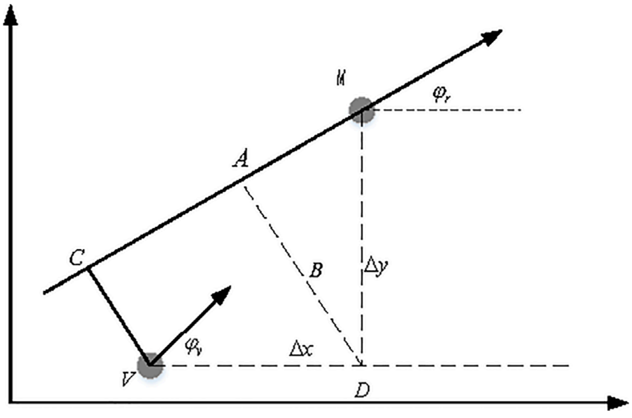

FIGURE 8 | Calculation of lateral and heading deviation.

great, and the proportion coefficient becomes smaller to reduce overshoot and oscillation; on the contrary, when the following effect is poor and the heading angle error becomes larger, the proportion parameter becomes larger accordingly, which improves the response speed and rapidly follows the desired trajectory.

4 VEHICLE TEST AND VALIDATION

The effectiveness of dead reckoning and the RA control method is verified in this section. The real vehicle tests were carried out in some typical conditions including straight line, S-shaped, and right-angle bending, based on an SUV model. The experimental results are shown in **Figures 9–13**.

The straight line RA test result is illustrated in **Figure 9**. In this straight line test, when the vehicle moves about 38 m and around 36 s, the RA state changes from 1 to 2 and the RA function is activated, and the vehicle starts reversing at a fixed speed of 3 km/h. In the whole process, the wheel angle control quantity is smooth, the forward and reverse tracks coincide, with the lateral error being less than 0.2 cm and the heading angle error being less than 0.2°. Although a few sample periods have a jump, it is due to the temporary jump of each value including the target track point and vehicle preview point, and because of the mechanical filtering effect on the high-frequency signal, there is no sudden change in the intuitive perception.

As shown in **Figure 10**, in the S-shaped RA scenario, the forward S-shaped trajectory and the reverse trajectory coincide, and the control quantity is smooth without jitter. Although the deviation becomes larger when reversing due to the failure of the optimal preview time, the lateral error

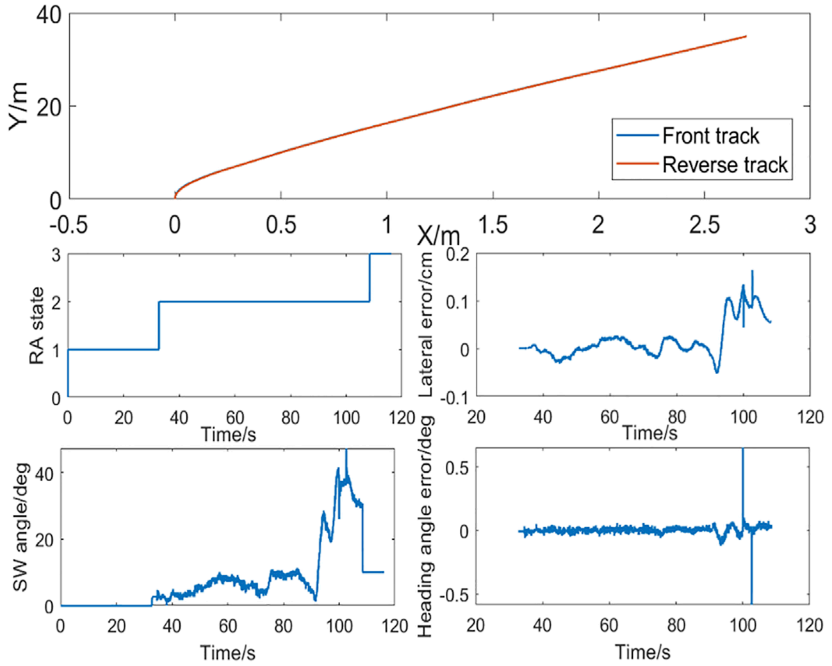

FIGURE 9 | RA in straight line condition.

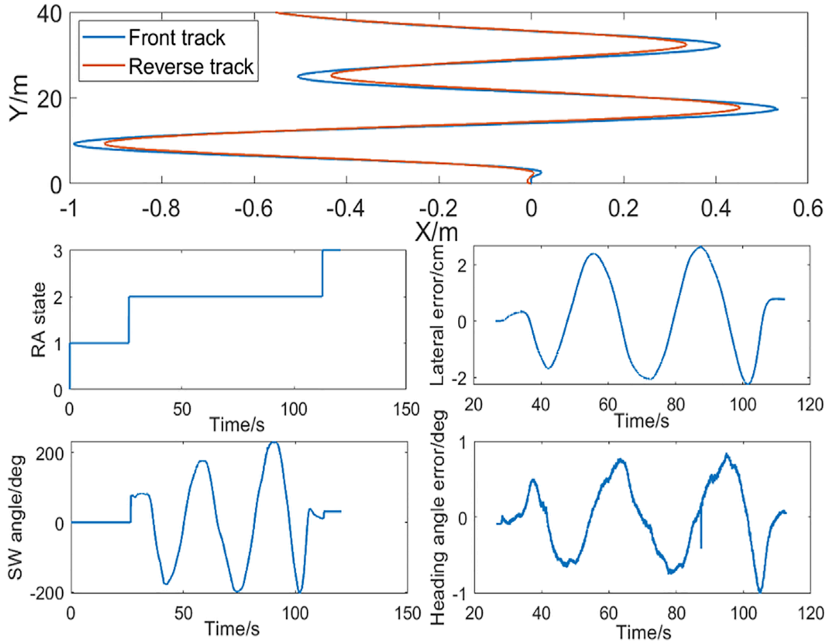

FIGURE 10 | RA in S-shaped condition.

is always less than 3 cm, and the heading angle error is less than 1°.

As shown in **Figure 11**, in the right-angle bending RA scenario, although the error increases at the turning point, the forward trajectory coincides with the reverse trajectory, and the control quantity is smooth without jitter, the lateral error is always less than 2 cm, and the heading angle error is less than 0.5°.

As shown in **Figure 12**, there is a high degree of convergence between the forward trajectory and the reverse trajectory. In the tracking process, due to the external impact when crossing the

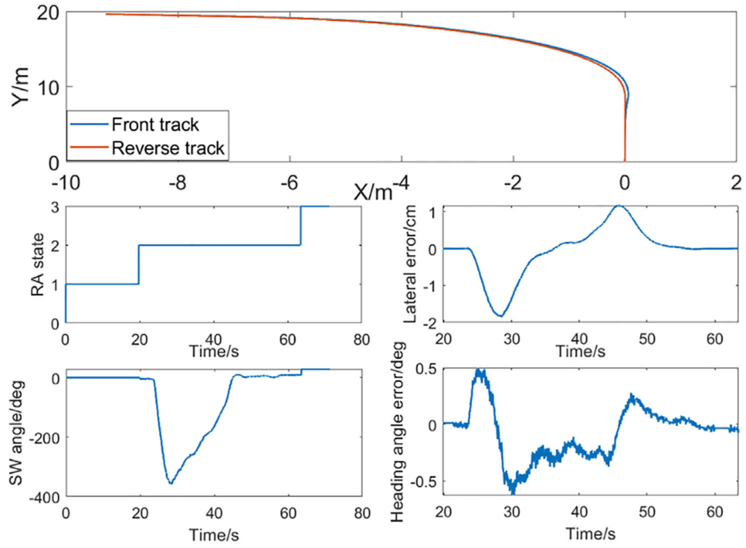

FIGURE 11 | RA in right-angle bending condition.

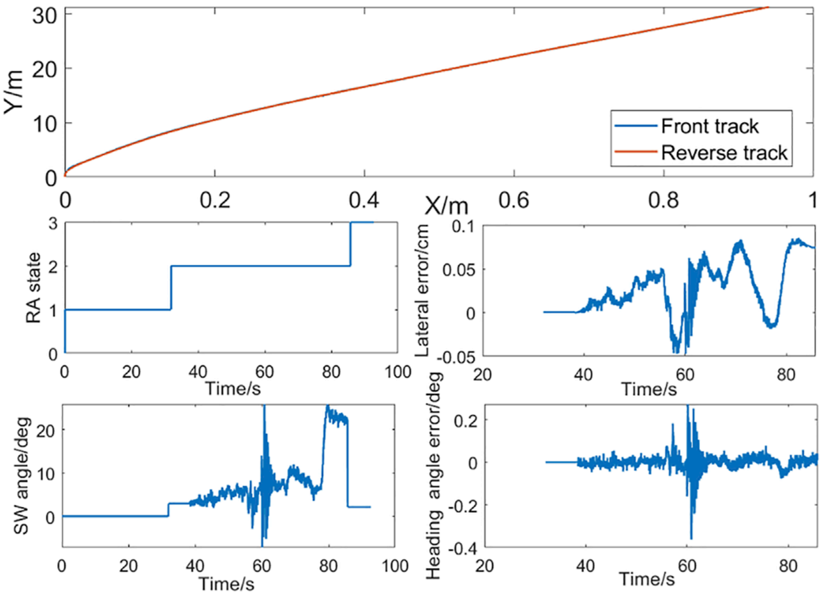

FIGURE 12 | RA in a speed bump.

speed belt, the steering wheel angle oscillates temporarily after the impact on the steering system due to the driver's hands off, which leads to the jitter of the point given by the dead reckoning, but it converges quickly. In the process of being hit by the speed bump, the lateral error and heading angle error are kept to a small level.

As shown in **Figure 13**, after a right-angle bending, the vehicle enters about 8% slope consisting of both longitudinal and lateral slopes. In the whole process, the forward trajectory and reverse trajectory have a high degree of overlap. On the ramp, the lateral error is less than 2 cm, and the heading angle error is less than 1°. The left and right wheel bearing are different due to the existence of the lateral slope, which leads to a small vibration in the steering wheel and a certain degree of the dead reckoning jitter; error has also been accumulated, directly leading to larger error when it enters the flat road and turns right-angle bending, but the lateral error and the heading angle error are always controlled in a small level.

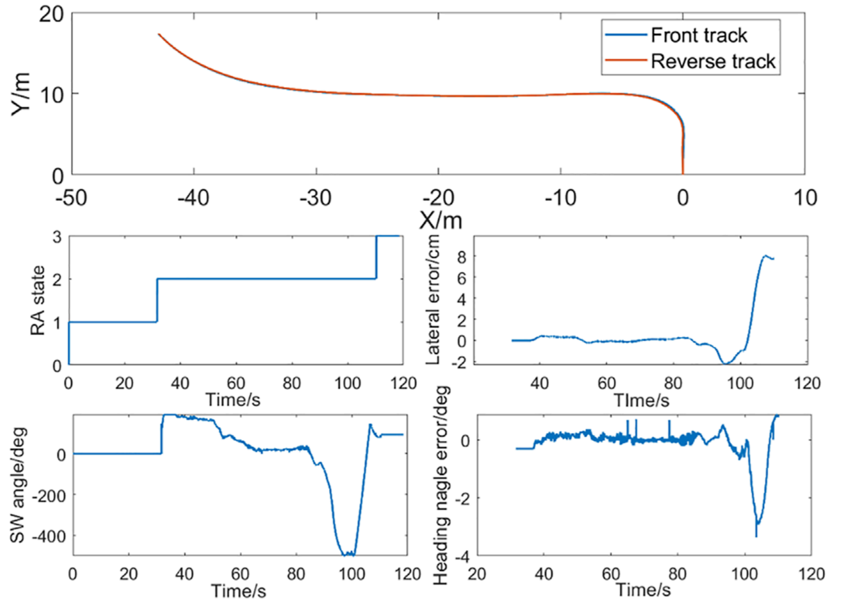

FIGURE 13 | RA in a slope.

5 CONCLUSION

In this study, the dead reckoning method with redundant design is proposed, which makes full use of the information of four wheels and eliminates the influence of slip of the wheels on positioning. At the same time, in view of the modeling complexity for position estimation, an ELM is introduced to estimate the heading angular rate and compensate for the dead reckoning. As for tracking control, a feed-forward and feedback PID controller with preview is designed. The proposed positioning and tracking control methods are proved effective, and the design satisfies the requirements of performance indexes via a variety of scenario tests. In addition, considering the mechanical wear and aging with the long-term use of the vehicle system, the ELM-based compensation method may face performance degradation problems; therefore, the future work will focus on the online update of the compensation model to improve the reliability of the RA function.

DATA AVAILABILITY STATEMENT

The raw data supporting the conclusion of this article will be made available by the authors, without undue reservation.

AUTHOR CONTRIBUTIONS

HD: conceptualization, investigation, experimental data analysis, and original draft writing; YY: extreme learning machine algorithm, experimental data collection, and original draft writing; MZ: tracking controller validation and experimental data analysis; and MK: conceptualization, control algorithm design, and review and editing.

FUNDING

This work is supported by the Fundamental Research Funds for the Central Universities (Grant No. N2108006).

REFERENCES

Alvarez, J. C., Alvarez, D., López, A., and González, R. C. (2012). Pedestrian Navigation Based on a Waist-Worn Inertial Sensor. *Sensors* 12 (8), 10536–10549. doi:10.3390/s120810536

Bayuwindra, A., Aakre, O. L., Ploeg, J., and Nijmeijer, H. (2016). "Combined Lateral and Longitudinal CACC for a Unicycle Type Platoon [J]," in 2016 IEEE Intelligent Vehicles Symposium (IV), 527–532.

Beauregard, S. (2009). *Infrastructureless Pedestrian Positioning [D]*. Bremen, Germany: Doktor-ingenieur faculty of mathematics informatics University of Bremen.

Chen, Y.-b., Luo, G.-c., Mei, Y.-s., Yu, J.-q., and Su, X.-l. (2016). UAV Path Planning Using Artificial Potential Field Method Updated by Optimal Control Theory. *Int. J. Syst. Sci.* 47 (6), 1407–1420. doi:10.1080/00207721.2014.929191

Coulter, R. C. (1992). *Implementation of the Pure Pursuit Path Tracking algorithm[R]*. Pittsburgh: Carnegie Mellon University Pittsburgh PA Robotics Institute, CMU-RI-TR-92-01.

Cui, S., Pei, X., Jiang, Y., Wang, G., Fan, X., Yang, Q., et al. (2021). Liquefaction within a Bedding Fault: Understanding the Initiation and Movement of the Daguangbao Landslide Triggered by the 2008 Wenchuan Earthquake (Ms = 8.0). *Eng. Geol.* 295, 106455. doi:10.1016/j.enggeo.2021.106455

Falcone, P., Borrelli, F., Asgari, J., Tseng, H. E., and Hrovat, D. (2007). Predictive Active Steering Control for Autonomous Vehicle Systems. *IEEE Trans. Contr. Syst. Technol.* 15 (3), 566–580. doi:10.1109/tcst.2007.894653

Guo, K., and Fancher, P. S. (1983). "Preview-follower Method for Modelling Closed-Loop Vehicle Directional Control [J]," in Massachusetts Inst. of Tech., 19th Annual Conference.

Guo, K., and Guan, H. (1993). Modelling of Driver/vehicle Directional Control System [J]. *Veh. Syst. Dyn.* 22 (1), 141–184. doi:10.1080/00423119308969025

He, Y., and Kusiak, A. (2017). Performance Assessment of Wind Turbines: Data-Derived Quantitative Metrics. *IEEE Trans. Sustain. Energy* 9 (1), 65–73.

Hess, W., Kohler, D., Rapp, H., and Andor, D. (2016). "Real-time Loop Closure in 2D LIDAR SLAM[C]," in Robotics and Automation (ICRA), 2016 IEEE International Conference on. IEEE (Stockholm, Sweden: IEEE), 1271–1278.

Ho, N.-H., Truong, P., and Jeong, G.-M. (2016). Step-Detection and Adaptive Step-Length Estimation for Pedestrian Dead-Reckoning at Various Walking Speeds Using a Smartphone. *Sensors* 16 (9), 1423. doi:10.3390/s16091423

Huang, G. B., Zhu, Q. Y., and Siew, C. K. (2006). Extreme Learning Machine: Theory and Applications. *Neurocomputing* 70 (1), 489–501. doi:10.1016/j.neucom.2005.12.126

Huang, G., Huang, G.-B., Song, S., and You, K. (2015). Trends in Extreme Learning Machines: A Review. *Neural Netw.* 61, 32–48. doi:10.1016/j.neunet.2014.10.001

Jian, L., Chen, X., Luo, M., and Zhou, Y. (2020). Cooperative Localization for Multiple AUVs Based on the Rough Estimation of the Measurements [J]. *Appl. Soft Comput. J.* 91, 106197. doi:10.1016/j.asoc.2020.106197

Jiménez, A. R., Zampella, F., and Seco, F. (2014). Improving Inertial Pedestrian Dead Reckoning by Detecting Unmodified Switched-On Lamps in Buildings [J]. *Sensors* 14, 731–769.

Kang, M.-x., and Gao, J.-w. (2020). Design of an Eco-Gearshift Control Strategy under a Logic System Framework. *Front. Inf. Technol. Electron Eng.* 21 (2), 340–350. doi:10.1631/fitee.1900459

Le, S., Wu, Y., Guo, Y., and Vecchio, C. D. (2021). Game Theoretic Approach for a Service Function Chain Routing in NFV with Coupled Constraints. *IEEE Trans. Circuits Syst. II* 68, 3557–3561. Published online. doi:10.1109/TCSII.2021.3070025

Leppäkoski, H., Collin, J., and Takala, J. (2013). Pedestrian Navigation Based on Inertial Sensors, Indoor Map, and WLAN Signals [J]. *J. Signals Process. Syst.* 71 (3), 287–296.

Li, H., Deng, J., Feng, P., Pu, C., Arachchige, D. D. K., and Cheng, Q. (2021a). Short-Term Nacelle Orientation Forecasting Using Bilinear Transformation and ICEEMDAN Framework. *Front. Energy Res.* 9, 780928. doi:10.3389/fenrg.2021.780928

Li, H., Deng, J., Yuan, S., Feng, P., and Arachchige, D. D. K. (2021b). Monitoring and Identifying Wind Turbine Generator Bearing Faults Using Deep Belief Network and EWMA Control Charts. *Front. Energy Res.* 9, 799039. doi:10.3389/fenrg.2021.799039

Li, H., He, Y., Xu, Q., Deng, j., Li, W., and Wei, Y. (2022). Detection and Segmentation of Loess Landslides via Satellite Images: a Two-phase Framework. *Landslides* 19, 673–686. doi:10.1007/s10346-021-01789-0

Liu, K., Asher, Z., Gong, X., Huang, M., and Kolmanovsky, I. (2019). Vehicle Velocity Prediction and Energy Management Strategy Part 1: Deterministic and Stochastic Vehicle Velocity Prediction Using Machine Learning (No. 2019-01-1051). *SAE Tech. Pap.*

Marino, R., Scalzi, S., and Netto, M. (2011). Nested PID Steering Control for Lane Keeping in Autonomous Vehicles. *Control Eng. Pract.* 19 (12), 1459–1467. doi:10.1016/j.conengprac.2011.08.005

Moujahid, A., Tantaoui, M. E., Hina, M. D., Soukane, A., Ortalda, A., ElKhadimi, A., et al. (2018). Machine Learning Techniques in ADAS: A Review, in 2018 International Conference on Advances in Computing and Communication Engineering (ICACCE), 235–242.

Ourmazd, A. (2020). Science in the Age of Machine Learning. *Nat. Rev. Phys.* 2 (7), 342–343. doi:10.1038/s42254-020-0191-7

Shen, X., Zhang, X., Ouyang, T., Li, Y., and Raksincharoensak, P. (2020). Cooperative Comfortable-Driving at Signalized Intersections for Connected and Automated Vehicles. *IEEE Robot. Autom. Lett.* 5 (4), 6247–6254. doi:10.1109/LRA.2020.3014010

Shin, S. H., Lee, M. S., Park, C. G., and Hong, H. S. (2010). Pedestrian Dead Reckoning System with Phone Location Awareness Algorithm[C]//Position Location and Navigation Symposium. *IEEE Xplore*, 97–101.

Skog, I., and Handel, P. (2009). In-Car Positioning and Navigation Technologies-A Survey. *IEEE Trans. Intell. Transp. Syst.* 10 (1), 4–21. doi:10.1109/tits.2008.2011712

Thrun, S., Montemerlo, M., Dahlkamp, H., Stavens, D., Aron, A., Diebel, J., et al. (2006). Stanley: The Robot that Won the DARPA Grand Challenge. *J. Field Robot.* 23 (9), 661–692. doi:10.1002/rob.20147

Tian, Z., Zhang, Y., Zhou, M., and Liu, Y. (2014). Pedestrian Dead Reckoning for MARG Navigation Using a Smartphone. *EURASIP J. Adv. Signal Process.* 2014 (1), 65. doi:10.1186/1687-6180-2014-65

Wang, J., Ni, D., and Li, K. (2014). RFID-based Vehicle Positioning and its Applications in Connected Vehicles. *Sensors* 14 (3), 4225–4238. doi:10.3390/s140304225

Woodman, O. J. (2007). *An Introduction to Inertial Navigation [J]*. Cambridge: University of Cambridge, Computer Laboratory. Tech. Rep. UCAMCL-TR-696.

Wu, Y., Zhang, J., and Shen, T. (2022). A Logical Network Approximation to Optimal Control on Continuous Domain and its Application to HEV Control. *Sci. CHINA Inf. Sci.* doi:10.1007/s11432-021-3446-8

Zhang, H., Yuan, W., Shen, Q., Li, T., and Chang, H. (2015). A Handheld Inertial Pedestrian Navigation System with Accurate Step Modes and Device Poses Recognition. *IEEE Sensors J.* 15 (3), 1421–1429. doi:10.1109/jsen.2014.2363157

Zhou, J., Wei, J., Yang, T., Zhang, P., Liu, F., and Chen, J. (2021). Seepage Channel Development in the Crown Pillar: Insights from Induced Microseismicity. *Int. J. Rock Mech. Min. Sci.* 145, 104851. doi:10.1016/j.ijrmms.2021.104851

Ziegler, J., Bender, P., Schreiber, M., Lategahn, H., Strauss, T., Stiller, C., et al. (2014). Making Bertha Drive-An Autonomous Journey on a Historic Route. *IEEE Intell. Transp. Syst. Mag.* 6 (2), 8–20. doi:10.1109/mits.2014.2306552

Conflict of Interest: HD, YY, and MZ were employed by Guangzhou Automobile Group Co., Ltd

The remaining author declares that the research was conducted in the absence of any commercial or financial relationships that could be construed as a potential conflict of interest.

BRIEF RESEARCH REPORT
published: 23 May 2022
doi: 10.3389/fenrg.2022.906107

Insulator Fouling Monitoring Based on Acoustic Signal and One-Dimensional Convolutional Neural Network

Li Hao[1], *Li Zhenhua*[1,2]*, *Cheng Ziyi*[1], *Chen Xingxin*[1] *and Yanchun Xu*[1]

[1]*Electrical Engineering and New Energy, China Three Gorges University, Yichang, China,* [2]*Hubei Provincial Key Laboratory for Operation and Control of Cascaded Hydropower Station, China Three Gorges University, Yichang, China*

Aiming at the problem of pollution insulator discharge mode monitoring in high voltage line, a new one-dimensional convolutional neural network structure (1D-CNN) was designed, and a pollution insulator discharge mode monitoring method based on acoustic emission signal and 1D-CNN was proposed. Firstly, the data was collected in laboratory of acoustic emission signal under different discharge after sliding access way to expand the sample quantity. Thereafter, the sample time and frequency domain was used along with a third octave data as input, using convolution neural network to discharge signal samples adaptive feature extraction and feature dimension reduction. Then, appropriate stride convolution alternative pooling layer was used in order to reduce the training model parameters and the amount of calculation. Finally, Softmax function was used to classify the predicted results. The identified results show that the model can achieve a recognition rate of more than 99.84%, which effectively solves the process of manual data preprocessing in the traditional insulator pollution degree monitoring method. Moreover, at the same time it can be effectively applied to the pollution insulator discharge mode monitoring task.

Keywords: discharge of polluted insulator, convolutional neural network, acoustic emission signal, fault diagnosis, deep learning

Edited by:
Xun Shen,
Tokyo Institute of Technology, Japan

Reviewed by:
Sandeep Kumar Duran,
Lovely Professional University, India
Gaurav Sachdeva,
DAV University, India

****Correspondence:***
Li Zhenhua
lizhenhua1993@163.com

Specialty section:
This article was submitted to
Smart Grids,
a section of the journal
Frontiers in Energy Research

Received: *28 March 2022*
Accepted: *12 April 2022*
Published: *23 May 2022*

Citation:
Hao L, Zhenhua L, Ziyi C, Xingxin C and Xu Y (2022) Insulator Fouling Monitoring Based on Acoustic Signal and One-Dimensional Convolutional Neural Network.
Front. Energy Res. 10:906107.
doi: 10.3389/fenrg.2022.906107

INTRODUCTION

Among the power system accidents that have occurred in my country in recent years, the insulator pollution flashover accident is one of the main disasters. In the atmospheric environment, the pollution in the air will adhere to the surface of the insulator and become damp, resulting in a pollution flashover accident (Ahmadi-Joneidi et al., 2013; Wang et al., 2014), which seriously affects the safe and smooth operation of the power grid and causes a lot of economic loss. The contamination discharge of insulators is accompanied by the generation of acoustic signals, and the intensity of the acoustic signals changes with the degree of discharge, which can better characterize the external insulation state of the insulator under the current operating state (Gencoglu and Cebeci, 2009; Su et al., 2009; Moula et al., 2013; Li et al., 2021b). Therefore, in practical engineering, the state evaluation of the external insulation state of the insulator can be realized by analyzing and processing the acoustic signals of the insulator discharge under different pollution states.

Scholars at home and abroad have carried out a lot of explorations in the acquisition, denoising, feature selection and extraction of the discharge acoustic signals of polluted insulators under operating conditions, and the establishment of on-line diagnosis and prediction models for insulator pollution. Literature (Tian et al., 2016) believes that the insulator pollution discharge consists of three stages, namely corona discharge, partial discharge and arc discharge, and the characteristics of the acoustic emission signal generated by the discharge are obviously different. Reference Tian et al. (2015) proposes to perform empirical mode decomposition on complex acoustic emission signals, and adaptively decompose the original acoustic signal into several components in different frequency bands, that is, eigenmode components. The energy distribution is compared and identified. In the literature (Wang and Nie, 2016), by studying the time-frequency characteristics of acoustic signals at different fouling degrees, it was found that the acoustic signal contains four characteristic quantities in both the mean value in the time domain and the spectral characteristics in the frequency domain, and the four characteristic quantities, the mean value, the maximum value, the standard deviation and the amplitude of the real part of the FFT of the acoustic signal in the time domain, were used for correlation analysis of the development process of insulator fouling discharge. In the literature (Wang et al., 2021), after manually simulating the effects of different soluble fouling adhesion densities and gray densities on the acoustic emission signals of glass insulators, a generalized regression neural network-based insulator hazard prediction model was established with the mean value of signal amplitude and the area of the maximum IFT semi-perimeter envelope as the main input feature quantities, and more accurate prediction results were obtained. In order to improve the prediction accuracy, the traditional machine learning classification method needs to preprocess the data to extract the data features and select an appropriate classification method.

For these series of problems, this paper considers Deep learning techniques to solve them. In recent years, many scholars have applied deep learning to the field of fault diagnosis and achieved very good results (Dong et al., 2014; Banik et al., 2016; Li et al., 2020; Yang et al., 2022a). Among them, recurrent neural networks (RNN) and convolutional neural networks (CNN) are widely used, and convolutional neural networks have been used by many scholars to build fault diagnosis models based on the feature processing of fault signal-time spectrograms due to their powerful processing ability of two-dimensional images (Li et al., 2019; Li et al., 2021a; Li et al., 2021b). Li et al. (2021c), proposed the bilinear transformation, effective data decomposition techniques, long-short-term-memory recurrent neural networks (LSTM-RNNs), and error decomposition correction methods. In the proposed approach, the angular wind direction data is firstly transformed into time-series to accommodate the full range of yaw motion. Then, the continuous transformed series are decomposed into a group of subseries using a novel decomposition technique. Moreover, Li et al. (2021d) utilized a data-driven approach for condition monitoring of generator bearings using temporal temperature data. During the analysis, four algorithms, the support vector regression machine, neural network, extreme learning machine, and the deep belief network are applied to model the bearing behavior. Comparative analysis of the models has demonstrated that the deep belief network is most accurate. It has been observed that the bearing failure is preceded by a change in the prediction error of bearing temperature. Convolutional neural networks tend to achieve recognition rates of more than 99% in the direction of fault diagnosis, but the current research in the direction of insulator fouling monitoring usually only uses traditional machine learning classification. Therefore, this paper proposes a one-dimensional CNN-based fouled insulator discharge pattern recognition algorithm, which does not require complex and time-consuming manual feature extraction, but simply takes the un-preprocessed time-frequency discharge signal as input, and the model uses the powerful feature learning capability of CNN to directly train the input signal as learning samples, and completes adaptive feature learning by combining with fully connected layers to realize the model for insulator fouling degree. The model uses the powerful feature learning capability of CNN to directly use the input signal as the learning sample for training, and completes the adaptive feature learning in combination with the fully connected layer to realize the model's demand for insulator fouling degree monitoring, and gets good results after experimental verification.

CONVOLUTIONAL NEURAL NETWORKS

Convolutional Neural Network Operations

CNNs usually include an input layer, a convolutional layer, a pooling layer, a fully connected layer and an output layer (Bashivan et al., 2015; Ye et al., 2021; Zhang L. et al., 2021). The convolutional layer and adjacent layers use local links and weight sharing to perform operations, while the pooling layer can also largely reduce the dimensionality of the input to prevent overfitting of the model during training and improve the generalization of the model. The pooling layer can also largely reduce the input dimension, prevent overfitting of the model during training, and improve the generalization capability of the model. The model uses alternating convolutional and pooling layers to extract features from the input data, and the learning ability of the CNN reliably increases with the number of layers of the network. The convolution operation procedure (Sajjad et al., 2019; Zhang et al., 2022) is illustrated as below.

$$y_i^{(l+1)}(j) = K_i^l * X^l(j) + b_i^l \tag{1}$$

In the formula: K_i^l and b_i^l is the weight and bias of the i convolution kernel in the l layer; $X^l(j)$ is the local region in the l layer; $y_i^{l+1}(j)$ is the input of the first neuron in the result of the j convolution kernel operation in the $l+1$ layer.

The activation function is set after the convolutional layer, and when the data is extracted by features, the activation function can increase its nonlinear factor. In this paper, the LeakyReLU function (Zhang W. et al., 2021) is used. The LeakyReLU function solves the neuron death problem by giving all negative values of the inputs a slope greater than 0. The schematic diagram of LeakyReLU is as follows

$$a_i^{l+1}(j) = max\left(0, y_i^{l+1}(j)\right) + leak * min\left(0, y_i^{l+1}(j)\right) \quad (2)$$

Among them, $y_i^{l+1}(j)$ indicates the output value of the convolution operation, and $a_i^{l+1}(j)$ denotes the activation value of $y_i^{l+1}(j)$.

The pooling layer usually acts after the convolution layer to reduce the feature dimensionality and prevent overfitting. The pooling layer consists of two types of pooling, maximum pooling and average pooling, where the maximum pooling equation is as follows.

$$p_i^{l+1}(j) = \underset{(j-1)W+1 \le t \le jW_i^l}{max} \left\{q_i^l(t)\right\} \quad (3)$$

In the formula: $q_i^{l+1}(t)$ denotes the value of the t neuron in the i feature out of the l layer, $t \in [(j-1)W+1, jW]$, W indicates the width of the pooling area, $p_i^{(l+1)}(j)$ denotes the value of the j neuron in the i feature of the $l+1$ layer.

The Softmax classifier is most widely used in the output classification operation of the output layer (Zhao et al., 2017; Yang, 2021). The process is to output the logits values obtained from the convolution layer as a probability distribution and then perform pattern recognition, and the Softmax function operates as follows.

$$f\left(z_j\right) = \frac{e^{z_j}}{\sum_k^n e^{z_k}} \quad (4)$$

In the above stated formula: j is some classification in k; z_j is the value of the category.

Principle of One-Dimensional Convolutional Neural Network

The one-dimensional convolutional neural network can perform feature recognition on the part of the data sequence, use the convolution kernel to perform input transformation on the input sequence segment, and make the sequence features of a part of the sequence which can be saved in other locations of the sequence, making the one-dimensional convolutional neural network. The processing principle for different positions of the sequence is invariant (for time shift) (Toyoda and Wu, 2019; Madhiarasan, 2020; Le et al., 2021; Yang et al., 2021; Laghridat et al., 2022). One-dimensional convolution can extract partial sequence segments from time series and through the interaction of convolution and pooling, adaptive line feature extraction and dimensionality reduction are performed on the data.

ONE-DIMENSIONAL CONVOLUTIONAL NEURAL NETWORK INSULATOR MONITORING MODEL

1D-CNN Model Overview

The transition coupling of different discharge stages of dirty insulators makes the discharge acoustic signals of dirty insulators uncertain, complex and big data. Because the core of the discharge pattern recognition of dirty insulators is to distinguish the pattern expression in the specific discharge signal under different discharge patterns so as to realize the recognition of the discharge pattern. The advantage of the recognition method based on CNN algorithm lies in the feature extraction and classification of massive data.

Therefore, this paper proposes a discharge mode monitoring algorithm for dirty insulators based on one-dimensional convolutional neural network. It consists of a convolution layer and an output layer. The convolution layer implements the adaptive feature extraction operation on the discharge signal data, and the nonlinear robust feature with the gradually decreasing matrix width is obtained through the convolution operation. Unlike 2D-CNN processing image data, the pooling layer does not compress the convolutional data ideally. Therefore, this paper does not use the pooling layer, but uses stridden convolution with a suitable number of steps in the convolutional layer instead of the pooling layer to perform the compression operation. The output layer is composed of a fully connected layer, and every two connected layers are connected by a finite number of neurons, and the number of nodes is the same as the number of discharge types.

The cross-entropy loss function is used in the training process of the model, and the Adam optimizer (Nie et al., 2016; Wu et al., 2020; Anjaiah et al., 2022; Yang et al., 2022b) with fast convergence speed and stable convergence process is used to optimize the model based on gradient descent. At the same time, the model uses the Softmax function to output the cross-entropy between the probability distribution of the acoustic emission signal type and the probability distribution of the discharge type of the dirty insulator as the cost function. The formula for calculating cross entropy is stated below.

$$H(p,q) = -\sum_x p(x)lnq(x) \quad (5)$$

In the formula: $p(x)$ is the probability distribution of different discharge patterns; $q(x)$ is the probability distribution of the model output prediction results.

Data Pre-Processing

The data pre-processing mainly includes: data enhancement of the raw acoustic signal data using data window sliding fetch, generation of training and test sample sets, labeling of discharge types, and introduction of the 1/3 octave concept to amplify the differential features of different discharge mode signals in the high or low frequency bands.

The process of network training in Deep learning requires sufficient data samples, and the experimental data used in this paper are limited, in order to expand the number of samples while preserving the correlation between adjacent timing signals of the same discharge signal. In this paper, a sliding window fetching method is proposed to divide the data into small samples to achieve the enhancement of the number of data samples.

Different from other models that only use signal time-frequency features as model input, this paper introduces the

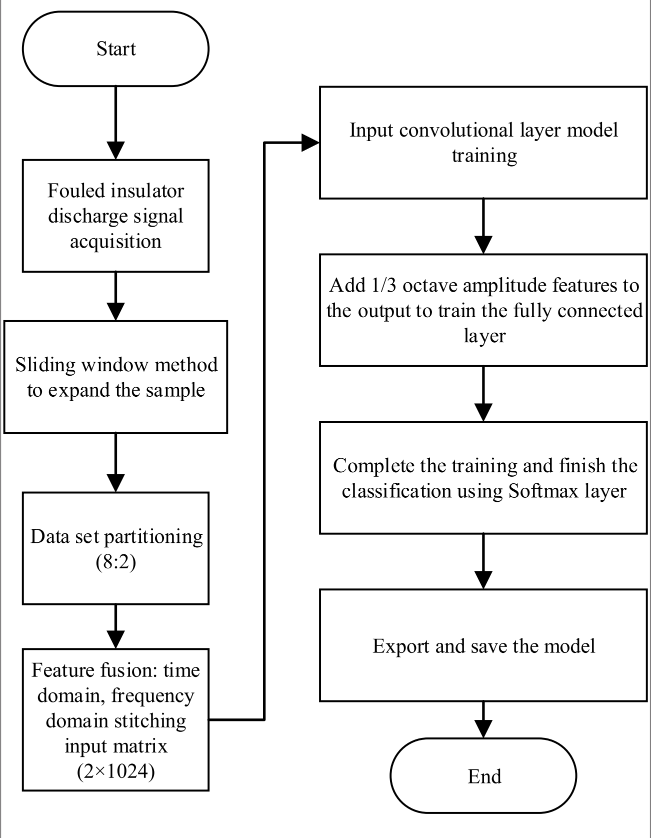

FIGURE 1 | Fouled insulator discharge mode monitoring process.

concept of octave. There are two main ways of expressing frequency. One is equal-width frequency range, which means that the coordinate difference between adjacent frequencies on the X-axis is constant. The other is octave, which means that the ratio of adjacent frequency coordinates on the X-axis is a fixed constant. Generally speaking, when we analyze the spectral characteristics of the signal, we do not study all the frequencies in the signal one by one, but the octave is to divide the signal into frequency bands to display the sound pressure levels of different frequency bands of the signal data. Since the gap between the discharge signals of different pollution levels often exists in the high frequency or low frequency band, this paper uses the 1/3 octave amplitude feature as a feature input of the model and the 1/3 octave frequency of the three discharge modes is used.

One-Dimensional Convolutional Neural Network Intelligent Monitoring Process

The proposed one-dimensional convolutional neural network fouling insulator discharge pattern monitoring process is shown in **Figure 1**. The original data signal collected from the experiment is augmented by the sliding window method for the number of samples and divided into training set and test set; the one-dimensional convolutional neural network model is established on Pytorch version 1.11.0, and the model is trained by gradient descent using mini batch after inputting sample data from the training set, where the hyperparameter of batch size is 64. The accuracy and loss function curves of the training set and test set are recorded and the predicted discharge pattern is output after the model is completed training. The accuracy and loss function curves of the training set and test set are recorded and the predicted signal discharge patterns are output, and finally the model performance is evaluated visually using the t-distribution Stochastic Neight-bor Embedding (t-SNE) and the test set confusion matrix.

FOULED INSULATOR DISCHARGE PATTERN MONITORING EXPERIMENT

Experimental Design and Data Description

In order to verify the effect of the monitoring model proposed in this paper, a large number of discharge tests of fouled insulators were conducted in the high-voltage test chamber, mainly collecting sound data of corona discharge, surface discharge and breakdown arc discharge of insulators when fouled insulators were subjected to processing frequency or shock voltage, and recording the corresponding discharge phenomena. The test equipment includes: frequency voltage generator, shock voltage generator, oscilloscope, sound acquisition device and various types of fouling production tools (brush, sodium chloride, diatomaceous earth, test, spray pot and pure water).

In this experiment, the sound signals of 2 wet porcelain insulators with different degrees of fouling discharging at 10 different locations were collected and the equivalent attached salt densities was used to measure the degree of fouling of insulators. Each insulator specimen was coated with sodium chloride and diatomaceous earth, after calculated weighing, plus an appropriate amount of distilled water, and mixed thoroughly in a porcelain bowl. In order to increase the degree of adhesion an appropriate amount of dextrin could be added, and finally evenly applied to the surface of the insulator with a brush. The fouled insulator specimens made in this way can be tested without sampling, and this easy-to-operate pollution method is mostly used in China. Since sodium chloride is water-absorbent, it can be fully dried before weighing, and then weighed with a balance to ensure the experimental accuracy.

The ratio of gray density to salt density of the actual operating insulators varies greatly, and the actual local accumulation of dirt, the gray to salt ratio is taken as 5:1.

TABLE 1 | 1D-CNN algorithm and other algorithms accuracy comparison table.

No.	Algorithm	Accuracy
1	Artificial features +XGBoost	87.5%
2	FFT+1/3 Octave +BPNN	94.5%
3	FFT+1D-CNN	96.82%
4	FFT+1/3 Octave +1D-CNN	99.84%

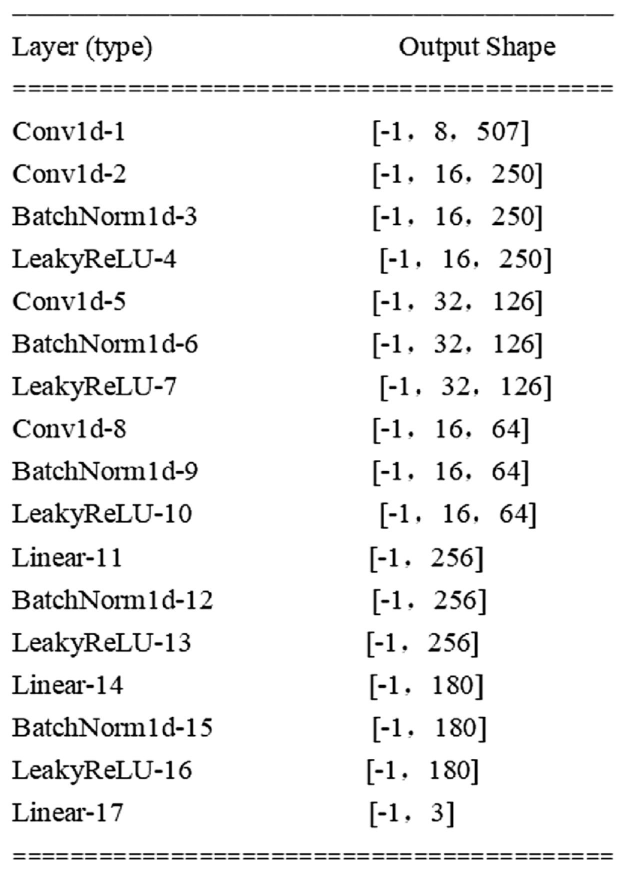

```
________________________________________
Layer (type)                  Output Shape
========================================
Conv1d-1                  [-1, 8, 507]
Conv1d-2                  [-1, 16, 250]
BatchNorm1d-3             [-1, 16, 250]
LeakyReLU-4                [-1, 16, 250]
Conv1d-5                  [-1, 32, 126]
BatchNorm1d-6             [-1, 32, 126]
LeakyReLU-7                [-1, 32, 126]
Conv1d-8                  [-1, 16, 64]
BatchNorm1d-9             [-1, 16, 64]
LeakyReLU-10               [-1, 16, 64]
Linear-11                 [-1, 256]
BatchNorm1d-12            [-1, 256]
LeakyReLU-13             [-1, 256]
Linear-14                 [-1, 180]
BatchNorm1d-15            [-1, 180]
LeakyReLU-16             [-1, 180]
Linear-17                 [-1, 3]
========================================
```

FIGURE 2 | 1D-CNN output size of each network layer.

Under this gray to salt ratio, the mass of salt and ash to be painted on the whole insulator surface with different attached salt density is shown in **Table 1** below. The above-mentioned stain coated in porcelain insulator 2 pieces as a group, apply the industrial frequency voltage, the amplitude is the rated voltage of insulator string, record the industrial frequency voltage experiment results, then use the voltage reduction method, time 2 min each time, determine the flashover voltage, record the discharge sound.

The acoustic emission signals of three discharge states, namely corona, surface discharge and arc, were collected at a sampling frequency of 131072 HZ. 655360 data points were included for the corona and surface discharge states, and 1,048,000 data points were included for the arc discharge state. After a simple frequency domain analysis, it was found that the sampling frequency was too high and the actual main frequency was very low. So sparse sampling was performed, i.e., every 100 data points were sampled once. Each data is sampled by sliding window sampling method with 1024 data points as a sample and 50 data points as a step to achieve sample set expansion, and for each insulator fouling discharge mode 80% of the data set is randomly selected for training and 20% of the data set is used for testing. Therefore, the sparsely sampled and expanded data set consists of 4930 training samples and 1266 test samples, and the category labels are set to 0, 1, and 2. The input to the convolution layer of each model is the time-domain signal of one sample plus the Fourier-transformed frequency-domain signal splicing matrix (2 × 1024), and the 1/3-octave amplitude features of the sample are spliced with the convolution output feature matrix and input to the full connected layer for training. The size and number of convolutional kernels in the four convolutional layers of the network model are set to 16 × 1, 16 × 1, 8 × 1, 8 × 1 and 16, 16, 8 and 8, respectively, and the convolutional kernel step size is set to 2. Data normalization is performed using Batch Normalization and supplemented with padding as input mapping.

Analysis of Experimental Results

The output size of each network layer of the 1D-CNN model proposed in this paper is shown in **Figure 2**. The variation of the accuracy of the 1D-CNN algorithm with the number of iterations analyzed are the recognition rate and loss function value of the fouled insulator discharge state of the test set samples, respectively. As the number of iterations increases, the accuracy of the test set output of the model also gradually increases and the value of the loss function gradually decreases. After iteration, the accuracy of the test set reaches 99.84% and is similar to that of the training set, and there is no overfitting phenomenon.

In this paper, the performance of the 1D-CNN algorithm for data processing was also visualized and analyzed. In this paper, the t-distribution domain embedding algorithm was used to visualize and analyze the features of the fouled insulator discharge signal after convolution with different convolution layers in a 2-D distribution, as shown in **Figure 3**.

In order to better evaluate the recognition effect of the model, this paper also used the validation set to input into the trained convolutional neural network model for simulation validation, where the accuracy of the surface discharge state in the data samples of fouled insulators reached 100%, and the accuracy of the corona discharge and arc discharge states also reached 99.13% and 99.6%, respectively.

To compare the classification effectiveness of the algorithms studied in this paper with manually extracted features plus machine learning classification algorithms and other Deep learning algorithms, XGBoost, Back Propagation Neural Network (BPNN) and 1D-CNN algorithms were selected for comparison through experiments. XGBoost and BP are common algorithms in machine learning and Deep learning, respectively. Among them, XGBoost algorithm is to classify the statistical features of the time-frequency domain of the discharge signal, and BPNN is to input the time-frequency and 1/3 octave data into the BP network for classification, both of which are commonly used classification algorithms. The final accuracy obtained by experimentally comparing the three discharge pattern recognition algorithms is shown in **Table 1**.

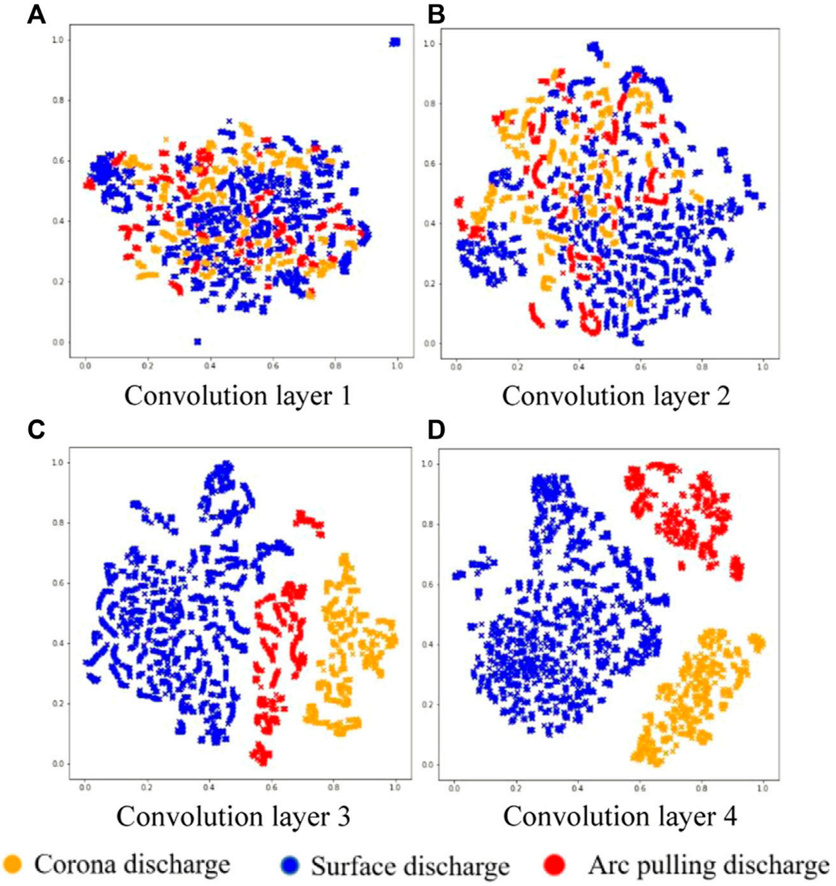

FIGURE 3 | Visualization results of discharge signal data samples. **(A)** Convolution layer 1 123 **(B)** Convolution layer 2. **(C)** Convolution layer 312 3 **(D)** Convolution layer 4.

CONCLUSION

In this paper, we proposed an algorithm of fouling insulator discharge pattern recognition based on acoustic signal and 1D-CNN for fouling insulator discharge pattern monitoring model. And the experiments were designed to collect the acoustic emission signal data of fouled insulator discharge under different modes, and the practicality and accuracy of this model were verified by using this as a sample simulation. It solves the complexity of the previous manual production of features, and becomes a new direction to solve the problem of insulator fouling degree monitoring.

The main contributions of this study are.

(1) A novel one-dimensional convolutional neural network structure (1D-CNN) was designed, and an insulator fouling detection model based on acoustic signals and 1D-CNN was proposed, which enabled the model to adaptively extract and classify features from time-frequency signal data and obtained a high recognition accuracy.
(2) In the case of limited data, the sliding window method was used to divide the data for fetching, and the concept of 1/3 octave range was introduced to optimize the training process of the model.
(3) The performance of the convolutional layer in the 1D-CNN algorithm was visualized using the t-SNE visualization algorithm, and the intrinsic mechanism of the 1D-CNN algorithm was explored.
(4) Through comparison tests with the traditional XGBoost and BPNN algorithms, the superiority of the proposed model in terms of accuracy was verified, and it could be effectively used for the early warning of fouling insulator flicker.

DATA AVAILABILITY STATEMENT

The raw data supporting the conclusion of this article will be made available by the authors, without undue reservation.

AUTHOR CONTRIBUTIONS

LH, CZ and CX conceived the experimental ideas and designed and implemented the experiments under the leadership of LZ. XY compiled the data and LH wrote the manuscript.

FUNDING

This project was supported by the Key Project of Science and Tech-nology Research Plan of Education of Hubei under Grant D20201203.

ACKNOWLEDGMENTS

The authors would like to thank the reviewers for their valuable comments and suggestions to improve the quality of this paper.

REFERENCES

Ahmadi-Joneidi, I., Majzoobi, A., Shayegani-akmal, A. A., Mohseni, H., and Jadidian, J. (2013). Aging Evaluation of Silicone Rubber Insulators Using Leakage Current and Flashover Voltage Analysis. *IEEE Trans. Dielect. Electr. Insul.* 20, 212–220. doi:10.1109/TDEI.2013.6451360

Anjaiah, K., Dash, P. K., and Sahani, M. (2022). A New Protection Scheme for PV-Wind Based DC-ring Microgrid by Using Modified Multifractal Detrended Fluctuation Analysis. *Prot. Control Mod. Power Syst.* 7, 8. doi:10.1186/s41601-022-00232-3

Banik, A., Dalai, S., and Chatterjee, B. (2016). Autocorrelation Aided Rough Set Based Contamination Level Prediction of High Voltage Insulator at Different Environmental Condition. *IEEE Trans. Dielect. Electr. Insul.* 23, 2883–2891. doi:10.1109/tdei.2016.7736849

Bashivan, P., Rish, I., Yeasin, M., and Codella, N. (2015). *Learning Representations from EEG with Deep Recurrent-Convolutional Neural Networks*. arXiv. 1511.06448 [Preprint]Available at: https://arxiv.org/abs/1511.06448 (Accessed Feb 29, 2016).

Dong, B., Jiang, X., Zhang, Z., Hu, J., Hu, Q., and Shu, L. (2014). Effect of Environment Factors on Ac Flashover Performance of 3 Units of Polluted Insulator Strings under Natural Fog Condition. *IEEE Trans. Dielect. Electr. Insul.* 21, 1926–1932. doi:10.1109/tdei.2014.004214

Gencoglu, M. T., and Cebeci, M. (2009). Computation of AC Flashover Voltage of Polluted HV Insulators Using a Dynamic Arc Model. *Euro. Trans. Electr. Power* 19, 689–701. doi:10.1002/etep.249

Laghridat, H., Essadki, A., and Nasser, T. (2022). Coordinated Control by ADRC Strategy for a Wind Farm Based on SCIG Considering Low Voltage Ride-Through Capability. *Prot. Control Mod. Power Syst.* 7, 7. doi:10.1186/s41601-022-00227-0

Le, S., Wu, Y., Guo, Y., and Vecchio, C. D. (2021). Game Theoretic Approach for a Service Function Chain Routing in NFV with Coupled Constraints. *IEEE Trans. Circuits Syst. II* 68 (12), 3557–3561. doi:10.1109/TCSII.2021.3070025

Li, H., Deng, J., Feng, P., Pu, C., Arachchige, D. D. K., and Cheng, Q. (2021). Short-Term Nacelle Orientation Forecasting Using Bilinear Transformation and ICEEMDAN Framework. *Front. Energy Res.* 9, 780928. doi:10.3389/fenrg.2021.780928

Li, H., Deng, J., Yuan, S., Feng, P., and Arachchige, D. D. K. (2021). Monitoring and Identifying Wind Turbine Generator Bearing Faults Using Deep Belief Network and EWMA Control Charts. *Front. Energy Res.* 9, 799039. doi:10.3389/fenrg.2021.799039

Li, Z., Jiang, W., Abu-Siada, A., Li, Z., Xu, Y., and Liu, S. (2021). Research on a Composite Voltage and Current Measurement Device for HVDC Networks. *IEEE Trans. Ind. Electron.* 68, 8930–8941. doi:10.1109/TIE.2020.3013772

Li, Z., Tao, Y., Abu-Siada, A., Masoum, M. A. S., Li, Z., Xu, Y., et al. (2019). A New Vibration Testing Platform for Electronic Current Transformers. *IEEE Trans. Instrum. Meas.* 68 (3), 704–712. doi:10.1109/TIM.2018.2854939

Li, Z., Xiang, X., Hu, T., Abu-Siada, A., Li, Z., and Xu, Y. (2020). An Improved Digital Integral Algorithm to Enhance the Measurement Accuracy of Rogowski Coil-Based Electronic Transformers. *Int. J. Electr. Power & Energy Syst.* 118, 105806. doi:10.1016/j.ijepes.2019.105806

Li, Z., Yu, C., Abu-Siada, A., Li, H., Li, Z., Zhang, T., et al. (2021). An Online Correction System for Electronic Voltage Transformers. *Int. J. Electr. Power & Energy Syst.* 126, 106611. doi:10.1016/j.ijepes.2020.106611

Madhiarasan, M. (2020). Accurate Prediction of Different Forecast Horizons Wind Speed Using a Recursive Radial Basis Function Neural Network. *Prot. Control. Mod. Power Syst.* 5, 230–238. doi:10.1186/s41601-020-00166-8

Moula, B., Mekhaldi, A., Teguar, M., and Haddad, A. (2013). Characterization of Discharges on Non-uniformly Polluted Glass Surfaces Using a Wavelet Transform Approach. *IEEE Trans. Dielect. Electr. Insul.* 20, 1457–1466. doi:10.1109/TDEI.2013.6571469

Nie, D., Zhang, H., Adeli, E., Liu, L., and Shen, D. (2016). "3D Deep Learning for Multi-Modal Imaging-Guided Survival Time Prediction of Brain Tumor Patients," in *International Conference on Medical Image Computing and Computer-Assisted Intervention* (Cham: Springer), 212–220. doi:10.1007/978-3-319-46723-8_25

Sajjad, M., Khan, S., Hussain, T., Muhammad, K., Sangaiah, A. K., Castiglione, A., et al. (2019). CNN-based Anti-spoofing Two-Tier Multi-Factor Authentication System. *Pattern Recognit. Lett.* 126, 123–131. doi:10.1016/j.patrec.2018.02.015

Su, Z. A., Chen, J. S., and Wang, C. K. (2009). Application of Vibration Method in Bearing Noise Measurement. *J. Harbin Bear.* 30, 59–62. doi:10.3969/j.issn.1672-4852.2009.02.030

Tian, S., Jin, Y., Shu, N., Shao, C., and Zhang, Y. (2016). *China Electr. power* 49 (07), 15–19+38. doi:10.11930/j.issn1004-9649.2016.07.015.05

Tian, X., Meng, F., and Tian, S. (2015). Identification of Pollution Insulator Discharge Based on Energy Distribution of Empirical Mode Decomposition and Grey Similarity Correlation Degree [J]. *Smart power grid* 3 (04), 298–302. doi:10.14171/j.2095-5944.sg.2015.04.004

Toyoda, M., and Wu, Y. (2019). Mayer-type Optimal Control of Probabilistic Boolean Control Network with Uncertain Selection Probabilities[J]. *IEEE Trans. Cybern.* 51 (6), 3079–3092. doi:10.1109/TCYB.2019.2954849

Wang, C., Li, T., Peng, Q., Tu, Y., Zou, L., and Zhang, S. (2014). "Study of Composite Insulator Leakage Current Characteristics in Contamination and Humidity Conditions," in 2014 IEEE Conference on Electrical Insulation and Dielectric Phenomena (CEIDP), 353–356. doi:10.1109/CEIDP.2014.6995783

Wang, H., and Nie, J. (2016). Time-frequency Characteristics Analysis of Fouling Discharge Sound Signals of High-Voltage Insulators[J]. *Electroceramic Light. arrester* (02), 12–17. doi:10.16188/j.isa.1003-8337.2016.02.003

Wang, Y., Shi, W., Xing-bo, H., Jiang, X., Zhang, C., and Zhang, Z. (2021). Fouling Flash Prediction Model for Glass Insulators Based on Acoustic Emission Characteristics[J]. *Power Constr.* 42 (05), 138–144. doi:10.12204/j.issn.1000-7229.2021.05.015

Wu, Y., Guo, Y., and Toyoda, M. (2020). Policy Iteration Approach to the Infinite Horizon Average Optimal Control of Probabilistic Boolean Networks. *IEEE Trans. Neural Netw. Learn Syst.* PP (7), 2910–2924. doi:10.1109/TNNLS.2020.3008960

Yang, N. (2021). "A Comprehensive Review of Security-Constrained Unit Commitment," in *Journal of Modern Power Systems and Clean Energy*, 1–14. doi:10.35833/MPCE.2021.000255

Yang, N., Qin, T., Wu, L., Huang, Y., Huang, Y., Xing, C., et al. (2022). A Multi-Agent Game Based Joint Planning Approach for Electricity-Gas Integrated Energy Systems Considering Wind Power Uncertainty. *Electr. Power Syst. Res.* 204, 107673. ISSN 0378-7796. doi:10.1016/j.epsr.2021.107673

Yang, N., Yang, C., Wu, L., Shen, X., Jia, J., Li, Z., et al. (2022). Intelligent Data-Driven Decision-Making Method for Dynamic Multisequence: An E-Seq2Seq-Based SCUC Expert System. *IEEE Trans. Ind. Inf.* 18, 3126–3137. doi:10.1109/TII.2021.3107406

Yang, N., Yang, C., Xing, C., Ye, D., and Jia, J. (2021). Deep Learning-Based SCUC Decision-Making: An Intelligent Data-Driven Approach with Self-Learning Capabilities. *IET Gener. Transm. Distrib.*, 1–12. doi:10.1049/gtd2.12315

Ye, J., Zhao, D., and Zhang, L. (2021). Research on Combined Electricity and Heating System Scheduling Method Considering Multi-Source Ring Heating Network[J]. *Front. Energy Res.*, 826. doi:10.3389/fenrg.2021.800906

Zhang, L., Cheng, L., and Alsokhiry, F. (2022). A Novel Stochastic Blockchain-Based Energy Management in Smart Cities Using V2S and V2G[J]. *IEEE Trans. intelligent Transp. Syst.*, 1–8. doi:10.1109/tits.2022.3143146

Zhang, L., Xie, Y., Ye, J., Xue, T., Cheng, J., Li, Z., et al. (2021). Intelligent Frequency Control Strategy Based on Reinforcement Learning of Multi-Objective Collaborative Reward Function. *Front. Energy Res.* 9, 587. doi:10.3389/fenrg.2021.760525

Zhang, W., Yan, W., Yuan-yuan, L., Jiang, J., Zhang, K., and Zhang, Y. (2021). Intrusion Detection Algorithm Based on CA-ResNet Network and NADAM Optimization [J]. *J. Chongqing Normal Univ. Nat. Sci. Ed.* 38 (04), 97–106. doi:10.11721/cqnuj20210418

Zhao, Z., Fan, X., Qi, Y., and Zhai, Y. (2017). "Multi-angle Insulator Recognition Method in Infrared Image Based on Parallel Deep Convolutional Neural Networks," in *Computer Vision*. Editors J. Yang, Q. Hu, M.-M. Cheng, L. Wang, Q. Liu, and X. Baiet al. (Singapore: Springer Singapore), 303–314. doi:10.1007/978-981-10-7305-2_27

Conflict of Interest: The authors declare that the research was conducted in the absence of any commercial or financial relationships that could be construed as a potential conflict of interest.

ORIGINAL RESEARCH
published: 27 May 2022
doi: 10.3389/fenrg.2022.899692

Hybrid Short-Term Wind Power Prediction Based on Markov Chain

Liangsong Zhou[1], *Xiaotian Zhou*[2], *Hao Liang*[2], *Mutao Huang*[1]* *and Yi Li*[3]

[1]School of Electrical and Electronic Engineering, Huazhong University of Science and Technology, Wuhan, China, [2]Department of Electrical and Computer Engineering, University of Alberta, Edmonton, AB, Canada, [3]College of Engineering, University of Washington, Seattle, WA, United States

This article proposes a combined prediction method based on the Markov chain to realize precise short-term wind power predictions. First, three chaotic models are proposed for the prediction of chaotic time series, which can master physical principles in wind power processes and guide long-term prediction. Then, considering a mechanism switching between different physical models via a Markov chain, a combined model is constructed. Finally, the industrial data from a Chinese wind farm were taken as a study case, and the results validated the feasibility and superiority of the proposed prediction method.

Keywords: wind power prediction, combined model, Markov chain, chaotic time series, data-driven

Edited by:
Shuang Zhao,
Hefei University of Technology, China

Reviewed by:
Man Zhang,
Hefei University of Technology, China
Zhiqing Yang,
RWTH Aachen University, Germany

***Correspondence:**
Mutao Huang
huangmutao@hust.edu.cn

Specialty section:
This article was submitted to
Smart Grids,
a section of the journal
Frontiers in Energy Research

Received: *19 March 2022*
Accepted: *01 April 2022*
Published: *27 May 2022*

Citation:
Zhou L, Zhou X, Liang H, Huang M and Li Y (2022) Hybrid Short-Term Wind Power Prediction Based on Markov Chain.
Front. Energy Res. 10:899692.
doi: 10.3389/fenrg.2022.899692

1 INTRODUCTION

To solve the global energy crisis and environmental pollution around the world, wind energy has become one of the most potential sources due to its clean and renewable properties (Brouwer et al., 2016; Yang et al., 2021a). In China, America, and many European countries, more and more wind power generation has been highly concentrated to the power system in the past decades (Huber et al., 2014; Yang et al., 2021b; Yang et al., 2022a), while in this case, the intermittency and variability of wind bring great challenges to the safety of power systems (Tang et al., 2020; Yang et al., 2022b). Therefore, an accurate wind power prediction system is required by system operators to mitigate the undesirable effects. Especially as the installed capacity of wind farms increases, this situation is more urgent than ever.

Currently, the major wind power prediction system related to power system schedule is based on short-term predictions. The existing short-term wind power prediction methods are mainly data-driven models, also known as statistical models. These methods usually utilize the statistical features of historical data and machine learning algorithms to train and build models, for example, auto-regressive and moving average models (ARMA), KNN, neural networks (NNs), support vector machines (SVMs), extreme learning machines (ELMs), and so on (Valipour et al., 2013; Doucoure et al., 2016; Tang et al., 2021). For instance, in Kanna and Singh (2012), several data-driven models were introduced for short-term wind power prediction. In Liu et al. (2012), an ELM-based wind power prediction model was also applied to the real wind farm data. All of these models could achieve high accuracy in short-term prediction, but their shortage is also obvious since residuals are cumulated as prediction is going on.

To improve the performance of wind power predictions, there are several ways for model improvement. This first type is to consider the combination of physical and statistical factors of data together. In this way, the multiple step prediction could be improved with the assistance of physical trends. For example, one useful model considering wind power data's physical factors is based on chaotic time series prediction, since the process of wind was validated to obey the variance of the chaotic system (Lange and Focken 2006). In Lei et al. (2007), wind power data were verified as a chaotic time series and reconstructed for wind power prediction. The second type is to consider different patterns in time series data and to build a hybrid prediction model. For example, some short-term prediction models utilize signal decomposition to generate different patterns, for example, wavelet decomposition and empirical mode decomposition (EMD) (An et al., 2011; Li et al., 2021a), and then combine predictions of different patterns for the final prediction. In this way, the prediction can be improved with more robustness. The more direct way is to use different models to reflect different patterns in prediction. For example, in Tascikaraoglu and Uzunoglu (2014), a linear combined model was proposed to average the prediction results of different methods. In Ouyang et al. (2016), a Markov chain was regarded as a switching regime to select different parameters in a prediction model.

Considering the aforementioned descriptions, this article proposed a hybrid model which considers the aforementioned two factors to realize precise short-term wind power prediction. The advantages of the proposed model can be summarized as follows: First, considering the physical characteristics of wind power time series, different chaotic time series models are used to form the model library. Since chaotic time series models are physics-based models, they are more reliable than data-driven models, especially in long-term trend prediction. Second, considering the mechanism of hybrid modeling, this study considers using the Markov chain to estimate wind patterns and to guide the selection of suitable physical models in prediction. Finally, combining these contributions to realize a high-precision wind power prediction, industrial wind power data are studied to validate the effectiveness of the proposed method.

2 PREDICTION MODEL FOR CHAOTIC TIME SERIES

Generally, if time series data are from a chaotic system, it is possible to reproduce the dynamics information of its related system. To realize this idea, time series data are usually embedded into a new diffeomorphism space where data have the same dynamic behaviors as the original space and better representation ability (Rand and Young 1988; Chen et al., 2019). Therefore, data in the reconstructed phase space would be better for modeling and data mining. Here, referring to Packard et al. (1980), wind power time series could be reconstructed as chaotic time series according to Takens' theory (Rand and Young 1988), expressed in the following form:

$$\mathbf{x}_n = \left(x_n, x_{n+\tau}, \cdots x_{n+(m-1)\tau}\right) \in R^m, n = 1, 2\cdots, N_0 = N - (m-1)\tau, \tag{1}$$

where $\{x_n\}$ represents the series of wind power data; x_n is the reconstructed data, which is a vector x_n R^m; and τ and m are delay time and embedding dimension parameters, which can be calculated by using the mutual information (MI) method (Fraser and Swinney 1986) and false nearest neighbors (FNN) method (Xiong et al., 2017), respectively. Then, based on the reconstructed chaotic time series in **eq. 1**, several prediction models could be built, for example, local prediction models, global prediction methods, prediction methods based on the Lyapunov exponent and Volterra prediction models (Zhang and Liang 2012; Jinquan et al., 2016). Considering the prediction precision, the global prediction method is rarely used in wind power prediction, so three selected models are introduced as follows.

2.1 Local Linear Model With First Order

Local prediction models have different orders, but the first-order linear model is used the most. Assuming a given point $x(t)$ in the phase space, q nearest points $x_i(t)$, $i = 1,2\ldots, q$, are taken as reference in prediction. Then the prediction model is described in **eq. 2**:

$$\begin{cases} \begin{bmatrix} \mathbf{x}_1(t+k) \\ \mathbf{x}_2(t+k) \\ \vdots \\ \mathbf{x}_q(t+k) \end{bmatrix} = A + B* \begin{bmatrix} \mathbf{x}_1(t) \\ \mathbf{x}_2(t) \\ \vdots \\ \mathbf{x}_q(t) \end{bmatrix}, \\ i = 1, 2, \cdots, q; k = 1, 2, \cdots; \end{cases} \tag{2}$$

where A and B are the coefficient matrixes of the prediction model, which can be trained by the least square method, and k is the prediction time interval, but its value cannot be too large since the evolution over a long period is not linear for chaotic systems.

Then the prediction is calculated as $x(t+k) = A + B*\mathbf{x}(t)$.

2.2 Prediction Method Based on the Lyapunov Exponent

In the chaotic system, it is known that two nearby tracks are linear in the short term and have an exponent trend in the longer term. This feature is utilized in the prediction method based on the Lyapunov exponent. Then the prediction model is expressed in **eq. 3**:

$$L_{t+k} = L_t \cdot e^{\lambda_k}, \tag{3}$$

where k is the prediction time interval, L_t is the distance between $\mathbf{x}(t)$ and its nearest neighbor $\mathbf{x}(t')$, L_{t+k} is the distance between $\mathbf{x}(t+k)$ and $\mathbf{x}(t'+k)$, λ_k is the Lyapunov exponent related to the interval k, and it is calculated when $T = k$.

2.3 Volterra Prediction Model

The Volterra algorithm is a non-linear filter and can be expressed in **eq. 4**:

$$\begin{aligned} x(n+1) = h_0 &+ \sum_{t=0}^{+\infty} h_1(t)x(n-t) + \sum_{t_1=0}^{+\infty}\sum_{t_2=0}^{+\infty} h_2(t_1,t_2)x(n-t_1)x(n-t_2) \\ &+ \sum_{t_1=0}^{+\infty}\sum_{t_2=0}^{+\infty}\cdots\sum_{t_p=0}^{+\infty} h_p\left(t_1,t_2\cdots t_p\right)\prod_{j=1}^{p} x\left(n-t_j\right) + \cdots, \end{aligned} \tag{4}$$

where $x(n+1)$ is the predicted value, $x(n-t)$ are historical values, p is the order of a Volterra filter, and h is the coefficient corresponding to different elements. It is seen that a Volterra filter with a high order is complex, so a second-order model is usually used for predicting wind power time series, as described in **eq. 5**:

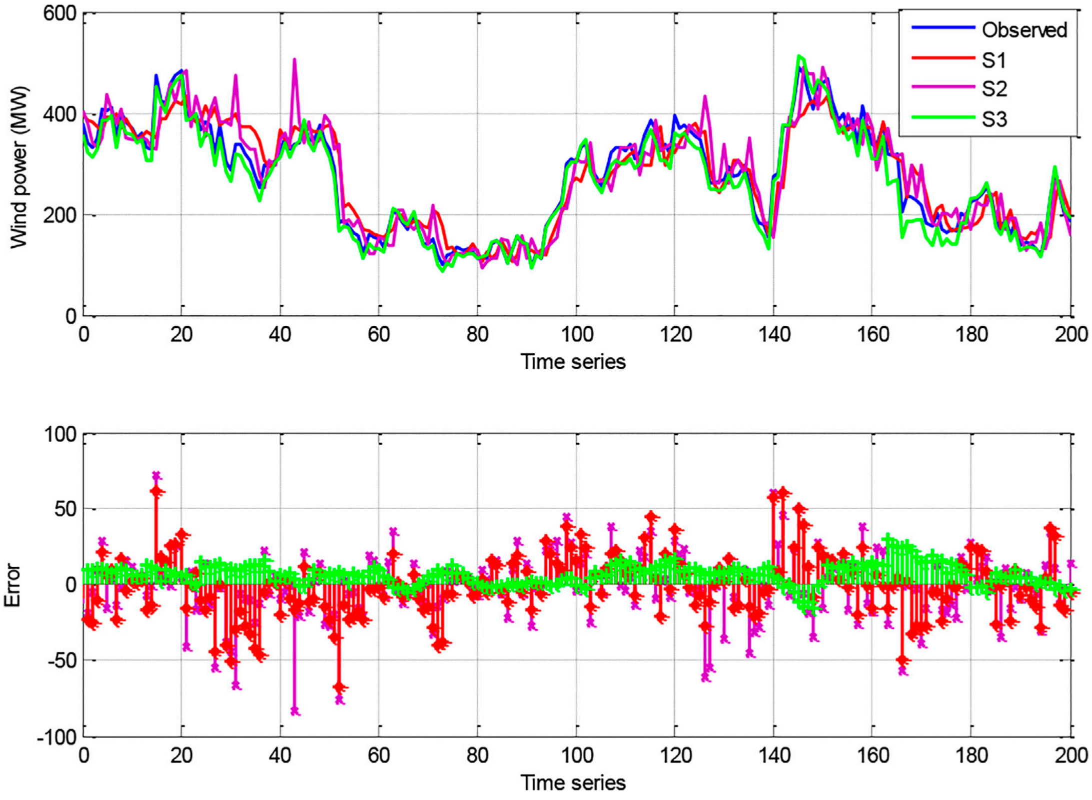

FIGURE 1 | Wind power prediction based on three given chaotic time series models.

TABLE 1 | Four error metrics of three individual chaotic prediction models.

	MAE	*RMSE*	*SDofAE*	*CC*
S_1	18.578	28.477	19.694	0.9470
S_2	18.460	26.230	19.128	0.9354
S_3	17.907	21.556	18.431	0.9838

$$x(t+k) = h_0 + \sum_{u=0}^{m-1} h_1(u)x(t-u\tau) + \sum_{v=0}^{m-1}\sum_{w=0}^{m-1} h_2(v,w)x(t-v\tau)x(t-w\tau), \tag{5}$$

where m is the embedded dimension, τ is the delay time, k is the prediction time interval, and u, v, and w represent the index of the selected data.

3 HYBRID MODELING WITH THE MECHANISM OF MARKOV CHAIN

The previously mentioned three models were proposed to apply in chaotic time series prediction in many references. The three methods perform differently in different scenarios and even have different accuracy in the same period in same scenario. Therefore, a suitable solution to achieve relatively better performance is to construct a combined model as described as follows:

$$\hat{y} = \sum w_i \cdot \hat{y}_i, \tag{6}$$

where $\hat{y}_i$ represents the output of an individual prediction model, $\hat{y}$ is the final output of the combined model, and w_i is the weight coefficient for the combination of different models.

In Ouyang et al. (2016), the Markov chain was used as a regime switching different models to improve the accuracy of short-term wind power prediction. The process is decided by the transition probability matrix of a Markov chain. In this article, a new combined model based on the transition probability and prediction models of chaotic time series is proposed to predict wind power.

By assuming these three chaotic time series models as three different patterns, as $\{S_1, S_2, S_3\}$, the idea of the Markov process is to suppose that the states s_{t+1} are related to the states s_t, described in **eq. 7**:

$$P_{ij}(t,t+1) = P\left(s_{t+1} = S_j \middle| s_t = S_i\right), \tag{7}$$

where P_{ij} $(t,t+1)$ is the transition probability on the condition of satisfying the current pattern S_i and the next pattern S_j. Assuming the wind power time series as Ω_t and the *tth* value is y_t, then the forward probability is defined in **eq. 8**:

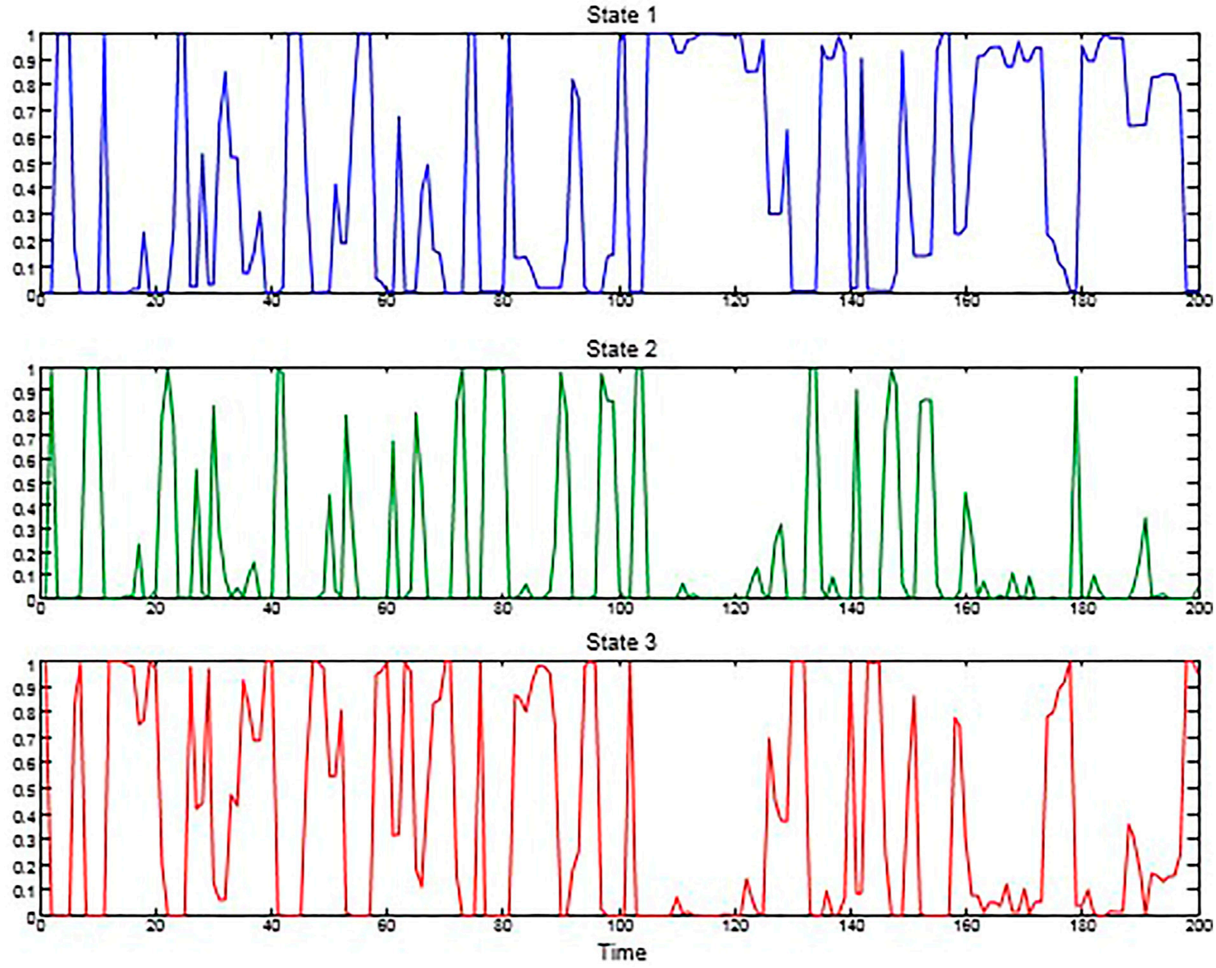

FIGURE 2 | Probability of three states (three models) at each time.

$$p_{t|t}^{(j)} = P(s_t = j|\Omega_t) = \frac{P(y_t, s_t = j|\Omega_{t-1})}{P(y_t|\Omega_{t-1})}, \tag{8}$$

where $p_{t|t}^{(j)}$ is the probability of $s_t = j$ with a given series Ω_t, and the numerator and denominator are calculated by **eq. 9**:

$$\begin{cases} P(y_t, s_t = j|\Omega_{t-1}) = p_{t|t-1}^{(j)} \cdot P(y_t|s_t = j, \Omega_{t-1}), \\ p_{t|t-1}^{(j)} = P(s_t = j|\Omega_{t-1}), \\ P(y_t|\Omega_{t-1}) = \sum_{j=1}^{N} P(y_t, s_t = j|\Omega_{t-1}), \end{cases} \tag{9}$$

where $N = 3$, since there are only three available prediction models. Conversely, assuming that the whole wind power time series is given as Ω_T (where T is the length of the given time series), the backward probability is calculated in **eq. 10**:

$$p_{t|T}^{(j)} = P(s_t = j|\Omega_T). \tag{10}$$

Combining the forward probability and backward probability, the probability of states at each time is calculated by using the maximum likelihood estimation (MLE) method. Then the weights of the combined model in **eq. 6** are decided by the calculated probability, and the final prediction model is expressed as eqn 11:

$$\hat{y}_t = p_1 \cdot \hat{y}_1 + p_2 \cdot \hat{y}_2 + p_3 \cdot \hat{y}_3, \tag{11}$$

where p_i is the probability of the *ith* model.

4 EXPERIMENTS AND DISCUSSION

4.1 Prediction Based on Individual Models

In this study, a real-world wind power dataset from Chinese wind farms is taken for the case study. This dataset collected samples for 2 years with a sampling period of 15 min. There are a total of 70,176 samples. By taking 70% of the data (viz., historical data from the last 17 months) as the training set, the data from the rest of the months are used for validation and testing. First, the phase space of the data is reconstructed based on **eq. 1** by applying the reconstruction parameters with $\tau = 7$ and $m = 9$ based on MI and

TABLE 2 | Wind power prediction using various methods.

		MAE	*RMSE*	*SDofAE*	*CC*
Combined method	Proposed	16.398	17.887	14.421	0.9650
	Linear	16.660	22.541	16.831	0.9854
	MSAR	16.547	19.538	15.482	0.9768
Data-driven	SVM	18.610	26.789	19.290	0.9276
	ELM	18.651	27.885	19.797	0.9359
	NN	17.741	24.154	16.402	0.9506

FNN. Then the reconstructed chaotic time series are used to train and predict wind power based on three models introduced in **Section 2**.

Figure 1 depicts the prediction results of three models: S_1, S_2, and S_3 (representing local linear prediction models with first-order, prediction models based on the Lyapunov exponent, and Volterra prediction models, respectively). **Figures 1A,B** present the predicted wind power and prediction errors, respectively. It is qualitatively found that these three models have good performance in predicting wind power in **Figure 1A**. However, the prediction errors in **Figure 1B** illustrate that each model have its best prediction performance at different local times.

Moreover, to evaluate the time series prediction performance quantitatively, some useful error metrics could be applied (He et al., 2017). For example, the commonly used mean absolute error (MAE), mean squared error (MSE), root-mean-square error (RMSE), and the standard deviation of absolute error (SDofAE) are possible options. These metrics have advantages in evaluating the error on prediction amplitude and are commonly used in prediction research. Moreover, a kind of transverse error metric could also be used for evaluation, such as correlation coefficient (CC), which aims to evaluate the prediction model's performance in time delay. In this study, four selected metrics are given to evaluate the performance of wind power time series predictions:

$$\begin{cases} MAE = \sum_{i=1}^{n} \left| y_i - \hat{y}_i \right| \Big/ n, \\ RMSE = \sqrt{\sum_{i=1}^{n} \left(y_i - \hat{y}_i \right)^2 \Big/ n}, \\ SDofAE = \sqrt{\sum_{i=1}^{n} \left(\left| y_i - \hat{y}_i \right| - MAE \right)^2 \Big/ n}, \\ CC = \dfrac{\operatorname{cov}(y, \hat{y})}{\sqrt{Dy}\sqrt{D\hat{y}}}, \end{cases} \tag{12}$$

where y_i and $\hat{y}_i$ are predicted and observed values of wind power time series, respectively, and n is the number of testing data points. According to the definition of error metrics before, we can see that the former three (MAE, RMSE, and SDofAE) are required to be small when the model performs well. However, on the other hand, the value of CC needs to be as close to 1 as possible.

Table 1 shows the values of four error indicators in wind power prediction. S_1, S_2, and S_3 represent the three prediction models introduced in **Section 2**, respectively. It is seen that the difference between the former three models is not large and that S_1 has the worst prediction performance, while S_3 has the best prediction performance according to the values of the error indicators.

4.2 Prediction Based on the Proposed Hybrid Model

According to the description of the proposed method, a combined model could effectively improve the shortages of individual models at local prediction. Therefore, a combined model is proposed in **eq. 11**, where its weights are selected as the transition probability of the Markov chain. Taking the three given prediction models as three states, the transition probabilities of states at each time are calculated based on **eqs 7–10**.

Figure 2 depicts the transition probability of three states in the same period as **Figure 1**. It is seen that the wind power is predicted by one model with a given probability at each time. Therefore, if the probability of each state is taken as the weight of the combined model in **eq. 11**, then wind power for the same period with **Figure 1** can be predicted.

Then, also making use of the given error metrics in evaluation, the performance of the proposed method is presented in the following table. For the consideration of the comparison study, several other prediction methods are also evaluated, such as two combined models, namely, a linear combined model of S_1, S_2, and S_3 and a Markov-switching-autoregression model (MSAR), three generally used data-driven models based on neural networks (NNs), support vector machine (SVM) (Li et al., 2021b), and extreme learning machine (ELM) (Shen et al., 2020). All of their results are presented in **Table 2**.

Table 2 shows the error metrics of wind power prediction based on different models, including individual data-driven models and combined models. Through the comparison, some phenomena could be found. First, the combined models generally outperform all of these individual models, including the common statistical models and the chaotic time series models in **Table 1**, which validates the effectiveness of combined models in improving wind power prediction performance. Second, through comparison between individual and combined chaotic models, it is seen that considering the combination or switching of different physical models is helpful to improve prediction accuracy. Moreover, the switching mechanism with consideration of the Markov chain can outperform the simple linear combination model. Finally, the proposed method combining both the chaotic time series model and the Markov chain could further improve the prediction performance. In the comparison study, it is reasonable that for individual chaotic time series, models cannot achieve obvious superiority than traditional data-driven models which can achieve high-precision in short-term prediction. However, chaotic time series models are more reliable than data-driven models since they consider physical principles of the wind development process. Therefore, chaotic models would be helpful to capture wind trends, and guarantee good accuracy in the long-term prediction in the future study.

5 CONCLUSION

To realize precise short-term wind power prediction, this article proposed a more reliable combined model considering both chaotic time series modeling and the Markov chain mechanism. First, by reconstructing the wind power data into a new space with the consideration of the wind's chaotic physical features, three chaotic time series models consist of the primary model library. Second, by taking different models as the states of the Markov chain, and a combined model utilizing the transition probability of the Markov chain as the weight is constructed. The results of **Table 2** verify that the combined model based on the Markov chain is feasible to predict wind power. Moreover, through the comparison study, the proposed method is validated to improve the precision of wind power prediction, which will be helpful for direct scheduling and planning in the power system in the future.

DATA AVAILABILITY STATEMENT

The original contributions presented in the study are included in the article/Supplementary Materials, further inquiries can be directed to the corresponding author.

AUTHOR CONTRIBUTIONS

LZ put forward the main research points; MH completed manuscript writing and revision; XZ, YL, and HL completed simulation research; LZ collected relevant background information; and MH revised grammar and expression. All authors contributed to manuscript revision, read, and approved the submitted version.

REFERENCES

An, X., Jiang, D., Liu, C., and Zhao, M. (2011). Wind Farm Power Prediction Based on Wavelet Decomposition and Chaotic Time Series. *Expert Syst. Appl.* 38 (9), 11280–11285. doi:10.1016/j.eswa.2011.02.176

Brouwer, A. S., van den Broek, M., Özdemir, Ö., Koutstaal, P., and Faaij, A. (2016). Business Case Uncertainty of Power Plants in Future Energy Systems with Wind Power. *Energy Policy* 89, 237–256. doi:10.1016/j.enpol.2015.11.022

Chen, H., Zhang, J., Tao, Y., and Tan, F. (2019). Asymmetric GARCH Type Models for Asymmetric Volatility Characteristics Analysis and Wind Power Forecasting. *Prot. Control. Mod. Power Syst.* 4 (1), 1–11. doi:10.1186/s41601-019-0146-0

Doucoure, B., Agbossou, K., and Cardenas, A. (2016). Time Series Prediction Using Artificial Wavelet Neural Network and Multi-Resolution Analysis: Application to Wind Speed Data. *Renew. Energ.* 92, 202–211. doi:10.1016/j.renene.2016.02.003

Fraser, A. M., and Swinney, H. L. (1986). Independent Coordinates for Strange Attractors from Mutual Information. *Phys. Rev. A.* 33 (2), 1134–1140. doi:10.1103/physreva.33.1134

He, Y., Kusiak, A., Ouyang, T., and Teng, W. (2017). Data-driven Modeling of Truck Engine Exhaust Valve Failures: a Case Study. *J. Mech. Sci. Technol.* 31 (6), 2747–2757. doi:10.1007/s12206-017-0518-1

Huber, M., Dimkova, D., and Hamacher, T. (2014). Integration of Wind and Solar Power in Europe: Assessment of Flexibility Requirements. *Energy* 69, 236–246. doi:10.1016/j.energy.2014.02.109

Jinquan, Z., Yujie, Z., Pan, Z., Xiaoming, J., and Chao, F. (2016). Development of a WAMS Based Testplatform for Power System Real Timetransient Stability Detection and Control. *Prot. Control. Mod. Power Syst.* V1 (1), 37–47.

Kanna, B., and Singh, S. N. (2012). AWNN-assisted Wind Power Forecasting Using Feed-Forward Neural Network. Sustainable Energy. *IEEE Trans.* 3 (2), 306–315.

Lange, M., and Focken, U. (2006). *Physical Approach to Short-Term Wind Power Prediction*. Berlin: Springer, 1–208.

Lei, D., Lijie, W., Shi, H., Shuang, G., and Xiaozhong, L. (2007). "Prediction of Wind Power Generation Based on Chaotic Phase Space Reconstruction Models," in Power Electronics and Drive Systems, 2007. PEDS'07. 7th International Conference on (Bangkok, Thailand: IEEE), 744–748. doi:10.1109/peds.2007.4487786

Li, H., Deng, J., Feng, P., Pu, C., Arachchige, D. D., and Cheng, Q. (2021). Short-Term Nacelle Orientation Forecasting Using Bilinear Transformation and ICEEMDAN Framework. *Front. Energ. Res.* 697, 780928. doi:10.3389/fenrg.2021.780928

Li, H., Deng, J., Yuan, S., Feng, P., and Arachchige, D. D. (2021). Monitoring and Identifying Wind Turbine Generator Bearing Faults Using Deep Belief Network and EWMA Control Charts. *Front. Energ. Res.* 9, 799039. doi:10.3389/fenrg.2021.799039

Liu, Y., Shi, J., Yang, Y., and Lee, W.-J. (2012). Short-Term Wind-Power Prediction Based on Wavelet Transform-Support Vector Machine and Statistic-Characteristics Analysis. *IEEE Trans. Ind. Applicat.* 48 (4), 1136–1141. doi:10.1109/tia.2012.2199449

Ouyang, T., Zha, X., Qin, L., Xiong, Y., and Xia, T. (2016). Wind Power Prediction Method Based on Regime of Switching Kernel Functions. *J. Wind Eng. Ind. Aerodynamics* 153, 26–33. doi:10.1016/j.jweia.2016.03.005

Packard, N. H., Crutchfield, J. D., Farmer, J. D., and Shaw, R. S. (1980). Geometry from a Time Series. *Phys. Rev. Lett.* 45 (9), 712–716. doi:10.1103/physrevlett.45.712

Rand, D., and Young, L. S. (1988). *Dynamical Systems and Turbulence, Lecture Notes in Mathematics*. Berlin, Germany: Springer-Verlag, 366381.

Shen, X., Zhang, X., Ouyang, T., Li, Y., and Raksincharoensak, P. (2020). Cooperative Comfortable-Driving at Signalized Intersections for Connected and Automated Vehicles. *IEEE Robot. Autom. Lett.* 5 (4), 6247–6254. doi:10.1109/lra.2020.3014010

Tang, Z., Zhao, G., and Ouyang, T. (2021). Two-phase Deep Learning Model for Short-Term Wind Direction Forecasting. *Renew. Energ.* 173, 1005–1016. doi:10.1016/j.renene.2021.04.041

Tang, Z., Zhao, G., Wang, G., and Ouyang, T. (2020). Hybrid Ensemble Framework for Short-Term Wind Speed Forecasting. *IEEE Access* 8, 45271–45291. doi:10.1109/access.2020.2978169

Tascikaraoglu, A., and Uzunoglu, M. (2014). A Review of Combined Approaches for Prediction of Short-Term Wind Speed and Power. *Renew. Sustain. Energ. Rev.* 34, 243–254. doi:10.1016/j.rser.2014.03.033

Valipour, M., Banihabib, M. E., and Behbahani, S. M. R. (2013). Comparison of the ARMA, ARIMA, and the Autoregressive Artificial Neural Network Models in Forecasting the Monthly Inflow of Dez Dam Reservoir. *J. Hydrol.* 476, 433–441. doi:10.1016/j.jhydrol.2012.11.017

Xiong, Y., Zha, X., Qin, L., Ouyang, T., and Xia, T. (2017). Research on Wind Power Ramp Events Prediction Based on Strongly Convective Weather Classification. *IET Renew. Power Generation* 11 (8), 1278–1285. doi:10.1049/iet-rpg.2016.0516

Yang, N., Dong, Z., Wu, L., Zhang, L., Shen, X., Chen, D., et al. (2021). A Comprehensive Review of Security-Constrained Unit Commitment. *J. Mod. Power Syst. Clean Energ.*.

Yang, N., Qin, T., Wu, L., Huang, Y., Huang, Y., Xing, C., et al. (2022). A Multi-Agent Game Based Joint Planning Approach for Electricity-Gas Integrated Energy Systems Considering Wind Power Uncertainty. *Electric Power Syst. Res.* 204, 107673. doi:10.1016/j.epsr.2021.107673

Yang, N., Yang, C., Wu, L., Shen, X., Jia, J., Li, Z., et al. (2021). Intelligent Data-Driven Decision-Making Method for Dynamic Multi-Sequence: An E-Seq2Seq Based SCUC Expert System. *IEEE Trans. Ind. Inform.* 18, 3126. doi:10.1109/TII.2021.3107406

Yang, N., Yang, C., Xing, C., Ye, D., Jia, J., Chen, D., et al. (2022). Deep Learning-based SCUC Decision-making: An Intelligent Data-driven Approach with Self-learning Capabilities. *IET Generation Trans. Dist* 16 (4), 629–640. doi:10.1049/gtd2.12315

Zhang, X., and Liang, J. (2012). Chaotic Characteristics Analysis and Prediction Model Study on Wind Power Time Series. *Acta Phys. Sin.* 61 (19), 70–81. doi:10.7498/aps.61.190507

Conflict of Interest: The authors declare that the research was conducted in the absence of any commercial or financial relationships that could be construed as a potential conflict of interest.

frontiers | Frontiers in Energy Research

BRIEF RESEARCH REPORT
published: 02 June 2022
doi: 10.3389/fenrg.2022.908544

Short-Term Prediction of Building Sub-Item Energy Consumption Based on the CEEMDAN-BiLSTM Method

Zhanbin Lin *

School of Management, Guangdong University of Technology, Guangzhou, China

In order to improve the accuracy of the short-term prediction of building energy consumption, this study proposes a short-term prediction model of building energy consumption based on the CEEMDAN-BiLSTM method. In this study, the energy consumption data of an office building in 2019 are selected as a sample, and CEEMDAN is used to decompose the energy consumption data into multiple components, and the strong correlation components are selected and sent to the BiLSTM network. The final energy consumption prediction results are obtained by superimposing the prediction results of each sub-component, and five models are built simultaneously to compare the errors with the proposed models. The results showed that the weather type has a great influence on the accuracy of energy consumption prediction. When the weather fluctuates greatly, the prediction error of energy consumption by a single prediction model is large. When the weather suddenly changes, the EMD-LSTM model has a big error in the prediction of air conditioning energy consumption. After CEEMDAN decomposition of energy consumption data, more detailed components can be extracted, which makes the BiLSTM prediction algorithm more accurate. Compared with the CEEMDAN-LSTM model, the CEEMDAN-BiLSTM model reduces e_{RMSE}, e_{MAPE}, and e_{TIC} by 4.1%, 9.441, and 1.3%, respectively. The proposed model can effectively improve the accuracy of short-term prediction of building energy consumption.

Keywords: short-term forecast, sub-item energy consumption of buildings, modal decomposition, weather classification, energy consumption

Edited by:
Xun Shen,
Tokyo Institute of Technology, Japan

Reviewed by:
S. Sardana,
Indian Institute of Technology, Dhanbad, India
Sandeep Singh Nanglu,
Sri Sai Group of Institutes, Badhani, India

***Correspondence:**
Zhanbin Lin
Lin_diligence@163.com

Specialty section:
This article was submitted to Smart Grids, a section of the journal Frontiers in Energy Research

Received: *30 March 2022*
Accepted: *18 April 2022*
Published: *02 June 2022*

Citation:
Lin Z (2022) Short-Term Prediction of Building Sub-Item Energy Consumption Based on the CEEMDAN-BiLSTM Method. Front. Energy Res. 10:908544. doi: 10.3389/fenrg.2022.908544

INTRODUCTION

In the past few decades, with the acceleration of urbanization, the demand for building energy has greatly increased. The question as to how to reduce building energy consumption has attracted researchers' attention (Ding et al., 2021; Somu et al., 2021). However, there are many factors affecting energy consumption, and building energy prediction is still a complicated task (Yakut and Zkan, 2020; Han et al., 2021; Oh, 2021). An important means of building energy conservation and emission reduction is fine management of building energy consumption, and the basis of this work is an accurate prediction of building energy consumption so as to support the optimal management of building operation and achieve the goal of energy conservation and emission reduction.

At present, there are two main prediction methods of building energy consumption, including the physical modeling method and the artificial intelligence method. Physical-based modeling methods can be divided into simplified engineering algorithms and comprehensive methods. Simplified engineering algorithms mainly include the full-load operation method and degree-day method.

Comprehensive methods use thermodynamic equations to accurately calculate building energy consumption (Khattari et al., 2020; Runge and Zmeureanu, 2019). However, physical methods usually require a large number of detailed inputs of buildings and their environment, such as the heating system, ventilation system, air conditioning system, insulation thickness, thermal characteristics, internal occupancy load, and solar energy information (Pinanggih et al., 2021).

In the field of building energy prediction, an artificial neural network, as an effective method to predict the relationship between data input and output, has entered the researchers' field of vision. The artificial neural network is a novel computing method based on the human neural activity, which is suitable for dealing with complex linear and nonlinear mapping problems. Because of its powerful nonlinear mapping capability, the neural network has gained more and more recognition in the engineering field (Shapi et al., 2020). The literature (Runge and Zmeureanu, 2019) summarizes the application of artificial neural networks in the hourly prediction of building energy consumption, and the results showed that the neural network model has achieved good results in single-step and multi-step prediction. The literature (Ma et al., 2018) based on historical meteorological data shows that the support vector machine model is used to predict the monthly electricity consumption of buildings, and it is stated that the accuracy of the support vector machine is better than that of the neural network. The literature (Li et al., 2009) based on using the SVM algorithm to predict the hourly load of a single office building shows that the root mean square error is only 1.17%, and the prediction effect is good. The literature report by Wang et al. (2018) optimizes the parameters of the short-term model of building energy consumption by the cross-validation method. The literature results (Bagnasco et al., 2015) based on using multilayer perceptron to predict the electricity consumption of hospital facilities according to meteorological data and time changes showed that the artificial neural network performs better in winter. The literature by Neto and Fiorelli (2008) compares the neural network with the EnergyPlus energy simulation tool, and the results showed that the neural network has higher prediction accuracy.

Many achievements have been made in the aforementioned research, but each method has some limitations. Physical prediction methods need to rely on detailed building and historical meteorological data information, but it is difficult to obtain detailed operational data in building structures to determine relevant parameters, and the calculation process is prone to deviation, which leads to unsatisfactory prediction results. Although the artificial intelligence method does not need to know the specific principle of energy consumption deeply, the traditional neural network algorithm has a slow convergence speed, serious local over-fitting, and limited scope of application. In order to better improve the accuracy of building sub-item energy consumption prediction, this study classifies the weather types, uses the CEEMDAN method to carry out the modal decomposition of energy consumption historical data, and sends the strong correlation components to the BiLSTM neural network. In order to verify the prediction accuracy of the CEEMDAN-BiLSTM model, BP, SVR, LSTM, EMD-LSTM, and CEEMDAN-LSTM models were established simultaneously and compared with the proposed model. The results clearly showed the accuracy of the proposed prediction model. The prediction method of building energy consumption based on deep learning proposed in this study can provide a reference for related research and application of building energy consumption prediction.

PRINCIPLE OF THE CEEMDAN AND BILSTM ALGORITHM

Principle of the CEEMDAN Algorithm

Empirical mode decomposition (EMD) is to decompose data into multiple IMF components according to the fluctuation scale of data series, but modal aliasing is easy to occur when decomposing nonlinear and non-stationary sequences. The ensemble empirical mode decomposition (EEMD) adds white noise with different amplitudes to the original sequence to suppress the aliasing phenomenon to a certain extent, but the calculation efficiency of EEMD is low. Therefore, this study adopts the self-adaptive noise complete empirical mode decomposition method, which adds white noise with different amplitudes to each component to obtain the optimal IMF component (Ali et al., 2021). The CEEMDAN method has lower iteration times than the EEMD method and also solves the problem of modal aliasing. The steps of CEEMDAN are as follows.

1) Gaussian white noise with different amplitudes is added to the original signal $x(n)$, $\omega^i(n)\,(i = 1, 2\cdots, I)$, and the ith signal can be expressed as follows:

$$x^i(n) = x(n) + \varepsilon_i \omega^i(n), \tag{1}$$

where $x^i(n)$ is the ith signal; $x(n)$ is the original signal, ε_i is the parameter to control white noise, and Gaussian white noise with different amplitudes is added to the signal through the value of ε_i.

2) EMD decomposition is carried out on the ith signal $x^i(n)$ to obtain the first-order modal component IMF1:

$$\text{IMF1} = \frac{1}{I}\sum_{i=1}^{1}\text{IMF}_1^i. \tag{2}$$

3) The first-order residual $r_1(n)$ is calculated as follows:

$$r_1(n) = x(n) - \text{IMF}_1. \tag{3}$$

4) The first-order modal component IMF2 is calculated as follows:

$$\text{IMF}_2 = \frac{1}{I}\sum_{i=1}^{1}E_1\{r_1(n) + \varepsilon_1 E_1[\omega^i(n)]\}. \tag{4}$$

Here, E_i represents the first-order IMF.

5) The first IMF can be obtained by calculating the k residual, and the $k+1$ residual is k.

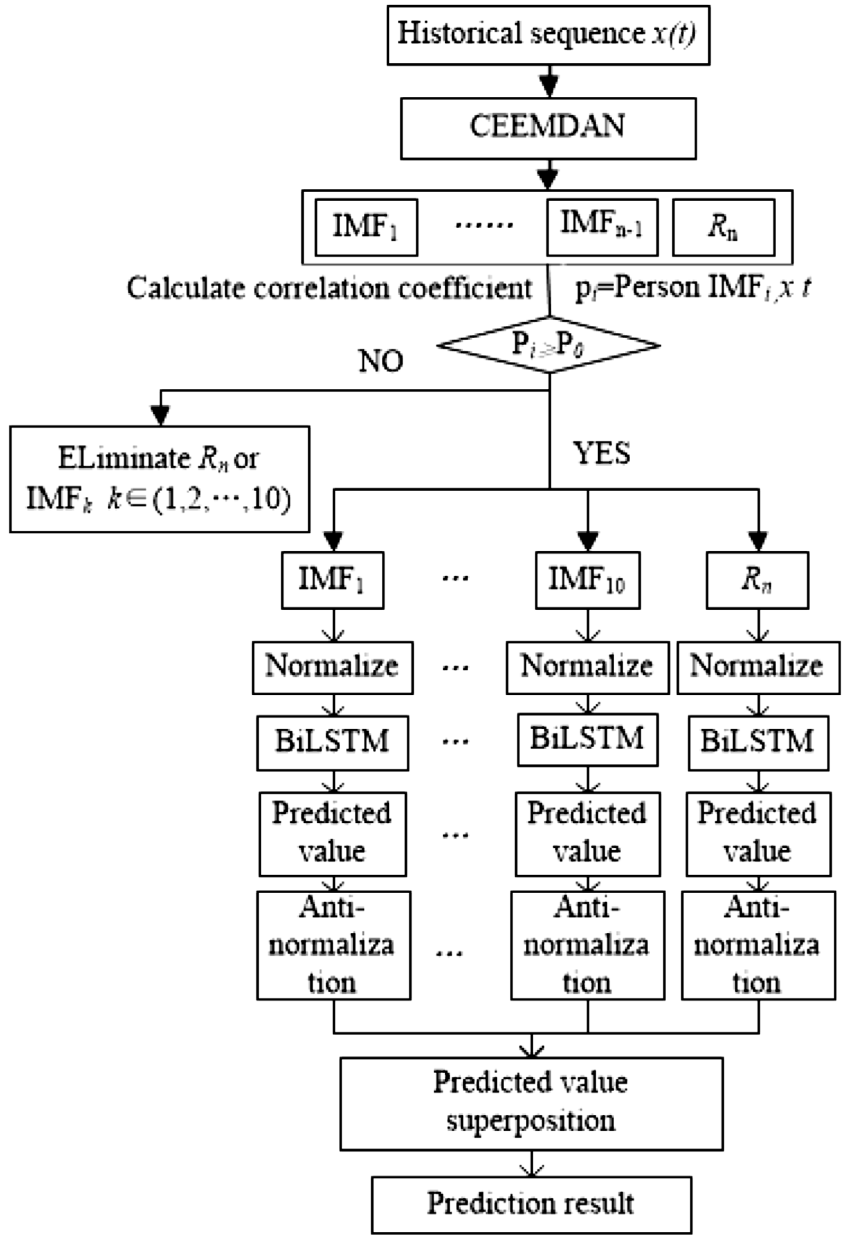

FIGURE 1 | CEEMDAN-BiLSTM model framework structure diagram.

$$r_k(n) = r_k - 1(n) - \mathrm{IMF}_n. \tag{5}$$

The component $k+1$ is as follows:

$$\mathrm{IMF}_n = \frac{1}{I}\sum_{i=1}^{1} E_1\{r_k(n) + \varepsilon_k E_k[\omega^i(n)]\}. \tag{6}$$

6) When the surplus is no longer decomposed, the highest order of IMF is obtained. At this point, the original signal is

$$x(n) = R(n) + \sum_{k=1}^{k} \mathrm{IMF}_k. \tag{7}$$

BiLSTM Layer Model Structure

Recurrent neural networks (RNNs) can be modeled according to the inherent characteristics of time series and can store information before and after collecting data, but the RNN model has the problem of gradient explosion or gradient disappearance. LSTM solves the gradient problem of the RNN by adding a gate controller and memory unit in the hidden layer.

The first step of LSTM is to calculate the forgotten information. The energy consumption data of the current module and the output A of the energy consumption data of the previous module are taken as inputs, and the state of the pre-neuron cells is mapped to the h_{t-1} range from 0 to 1. The calculation formula is as follows:

$$f_t = \sigma\left(W_f * [h_{t-1}, x_t] + b_f\right). \tag{8}$$

The second step of the LSTM model is to calculate the memory information. The input is the current building energy consumption data h_{t-1}, and the activation function sigmoid determines i_t, creates a new candidate value $\tilde{C}_t$, adds it to neurons, and updates the neuron state to get the final memory state C_t. The formulae are as follows:

$$i_t = \sigma(W_i * [h_{t-1}, x_t] + b_i), \tag{9}$$

$$\tilde{C}_t = \tanh(W_c * [h_{t-1}, x_t] + b_c), \tag{10}$$

$$C_t = f_t * C_{t-1} + i_t * \tilde{C}_t. \tag{11}$$

The third step of the LSTM model is to select the output value. The output neuron state o_t is determined by the sigmoid activation function, and the output part h_t is obtained by processing o_t by the tanh function. The formulae are as follows:

$$o_t = \sigma(W_o * [h_{t-1}, x_t] + b_o), \tag{12}$$

$$h_t = o_t * \tanh(C_t). \tag{13}$$

The LSTM model enhances the memory of neurons through three gating units, discards useless information, and solves the problem of long dependence. However, the LSTM model cannot make full use of the data information before and after building sub-item energy consumption, so this study uses the BiLSTM model to identify the features of modal components. The BiLSTM neural network can obtain complete data information before and after energy consumption. The front layer LSTM obtains the intrinsic characteristics of the building energy consumption data in front: the back-layer LSTM obtains the intrinsic characteristics of the building energy consumption data in the back and finally combines the two to obtain the building energy consumption data characteristics. The formulae are as follows:

$$\vec{h}_t = \overrightarrow{LSTM}(x_t), \tag{14}$$

$$\overleftarrow{h}_t = \overleftarrow{LSTM}(x_t), \tag{15}$$

$$h_t = \langle \vec{h}_t, \overleftarrow{h}_t \rangle. \tag{16}$$

Among them, $\vec{h}_t$ obtains semantic feature information of forward building energy consumption data through forward LSTM, and $\overleftarrow{h}_t$ obtains semantic feature information of backward building energy consumption data through backward LSTM. $\overrightarrow{LSTM}(x_t)$ represents the front-to-back feature, and $\overleftarrow{LSTM}(x_t)$ represents the back-to-front feature. Finally, the hidden layer state E is the characteristic of building energy consumption data.

CEEMDAN-BiLSTM Coupling Model

The data series of energy consumption is affected by many factors and belongs to nonlinear and non-stationary signals. Therefore, this study puts forward the CEEMDAN-BiLSTM prediction model. First, the sub-energy consumption sequence was decomposed into multiple sub-components by the CEEMDAN method, and the strong correlation sub-components were screened out for normalization. Then, the strong correlation components were sent into the BiLSTM model to obtain the predicted values of the sub-components. Finally, the predicted values of the sub-components were reversely normalized to obtain the final energy consumption prediction results. The CEEMDAN-BiLSTM model structure is shown in **Figure 1**.

The specific modeling process is as follows:

1) CEEMDAN decomposition

The original energy consumption sequence $x(t)$ is decomposed into multiple IMF and residual components R_{n} by the CEEMDAN method.

2) IMF component screening

Calculate the Pearson correlation coefficient of the original sequence $x(t)$ and each sub-component, and the formula is as follows:

$$p_0 = \frac{\sum_{i=1}^{n} p_i}{2 * (n+1)}, \tag{17}$$

where p_{i} represents the Pearson correlation coefficient of two continuous variables, and n is the number of subcomponents. P_0 is the threshold of the correlation coefficient, and strong correlation components can be screened out according to p_0.

3) BiLSTM network prediction

In order to avoid the influence of different dimensions of energy consumption series after CEEMDAN decomposition, the strong correlation components are normalized. The specific parameters of the BiLSTM model are set as follows: in order to prevent over-fitting, dropout is set to 0.5; the absolute error function is the loss function, tanh is the activation function, adam is the optimization function, and the training times are set to 1,000 times. The LSTM layer node number is set to 50; the batch size is set to 72.

BUILDING SUB-ITEM ENERGY CONSUMPTION PREDICTION MODEL

Modeling Classification Basis

Building energy consumption consists of air conditioning energy consumption, lighting energy consumption, and power energy consumption. The energy consumption of air conditioning is mainly composed of air conditioning terminals, cold and hot stations, and other pieces of equipment. Lighting energy consumption mainly consists of landscape lighting, corridors, emergency, and lighting equipment. Power consumption is mainly composed of fans, elevators, and water supply devices. Moreover, the energy consumption of lighting power has a strong correlation with the work and the rest of the staff, and the energy consumption of air conditioning

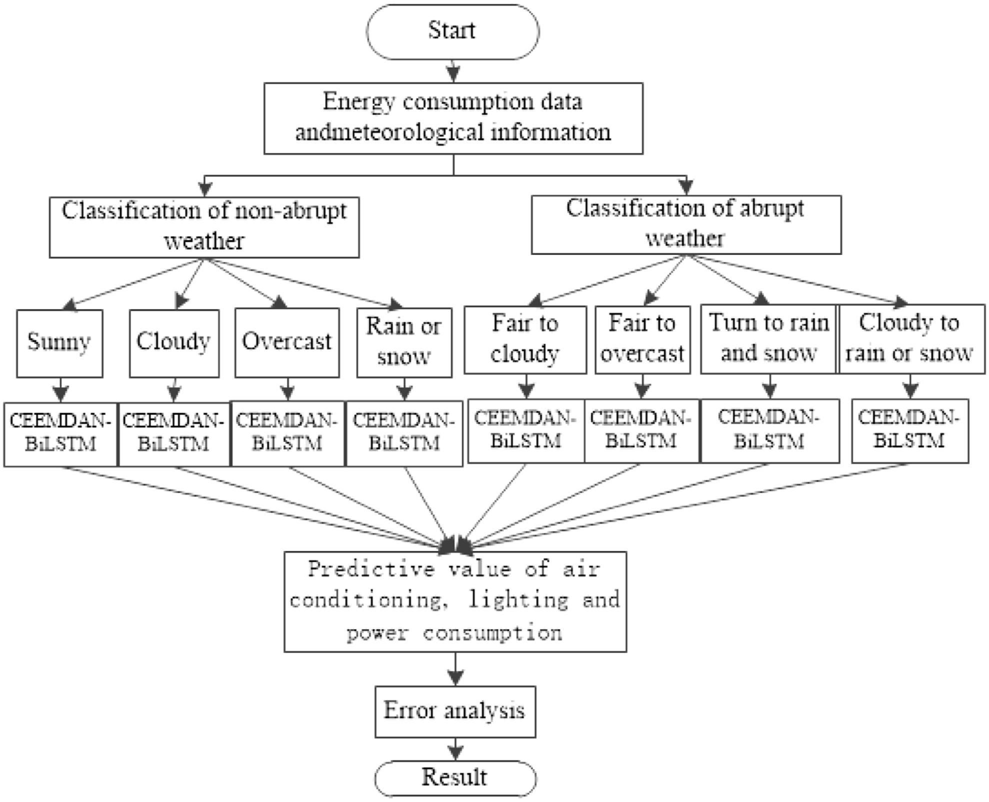

FIGURE 2 | CEEMDAN-BiLSTM model prediction process.

has a certain trend with the seasons and temperatures. Analysis of a specific load of energy consumption shows that when the weather changes, lighting, air conditioning, and ventilator equipment will also be adjusted accordingly, and when the weather suddenly changes, the energy consumption of each sub-item will also fluctuate greatly.

Because the energy consumption of buildings is quite different between abrupt weather and non-abrupt weather, the weather is divided into abrupt weather and non-abrupt weather according to the meteorological classification index. The itemized short-term prediction process of building energy consumption based on the CEEMDAN-BiLSTM model is shown in **Figure 2**. The following are selected as characteristic quantities: 24 h of the day, outdoor hourly average relative humidity, hourly average wind speed, outdoor hourly average temperature, holidays, and weather changes. In order to improve the accuracy of the forecast, abrupt weather and non-abrupt weather are subdivided into four weather types. The historical data of lighting energy consumption, air-conditioning energy consumption, and power energy consumption of different weather types are decomposed by CEEMDAN so as to become a stable energy consumption series. Different meteorological factors are added to the decomposed strong correlation subcomponents as the prediction conditions of the BiLSTM model. The predicted values of sub-components are reversely normalized and superimposed to obtain the final energy consumption prediction result.

Evaluating Indicator

Synchronous BP, SVM, LSTM, EMD-LSTM, and CEEMDAN-LSTM models are established, and the calculation accuracy is compared with the proposed models. The average absolute percentage error e_{MAPE}, root mean square error e_{RMSE}, and Hill inequality coefficient e_{TIC} are selected to evaluate the model accuracy, and the expressions are as follows (18)~(20).

$$e_{\mathrm{TIC}} = \frac{\sqrt{\sum_{i=1}^{Z} \left(y_i' - y_i\right)^2}}{\sqrt{\sum_{i=1}^{Z} \left(y_i'\right)^2} + \sqrt{\sum_{i=1}^{Z} \left(y_i\right)^2}}, \tag{18}$$

$$e_{\mathrm{REMS}} = \sqrt{\frac{\sum_{i=1}^{Z} \left(y_i' - y_i\right)^2}{Z}}, \tag{19}$$

$$e_{\mathrm{MAPE}} = \frac{1}{Z} \sum_{i=1}^{Z} \left| \frac{y_i' - y_i}{y_i} \right|, \tag{20}$$

where z is the purpose of the test sample, y' is the predicted value of building energy consumption, and y is the actual value of building energy consumption.

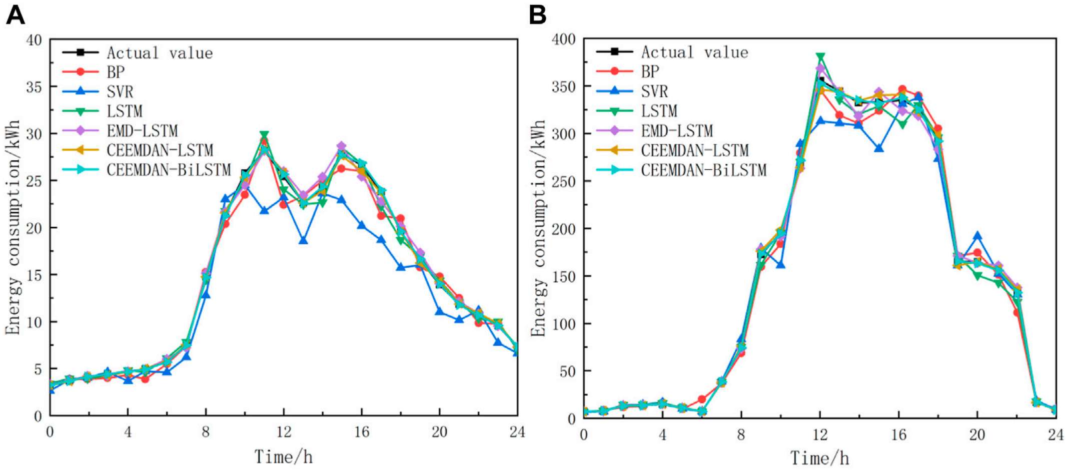

Sunny weather lighting

Sunny weather air conditioner

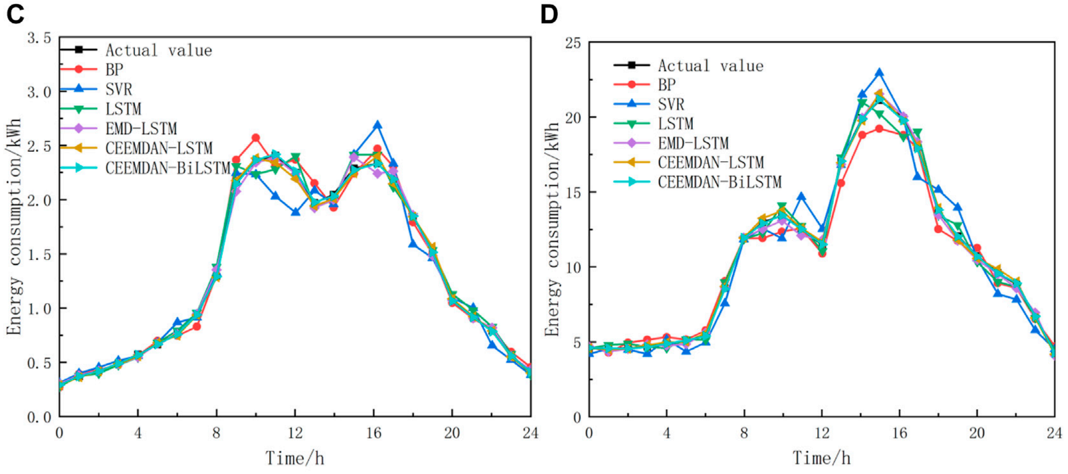

Sunny weather power

Turn to rain weather lighting

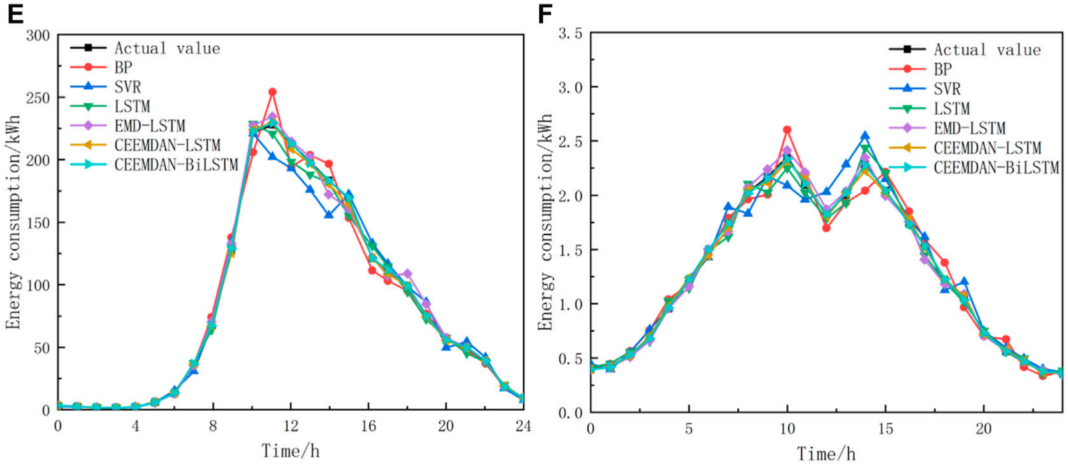

Turn to rain weather air conditioner

Turn to rain weather power

FIGURE 3 | Prediction results of different models. **(A)** Sunny weather lighting. **(B)** Sunny weather air conditioner. **(C)** Sunny weather power. **(D)** Turn to rain weather lighting. **(E)** Turn to rain weather air conditioner. **(F)** Turn to rain weather power.

TABLE 1 | Prediction errors of different models.

Type	XP-70	e_{MAPE}	e_{RMSE}	e_{TIC}	Type	XP-70	e_{MAPE}	e_{RMSE}	e_{TIC}
Sunny weather lighting	BP	0.214	13.171	0.047	Turn to rain weather lighting	BP	0.297	18.363	0.119
	SVM	0.251	16.228	0.056		SVM	0.229	14.957	0.084
	LSTM	0.184	9.928	0.043		LSTM	0.216	12.788	0.091
	E-L	0.170	9.885	0.032		E-L	0.194	10.984	0.069
	C-L	0.165	7.874	0.026		C-L	0.176	9.549	0.057
	C-B	0.146	7.260	0.025		C-B	0.148	9.308	0.048
Sunny weather air conditioner	BP	0.37	221.837	0.214	Turn to rain weather air conditioner	BP	0.362	228.188	0.194
	SVM	0.418	257.109	0.202		SVM	0.451	272.092	0.224
	LSTM	0.334	169.663	0.139		LSTM	0.311	180.398	0.171
	E-L	0.266	154.198	0.142		E-L	0.299	169.867	0.143
	C-L	0.211	129.751	0.112		C-L	0.262	130.153	0.111
	C-B	0.200	117.686	0.101		C-B	0.218	123.652	0.111
Sunny weather power	BP	0.2485	3.312	0.128	Turn to rain weather power	BP	0.296	3.814	0.176
	SVM	0.2825	3.934	0.182		SVM	0.286	3.502	0.172
	LSTM	0.2395	3.172	0.126		LSTM	0.248	2.758	0.149
	E-L	0.183	2.303	0.082		E-L	0.198	2.166	0.102
	C-L	0.1615	1.856	0.086		C-L	0.188	2.108	0.094
	C-B	0.16	1.672	0.067		C-B	0.16	1.932	0.087

RESULTS AND DISCUSSION

The effectiveness of the CEEMDAN-BiLSTM model is verified by the weather conditions and energy consumption data of an office building in Fuzhou, Fujian Province in 2019. According to statistics, there were 273 abrupt weather days in Central Africa in 2019, including 111 sunny days, 47 cloudy days, 53 overcast days, 62 rainy days and 92 abrupt weather days. In non-abrupt weather, considering sunny weather as an example for analysis, 25 days were selected as training samples and 8 days as test samples in sunny weather. For a sudden change in weather, the weather from sunny to rainy is considered as an example. Among the 16 days of weather from sunny to rainy, 12 days were selected as training samples and 4 days as test samples.

The forecast results of lighting, air conditioning, and power consumption in sunny weather are shown in **Figures 3A–C**. In sunny weather, the fluctuation of the building energy consumption curve is small, and the change in energy consumption has certain regularity. Except for BP and SVM models, the other four models all showed good prediction effects. In the prediction curves of air-conditioning energy consumption and power energy consumption, it can be observed that the LSTM model based on the CEEMDAN method has the highest fitting degree to the curve, and the prediction effect of the combined model is obviously better than that of the single prediction model. The forecast results of each sub-item energy consumption under abrupt weather conditions are shown in **Figures 3D,F**. Under abrupt weather conditions, affected by various meteorological factors, the energy consumption curve fluctuates greatly, and the predicted power of each model deviates from the actual power. After the sudden change of weather, the predicted value of the lighting energy consumption of the BP neural network is lower than the actual energy consumption. Compared with the other two combined models, the EMD-LSTM model has more chaotic curves, resulting in larger errors.

In order to compare the prediction effects of each model more accurately, the errors of the six models are plotted in **Table 1**. In sunny weather, most indexes of the combined model based on the LSTM algorithm are better than those of the single model. According to the analysis of the prediction results of lighting energy consumption, it can be seen that the e_{RMSE}, e_{MAPE}, and e_{TIC} indexes of the four deep learning models have little difference. Compared with EMD-LSTM and CEEMDAN-LSTM, the e_{MAPE} value of the CEEMDAN-BiLSTM prediction model is reduced by 2.4 and 1.9%, respectively. CEEMDAN-LSTM model has obvious performance advantages in predicting air-conditioning energy consumption. Compared with EMD-LSTM and CEEMDAN-LSTM combined models, the e_{RMSE} of the CEEMDAN-LSTM model is reduced by 6.6 and 1.1%, respectively, the e_{MAPE} is reduced by 36.512 and 12.065, respectively, and the e_{TIC} is reduced by 4.1 and 1.1%, respectively. The LSTM model is not sensitive enough to power consumption, while EMD-LSTM, CEEMDAN-LSTM, and CEEMDAN-BiLSTM models extract curve details through modal decomposition, which makes the prediction algorithm more accurate. Under abrupt weather conditions, both BP and SVM prediction models have large errors in energy consumption. The combination model has an excellent prediction effect on lighting energy consumption and power energy consumption. In this comparison in a smaller numerical range, the combination model can be used directly. The CEEMDAN-BiLSTM model has the best performance in the short-term hourly prediction of air conditioning energy consumption, and the e_{MAPE} value is reduced by 14.4, 23.3, 9.3, 8.1, and 4.4%, respectively, compared with BP, SVM, LSTM, EMD-LSTM, and CEEMDAN-LSTM models, that is, CEEMDAN decomposition improves the prediction performance of the model to a certain extent. After the power consumption data is decomposed by CEEMDAN, the details that can be extracted by the LSTM network and BiLSTM network are further increased, so CEEMDAN has a positive effect on energy consumption prediction.

In this study, the predicted values and effective values of all test samples of building energy consumption are counted. Compared with the CEEMDAN-BiLSTM model, the CEEMDAN-LSTM model reduces e_{MAPE}, e_{RMSE}, and e_{TIC} by 4.1, 9.441, and 1.3%, respectively. In other words, after CEEMDAN modal decomposition of building energy consumption, the BiLSTM network is more accurate than the LSTM network prediction algorithm.

CONCLUSION

In this study, a short-term prediction model of building energy consumption based on the CEEMDAN-BiLSTM method is proposed. The energy consumption data of lighting, air conditioning, and power are decomposed by CEEMDAN and then sent to the BiLSTM network for energy consumption prediction. At the same time, five models are established and compared with the proposed model. The CEEMDAN-BiLSTM model solves the problem of low accuracy of traditional forecasting methods when energy consumption fluctuates. The main conclusions are as follows:

1) BP and SVM models are simple in structure, showing large errors in all kinds of weather, so they are not suitable for the prediction of energy consumption series. The accuracy of the LSTM model is difficult to guarantee when the energy consumption fluctuates greatly. When the weather suddenly changes, the EMD-LSTM model shows a big error in the prediction of air conditioning energy consumption.
2) More detailed components can be extracted by CEEMDAN decomposition of energy consumption curve data, which makes the prediction of the BiLSTM network more accurate.
3) The difference between the predicted energy consumption of the CEEMDAN-LSTM model and the actual energy consumption is small, and the prediction accuracy meets the requirements of short-term prediction.

DATA AVAILABILITY STATEMENT

The original contributions presented in the study are included in the article/supplementary material; further inquiries can be directed to the corresponding author.

AUTHOR CONTRIBUTIONS

ZL basically completed all the contents of the article independently.

REFERENCES

Ali, H., Azalan, M., Zaidi, A., Amran, T. S. T., and Elshaikh, M. (2021). Feature Extraction Based on Empirical Mode Decomposition for Shapes Recognition of Buried Objects by Ground Penetrating Radar. *J. Phys. Conf. Ser.* 1878 (1), 012022. doi:10.1088/1742-6596/1878/1/012022

Bagnasco, A., Fresi, F., Saviozi, M., and Vinci, A. (2015). Electrical Consumption Forecasting in Hospital Facilities: An Application Case. *Energy & Build.* 103 (SEP.), 261–270. doi:10.1016/j.enbuild.2015.05.056

Ding, S., Li, R., Wu, S., and Zhou, W. (2021). Application of a Novel Structure-Adaptative Grey Model with Adjustable Time Power Item for Nuclear Energy Consumption Forecasting. *Appl. Energy* 298 (3), 117114. doi:10.1016/j.apenergy.2021.117114

Han, Q., Ikbal, M. A., and Khanna, S. (2021). Prediction of Energy Consumption of Numerical Control Machine Tools and Analysis of Key Energy : aving Technologies[J]. *IET Collab. Intell. Manuf.* 3, doi:10.1049/cim2.12001

Khattari, Y., El-Otmany, H., Rhafiki, T. E., Kousksou, T., Ahmed, A., and Ghoulam, E. B. (2020). Physical Models to Evaluate the Performance of Impure Phase Change Material Dispersed in Building Materials. *J. Energy Storage* 31, 101661. doi:10.1016/j.est.2020.101661

Li, Q., Meng, Q., Cai, J., Yoshino, H., and Mochida, A. (2009). Applying Support Vector Machine to Predict Hourly Cooling Load in the Building. *Appl. Energy* 86 (10), 2249–2256. doi:10.1016/j.apenergy.2008.11.035

Ma, Z., Ye, C., Li, H., and Ma, W. (2018). Applying Support Vector Machines to Predict Building Energy Consumption in China. *Energy Procedia* 152, 780–786. doi:10.1016/j.egypro.2018.09.245

Neto, A. H., and Fiorelli, F. (2008). Comparison between Detailed Model Simulation and Artificial Neural Network for Forecasting Building Energy Consumption. *Energy Build.* 40 (12), 2169–2176. doi:10.1016/j.enbuild.2008.06.013

Oh, J. S. (2021). A Comparative Study on Energy Consumption Forecast Methods for Electric Propulsion Ship. *J. Mar. Sci. Eng.* 10. doi:10.3390/jmse10010032

Pinanggih, D. H., Abdullah, A. G., and Hakim, D. L. (2021). Prediction of Energy Consumption Using Artificial Neural Network Method in One of Shopping Center in Cirebon City[J]. *IOP Conf. Ser. Mater. Sci. Eng.* 1098 (4), 042011. doi:10.1088/1757-899x/1098/4/042011

Runge, J., and Zmeureanu, R. (2019). Forecasting Energy Use in Buildings Using Artificial Neural Networks: A Review. *Energies* 12 (17), 3254. doi:10.3390/en12173254

Shapi, M., Ramli, N. A., and Awalin, L. J. (2020). Energy Consumption Prediction by Using Machine Learning for Smart Building: Case Study in Malaysia. *Dev. Built Environ.* 5, 100037. doi:10.1016/j.dibe.2020.100037

Somu, N., Gauthama, R., and Ramamritham, K. (2021). A Deep Learning Framework for Building Energy Consumption Forecast. *Renew. Sustain. Energy Rev.* 137, 110591. doi:10.1016/j.rser.2020.110591

Wang, W., Pan, Y., and Huang, Z. (2018). Application of Gradient Progressive Regression Tree to Short-Term Prediction of Building Energy Consumption. *Build. Energy Conserv.* 46 (3), 5.

Yakut, E., and Zkan, E. (2020). Modeling of Energy Consumption Forecast with Economic Indicators Using Particle Swarm Optimization and Genetic Algorithm: An Application in Turkey between 1979 and 2050. *Alphanumeric J.* 8 (1), 59–78. doi:10.17093/alphanumeric.747427

Conflict of Interest: The authors declare that the research was conducted in the absence of any commercial or financial relationships that could be construed as a potential conflict of interest.

frontiers | Frontiers in Energy Research

BRIEF RESEARCH REPORT
published: 15 June 2022
doi: 10.3389/fenrg.2022.931031

Analysis of Digital Operation of Rural Sewage Treatment System in Big Data Environment by Discrete Dynamic Modeling Technology

Wang Lixuan*

Hebei Chemical & Pharmaceutical College, Shijiazhuang, China

Sewage treatment is a process with high energy consumption and pollution. In the current situation of energy shortage and fierce competition in the paper industry market, how to reduce the energy cost is related to the survival and development of every sewage treatment plant. With the rise of big data environment in the internet, discrete dynamic modeling technology has developed very rapidly. Discrete dynamic modeling technology is a dynamic model system that can connect the information of different things, so as to form a dynamic model system that can control all devices or data. The object attributes processed by the model system also determine the nature of the dynamic model system. As we all know, the big data environment is a large database with complex data types, so the dynamic model system in the big data environment is nonlinear. This paper mainly studies the historical development trend of big data environment and discrete dynamic modeling technology, as well as the stability method of five level H-bridge when discrete dynamic modeling technology controls rural sewage treatment system. Finally, the control of chaotic bifurcation in discrete dynamic model system under digital background is studied. It includes the rectifier modeling of the current data required by large devices in the sewage treatment system and the result analysis of the generated values.

Keywords: energy consumption, discrete dynamic model, sinusoidal pulse width modulation SPWM, five level H-bridge, rectifier

Edited by:
Xun Shen,
Tokyo Institute of Technology, Japan

Reviewed by:
Kuldeep Singh,
Govt polytechnic Manesar, India
Waseem Akram,
Lovely Professional University, India

****Correspondence:***
Wang Lixuan
wanglixuan1111@163.com

Specialty section:
This article was submitted to
Smart Grids,
a section of the journal
Frontiers in Energy Research

Received: *28 April 2022*
Accepted: *16 May 2022*
Published: *15 June 2022*

Citation:
Lixuan W (2022) Analysis of Digital Operation of Rural Sewage Treatment System in Big Data Environment by Discrete Dynamic Modeling Technology.
Front. Energy Res. 10:931031.
doi: 10.3389/fenrg.2022.931031

INTRODUCTION

With increasing strictness in emission limits of pollutants, the cost of water pollution control is increasing with every year. The energy consumption of the sewage treatment plant accounts for about 40% of the operating cost. High energy consumption seriously hinders the construction and operation of sewage treatment plants, so many sewage treatment plants are unable to sustain development, so it is the trend of the industry to reduce energy consumption and achieve sustainable development of sewage treatment.

Discrete dynamic modeling technology has been fully integrated into human beings. This technology has very high practical value in society. Because, the essence of this technology belongs to the modeling knowledge in mathematics, it is difficult to fully master the discrete dynamic modeling technology (matekenya Dunstan et al., 2021) (Dunstan et al., 2021). With the historical development of discrete dynamic modeling technology, researchers around the world have invested a lot of human and material resources in the exploration and innovation of this technology, breakthrough in application fields and system R and D. Discrete dynamic modeling technology is also evolving with the development trend of computer science, and is gradually applied in various fields (Alain djazet et al., 2020) (Djazet et al., 2020). Although the development of discrete dynamic modeling technology has not reached the final form, data errors often occur in the application process. However, the future development prospect of this technology is very broad, and its development has also become a hot spot of social concern (Zhongxin Ni et al., 2020) (Ni et al., 2021). With the innovation of material industry, the material of manufacturing discrete dynamic model system has achieved the goal of reducing manufacturing cost. Due to the characteristics of low manufacturing cost, discrete dynamic modeling technology is gradually applied to various industries.

Discrete dynamic modeling technology began to be developed abroad earlier, and relevant foreign researchers are more mature in terms of cognition and reference methods of this technology. Discrete dynamic modeling technology originated from mathematical model, and then applied to data statistics, discrimination, and calculation and so on. Discrete dynamic modeling technology mainly depends on the data information generated by things. By classifying, calculating and assimilating the data, the overall data trend is finally obtained, which also provides convenience for users applying discrete dynamic modeling technology (A. I. sukhinov et al., 2020) (Sukhinov et al., 2020). In the process of realizing discrete dynamic modeling technology, the principle of data transportation should be followed. The data information of things is processed and analyzed through a special data transmission device. Discrete dynamic model system can be regarded as an integrator of data. It not only includes big data environment, but also includes data processing system and anti loss system (D. a. Komarov et al., 2020) (Komarov et al., 2020). We can regard the discrete dynamic model system as an internal memory of the computer. It is a model environment for interacting with data. People can clearly understand all kinds of information between data through the computer.

This paper is mainly composed of three parts.

1) Firstly: introduces the application of discrete dynamic modeling technology in rural sewage treatment system, and the development status of discrete dynamic modeling technology.
2) Secondly: Research the stability of rural sewage treatment system under discrete dynamic modeling technology and the control of rural sewage treatment system under discrete dynamic modeling technology.
3) Thirdly: result analysis of rural sewage treatment system under discrete dynamic modeling technology, and the control result analysis of rural sewage treatment system under discrete dynamic modeling technology.

RELATED WORK

The related concepts of discrete dynamic modeling technology have been put forward a long time ago, and its emergence indirectly reflects the positive development of big data in the Internet. It also promotes the innovation and application of discrete dynamic modeling technology (Nauman Raza et al., 2020) (Raza et al., 2020). The embryonic stage of discrete dynamic modeling technology first appeared in the 1950s. Subsequently, it appeared in the paper jointly issued by French mathematician David Ruelle and Dutch mathematician Floris Takens, and proposed the formation mechanism of using chaotic data to describe the results for the first time in the field of mathematics. Later, mathematicians from various countries put forward more kinds of related concepts and began to carry out experimental application in the 1970s (Antonio gon ç Alves et al., 2020) (Gonçalves et al., 2020). However, due to the immature development of computers at that time, the progress of experimental application was very slow. Many error messages also appeared in the application process, so that the technology was affected by conditions and did not get very big response at that time (lorella Fatone et al., 2020) (Fatone and Mariani, 2020). Then, due to the development of computers in the 1990s, discrete dynamic modeling technology gradually broke through the difficulties. Relevant researchers have applied discrete dynamic modeling technology to the processing of stock data and achieved great success. This is also the first time that discrete dynamic modeling technology has been applied to human life (Wen Ling Tian et al., 2020) (Tian et al., 2020).

The development speed of discrete dynamic modeling technology in the United States is faster than that in other countries. The first successful application of discrete dynamic systems to practice was in the United States (Mengjie Zhang et al., 2019) (Zhang et al., 2019). Discrete dynamic modeling technology is combined with stock information to systematically analyze the rise and fall data of various stocks. The stock information data processed with discrete dynamic modeling technology can better reflect the fluctuation trend of stock data over a period of time compared with all kinds of disorderly data (babita K. Verma et al., 2019) (Verma et al., 2019). With the application of discrete dynamic modeling technology to integrate stock data, it is gradually applied to other directions in the financial field. The introduction of this technology has also taken a big step forward for the American economy.

Japan's discrete dynamic modeling technology has made a breakthrough in medicine (Wei Chao Li et al., 2019) (Li et al., 2019). They use discrete dynamic modeling technology to integrate the patient's vital signs data, and then transmit the processed vital signs data to the screen, so as to observe the patient's vital signs in real time. Japanese researchers have used the discrete dynamic model system to create a data collection database for data, which can not only collect the vital signs data of patients, but also classify and calculate the data (Truong thi Nguyen et al., 2019) (Nguyen et al., 2019). However, at that time, the technology was not widely used in major hospitals. Later, with the development of society, people gradually realized the importance of medical treatment and began to apply it on a large scale. Today, medical institutions all over the country have fully covered the technology.

France applies discrete dynamic modeling technology to military field. They mainly apply discrete dynamic modeling technology to detect vehicle faults. In order to improve the

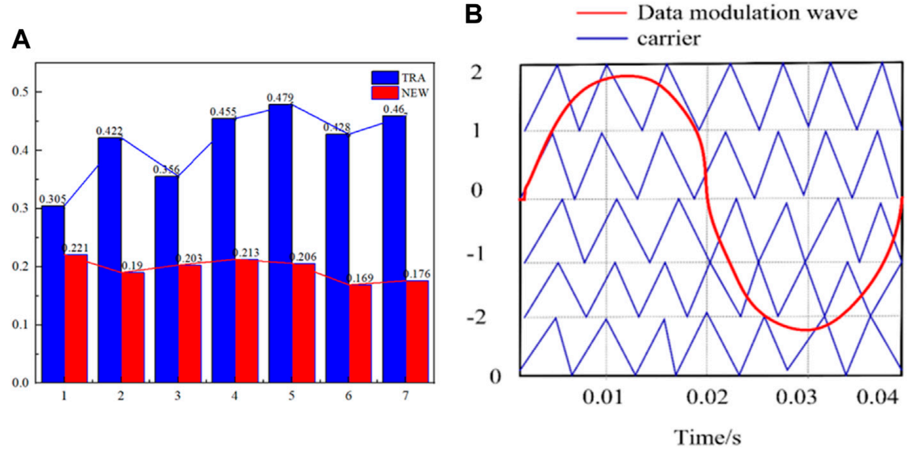

FIGURE 1 | Five level data modulation diagram.

work quality of inspectors, discrete dynamic modeling technology needs to be combined with the original data information of normal vehicle components. Then compare the real-time information transmitted by the tested vehicle with the data. Once the data deviation is large, the tester can accurately find the fault and repair the vehicle in time (Joseph F. hair et al., 2019) (Hair et al., 2019). The introduction of this technology can greatly save the capital cost of the army. In the actual combat drill, the quality of vehicles is also directly related to the training effect, which also provides a guarantee for the safety of soldiers.

China has moved discrete dynamic modeling technology to the transportation industry. As we all know, Chinese people generally like to shop online, and the transportation volume of goods is also very huge. Because discrete dynamic modeling technology can classify and process the data of things, it can accurately store and output the package information. Classify the package data information to the greatest extent, so as to improve the delivery speed of products (Daniel Ioan et al., 2019) (Ioan et al., 2019). The combination of discrete dynamic modeling technology and transportation industry has directly affected the domestic economy and made China the largest transportation country in the world (Li et al., 2021a; Li et al., 2021b; Le et al., 2021; Toyoda and Wu, 2021; Wu et al., 2021; Zhang et al., 2022).

What is mentioned above is the historical development trend and status of discrete dynamics modeling technology in each country, both of which reflect the remarkable characteristics of discrete dynamics modeling technology for social development.

METHODOLOGY

Study on Stability of Rural Sewage Treatment System Based on Discrete Dynamic Modeling Technology

The rural sewage treatment system contains five level H bridge. Usually, in order to observe the stability of the bridge in the sewage treatment equipment, the discrete dynamic modeling technology is combined to observe the data. At present, the phenomenon of bifurcation and chaos in the bridge is of practical significance to the correlation design of data parameter information and stability analysis. When analyzing and processing the stability of data parameters, it is mainly to build a discrete dynamic model based on the state of bridge inverter, and then analyze the data information. The discrete dynamic model constructed cannot be an ordinary discrete model, but must be a discrete dynamic model for accurate analysis of data. Because the composition of the bridge is a very complex form of current pulse, the number of levels obtained during data sampling in the sewage treatment system are different. In order to solve this problem, this paper introduces the virtual ergodic modeling method into the refined discrete dynamic model. With the addition of this method, the influence of data complexity on system stability is easily solved.

As shown in **Figure 1A**, the power consumption per ton of sewage in traditional sewage treatment is between 0.305 and 0.5 kW h, and the fluctuation is large, with a fluctuation range of up to 57%. The energy consumption after using discrete dynamic modeling technology is between 0.167 and 0.221, and the fluctuation range is reduced to about 32%. The most important thing is that the overall power consumption shows a downward trend, up to 64.7%, that is, the same ton of wastewater is treated. the power consumption is reduced by 64.7%

The virtual traversal method mainly samples the data at different times, and obtains the model mapped within the system from the obtained data and the state variables in a period of time. For the five level H-bridge, the virtual ergodic method combined with carrier modulation is used to determine the dynamic model of the system. The modulation schematic diagram of five level SPWM is shown in **Figure 1B**.

It can be seen from **Figure 1B** that the level generated in different time periods is different, so it is difficult to establish the discrete dynamic system within the sampling time. Combined with the modulation principle of the above five-level SPWM, this paper extends the level state in the sewage treatment system, and then constructs the discrete dynamic model. The level expansion phase equation in the system is as follows:

$$\frac{di}{dt} = -\frac{R}{L} i + \frac{\delta E}{L}, \delta \in \{2, 1\} \cup \{1, 0\} \cup \{0, -1\} \cup \{-1, -2\} \tag{1}$$

Among them, the generated level coefficient can be taken within a period of time, and the value can be eight values. In the ordinary sampling time period, only two values can be taken, so the method studied in this paper is called virtual traversal method. In order to solve the above formula, a standard differential equation is given as follows:

$$\frac{dy}{dt} = ay + b, y = -\frac{a}{b} + C_e^{at} \tag{2}$$

After the numerical solution is brought in, the solution of the equation is obtained, and then the current state is transmitted. After the final current goes through the eighth state, the relevant formula about the value is as follows:

$$i_{n+1} = \frac{\delta_8 E}{R} + \left(i_n - \frac{\delta_1 E}{R}\right) e^{-\frac{R}{L}T^2} + \left\{ \sum_{k=1}^{7} \left[\frac{(\delta_k - \delta_{k+1})E}{R} e^{\frac{R}{L}\sum_{j=1}^{k} d_j T_s} \right] \times \right\} e^{-\frac{R}{L}T_S} \tag{3}$$

The above contents are also the final discrete dynamic model of sewage treatment system and discrete dynamic modeling technology. In the above formula, it is mainly obtained by comparing the device modulation wave with the carrier wave. In this experiment, the duty cycle inside the model needs to be determined. Since the current has eight states, it can be seen that there are eight duty cycles. Since the duty cycle can be expressed by matrix function, the symbolic function is used to unify the duty cycle. The relevant formula is as follows:

$$\operatorname{sgn}(x) = \left\{ \begin{array}{c} 1, x \geq 0 \\ -1, x < 0 \end{array} \right\} \tag{4}$$

$$\frac{d\operatorname{sgn}(x)}{dx} = 2\delta(x) \tag{5}$$

It should be noted that in the function formula, the function is meaningful only when it is zero. Finally, the duty cycle is finally expressed with the above symbols, and the form formula is as follows:

$$[d1 \ldots d7]^T = T(V^*) = T_s. \left[\frac{\operatorname{sgn}(x) + \operatorname{sgn}(x')}{2} (V^*) \right] \tag{6}$$

According to the above formula, the key content of the virtual traversal method is to obtain all the data information of the internal state of the system. The combination of discrete dynamic modeling technology and rural sewage treatment system focuses on the composition between data duty cycle and modulation. Only when the data between them are expressed in a functional way can the stability of the whole system be analyzed later. In this paper, the method of transforming data relationship into symbolic function is also very suitable for solving the modeling problem of device data in the system.

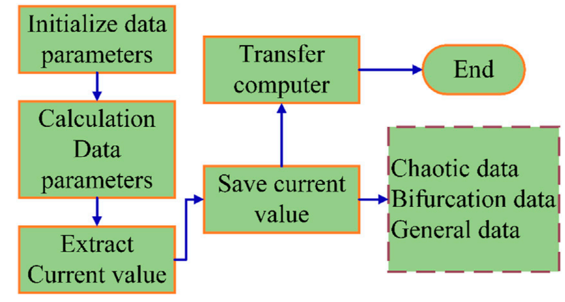

FIGURE 2 | Flow chart for judging system stability.

After the discrete dynamic model system is established, the stability of the inverter bridge can be analyzed. The process of determining whether the system is stable is shown in **Figure 2**.

As can be seen from **Figure 2**, the flow chart is mainly divided into three layers. The innermost layer is mainly used to calculate the current data, and the other two layers are mainly used to convert the data. In the process of calculation, the relevant formulas for the definition of variables and the characteristic equation of the matrix are as follows:

$$X = y_{R_{n-2}}, y_n = y_{R_{n-1}}, z_n = i_{n-1}, q_n = i_n \tag{7}$$

$$p(z) = a_0 z^4 + a_1 z^3 + a_2 z^2 + a_3 z + a_4 \tag{8}$$

According to the above formula, in the rural sewage treatment system in this paper, the data generated by four devices are mainly studied, so four new variable sets are defined. Then calculate and convert the data of the four variables, and finally transmit them to the visual end.

Because the system combines the virtual traversal method, the data calculation error caused by environmental factors can be avoided in the process of converting the current data generated by the internal devices of the sewage treatment system. Then the converted data parameters are transmitted to the computer to form a three-dimensional stable area of the sewage treatment system. The angle and area inside the three-dimensional stability region can analyze and judge the stability of the whole system, so as to improve the work efficiency and accuracy of the system.

Research on Control of Rural Sewage Treatment System Based on Discrete Dynamic Modeling Technology

In the process of control in the rural sewage treatment system using discrete dynamic modeling technology, in order to avoid the bifurcation chaos such as noise, irregular data oscillation and system instability during the operation of SPWM. In this paper, a nonlinear method is used to stroboscopic map the data to the whole system. This mapping method is also the main means to deal with chaos and bifurcation. The single-phase SPWM rectifier in the system mainly presents two states during operation. When

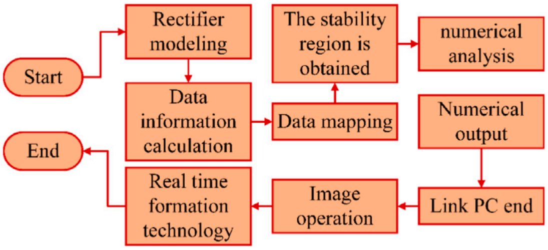

FIGURE 3 | Control flow chart of the system.

performing stroboscopic mapping, it needs to be solved twice continuously, which is also very difficult. In this paper, the stroboscopic mapping in the single-phase SPWM rectifier in the system is modeled by simplifying the calculation process. Then the chaos and bifurcation phenomena are analyzed by using discrete dynamic modeling technology. Finally, the control parameters that can control the whole system are obtained, and the control module in the whole rural sewage treatment system can be seen more intuitively. The specific design flow of the whole control system is shown in **Figure 3**.

As can be seen from **Figure 3**, firstly, the working principle of single-phase SPWM rectifier is modeled. Then the bifurcation phenomenon of the constructed model is analyzed, and finally the stability region is solved and the numerical value is analyzed. The control circuit in single-phase SPWM rectifier is mainly composed of two closed loops, and the corresponding formula is as follows:

$$\begin{cases} L\dfrac{di}{dt} = -Ri + E\sin(\omega t) - U_{dc} \\ C\dfrac{dU_{dc}}{dt} = -\dfrac{1}{R_L}U_{dc} \pm i \end{cases} \tag{9}$$

After calculating the working time of the data, the stroboscopic mapping of single-phase SPWM rectifier can be obtained. However, when dealing with more complex data information, the solution process becomes difficult. In this paper, Adomian polynomials are added to the original system model. With the addition of Adomian, the solution of nonlinear differential equations becomes easy. Adomian can automatically transform the solution into form, and the more data, the more accurate it is. Adomian's relevant formula is as follows:

$$Lu + Ru + Nu = g \tag{10}$$

$$A_n(u_0, u_1, \ldots, u_n) = \frac{1}{n!}\left[\frac{d^n}{d\lambda^n}N\left(\sum_{i=0}^{\infty}\lambda^i u_i\right)\right]_{\lambda=0} \tag{11}$$

The core content of Adomian polynomial is to solve the high-order derivative, and the polynomial is mainly composed of variables, so it is more suitable for the discrete dynamic system studied in this paper.

When analyzing the bifurcation phenomenon in the whole system, we must first understand the information of the relevant data generated by the bifurcation chaos phenomenon. The source of data is mainly generated by the peak current, and the peak current can be collected directly. The current peak segmentation number generated by the internal components of the sewage treatment system studied in this paper is 70, that is, when it is greater than 70, the data appear chaotic bifurcation phenomenon. By analyzing the bifurcation chaotic data of nonlinear attributes, it is convenient to judge the chaotic bifurcation characteristics of the whole system in a fixed time. As long as the trend of the image presented on the computer side is symmetrical, we can know that the whole system is running stably.

After taking some chaotic bifurcation data, the stroboscopic mapping method is added to the model system. In the process of adding, the transfer function formula of the controller is:

$$F(s) = K_p + \frac{K_r.s}{s^2 + \omega_1^2} \tag{12}$$

Before the controller transmits data, because there is still sinusoidal quantity in the rectifier, the sinusoidal quantity needs to be replaced by variables before data transmission. The formula related to variable substitution is as follows:

$$\begin{cases} \dfrac{dz}{dt} = \omega E\cos(\omega t) \\ \dfrac{d^2z}{dt^2} = -\omega^2 E\sin(\omega t) = -\omega^2 z \end{cases} \tag{13}$$

After replacing the data form, the controller maps the data transmitted to the computer to the SPWM rectifier in the discrete dynamic system. The related formulas of discrete mapping are as follows:

$$X_{n+1} = F(X) = \begin{Bmatrix} f1(x_n, y_n, m_n, z_n) \\ f2(x_n, y_n, m_n, z_n) \\ f3(x_n, y_n, m_n, z_n) \\ f4(x_n, y_n, m_n, z_n) \end{Bmatrix} \tag{14}$$

Through the above content, the whole discrete dynamic system is updated. Next, we need to solve the stable region in the system. In this paper, the Jacobian matrix method is mainly used for solving, and the relevant formulas are as follows:

$$J_m = \begin{bmatrix} \dfrac{d}{dx_n}f_m \cdots\cdot \dfrac{d}{ds_n}f_m \\ \cdots\cdot \\ \dfrac{d}{dx_n}f_m \cdots\cdot \dfrac{d}{ds_n}f_m \end{bmatrix} \tag{15}$$

Through the introduction of data, the eigenvalues of Jacobian matrix are obtained. By comparing and calculating with all data node values in the internal parameter area of the system, all characteristic values that meet the internal area of the system can be obtained. The higher the switching frequency of sewage treatment system components, the larger the stability range of the system. We can also operate the system by controlling the internal eigenvalues. Although the addition of control methods can systematically collect and track data, it also reduces the stability of the whole system to a certain extent.

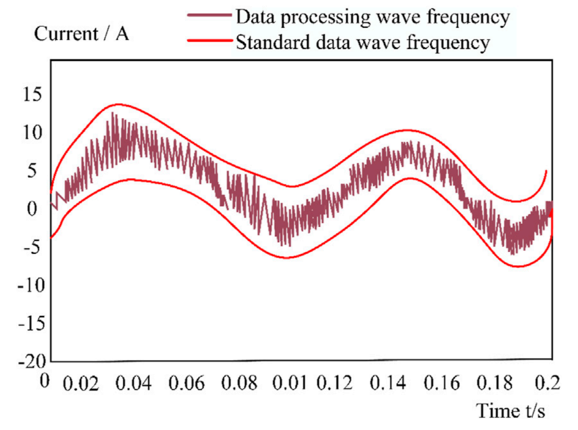

FIGURE 4 | Wave frequency diagram of discrete dynamic system when processing data.

Finally, the numerical value generated by the system in processing data is analyzed. Because the stroboscopic mapping can continuously iterate the data within the system, the waveform variables generated by the data in different states can be obtained. After collecting the internal current waveform, the system stores the filtered wave peak separately, and obtains the chaotic bifurcation of the data in the system. If sampling is selected at only one point, all output data results are limited to a single state; If data sampling is selected at two points, all output data results have only two states; If the data is sampled at many nodes, the data obtained is polymorphic and contains bifurcation chaos. According to the above content, only continuous sampling of multiple nodes can be helpful to the research content of this paper and improve the accuracy of the results.

RESULT ANALYSIS AND DISCUSSION

Stability Analysis of Rural Sewage Treatment System Based on Discrete Dynamic Modeling Technology

By combining the discrete modeling technology with the rural sewage treatment system, the data information of the current required in the components is obtained. In the initial stage of data processing, it is only data acquisition and transmission, in which the virtual traversal method of control data and system stability is added. After real-time collection, analysis and processing of the attributes and status of machine component data, the whole discrete dynamic system can be clearly monitored by the computer. The real-time waveform data generated in the process of system operation can indirectly analyze the stability of the whole discrete dynamic system. In order to further verify the overall stability of the combination of discrete modeling technology and rural sewage treatment system. In this paper, the internal current data of machine components are sampled, and a period of time during the operation of the system is intercepted. Finally, the stability of the whole system is verified by the sample data wave frequency generated by the system when processing data. The operating wave frequency of the obtained discrete dynamic system is shown in **Figure 4**.

It can be seen from **Figure 4** that the combined discrete dynamic model system processes the sample data generated by the machine over a period of time. From the electromagnetic wave frequency generated by the data in the figure, the operation process of the system processing data is very stable. Although the data frequency values in different periods still fluctuate significantly, they are all within the standard value. When the system is in a relatively stable operation state, it can play its original role with maximum efficiency. Therefore, according to the wave frequency generated by the above discrete dynamic system when processing data, it can be concluded that the discrete dynamic model system studied in this paper has good stability and good performance.

Analysis of Control Results of Rural Sewage Treatment System Based on Discrete Dynamic Modeling Technology

It is far from enough to design and study the stability of a system. Based on the enhanced discrete dynamic modeling technology, combined with the rural sewage treatment system, the control function is also added. The traditional discrete dynamic model can not directly control the model in the modeling process, and the algorithm can only control the data and system manually. For example, repeatedly adding data and switching the system. The discrete dynamic model studied in this paper combines the method of stroboscopic mapping. After being added into the system modeling, this method directly replaces the original status of artificial data and system control. In order to further verify the control performance of rural sewage treatment system under discrete dynamic modeling technology, five groups of sample data with different quantity and category are selected for processing. Finally, through the optimized discrete dynamic system, the data processing rate and the authenticity of the results are analyzed in

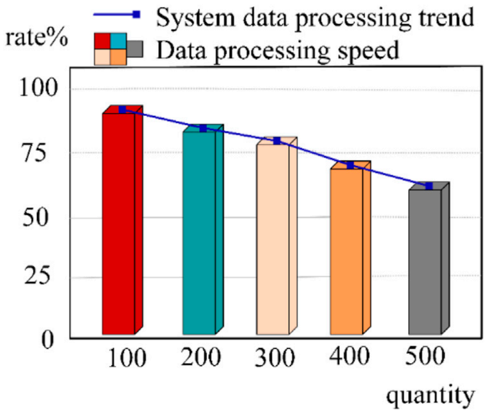

FIGURE 5 | Data processing efficiency diagram of optimized discrete dynamic system.

detail. The data processing efficiency trend of the optimized discrete dynamic system in the experiment is shown in **Figure 5**.

It can be seen from **Figure 5** that the optimized discrete dynamic system has very high data processing efficiency. The smaller the amount of data processed, the higher the processing rate of the corresponding system. Although the rate is reduced when processing huge data, the rate is still as high as 60%. It can be seen that the control performance of the whole system is very good. In the previous research data, the data processing rate of ordinary discrete model is no more than 40%, and system failures often occur. In contrast, the discrete dynamic model system studied in this paper can maintain the stability of the system and data, and can automatically control it. It also indirectly proves that the technology has strong social application value.

CONCLUSION

In the big data environment, discrete dynamic technology can be combined with many fields. This paper combines this technology with rural sewage treatment system. Firstly, the virtual traversal method is added to the system to construct the model, which strengthens the stability of the whole data and the system. Inside the virtual traversal method, all possible conditions are considered. In this way, the final model is established to improve the overall accuracy to the greatest extent. After ensuring the stability of the system, the model of SPWM rectifier in the system is transformed. By controlling the data type, the overall performance of the system is improved. It mainly uses the occupied space value to achieve the mapping between data, and also provides a new idea for stroboscopic mapping modeling. The final system has stable and controllable excellent properties, and can also analyze and process the data in the rural sewage treatment system. The sewage treatment method in this paper can not only reduce the expenditure of energy costs but also bring more economic benefits. Hence, the water consumption and drug consumption of the whole process will be optimized simultaneously.

DATA AVAILABILITY STATEMENT

The raw data supporting the conclusions of this article will be made available by the authors, without undue reservation.

AUTHOR CONTRIBUTIONS

WL independently completed all the contents of the article.

REFERENCES

Djazet, A., Fewo, S. I., Nkouankam, E. B. N., and Kofané, T. C. (2020). Stability Analysis for Moving Dissipative Solitons in Two-Dimensional Dynamical Model. *Eur. Phys. J. D* 74 (4), 67. doi:10.1140/epjd/e2020-100467-7

Dunstan, M., Xavier, E. A., Fatima, A., and Marta, G. (2021). *Using Mobile Data to Understand Urban Mobility Patterns in Freetown*. Sierra Leone: The World Bank.

Fatone, L., and Mariani, F. (2020). Systemic Risk Governance in a Dynamical Model of a Banking System with Stochastic Assets and Liabilities. *J. Econ. Interact. Coord.* 15 (12), 183–219. doi:10.1007/s11403-019-00277-y

Gonçalves, A., Mentré, F., Lemenuel-Diot, A., and Guedj, J. (2020). Model Averaging in Viral Dynamic Models. *AAPS J.* 22 (12), 48. doi:10.1208/s12248-020-0426-7

Hair, J. F., Ringle, C. M., Gudergan, S. P., Fischer, A., Nitzl, C., and Menictas, C. (2019). Partial Least Squares Structural Equation Modeling-Based Discrete Choice Modeling: an Illustration in Modeling Retailer Choice. *Bus. Res.* 12 (1), 115–142. doi:10.1007/s40685-018-0072-4

Ioan, D., Bărbulescu, R., Silveira, L. M., and Ciuprina, G. (2019). Reduced Order Models of Myelinated Axonal Compartments. *J. Comput. Neurosci.* 47 (2-3), 141–166. doi:10.1007/s10827-019-00726-4

Komarov, D. A., Maslennikov, S. P., Yakushkin, E. P., and Paramonov, Yu. N. (2020). Influence of External Electric Circuits on the Static and Dynamic Mode of Operation of Multipath Collectors of Powerful Klystrons. *J. Commun. Technol. Electron.* 65 (3), 306–310. doi:10.1134/s1064226920030080

Le, S., Wu, Y., Guo, Y., and Vecchio, C. D. (2021). Game Theoretic Approach for a Service Function Chain Routing in NFV with Coupled Constraints. *IEEE Trans. Circuits Syst. II* 68, 3557–3561. doi:10.1109/TCSII.2021.3070025

Li, H., Deng, J., Feng, P., Pu, C., Arachchige, D. D. K., and Cheng, Q. (2021). Short-Term Nacelle Orientation Forecasting Using Bilinear Transformation and ICEEMDAN Framework. *Front. Energy Res.* 9, 780928. doi:10.3389/fenrg.2021.780928

Li, H., Deng, J., Yuan, S., Feng, P., and Arachchige, D. D. K. (2021). Monitoring and Identifying Wind Turbine Generator Bearing Faults Using Deep Belief Network and EWMA Control Charts. *Front. Energy Res.* 9, 799039. doi:10.3389/fenrg.2021.799039

Li, W. C., Deng, G., Cao, W., Xu, C., Chen, J., and Lee, M. L. (2019). Discrete Element Modeling of the Hongshiyan Landslide Triggered by the 2014 Ms 6.5 Ludian Earthquake in Yunnan, China. *Environ. Earth Sci.* 78 (16), 520. doi:10.1007/s12665-019-8438-2

Nguyen, T-T., André, D., and Huger, M. (2019). Analytic Laws for Direct Calibration of Discrete Element Modeling of Brittle Elastic Media Using Cohesive Beam Model. *Comput. Part. Mech.* 6 (3), 393–409. doi:10.1007/s40571-018-00221-0

Ni, Z., Lu, X., and Xue, W. (2021). Does the Belt and Road Initiative Resolve the Steel Overcapacity in China? Evidence from a Dynamic Model Averaging Approach. *Empir. Econ.* 61. doi:10.1007/s00181-020-01861-z

Raza, N., Afzal, J., Bekir, A., and Rezazadeh, H. (2020). Improved TanΦ(ξ)2$\tan \left (\frac {\Phi (\xi)}Brazilian Journal of Physics\right)$ -Expansion Approach for Burgers Equation in Nonlinear Dynamical Model of Ion Acoustic Waves. *Braz. J. Phys.* (prepublish).

Sukhinov, A. I., Ougolnitsky, G. A., and Usov, A. B. (2020). Methods of Solving the Theoretic Game Models for Coordinating Interests in Regulating the Fishery Industry. *Math. Models Comput. Simulations* 12 (2), 176–184. doi:10.1134/s2070048220020143

Tian, W-L., Yang, S-Q., and Huang, Y-H. (2020). Discrete Element Modeling on Crack Evolution Behavior of Sandstone Containing Two Oval Flaws under Uniaxial Compression. *Arabian J. Geosciences* 13 (1), 418. doi:10.1007/s12517-020-05348-0

Toyoda, M., and Wu, Y. (2021). Mayer-type Optimal Control of Probabilistic Boolean Control Network with Uncertain Selection Probabilities. *IEEE Trans. Cybern.* 51, 3079–3092. doi:10.1109/tcyb.2019.2954849

Verma, B. K., Subramaniam, P., and Vadigepalli, R. (2019). Model-based Virtual Patient Analysis of Human Liver Regeneration Predicts Critical Perioperative Factors Controlling the Dynamic Mode of Response to Resection. *BMC Syst. Biol.* 13 (1), 9. doi:10.1186/s12918-019-0678-y

Wu, Y., Guo, Y., and Toyoda, M. (2021). Policy Iteration Approach to the Infinite Horizon Average Optimal Control of Probabilistic Boolean Networks. *IEEE Trans. Neural Netw. Learn Syst.* 32 (6), 2910–2924. doi:10.1109/TNNLS.2020.3008960

Zhang, M., Yuan, X., Guan, D., Liu, H., Zhang, G., Wang, K., et al. (2019). Eco-exergy Evaluation of New Wetlands in the Yanzhou Coalfield Subsidence Areas Using Structural-Dynamic Modelling. *Mine Water Environ.* 38 (4), 746–756. doi:10.1007/s10230-019-00628-y

Zhang, Y., Qian, T., and Tang, W. (2022). Buildings-to-distribution-network Integration Considering Power Transformer Loading Capability and Distribution Network Reconfiguration. *Energy* 244, 3104. doi:10.1016/j.energy.2022.123104

Conflict of Interest: The author declares that the research was conducted in the absence of any commercial or financial relationships that could be construed as a potential conflict of interest.

frontiers | Frontiers in Energy Research

ORIGINAL RESEARCH
published: 22 June 2022
doi: 10.3389/fenrg.2022.888298

A Possibilistic Risk Assessment Framework for Unmanned Electric Vehicles With Predict of Uncertainty Traffic

wen hu[1]*, *longyun kang*[1] *and zongguang yu*[2]

[1]*School of Electric Power, South China University of Technology, Guangzhou, China,* [2]*Internet of Things Engineering College, Jiangnan University, Wuxi, China*

At present, electric vehicles (EV) have entered a stage of rapid development. Meanwhile, with artificial intelligence (AI) technology fast improving and implementing many inventions in electric vehicles (EV), almost all EV sold in China are equipped with automatic driving technology to achieve safer and more energy-saving driving. In order to solve the problem of anti-collision in self-driving Smart EV under complex traffic, especially at intersections, most of the existing methods make sequential predictions for the driving level of vehicles, and it becomes difficult to deal with sudden changes in intentions of other vehicles. Therefore, a collision risk assessment framework based on other vehicles' trajectory prediction is proposed. The framework integrates the solutions of other vehicles' expected path planning, uncertainty description of driving process, trajectory change caused by obstacle intrusion, etc., as well as adopts the Gaussian mixture model to evaluate the risk according to the probability of collision. It realizes the real-time evaluation of the probability of collision and makes safe decisions and trajectory planning of the vehicles. After simulation and verification, it effectively solves the decision-making planning problem of autonomous vehicles under complicated traffic flow and demonstrates that the method is better than the current sequential prediction method (SORT\Karlman filter, etc.).

Keywords: electric vehicle, artificial intelligence, uncertainty prediction, decision-making, risk assessment

Edited by:
Xun Shen,
Tokyo Institute of Technology, Japan

Reviewed by:
Sandeep Kumar Duran,
Lovely Professional University, India
Gaurav Sachdeva,
DAV University, India

***Correspondence:**
wen hu
78157320@qq.com

Specialty section:
This article was submitted to Smart Grids, a section of the journal Frontiers in Energy Research

Received: *02 March 2022*
Accepted: *31 March 2022*
Published: *22 June 2022*

Citation:
hu w, kang l and yu z (2022) A Possibilistic Risk Assessment Framework for Unmanned Electric Vehicles With Predict of Uncertainty Traffic.
Front. Energy Res. 10:888298.
doi: 10.3389/fenrg.2022.888298

1 INTRODUCTION

Crossroads are one of the traffic scenes with the most complicated driving conditions. For autonomous vehicles, it is of great significance to further improve and ensure vehicle safety if they can sense the intention of other vehicles in advance and predict possible collision risks between themselves and the other vehicles.

At present, in the problem of collision avoidance in autonomous driving scenes, the trajectory planning and behavior decision of autonomous driving vehicles mainly need to consider other dynamic obstacles in traffic scenes. At the same time, including but not limited to the driving trajectories of the other motor vehicles, to determine the behavior decision and trajectory planning of the autonomous driving vehicles. The two main methods in the industry for this are planning-based method and optimization-based control method. Trajectory planning is a typical control method which includes advance planning based on prior environmental information in addition to real-time planning based on online space exploration (Wang et al., 2019; Wang and Huang, 2021), aiming at finding an optimal free path of colliding vehicles. Trajectory planning and collision avoidance based on the potential field have also been widely studied (Gianibelli et al., 2018; Chen and Yu, 2019). This method avoids collision behavior based on the potential field and uses the potential field to push vehicles away from certain obstacles. Planning-based methods are faced with the challenge of designing suitable collision avoidance paths, and it is difficult to find suitable optimal paths for a complex dynamic road condition. On the other hand, optimization-based control method (MPC) (Rothmund and Johansen, 2019) is also widely used for collision avoidance of unmanned vehicles. Collision avoidance is regarded as a coupling constraint, and the best collision avoidance algorithm is found for vehicles. There are also some researchers who speculate the upper limit of collision probability of the minimum collision time TTC (Shalev-Shwartz et al., 2017) based on the linear space and time of trajectory crossing to constrain the behavior decisions of unmanned vehicles such as deceleration and braking. However, this does not take into account the uncertainty and conservatism of obstacles, nor does it take into account the risk in the sense of probability. In recent years, many researchers have used AI methods to study path planning and collision avoidance of unmanned vehicles in a complex dynamic scenario, including the reinforcement learning methods of RL (Q-Learning) (Zhao et al., 2017) and POMDP (Hsu et al., 2008; Ponzoni Carvalho Chanel et al., 2012; Ragi and Chong, 2013). According to environmental rewards, calculate possible actions and get the next step. Some work has been put forward for a POMDP solution to model the uncertainty of target trajectory. But this solution needs to consider a large number of possible action sequences and the state of other vehicles, which must be completed in an ideal time and consume a lot of system resources and computing power. RL methods may suffer from problems caused by overfitting due to the complexity of environment and various characteristics of tasks. At the same time, less environmental knowledge may slow down the learning speed and cause unmanned vehicles to fall into local optimum.

The main contribution of this article is to develop a framework based on the collision risk assessment for obstacle avoidance in an unknown environment. This method predicts the environment along with preplanned tracks of other vehicles and analyzes the uncertainties. It includes other vehicles' expected path planning, uncertainty description of driving process, and trajectory change caused by obstacle intrusion. Through the analysis, modeling, and calculation of uncertainty, the prediction of other vehicles' trajectory based on probability is realized. The risk probability of collision is evaluated based on the other vehicles' trajectory. This result can be input to the decision control module for correcting or changing the motion planning of the own vehicle and can also trigger other safety algorithms of the own vehicle such as collision avoidance when necessary, moreover, ensuring vehicle safety to the greatest extent along with better driving efficiency.

2 Driving Uncertainty Analysis

Among the four factors that affect vehicle trajectory, the legal driving direction of the lane and geometric characteristics of the road are almost constant. This relevant information can be obtained through maps, high-precision maps, networks, or vehicle perception. The remaining three factors are uncertain with time and environment, which is the key and difficult point of other vehicles' trajectory prediction. It is also the key and difficult point of collision risk assessment. In this article, these three factors are summarized as three kinds of uncertainties that affect the trajectory of other vehicles and are analyzed, modeled, and calculated.

2.1 Uncertainty of Driving Intention

At present, the intelligent vehicle cannot accurately sense the driving intention of its driver, so the driving intention of its own vehicle is uncertain. As shown in **Figure 1A**, when turning around, turning left, going straight, and turning right are allowed in the lane in which other cars travel, the driving intention of the other cars is strongly uncertain when compared with that of the own car. Generally speaking, this uncertainty will decrease as the vehicle travels. For example, when a vehicle is at an intersection, there are possibilities of turning left, going straight, and turning around. When the vehicle travels halfway along the left-turn route, it can be judged that the vehicle is more likely to turn left. When the vehicle turns left and enters the other direction lane, the driving uncertainty disappears completely. Generally, an ego-vehicle's driving intention will not change in a driving process, but in a few special cases, the driving intention may also change. As shown in **Figure 1B**, because the ego-vehicle is unfamiliar with the road environment or misreads the road signs, it may suddenly switch to the left turn after driving on the straight line for a period of time.

2.2 Driving Process Uncertainty

Because people's perception, attention, operation ability, and other abilities cannot be as accurate as computers, and the vehicle's power system and control system cannot control the vehicle absolutely accurately, there is always some uncertainty in the vehicle trajectory during the driving process. This kind of uncertainty is interfered by the external environment to a certain extent, for example, talking with the ego-vehicle will distract the driver's attention, and fatigue driving will reduce the ego-vehicle's driving ability. Another characteristic of this kind of uncertainty is that it only appears when the vehicle is moving and disappears naturally when the vehicle is stationary. This kind of uncertainty is called the uncertainty of driving process in this article. There are two types of uncertainties in driving process, each with different characteristics: the first type is mainly caused by the lack of ability of the drivers or vehicles, which is objective and inevitable. However, this kind of uncertainty is often small and occurs randomly near the true value of the driving intention; the second type is mainly caused by the ego-vehicle's inattention. This kind of uncertainty may accumulate and enlarge and even eventually force drivers to change their driving intentions. For example, the vehicle originally wanted to go straight but because of the ego-vehicle's mistake, the vehicle continued to turn left and finally entered the left-turn lane. At this time, the ego-vehicle had to temporarily change its driving intention to turn left.

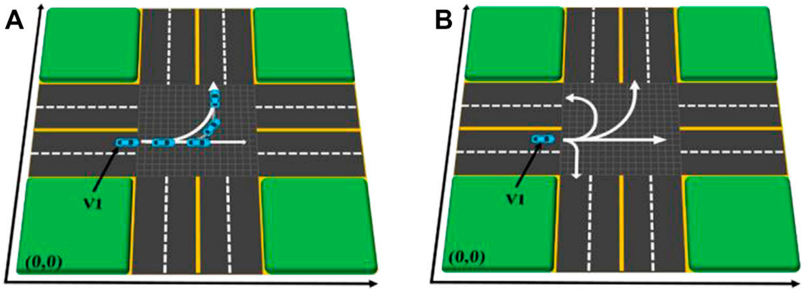

FIGURE 1 | Example of driving intention uncertainty. **(A)** Lane has multiple legal driving directions. **(B)** Driver temporarily changes driving intention.

2.3 Track Invasion Uncertainty

Due to the widespread existence of obstacles, vehicles often cannot drive according to the scheduled route, causing them to change the driving route constantly. However, obstacles may appear in any motion at any time and place, so the uncertainty caused by them is the most complicated and difficult to deal with. This kind of uncertainty is caused by external objects. In this article, it is called the uncertainty of other vehicles' track invasion. Compared with the uncertainty of driving intention, obstacles appear to more frequently lead to a higher frequency of vehicle route change. Compared with the uncertainty of driving process, the change of driving trajectory caused by obstacle intrusion is bigger and more significant.

2.4 Trajectory Planning Analysis of Other Collision Avoidance Effects

In addition to the above factors and uncertainties, there are many factors that affect the driving of vehicles in reality. The most common of which are the right-of-way rules. The right-of-way rules stipulate the priority right-of-way of different vehicles on the same road in a specific scene. The right-of-way division affects the running of vehicles and thus the assessment of collision risk. Based on the actual driving situation, this article focuses on the influence of vehicle arrival time, vehicle type, and vehicle driving intention on the right of way. In this article, it is determined that when a vehicle arrives at a certain position at different times, the vehicle that arrives first enjoys the right of way, and the vehicle that arrives later should give way; when the vehicle arrives at a certain position at the same time, consider the driving intention of the vehicle, such as turning left and right should be straight; and if two cars have exactly the same right of way, they are in a constant competitive state, and the vehicles stop at random for a period of time and then compete for the right of way again.

Besides the right of way, when vehicles avoid each other, it also affects each of their driving. In order to make the calculation easy to realize, when predicting the driving track of other vehicles V_i, only the influence of the remaining vehicles on V_i is considered while the influence of V_i on the other vehicles is not considered. For example, if the driving track of V_i is invaded by V_j, V_i may change the driving route to avoid V_j. At this time, the influence of the V_i route change on V_j is no longer considered. If V_j is affected by V_i and the driving route is adjusted, the influence of V_j on V_i after changing the route should be reconsidered. So repeated recursion will fall into an infinite loop.

3 Implementation of Risk Assessment Framework

The calculation process of the risk assessment framework proposed in this article can be divided into three steps as a whole, as shown in **Figure 2**. The framework needs the injection of the sensing module and the driving track of the vehicle generated by the decision control algorithm in the future. The calculation results of the risk assessment can be returned to the decision control module for correcting or reestablishing the new driving track. Other safety algorithms can also be triggered when necessary such as directly starting the collision avoidance system when the collision probability is high. The whole calculation process needs to be iterated in real time while driving according to the changed environments.

3.1 Grid Modeling of Road Environment

The first step of calculation is to realize the perception of the surrounding environment. In order to facilitate the calculation, this article uses a two-dimensional coordinate system to realize the gridding description of the whole environment space. As shown in **Figure 3**, **Figure 3A** is a realistic intersection simulation diagram, while **Figure 3B** is a gridded coordinate space. The origin of the coordinate system can be chosen arbitrarily when gridding. It only affects the calculation process and does not affect the calculation result. In **Figure 3**, the lower left corner is taken as the origin of coordinates.

3.2 Uncertainty Modeling of Other Vehicles' Trajectory

The second step is the focus of the whole calculation. It needs to deal with the three kinds of uncertainties mentioned above. Let the current time be t and the interval of iterative calculation be Δt. Then, the evaluation of the risk of collision between the own vehicle and other vehicles in the next n cycles has to be done. Let us assume that there are n other cars at the current intersection and take any other car V as an example to explain the prediction and calculation process of its driving track in the intersection.

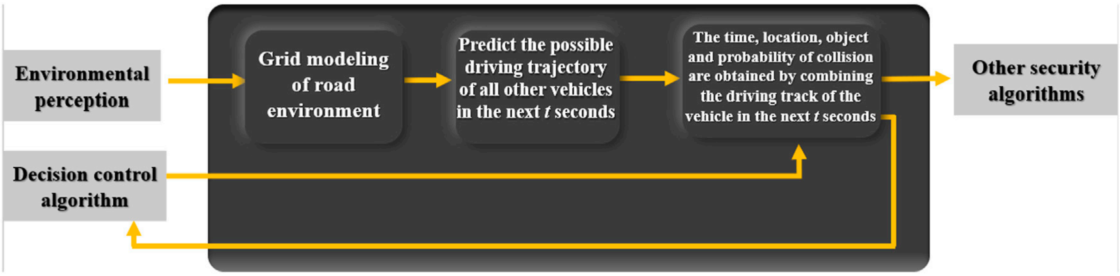

FIGURE 2 | Overall calculation process of risk assessment framework.

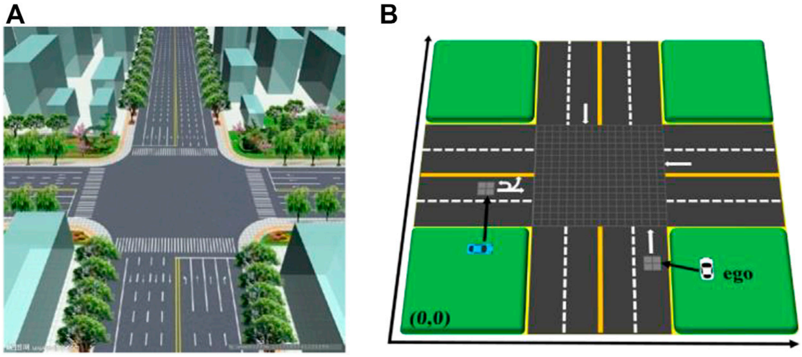

FIGURE 3 | Road space gridding at crossroads. **(A)** Intersection simulation Ddiagram. **(B)** Intersection grid modeling results.

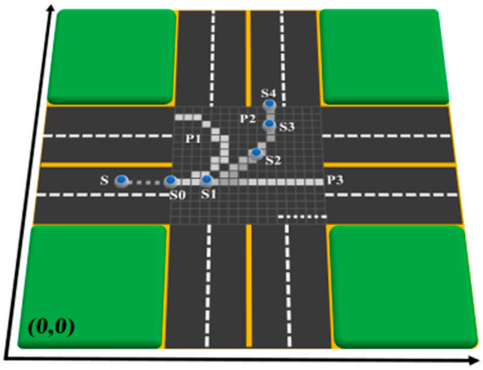

FIGURE 4 | Example of vehicle driving.

The essence of distribution probability lies in quantifying the uncertainty of driving intentions of various vehicles. This method holds that the probability distribution of the expected route is mainly affected by two factors: first, the statistical results of historical driving records, and second, the vehicle's trajectory in the past period of time. As shown in **Figure 4**, let the vehicle drive from s to S_0 and enter the intersection at S_0. When the vehicle is located at S_0, because the driving track from S to S_0 is not helpful in distinguishing and identifying the driving intention of the vehicles, the probability of the vehicles traveling on various paths can be quantified more accurately by using historical statistical data. When the vehicle is located in S_1, it can be considered that the possibility of turning around decreases while the probability of turning left along P_2 and going straight along P_3 increases. When the vehicle is located at S_2, it can be considered that the probability of turning around and going straight continues to decrease and the probability of turning left along P_2 increases. When the vehicle is located at S_3, it can almost be considered that the vehicle will definitely turn left. When the vehicle finally arrives at S_4, it turns left. After the turn is completed, the driving intention of the vehicle is determined to turn left, and the uncertainty is completely eliminated.

K possible driving paths are planned when the vehicle V enters the intersection. Assuming that a total of N vehicles have passed from the S_0 position in the past period of time, and the number of vehicles traveling along route I is N_i, the driving probability $P_i = N_i/N$ can be assigned to route P_i, and when the vehicle travels along the expected path, the uncertainty of driving intention can be estimated and quantified by using the driving trajectory in the past period of time. As shown in **Figure 5**, the vehicle enters the intersection from S_0, and arrives at S_1 after driving for a period of time, with a driving distance of L. As P_2 and F_3 completely overlap in the L part, the process from S_0 to S_1 can be considered as follows: the vehicle has traveled a distance of L length along P_2, traveled a distance of L along P_3, and a distance of 0 along P_1. Theoretically, the probability of different expected paths of vehicles can be calculated by using the following formula:

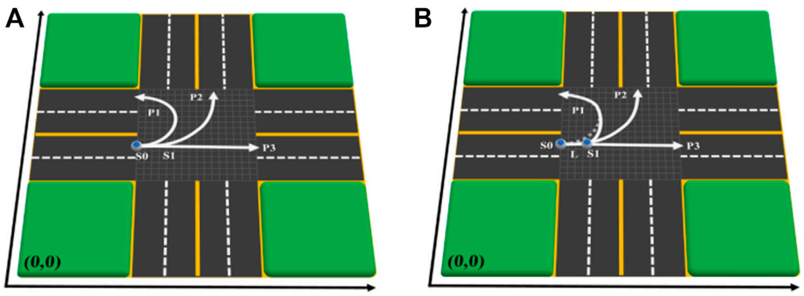

FIGURE 5 | Calculate the expected path probability by using the traveled trajectory. **(A)** Vehicle initial position S_O. **(B)** Vehicle driving to S_1.

$$N = \sum_{i=1}^{K} N_i,\ 1 = \sum_{i=1}^{K} P_i$$

$$\begin{cases} P_{\text{around}} = \dfrac{0}{L + L + 0} \\ P_{\text{left}} = \dfrac{L}{L + L + 0} \\ P_{\text{straight}} = \dfrac{L}{L + L + 0} \end{cases} \tag{1}$$

However, the above formula is prone to the extreme case of zero probability, which is inconsistent with the reality. Because even if the vehicle is located in S_1, there is still a certain probability of turning around, but this probability is smaller than turning left and going straight. Therefore, the above formula is adjusted based on Laplace's smoothing idea to avoid the situation that the probability is 0 or 1. The adjusted formula is as follows:

$$\begin{cases} P_{\text{around}} = \dfrac{0 + 1}{L + 1 + L + 1 + 0 + 1} \\ P_{\text{left}} = \dfrac{L + 1}{L + 1 + L + 1 + 0 + 1} \\ P_{\text{straight}} = \dfrac{L + 1}{L + 1 + L + 1 + 0 + 1} \end{cases} \tag{2}$$

The formula can be extended to the general situation, if the vehicle has k possible driving intentions at a certain position at the intersection, and the driving distance under the guidance of the i-th driving intention in the past period is L_i, the driving probability of the corresponding path under each intention in the future period is

$$P_{\text{i}} = \frac{L_{\text{i}} + 1}{\sum_{i=1}^{K} L + K},\ 1 = \sum_{i=1}^{K} P_{\text{i}} \tag{3}$$

The above method can deal with the general case of path probability allocation, but there are two special cases to be explained: 1) when a vehicle enters an unplanned location for some reason, the distance from the previous location to the current location should be specially treated when calculating; 2) some planned routes may disappear and some new planned routes may come into being during the driving process of the vehicles.

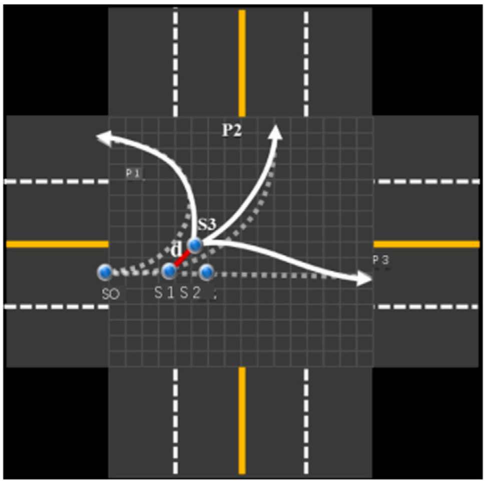

FIGURE 6 | Vehicle driving into unplanned location.

As shown in **Figure 6**, when the vehicle is located at S_1, it should arrive at S_2 at the next moment according to the planned expected route. However, due to some reasons, such as the ego-vehicle's inattention or obstacles at S_2, the vehicle actually enters S_3 at the next moment. However, the distance from S_1 to S_3 does not belong to any path among P_1, P_2, and P_3, so there will be ambiguity when using the above formula to calculate the probability. In order to ensure the smoothness of calculation, this article stipulates that d should be added to all L_i in this case, and the expected path of the vehicle should be replanned at the next moment.

In the second case shown in **Figure 7**, when the vehicle is in S_0, three expected paths are planned, namely P_1, P_2 and P_3. When the vehicle travels to S_1, because the direction of the front of the vehicle changes, the target area corresponding to P_1 is no longer visible (not within the 180-degree visual field), so P_1 disappears from the expected path and P_4 becomes the new expected path. At S_0, because the traffic rules stipulate that the inner lane is not allowed to turn right, there is therefore no driving intention to plan a right turn; at S_1, with the gradual exposure of the ego-vehicle's driving intention, it is more and more possible for the vehicle to turn right, so a right-turn path is added. Since there is

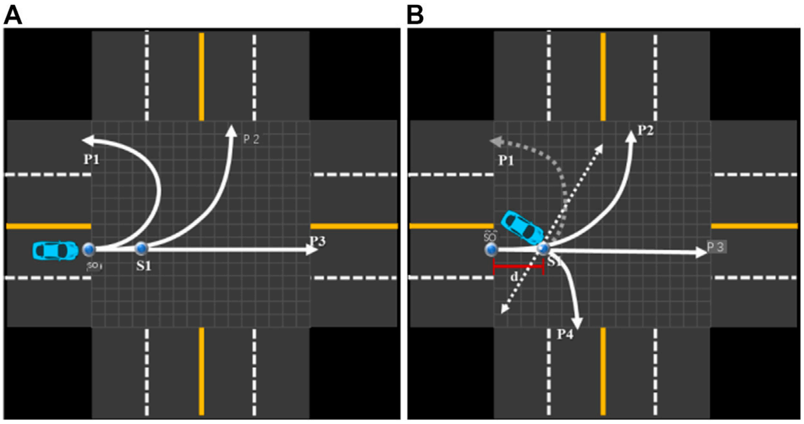

FIGURE 7 | Add and delete expected paths. **(A)** Vehicle initial position. **(B)** Replanning path with change of head direction.

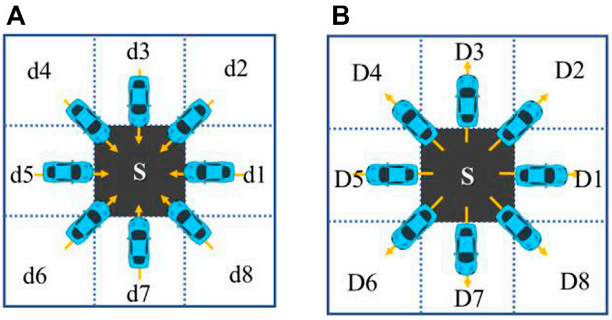

FIGURE 8 | Entry and exit of vehicles relative to a certain cell. **(A)** Enters a cell in any direction. **(B)** Leaves a cell in any direction. Definition: L4 = d, with Pright = $\frac{L_4+1}{\sum_{i=1}^{K'} L_i+K'}$.

no P_4 path in the process from S_0 to S_1, the right turn probability cannot be calculated by the above formula. It is stipulated in this article that the probability of the disappearing path is no longer calculated, the initial probability of a new route is calculated.

When calculating the expected path probability, it is not necessary to calculate the entire driving distance of the vehicle at the intersection. A time window can be set, and only the driving conditions within the time window can be considered, for example, only the driving conditions of the vehicle in the past 3 s can be considered.

Driving intention describes the uncertainty of vehicle trajectory from a macro perspective, while driving process describes the uncertainty of vehicle trajectory from a micro perspective. For the gridded intersection, the driving process of vehicles is equivalent to entering from one grid to another. Since the vehicle can travel to any feasible position in theory, it is also possible to enter a cell from any direction. As shown in **Figure 8A**, the vehicle may enter s from any direction of d1–d8. Similarly, as shown in **Figure 8B**, the vehicle may leave a cell from any angle. The essence of driving process uncertainty modeling is to measure the probability of leaving S from S along D_1–D_8. The traveling direction of the vehicle is controlled by the steering angle of the front wheel, and the direction of entering S affects the steering angle when the vehicle leaves. Therefore, the uncertainty modeling of driving process should consider both the direction when the vehicle enters and the direction when the vehicle leaves.

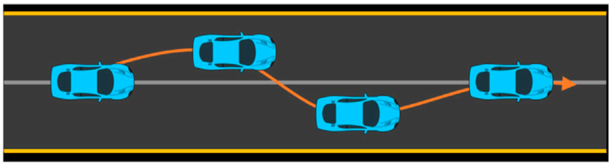

FIGURE 9 | Possible driving results around the intention of going straight.

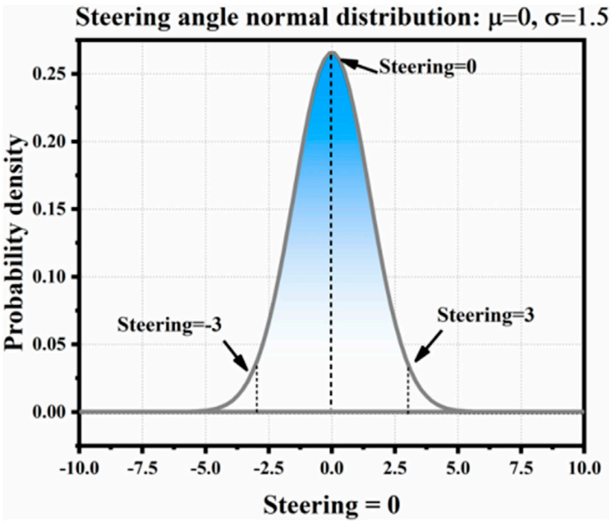

FIGURE 10 | Example of Gaussian distribution of the steering angle when going straight.

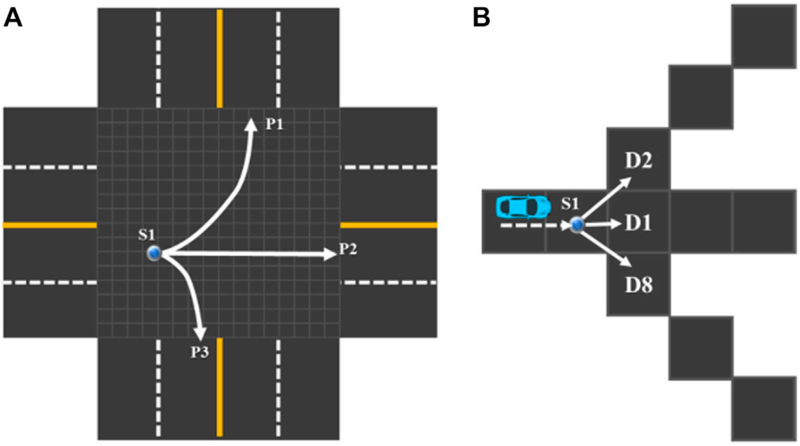

FIGURE 11 | The vehicle has multiple expected driving directions. **(A)** Vehicle with multiple expected driving paths. **(B)** Vehicle with multiple expected driving directions.

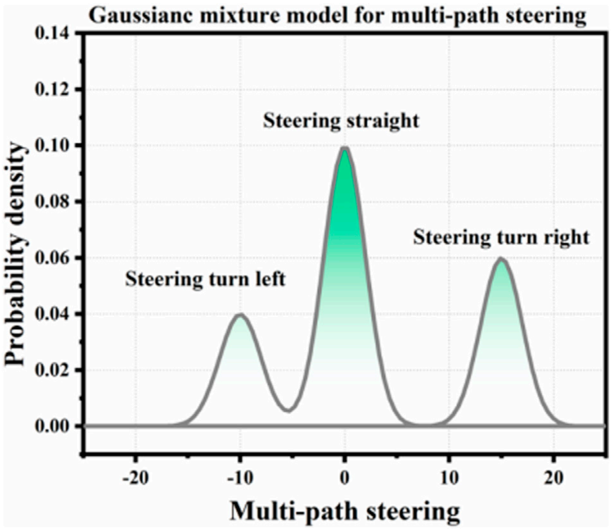

FIGURE 12 | Probability distribution of Gaussian mixture model corresponding to the steering angle.

Uncertainty can be considered as random error based on driving intention. As shown in **Figure 9**, the actual trajectory of straight vehicles is often not an absolute straight line but an up-and-down disturbance. In this article, Gaussian distribution is used to describe the uncertainty of driving process. The sample of distribution is the steering angle of the vehicle, that is, the deflection angle of the front wheel during steering. In this article, negative values are used to indicate left turn, while a positive value indicates a right turn. For example, −3 means 3° to the left, +3 means 3° to the right, and 0° means straight without deflection. For **Figure 9**, the corresponding steering angle distribution during driving is shown in **Figure 10**.

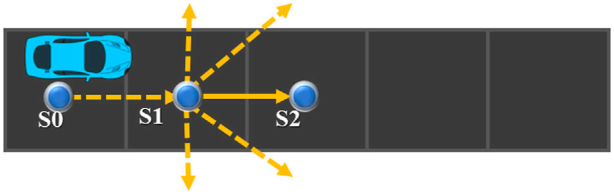

FIGURE 13 | Single expected driving direction.

There are two main reasons for describing the uncertainty of driving process with Gaussian distribution: 1) Gaussian distribution is a continuous distribution, and the steering angle which determines driving intention is taken as the distribution mean value, which can not only show the characteristics that the steering angle mainly changes around the mean value during driving but also allow the vehicle to deflect to any other direction, and the greater the deviation from the mean value, the smaller the probability. 2) Gaussian distribution is symmetrical about the mean, and its sampling probability on both sides of the mean is equal. This shows the randomness of driving deviation. As shown in **Figure 9**, the vehicle may shift above or below the centerline.

When the vehicle has only one expected path direction at the next moment, the steering angle distribution during driving from the current position to the next position can be described by Gaussian distribution, but there is often more than one expected path direction. This article uses Gaussian mixture distribution to deal with this situation. As shown in **Figure 11A**, when the vehicle is at S_1, there are three possible potential paths. Therefore, it is feasible to enter the next position from S_1 in three directions: D_2, D_1, and D_8. Let the probabilities in all directions be P_2, P_1, and P_8, and their specific values can be calculated by the method in the path probability allocation, in the previous section. Firstly, the steering angle distributions in the D_2, D_1, and D_8 directions are

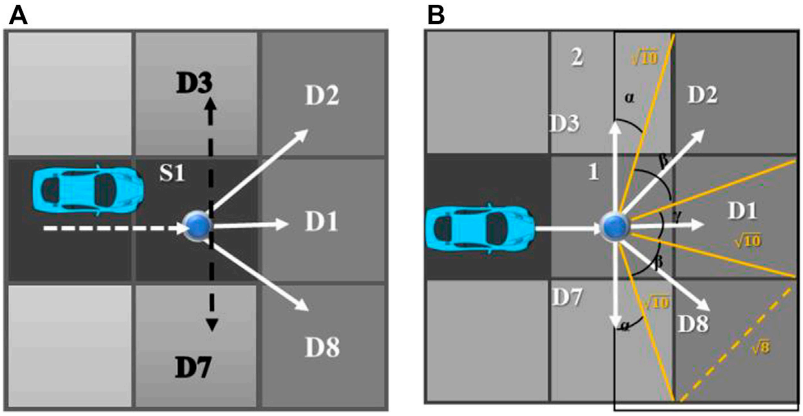

FIGURE 14 | Multiple expected driving directions and distribution angles. **(A)** Multiple expected driving directions. **(B)** Corresponding angle of expected driving direction.

modeled, and the corresponding deflection angles are, respectively, μ_2, μ_1, and μ_8. The variance of the corresponding Gaussian distribution is σ_2, σ_1, and σ_8, so the steering angle Gaussian mixture model in the next period from S_1 is shown as follows, with its corresponding distribution graph shown in **Figure 12**:

$$\begin{cases} P(X) = P_2 G(\mu_2, \sigma_2) + P_1 G(\mu_1, \sigma_1) + P_8 G(\mu_8, \sigma_8) \\ 1 = P_2 + P_1 + P_8 \end{cases} \tag{4}$$

Although the probability is assigned to each expected path (the sum of the probabilities of each path is 1), this result cannot be directly used to measure the probability of vehicles traveling in all directions. Because under this result, the probability of the vehicle traveling beyond the expected direction is 0. As shown in the following figure, theoretically, there is only one expected S_2 direction in **Figure 13**, but in practice, the vehicle may still drive up to the light blue position. Combined with the uncertainty of driving process, this article uses the steering angular distribution function to calculate the driving probability of vehicles in all directions.

As shown in **Figure 14A**, when the vehicle is located at S_1, there are three possible paths, namely D_2, D_I, and D_8. However, due to the uncertainty of the driving process, there is a certain probability that the vehicle will drive in the D_3 and D_7 directions. As shown in **Figure 14B**, taking the 180-degree visual field in the front direction as all possible driving directions, the corresponding angles of D_1, D_2, D_8, D_7, and D_3 are α, β, and γ. If the side length of the cell square is 2, then $\sin\alpha = 1/\sqrt{10}$, $\alpha = \arcsin(1/\sqrt{10})$ The (radian) angle is about 18.4° (−90° to −72°, 72°–90°). According to the cosine formula of a triangle, $\beta = \arccos(a^2 + b^2 - c^2/2ab)$, then $\beta \approx 0.93$; it is about 53.1° (−72° to −19°, 19°–72°).

According to α, β, there is $\gamma \approx 0.66$, which is about 38° (−19°, 19°). After calculating the values of α, β, and γ, combined with the probability density function of Gaussian mixture distribution, the corresponding probability areas at different angles can be obtained, which can be used as the probability of the vehicle traveling in this direction.

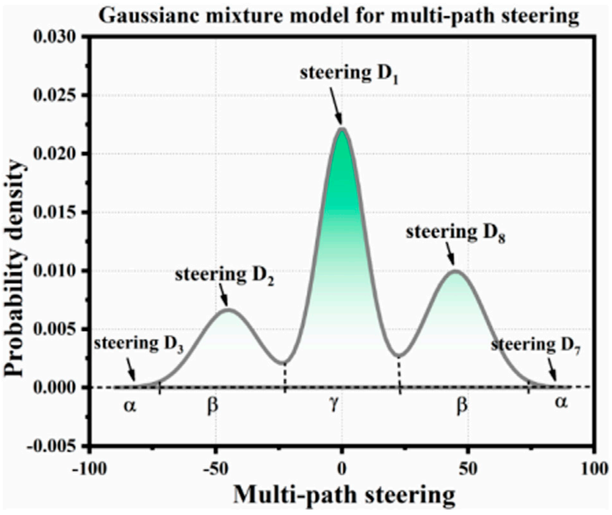

FIGURE 15 | Steering unmixing Gaussian distribution function image.

According to the above calculation results, the value of β is larger than α and γ, which is because the direction angles of D_2 and D_8 are larger than those of D_1, D_3, and D_7 in this scheme. The values of α, β, and γ can be adjusted according to the actual situation, or the variance value can be adjusted in the corresponding Gaussian distribution, to correct the probability of vehicles traveling in all directions. Generally speaking, the values of α, β, and γ and the variance of Gaussian components corresponding to each direction can be set as required or can be obtained by simulation and statistics according to the real situation. Let the probabilities of the preset directions D_2, D_1, and D_8 in **Figure 14A** be 0.2, 0.5, and 0.3, respectively, in which the variance of Gaussian distribution in D_1, D_3, and D_7 is 1.5, and the variance of Gaussian distribution in D_2 and D_8 is 2. The values of the corresponding steering distribution and the corresponding distribution of α, β, and γ are shown in **Figure 15**. In this

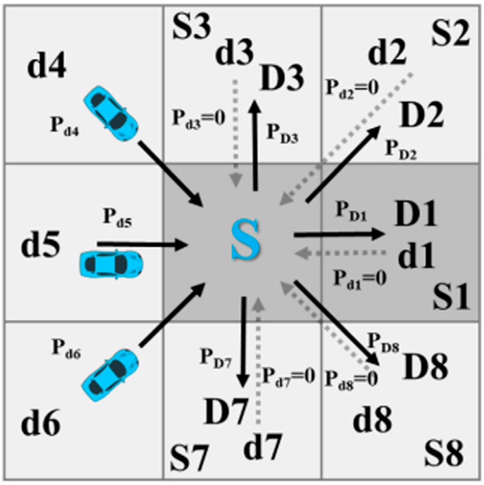

FIGURE 16 | Entering and leaving a cell in multiple directions.

example, the probability areas in the D_3 and D_7 directions corresponding to angle A are very small, so they are almost invisible in the figure.

Since the vehicle may enter a certain cell (position) from any direction, the probability of the vehicle arriving at a certain cell at time t is the sum of the probabilities of entering the cell in all directions, which can be used for the evaluation of the later collision risk. When the vehicle arrives at the $t+\Delta t$ time position from the t time position, its probability calculation includes two steps: 1) based on the direction of the vehicle entering the current cell at time t, the probability of entering the next cell from this direction is calculated. In this calculation, firstly, we were required to establish the steering distribution based on the driving direction, and then use the steering distribution to calculate the probability of going to the next cell and multiplying it with the probability of entering the cell at t time. 2) Iterative calculation, always entering the current cell in all directions and driving into the next cell at $t+\Delta t$, and accumulating all the probabilities of reaching a certain cell at $t+\Delta t$ to obtain the final probability of entering the cell at $t+\Delta t$.

As shown in **Figure 16**, if the vehicle could enter s from d_4, d_5, and d_6 directions at time t and their respective probabilities be P_{d4}, P_{d5}, and P_{d6}, the final probability of the vehicle reaching s at the moment of anti-engraving is $P_s = P_{d4} + P_{d5} + P_{d6}$, which in calculating the position and probability of time $t+\Delta t$ is according to the calculation steps introduced above:

1) Firstly, based on the situation that the vehicle enters s based on d_5 direction, the expected driving direction of the vehicle at $t+\Delta t$ time is only D_1 and the expected deflection angle of the vehicle when entering s from d_5 and leaving along D_1 is 0°. Therefore, the steering distribution of the vehicle in this case is a single Gaussian distribution with a mean value of 0. Let the standard deviation of the Gaussian distribution be assumed to be 16 (which can be set according to actual statistical results or simulation results in specific application), then the steering distribution of t time entering s along d_5 and $t+\Delta t$ time leaving s along D_1 is shown in **Figure 17**. Under this distribution, the probability distribution of vehicles leaving S along D_1, D_2, D_8, D_3, and D_7 is the probability area of the steering distribution at the corresponding angles (the angles corresponding to each direction have been calculated and explained in the previous section), which is calculated as $P_{d1} \approx 0.765$, $P_{D2} = P_{D8} \approx 0.118$, and $P_{D3} = P_{D7} \approx 0$. Here, the sum of P_{D1}, P_{D2}, and P_{D8} is greater than 1 due to rounding, not calculation error. The value of P_{D3}, P_{D7} is 0 because of the limited calculation accuracy. Theoretically, their values are all greater than 0. Based on the above results, it can be obtained that the probability of the vehicle entering S from d_5 at t time and entering S_1 at $t+\Delta t$ time is $P_{S1} = P_{d5} \times P_{d1}$; the calculation of S_2, S_8, S_3, and S_7 is entered and then analogized to $P_{si} = P_{di} \times P_{Di}$.

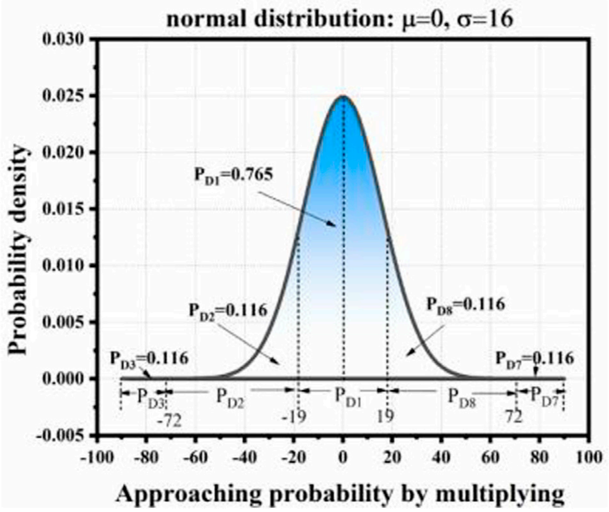

FIGURE 17 | Gaussian distribution of vehicles when D_5 enters D_1 and leaves. and leaving along D_1 direction, which corresponds to P_{D1} in the previous example.

2) Because it is possible for a vehicle to enter S from d_4, d_5, and d_6, the probabilities of entering S_1 at $t+\Delta t$ are calculated in these cases, the probability of the vehicle at S_1 at $t+\Delta t$ is the cumulative sum of the probabilities in all cases, $P_{S_1}^{t+\Delta t} = \sum P_{(S,di)}^{t} P_{Dj}^{di}$, where $P_{S_1}^{t+\Delta t}$ means the probability of reaching S_1 at time $t+\Delta t$, $P_{(S,di)}^{t}$ indicates the probability of reaching S along di direction at time t, which corresponds to P_{d5}, P_{d4}, and P_{d6} in **Figure 16**. In the above example, P_{Dj}^{di} indicates the probability of entering S along the di direction.

Combining the above two calculation steps, based on the uncertainty of path planning and driving process, the probability formula of the vehicle arriving at S at t time is as follows $P_S^t = \sum_{i=1}^{8} P_{di}^t$. The result can be used to evaluate the risk of collision at time t and position S. At $t+\Delta t$, the probability of the vehicle arriving at Sj is as formula, P_{Dj}^{di} is the path probability according to the planned path, the steering distribution of driving vehicles leaving S at time t is obtained, and then the probability area of the corresponding direction is obtained by using the distribution function.

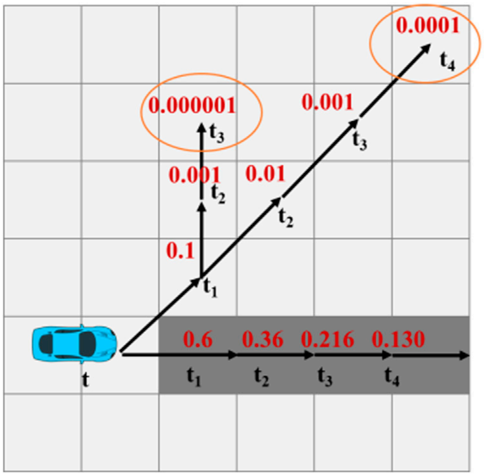

FIGURE 18 | Very low probability value of unexpected direction.

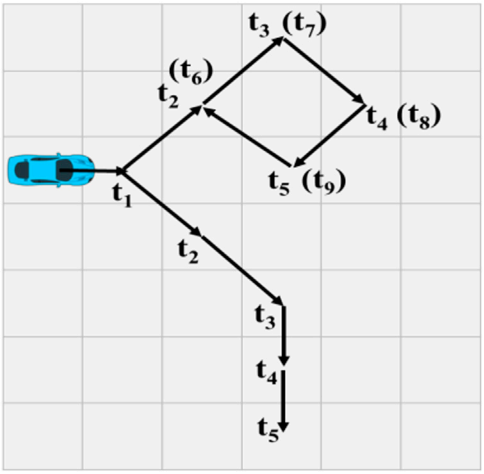

FIGURE 19 | Vehicle running in loop.

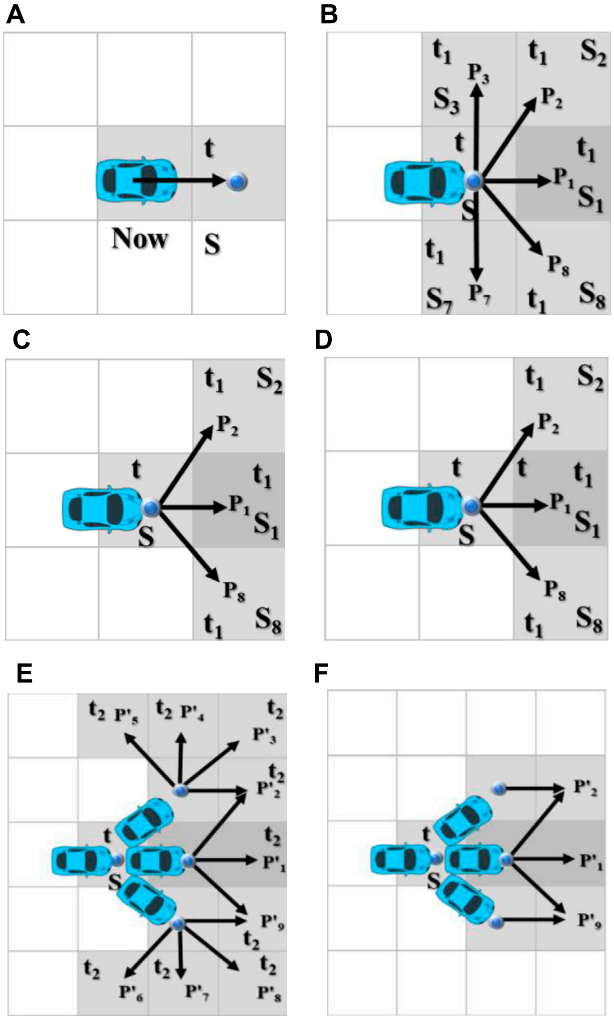

FIGURE 20 | Pruning and truncation of vehicle running probability. **(A)** *t* time entry diagram. **(B)** All feasible directions at t_1. **(C)** Feasible direction after pruning at t_1 time. **(D)** Possible position at t_1. **(E)** All feasible directions at t_2. **(F)** Feasible directions after pruning at t_2.

In theory, vehicles can travel to any position in any direction, which not only makes trajectory prediction difficult but also increases the amount of calculation greatly. However, through analysis, it can be found that most of the calculations are at a very low level of probability. Therefore, this part of the calculations is almost meaningless to the final risk assessment and can be optimized by probability pruning and truncation (to reduce the calculation amount and improve calculation efficiency). As shown in **Figure 18**, dark green is the expected driving direction of the vehicle, that is, the planned path direction, while the other directions are unexpected driving paths caused by the uncertainty of driving process. If the probability of driving from the current cell to the next cell on the expected path decreases by 0.6 times, the probability of reaching a specific cell from t_1 to t_4 becomes 0.6, 0.36, 0.216 and 0.130, respectively. These probability values correspond to the most likely driving path of the vehicle, which is very valuable for risk assessment. However, under the other two paths, the probability value decreases exponentially and quickly drops to a very low level, such as 0.0001 > 0.00001, etc., and the probability value will only be lower after further calculation. In theory, the probability value of reaching any position at any time will be very low but not zero, but the probability value below a certain level is almost meaningless for practical application. If a collision probability of 0.00000000001 is evaluated, it can be almost considered that the collision will not occur. In this article, the threshold R_{low} is set as the minimum value of probability pruning truncation. When R_{low} is less than or equal to, the calculation will be cut off to reduce the amount of calculation. As shown in **Figure 18**, it can be set that when the probability of the vehicle arriving at s = 0.0001, the probability of leaving from S and arriving at the new cell at *t*5 will no longer be calculated.

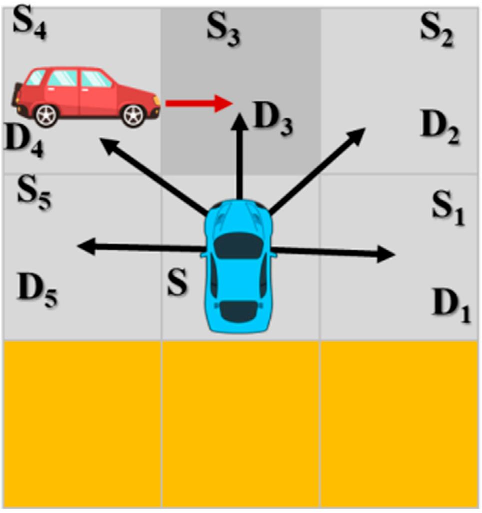

FIGURE 21 | Example of trajectory intrusion.

Probability truncation can not only reduce the amount of calculation but also avoid many meaningless calculations. As shown in **Figure 19**, the expected path of the vehicle is marked by dark green, but it is possible for the vehicle to enter the upper right cell at t_2 under the driving process uncertainty. Then, under the influence of driving process uncertainty, the vehicle may form a circle along the diamond; as shown in the figure, the gray arrow indicates the direction. This situation can continue indefinitely with the expansion of the time window, but under normal circumstances, almost no driver will drive the vehicle around the intersection.

A direct manifestation of probability truncation is that the sum of probabilities of vehicles arriving at all positions at time t is less than 1 (without considering the loss of calculation accuracy and rounding), and the value of probability sum will gradually decrease with time. As shown in **Figures 20A–C**, the vehicle enters S at time t along the straight direction, theoretically departs from S, and reaches S_i, S_2, S_3, S_8, and S_7 at t_1. Let the probability be P_1–P_8. If only S_L, S_2, and S_8 are left to reach after probabilistic pruning, then the sum of probabilities of vehicles arriving at each feasible position at t_1 is the sum of P_1, P_2, and P_8, which is obviously less than the sum of P_1–P_8 and less than 1, which is the probability loss caused by pruning and truncation. Furthermore, the theoretically accessible positions at t_2 and S_1, S_2, and S_8 are shown in **Figure 20E**. After pruning, only the cells as shown in **Figure 20F** are left. The probability values of all accessible positions of the vehicle at t_2 are also determined by P_1'–P_8'. The sum becomes P_1', P_2', and P_9'. In addition, there is a probability loss. The loss of probability can be understood as the cost of precision due to reducing the amount of calculation.

The uncertainty of driving intention and driving process mainly aims at the uncertainty of vehicle interior and driver, while the uncertainty of trajectory invasion focuses on the impact of real-time change of the external environment on vehicle trajectory. When obstacles (possibly, motor vehicles, bicycles, motorcycles, pedestrians, suddenly dropped goods, etc.) intrude into the expected driving position of the vehicle, the vehicle will be forced to respond, such as make detours and stops, all of which will change the vehicle's trajectory and thus change the time, location, and probability of collision with the vehicle.

In this article, we define trajectory intrusion from two aspects of time and space. In time, it includes the current time or future time in the time window. In space, it refers to the position where the current or future time of the obstacle overlaps with the possible entry position of other vehicles. As shown in **Figure 21**, if the other vehicle is located at s at the current moment, it may drive along D_1, D_2, D_3, D_4, and D_5 directions. The barrier is located at S_4, and it could be heading for S_3 at the next moment. When other vehicles drive into S_4 from S along the direction of D_4 because the position of obstacles at the current moment overlaps with the possible driving position of other vehicles at the next moment, the track of the other vehicles at S_4 is invaded at the next moment. When other vehicles enter S_3 from S along the direction of D_3, it is possible to drive into S_3 at the next moment due to obstacles. Therefore, the track of its car in S_3 is also invaded at the next moment. In short, if the obstacle is located at A at the moment, and if other vehicles drive to A at the next moment, then A is considered as a trajectory intrusion; if the obstacle and other vehicles are likely to drive to point B at the next moment, then point B is also a trajectory intrusion. In some special cases, such as different rights of way classes between vehicles, it can be considered that the tracks of vehicles with a higher right of way will not be invaded because they enjoy the right of way. At this time, only the tracks of vehicles with a lower right of way are invaded.

When encountering the track invasion, the actions taken by the vehicle is to stop and wait, that is, the vehicle stays still at the current position until the obstacles leave and then resumes driving, or detour, that is, the vehicle does not stop but travels in a nonintrusive direction to bypass the obstacle. Trajectory intrusion changes the route of vehicles, and the route and its probability are determined by path planning and steering distribution. Therefore, the trajectory intrusion will change the original steering distribution of the vehicle and the probability of driving along each direction. When a vehicle enters the next cell with a probability greater than the cutoff probability, it may be necessary to delete or add new paths and reallocate the probability of each path. So, trajectory intrusion uncertainty modeling should be combined with path planning and steering distribution to quantify different situations.

Here, the probability of obstacles reaching the intrusion position is taken as the rejection rate, and the steering distribution is regenerated by the rejection sample. As shown in **Figure 22A**, at time t, other vehicles are located at S, obstacles are located at S_4, and obstacles may be located at S_3 at the next time. S_4 and S_3 are both the positions where the tracks of other vehicles are invaded at the next moment. Let it have three expected driving directions, say D_2, D_3, and D_4 and the distribution probabilities of the three expected paths are $P_{D4} = 0.3$, $P_{D3} = 0.5$, and $P_{D2} = 0.5$, respectively, and their steering distribution is shown in **Figure 22B**. It can be seen that the probability areas in the D_3 and D_4 directions are large and the driving process in the D_4 direction is uncertain, so the Gaussian

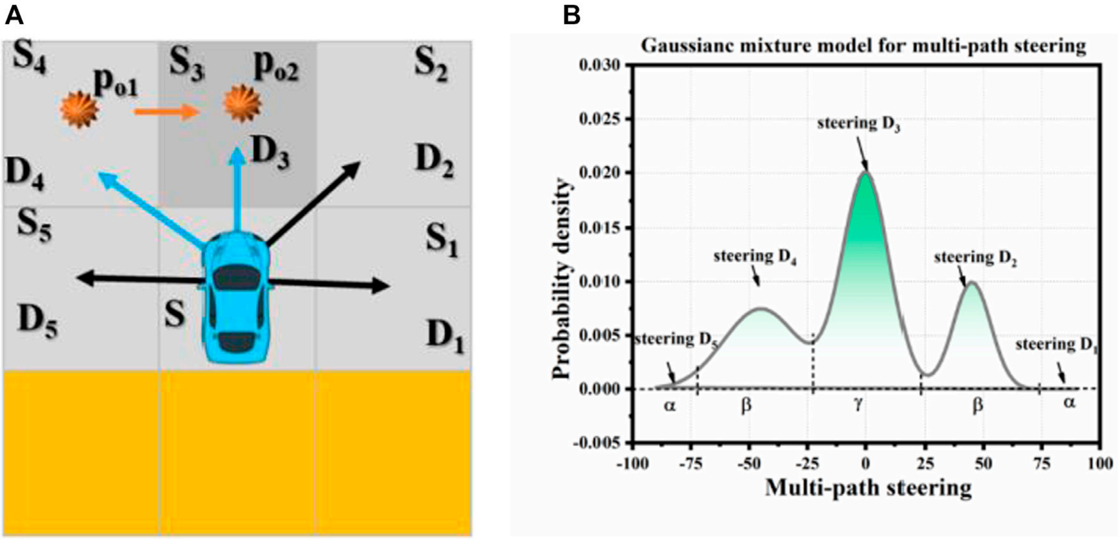

FIGURE 22 | Obstacle intrusion and original steering distribution of vehicles. **(A)** Expected driving direction of vehicles and position of obstacle intrusion. **(B)** Original steering distribution of vehicles.

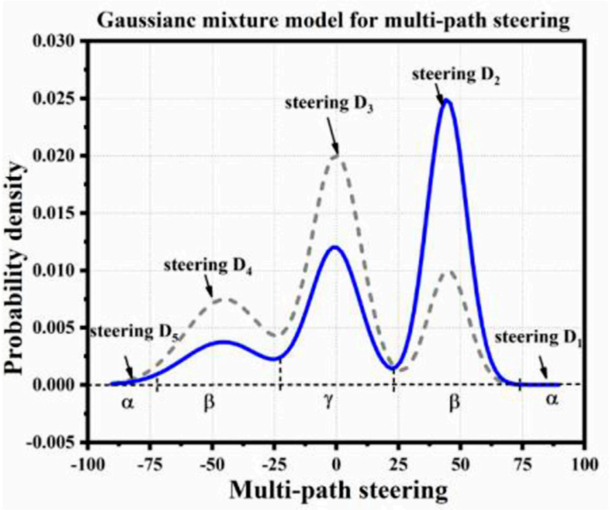

FIGURE 23 | Newly generated steering distribution after rejecting sampling.

distribution variance in the steering D_4 area is large, and it is "stout" on the graph. D_5 and D_1 are not preset directions, therefore, the corresponding probability area is small, and the eye flesh is almost invisible.

Let the probabilities of obstacles reaching S_4 and S_3 at time *t* be $P_{01} = 0.7$ and $P_{02} = 0.6$, respectively, and P_{01} and P_{02} are D_4, sampling steering with rejection rate in the D_3 direction, and relearning steering distribution with sampled samples as shown in **Figure 23**. In the figure, the red dotted line indicates the steering distribution before rejecting sampling, and the blue solid line indicates the new steering distribution learned after rejecting sampling. It can be seen from the figure that the probability areas in the D_4 and D_3 directions decrease to a certain extent, while the probability areas in the D_2 direction increase greatly. The probability areas in D_1 and D_5 directions increase slightly.

Although the new steering distribution can be obtained by taking the probability of obstacles reaching a certain position as the rejection rate, the simulation test shows that the discrimination between many new distributions and the old distributions is not obvious enough. As shown in **Figure 24**, let the arrival probabilities of obstacles in **Figure 24A** be $P_{01} = 0.3$ and $P_{02} = 0.2$, and the distribution probabilities of vehicles along the planned paths D_4, D_3, and D_2 before sampling rejection be $P_{D4} = 0.3$, $P_{D3} = 0.5$, and $P_{D2} = 0.2$. With P_{01} and P_{02} as rejection rates, the obtained steering distribution after sampling is shown in **Figure 24B**, and the curve difference between before-sampling and after-sampling is not obvious. Especially, along the D_3 direction, the probability of the vehicles entering is hardly affected by obstacles, but in fact, $P_{01} = 0.3$ and $P_{02} = 0.2$ are already relatively high probability values. This shows that it is not enough to show the influence of obstacles on the driving track by directly using the probability of arrival of obstacles as the rejection rate. In this article, it is considered that squeeze operation can be performed according to a certain mapping rule P_{oi}, to realize the influence of obstacles on the vehicle trajectory.

The squeeze mode can be flexibly selected according to the situation. For example, the analytic equation of a circle can be the squeezed function, and the value curve of P_{oi} can be extruded into the circular arc shape. As shown in **Figure 25A**, the red straight line is the original P_{oi}, according to the equation of circle, $(x - 1)^2 + y^2 = 1$ $y = \sqrt{(1 - (x - 1)^2)}$. The rejection rate after Squeeze is shown as the blue curve. **Figure 25B** shows the steering distribution generated by the rejection rate sampling after squeeze, which shows that the distribution difference is more obvious. Except for the equation of the circle, other functions that map P_{oi} to the range of 0–1 can be used as squeeze functions, such

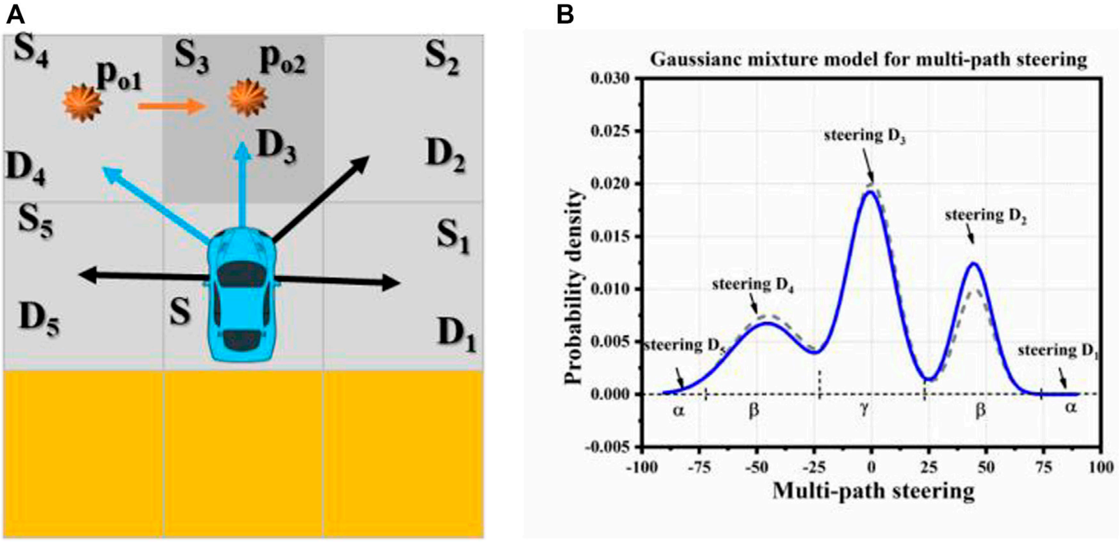

FIGURE 24 | There is no obvious difference in the distribution of new and old steering. **(A)** Expected driving direction of vehicles and position of obstacle intrusion. **(B)** New and old steering distribution.

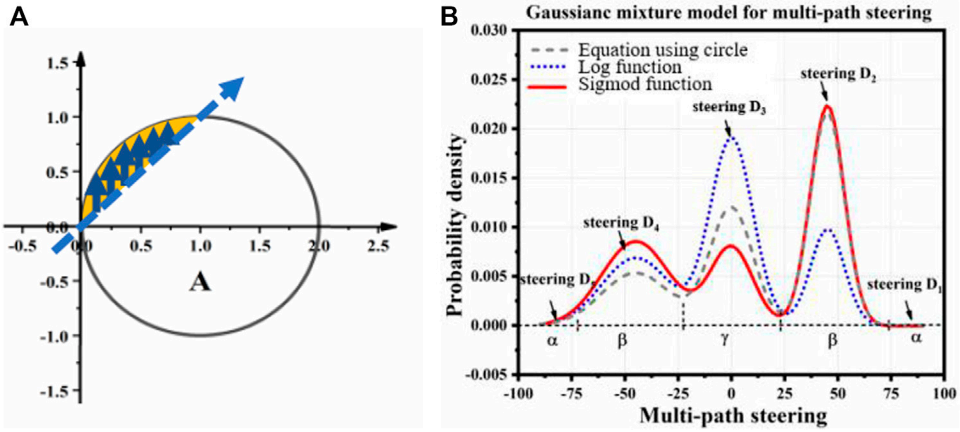

FIGURE 25 | Squeeze the arrival rate of obstacles to get the rejection rate. **(A)** Squeeze the equation of a circle **(B)** Squeeze the steering distribution.

as deformed log function, logistic function, sigmoid function, etc., and the rejection rate is amplified in different ways by different functions. To influence the new steering distribution.

It is also a common in driving to choose to stop when facing obstacles, so it is necessary to allocate probabilities between stopping and detouring. Let Δt be the time of iterative calculation of risk assessment, P_{wait}, P_{bypass}, then there is $1 = P_{wait} + P_{bypass}$, indicating that it is possible for other vehicles to stop moving in the next time. In reality, the probability of stopping is related to the distribution of obstacles. If the possibility of obstacles invading the track is high or more positions in the track are invaded by obstacles, the possibility of stopping and so on will increase accordingly. As shown in **Supplementary Figure S1**, there are five possible driving directions within the visual field of other vehicles 180, and the probability of each direction can be obtained from the steering distribution before it refuses to sample, which is set as P_{D1}–P_{D5}. In extreme cases, these five directions may be invaded by obstacles. Let the invasion probability be P_{01}–P_{05}. If the values of P_{01}–P_{05} are all 1, it is determined that the vehicle will be surrounded by obstacles at the next moment, then the probability of the vehicle stopping at this time is 1 to ensure driving safety. If the values of P_{01}–P_{05} are all 0, it is determined that no obstacle will invade the trajectory of the other vehicles at the next moment. Then, the probability of the vehicle stopping should be 0, which accords with the driving habits of people. Because P_{D1}–P_{D5} are calculated from the same steering distribution, there are $1 = \sum_{i=1}^{5} P_{Di}$. However, P_{01}–P_{05} may be invaded by five different obstacles, so there are $5 = \max \sum_{i=1}^{5} P_{oi}$ because there must be $0 \le P_{wait} \le 1$, where P_{wait} can be calculated from the weighted sum of P_{01}–P_{05}, and the calculation formula is $P_{wait} = \sum_{i=1}^{5} P_{Di} P_{oi}$, corresponding to $P_{bypass} = 1 - P_{wait}$.

The overall flow chart of calculation framework is shown as **Supplementary Figure S2**.

4 CALCULATION AND SIMULATION RESULTS

In this section, the calculation and simulation process are illustrated in the form of images. The simulation and verification are done using MATLAB and evaluated and verified using PreScan + CarSim. The calculation results show that the uncertain trajectory of interactive vehicles at intersections can be better predicted and analyzed, and the collision avoidance decision of unmanned vehicles can be better realized.

As shown in **Supplementary Figure S2A**, let us assume that there are three vehicles under the intersection at time *t*, namely, ego-vehicle and other vehicles v_1 and v_2; let us assume that there are general social vehicles with the same right-of-way level. **Supplementary Figure S3B** combines the sensing information of the sensing module. The driving intention uncertainty modeling method is used to plan the possible driving routes of other vehicles. Assume that the planning result is that the auto-driving vehicle v_L has three possible paths, which correspond to turning around, turning left, and going straight, as shown in the green cell of **Supplementary Figure S3B**; V_2 has a possible path (to simplify the explanation process, assume only one path), and the corresponding straight path is shown in the purple cell of **Supplementary Figure S3B**. Combined with the vehicle regulation and control module, the driving track of the vehicle in the future is obtained as shown in the blue cell in **Supplementary Figure S3B**.

Enlarge the red circle in **Supplementary Figure S3B** as shown. Before v_l reaches S, the three paths coincide, so the vehicle has only one expected heading direction. From time *t* to time t_1, the possible driving direction of v_l is shown in **Supplementary Figure S4A**, in which orange indicates the expected driving direction and blue indicates the unexpected but feasible direction. At this time, the steering distribution of v_l is a single Gaussian distribution. Let the variance of the Gaussian distribution be 12 when v_l goes straight, and its steering distribution is shown in **Supplementary Figure S4B**. According to the previous introduction, if the steering angle is greater than 0, it means turning right, less than 0 means turning left, and equal to 0 means going straight, including α_3~(90°, −72°), α_2~(72°, −19°), α_1~(19°, 19°), and $P_1 = 0.887$, $P_2 = 0.057$, $P_8 = 0.057$ by using the distribution probability area. the probability of taking values of P_3 and P_7 is extremely small. Below 10^{-9}, pruning and truncation according to probability can be ignored. Therefore, the possible position and probability of t_l time v_l are shown in **Supplementary Figure S4C**, and the dark shaded area is the unreachable area after probability pruning.

Since V1 may enter the unexpected paths as S2 and S8, it is necessary to replan the trajectory of V1 synchronously. At the end of t1, the three possible positons of V1 should be calculated at t_2. **Supplementary Figures S6A–C** show the possible driving directions of v_l at t_2 when it is located in three positions. Pay attention to the red S position, which may enter from three different directions by v_l. They are from S_2 to the right, S_8 to the left, and S_1 straight. At this time, the probability of v_l finally entering S at t_2 should be calculated according to the probability accumulation introduced above. The steering distribution at S_2, S_8, and S_1 is as shown in **Supplementary Figure S6B**, which shows that the probability of entering s from S_2 is $p = 0.057 \times 0.057$˜0.0032. The first 0.057 is the probability of arriving at S_2 at t_1, and the second 0.057 is the probability of arriving at s from S_2 at t_2. Similarly, the probability of entering S from S_8 is 0.0032. The probability of entering S from S_1 is $p = 0.887 \times 0.887$˜0.787. Here, if the truncation probability is 0.01, then 0.0032 is discarded directly because the value is too small, so the probability of reaching s is about 0.787.

From a macro point of view, after considering the uncertainty of driving process based on driving intention uncertainty, some new v_l possible positions are added, as shown in bright green in **Supplementary Figure S7**. The turning direction and right turning direction plan out a new driving path, and in the straight direction is finally unified to the original path. This describes that there are random left and right offsets in the straight line, but under the intention of going straight, the ego-vehicle quickly corrects the offset and returns to go the straight line.

Suppose V_L is located at s at a certain time, and there are no obstacles in all directions of travel at the next moment. The steering distribution at s is shown in **Supplementary Figure S8**. There are three expected driving directions, namely, the probability in D_2 direction is P_2, the probability along D_1 direction is P_2, and the probability of driving along D_8 direction is P_8. And we know the expectation of the Gaussian component in the straight direction is $\mu_1 = 0°$, α_2, α_8 direction is $\mu_2 = -45°$, $\mu_8 = -45°$. There are $P_2 = 0.3$, $P_1 = 0.5$, and $P_8 = 0.2$. At this time, the steering distribution Gaussian mixture model corresponding to V_L is shown in **Supplementary Figure S8B**, and it is assumed that the random offset of the vehicle going straight is small, and the variance of the D_1 direction component is $\sigma_1 = 6$. The random deviation of D_2 driving in the turning direction is slightly larger, $\sigma_2 = 8$. The shift of d_8 in the right turn direction is larger than that in D_8, $\sigma 3 = 10$. In this case, $P_{D2} = 0.300$, $P_{D1} = 0.500$, $P_{D8} = 0.198$, and the probability of the other directions is lower than the truncation probability and ignored.

Finally, the driving situation of V_L when encountering obstacles is considered. As shown in **Supplementary Figure S9**, the vehicle is located at s at time *t*, and it is possible for the vehicle to go to S_2 at time t_1, and it is possible for vehicles with obstacles to go to S_2 at time t_1. At this time, the possible trajectory evolution of V_L is shown in **Supplementary Figure S10**.

5 CONCLUSION

Crossroads are one of the most complex and difficult driving scenarios for autonomous driving. This article proposes a collision risk assessment framework for unmanned vehicles based on the prediction of other vehicles' driving trajectories with driving uncertainty. The framework is used to calculate the collision risk, collision position, and time between the vehicle and other vehicles in real time under the complex traffic environment of intersections, and the results can give more safe decision to optimize the driving trajectory of the vehicle. The results can also trigger other safety algorithms of the vehicle in case of emergency such as collision avoidance.

Through analysis, this method highlights that vehicle collision risk assessment lies in the prediction of other vehicles' driving track, which is mainly affected by road geometry, driver's driving intention, driver's operation, and vehicle control system's ability and traffic environments. Among them, there are large uncertainties, except the geometric features of roads, which are the difficulty of unmanned vehicles. In this article, the characteristics of three kinds of uncertainties and their relationship with other vehicles' driving tracks are analyzed in depth. Different modeling methods are proposed for each kind of uncertainty which is quantitatively described by probability. Finally, the calculation process of the three kinds of uncertainties is unified so as to obtain the time-related collision risk assessment framework of unmanned vehicles. The risk assessment framework can provide safer trajectory planning and collision avoidance input constraints for unmanned vehicles. Thereby, this will be improving the overall safety of unmanned vehicles greatly.

DATA AVAILABILITY STATEMENT

The original contributions presented in the study are included in the article/**Supplementary Material**; further inquiries can be directed to the corresponding author.

AUTHOR CONTRIBUTIONS

The main contribution of this article is to develop a framework based on collision risk assessment for unmanned electric vehicles in unknown environment. This method predicts the environment along the preplanned driving track and analyzes the uncertainties in the driving process. It includes the solutions to other vehicles' expected path planning, driving process uncertainty description, and trajectory change caused by obstacle intrusion, etc. Through the analysis, modeling, and calculation of uncertainty, the prediction of other vehicles' running track based on probability is realized. The risk probability of collision is evaluated based on other vehicles' running track. This result can be input to the decision control module for correcting or changing the running track of the own vehicle and can also trigger other safety algorithms of the own vehicle such as collision avoidance when necessary. Moreover, ensure vehicle safety to the greatest extent along with better driving efficiency.

SUPPLEMENTARY MATERIAL

The Supplementary Material for this article can be found online at: https://www.frontiersin.org/articles/10.3389/fenrg.2022.888298/full#supplementary-material

REFERENCES

Chen, H., and Yu, H. (2019). Research on the Algorithm of Dynamic Obstacle Avoidance Path Planning for Unmanned Vehicles Based on Potential Field Search [J] (In Chinese). *Beijing Automot.* 000 (004), 131

Gianibelli, A., Carlucho, I., and Paula, M. D. (2018). "An Obstacle Avoidance System for Mobile Robotics Based on the Virtual Force Field Method[C]," in IEEE Biennial Congress of Argentina (Argencon 2018. Ieee).

Hsu, D., Lee, W. S., and Rong, N. (2008). A Point-Based POMDP Planner for Target Tracking, ICRA 2008," in Robotics and Automation IEEE International Conference on, 2644

Li, H., Deng, J., Feng, P., Pu, C., Arachchige, D. D. K., and Cheng, Q. (2021). Short-Term Nacelle Orientation Forecasting Using Bilinear Transformation and ICEEMDAN Framework. *Front. Energy Res.* 9, 780928. doi:10.3389/fenrg.2021.780928

Li, H., Deng, J., Yuan, S., Feng, P., and Arachchige, D. D. K. (2021). Monitoring and Identifying Wind Turbine Generator Bearing Faults Using Deep Belief Network and EWMA Control Charts. *Front. Energy Res.* 9, 799039. doi:10.3389/fenrg.2021.799039

Lulu, H., Xie, H., Kang, S., and Yan, L. (2021). Trajectory Prediction Algorithm of Unmanned Vehicles at Urban Intersection Based on Edge Computing[J]. *J. Automot. Saf. Energy* 12 (2), 163.

Ponzoni Carvalho Chanel, C., Teichteil-Knigsbuch, F., and Lesire, C. (2012). "POMDP-based Online Target Detection and Recognition for Autonomous UAVs," in ECAI 2012 20th European Conference on Artificial Intelligence, 955

Ragi, S., and Chong, E. (2013). UAV Path Planning in a Dynamic Environment via Partially Observable Markov Decision Process. *IEEE Trans. Aerosp. Electron. Syst.* 49, 23972412. doi:10.1109/taes.2013.6621824

Rothmund, S. V., and Johansen, T. A. (2019). Risk-Based Obstacle Avoidance in Unknown Environments Using Scenario-Based Predictive Control for an Inspection Drone Equipped with Range Finding Sensors." in International Conference on Unmanned Aircraft Systems. ICUAS. doi:10.1109/icuas.2019.8797803

Shalev-Shwartz, S., Shammah, S., and Shashua, A. (2017). *On a Formal Model of Safe and Scalable Self-Driving Cars[J].*

Wang, Fei., and Huang, He. (2021). Research on Genetic Algorithm Based Anti-collision Control Strategy for Unmanned Vehicles[J]. *Mod. Electron. Technol.* 44 (9), 136-139

Wang, Y., Zhao, S., and Wang, X. (2019). "A Novel Collision Avoidance Method for Multiple Fixed-Wing Unmanned Aerial Vehicles[C]." in 2019 Chinese Automation Congress. CAC.

Xu, G., and Zong, X. (2019). A Research on Intelligent Obstacle Avoidance of Unmanned Vehicle Based on DDPG Algorithm[J] (In Chinese). *Automot. Eng.* 41

Zhao, Y., Zheng, Z., and Zhang, X. (2017). "Q Learning Algorithm Based UAV Path Learning and Obstacle Avoidence approach[C]." in Chinese Control Conference. IEEE.

Conflict of Interest: The authors declare that the research was conducted in the absence of any commercial or financial relationships that could be construed as a potential conflict of interest.

Frontiers in Energy Research

BRIEF RESEARCH REPORT
published: 18 July 2022
doi: 10.3389/fenrg.2022.930999

E-Commerce Logistics System Based on Discrete Dynamic Modeling Analysis

Gaofei Meng *

Hebei Chemical and Pharmaceutical College, Shijiazhuang, China

The development of green logistics in a low-carbon environment is an important way for logistics companies to reduce operating costs, and it is also a strategic measure to strengthen the construction of ecological civilization. This study improves the bat algorithm for single-delivery express delivery and multi-delivery, determines the optimal target and seeks the optimal solution, establishes the optimal logistics distribution scheme combined with corporate profits, and finally, compares it with other algorithms to verify the feasibility of the model. In the same experimental environment, it is proven that the performance of the built model is about 20% higher than that of other methods, and the planned path is the most reasonable. In the future application of e-commerce logistics system, it is a more efficient, reasonable, and perfect discrete logistics model.

Keywords: low-carbon environment, energy conservation and emission reduction, e-commerce, logistics system, discrete dynamic modeling, bat algorithm

Edited by:
Xun Shen,
Tokyo Institute of Technology, Japan

Reviewed by:
Gaurav Sachdeva,
DAV University, India
Sandeep Singh Nanglu,
Sri Sai Group of Institutes Badhani,
India

***Correspondence:**
Gaofei Meng
menggaofei1@163.com

Specialty section:
This article was submitted to
Smart Grids,
a section of the journal
Frontiers in Energy Research

Received: *28 April 2022*
Accepted: *30 May 2022*
Published: *18 July 2022*

Citation:
Meng G (2022) E-Commerce Logistics
System Based on Discrete Dynamic
Modeling Analysis.
Front. Energy Res. 10:930999.
doi: 10.3389/fenrg.2022.930999

INTRODUCTION

Under the influence of "Internet thinking," many industries have begun to establish connections with the Internet (Yong et al., 2019), of which the retail industry has the highest proportion of online sales. According to the statistics of the China Internet Network Information Center (CNNIC), by June 2019, the total number of online shopping users in China was 639 million, accounting for 74.82% in China, an increase of 2,870 compared with 2018 (Hafiz et al., 2020). Among them, the total number of mobile online shopping users was 622 million, accounting for 78.93% of China's mobile Internet users, an increase of 29.88 million from the end of 2018 (Wang et al., 2020). A large number of online purchases have generated a large number of express orders. According to the development data of China's express delivery industry during the "13th Five-Year Plan," the total order volume of China's express delivery industry will reach 70 billion person-times in 2020, and the per capita express delivery volume will rapidly increase from 0.01 person-time in 2,000 to about 50 person-time in 2020 (Asokan et al., 2020). In recent years, the profits of China's traditional manufacturing and offline retail industries have been greatly compressed by market competition. The first profit source theory expands profits by reducing labor costs and raw material costs that have achieved maximum profit growth, and the second profit source theory gradually narrows the gap between firms by increasing workers' labor productivity (Suganthi and Malathi, 2017).

Literature (Dantzig and Ramser, 2021) shows that online e-commerce reduces a large number of offline site, labor, maintenance and other costs, and is more competitive than offline site. Therefore, many enterprises choose to develop online business in order to reduce costs and obtain more profits. Among them, effective logistics services can ensure user experience while reducing costs. Therefore, driven by online business, logistics has gradually become closely related to people's lives. People can shop online through logistics and exchange goods through logistics. To a certain extent, the development of the logistics industry can reflect a country's modern technological level and economic globalization. The work of Chen et al. (2019) analyzes that the development speed of China's e-commerce logistics system has accelerated sharply in recent years. With the advent of the 5G era, major upstream companies have proposed the concept of "metaverse," which has stimulated the development of online e-commerce, and put forward views on the huge potential of China's logistics and express delivery industry in the future (Stodola, 2018). The work of Atefi et al. (2018) proposes that the logistics operation cost will not only affect the profits of e-commerce enterprises but also directly affect the user's purchasing experience, and then fundamentally affect the development of affiliated enterprises. Zhang and Chai (2010) pointed out that the market has gradually higher requirements for express delivery, and the transformation of the logistics system to fast, accurate, and low-cost distribution is an important issue that express delivery practitioners continue to solve.

Since most of the aforementioned studies are theoretical studies and no practical solutions have been proposed, this study, based on the development status of e-commerce logistics systems and combined with previous research results, aims at the unreasonable distribution routes and backward logistics and transportation system equipment in my country's e-commerce logistics systems. The lack of physical infrastructure construction and other issues, using mathematical models and big data computing methods conducted in-depth research. By establishing a fast logistics transportation scheduling model based on the discrete dynamic algorithm and optimizing it, the logistics system scheduling problem is optimized, and through simulation verification, the performance of the constructed e-commerce logistics system based on discrete dynamic modeling analysis is better than other methods, the planned path is the most reasonable, and the distribution route uses less resources.

RELATED RESEARCH

According to the relevant survey data in the past two years, the damage or loss of express packages has the greatest impact on users' logistics experience. Almost all respondents said that these are intolerable express problems. In addition, for some users who value the timeliness of distribution (accounting for about 90% of e-commerce logistics express users), the problem of untimely distribution is also one of the important problems affecting the experience (Cai et al., 2014). Therefore, the direction of enterprise express transformation is to ensure that the express can reach users safely under the condition of timeliness and control the corresponding cost to maximize profits. Through the unremitting efforts of relevant scientific researchers, at present, it is mainly through rational planning of express logistics and transportation scheduling scheme as an important way of transformation in this direction (Fachini and Armentano, 2020).

Express logistics transportation scheduling is mainly composed of path planning and vehicle scheduling. Therefore, researchers generally attribute the express logistics transportation scheduling problem to vehicle-routing problem (VRP) or vehicle-scheduling problem (VSP). In 1959, Dantzig and others proposed the vehicle-routing problem for the first time. Among them, the travel agency problem has attracted extensive attention of scholars, which is known as the most classic vehicle-routing problem. Subsequently, Christophe et al. proposed a tabu search algorithm to solve the vehicle path planning problem with Backhaul and time window. Petr et al. improved the ant colony algorithm for multi-site vehicle-routing problem and got a good application. Inspired by the genetic algorithm, atefi et al. applied an iterative local search algorithm to the tabu search algorithm, and proposed an improved genetic algorithm to solve vehicle-routing problem with a time window (Zheng et al., 2020). Li Yang and others put forward a two-stage mixed variable neighborhood search algorithm, which mainly solved the random demand vehicle routing problem based on the idea of optimizing and scheduling first, and proved the validity of the algorithm (Zhang et al., 2019) in the experimental simulation. On the whole, through the strategy of reducing the cost of labor and vehicles, scholars at home and abroad have paid high attention to the field of vehicle routing and planning (Bayzid and Warnow, 2018).

MATERIALS AND METHODS

Research on Discrete Bat Algorithm for Single Distribution Express Logistics Transportation Scheduling Problem

The single-delivery express logistics transportation scheduling problem is the most simplified case in the express logistics transportation scheduling problem. Under the premise that the number of warehouses is unique, the courier completes the distribution task of the corresponding user through the shortest distance, and finally returns to the path planning problem of Knight cargo hold (Wang, 2016). On the whole, the single-delivery express logistics transportation scheduling problem is basically similar to the classical traveling salesman problem. As for the traveling salesman problem, in the express logistics transportation scheduling problem, it has been studied for a long time and in great depth. The overall solution algorithms roughly fall into the following two categories: one is to design an optimized local heuristic search algorithm based on the characteristics of the traveling salesman problem. The other is the heuristic intelligent algorithm designed according to the penalty of the problem-type. The advantage of the local heuristic algorithm is that it can quickly solve the traveling salesman problem with a large number of cities. However, because its starting point is the characteristics of traveling salesman problem, its algorithm design accounts for a large proportion in solving the problem (Fan, 2019). Therefore, it has few applicable problem types, and it is easy to fall into local optimization in the calculation process, so it is unable to find the optimal value of the overall problem, Representative algorithms include 2-OPT and 3-OPT. Heuristic intelligent algorithms are more combined with big data technology and corresponding computing thinking of other disciplines, such as fireworks algorithm, genetic algorithm, immune algorithm, particle swarm optimization algorithm, and ant colony algorithm (Pan, 2018). These algorithms play an important role in heuristic intelligent algorithms and solving traveling salesman problems. For example, others solved the classical traveling salesman problem by improving the clustering and group algorithm, which effectively solved the hierarchical and progressive system scheduling of the product line assembly process based on division of labor and cooperation (Jin, 2017). The operation flow of complex mutation operator number evolution was effectively optimized by solving the classical suitcase problem combined with the multi-chromosome genetic algorithm (Guo and Lv, 2015). It has been found that the fireworks algorithm has better convergence and stability (Chen, 2019). Therefore, according to the characteristics of the fireworks algorithm, the chaotic strategy in the classical traveling salesman problem is optimized to solve the classical traveling salesman problem. However, to sum up, there is still little research and application of the bat algorithm in solving classical traveling salesman problem. Therefore, based on the bat algorithm, this article puts forward the optimization method of single distribution express logistics transportation scheduling problem, and carries out discrete dynamic modeling and analysis combined with e-commerce logistics system in the era of big data (Li et al., 2021a; Li et al., 2021b; Le et al., 2021; Toyoda and Wu, 2021; Wu et al., 2021; Zhang et al., 2022).

The bat algorithm (He et al., 2020; Li et al., 2021c; Eligüzel et al., 2022) is mainly abstractly expressed according to bat echolocation. Its specific principle is to map bat individuals into points in space, the process of finding the optimal solution by the algorithm, and simulate the process of bat searching prey. The optimal solution simulated by the final function is the optimal solution of the bat position. At the same time, the survival of the fittest of the bat population represents the situation of different solution replacement effects. It is our default that the bats that are more suitable for the environment will win, and the casual clothes that are not suitable for mitigation will be eliminated. This process is the feasible solution behavior with poor replacement effect of the central solution of the bionic principle. Based on the aforementioned principles, we make three basic assumptions for the idealized bat algorithm: first, it is assumed that all bats recognize the direction and position using echolocation, and the distance from obstacles or food to themselves. The feedback signals of obstacles and food through echolocation are different, and bats can perceive this difference. Second, in the process of flying at a fixed speed, bats can emit wavelengths of fixed frequency and certain loudness for the search and pursuit of prey, and their pulse emission frequency is always maintained between zero and one. Third, the maximum and minimum loudness of sound waves emitted by bats is fixed. According to the earlier mentioned assumptions, when a bat searches for a target normally, its position and speed are calculated as follows:

$$F_i = F_{\min} + (F_{\max} - F_{\min})\beta, \tag{1}$$

$$V_i^{i+1} = V_i^t + \left(X_i^t - X_*\right)F_i, \tag{2}$$

$$X_i^{i+1} = X_i^t + V_i^{i+1}. \tag{3}$$

Here, F_i is the sound frequency emitted by the ith bat, $F_{\max}$ is the maximum value of the sound wave, and $F_{\min}$ is the minimum value of the sound wave. β is a uniform random number, ranging from zero to one. V_i^t and V_i^{i+1} represent the velocity of the ith bat at t time and T + 1 time, respectively. X_i^t represents the position of the ith bat at time t, and X_i^{i+1} represents the specific position of the ith bat at time t + 1.

Finding a target is the first step to the success of bat hunting. Therefore, when bats find a target in biology, it means that it is close to the global optimal solution in mathematical formula. So usually we have found that the target is the node. At this time, we adopt the local search strategy to solve the optimal value on the optimal bat individual. At this time, the location update formula of local search is

$$X_{new} = X_{old} + \varepsilon A^t. \tag{4}$$

At this time, the formula of loudness and frequency of sound waves emitted by bats is updated as follows:

$$A_t^{t+1} = \alpha A_i^t, \tag{5}$$

$$r_i^t = r_i^0\left[1 - \exp(-\gamma t)\right]. \tag{6}$$

The single distribution logistics transportation scheduling model is essentially similar to the bat algorithm, which can be described as the bat finding the target location and evaluating the optimal solution in the local area algorithm. The former problem can be described as knowing the location of N recipients and targets, requiring couriers and bats to start from any point, continuously reach or pass through (n-1) pickup points, and finally return to the starting point, with the shortest total route distance. This problem is brought into the bat model to obtain the mathematical model of single distribution express logistics transportation, scheduling problem as follows:

$$MinD = \sum_{i=1}^{N-1} \left(d\left(S_i, S_{i+1}\right)\right) + d\left(S_N, S_1\right), \tag{7}$$

where $d(S_i, S_j)$ represents the distance between the ith receiving point and the jth receiving point, and the values of i and j range from zero to n. The coordinate position of receiving point I can be expressed as (X_i, Y_i) and the coordinate position of receiving point J can be expressed as (X_j, Y_j). When the coordinate positions of receiving points S_i and S_j are known, the distance formula between receiving point I and receiving point J is

$$d\left(S_i, S_j\right) = \sqrt{\left(X_i - X_j\right)^2 + \left(Y_i - Y_j\right)^2}. \tag{8}$$

According to the common sense, the distance from receiving point I to receiving point J is equal to the distance from receiving point J to receiving point I, so there are:

$$d\left(S_i, S_j\right) = d\left(S_j, S_i\right). \tag{9}$$

Discrete Bat Algorithm for the Rapid Logistics Transportation Scheduling Problem

The previously mentioned discusses the distribution scheduling of a distribution station with only one distributor and one distribution vehicle. However, in fact, multiple distributors in the same distribution center can mobilize multiple distribution vehicles to carry out the distribution tasks of multiple stations at the same time. Considering this situation, the single distribution logistics transportation scheduling problem model cannot solve.

Tion-scheduling problem is established based on the sub scenario. The ultimate purpose of this situation is to meet the needs of the receiving point and relevant requirements, and all distribution vehicles have the shortest driving path. At this time, all distribution points are called set $V = \{0, 1, 2, \cdots, N\}$, where zero represents the distribution center and the other points represent the distribution points. Call the collection of all delivery vehicles $K = \{0, 1, 2, \cdots, M\}$, and record the delivery package at the receiving point $d_i\,(i = 1, 2, 3, \cdots, N)$. The maximum load of each distribution vehicle is Q. The distance from receiving point I to receiving point J is recorded as c_{ij}. In order to ensure the accuracy of the results, this experiment verifies the solution ability of the optimized algorithm through three computational forces. Among them, C1 case is a single car express logistics transportation scheduling problem with 15 pickup points. C2 case is a single car express logistics transportation scheduling problem with 30 pickup points. C3 case is a single-vehicle logistics transportation scheduling problem with 50 pickup points. Then, there are

$$y_{is} = \begin{cases} 1, \text{Vehicle s} \\ 0, \text{other} \end{cases}, \tag{10}$$

$$x_{ijs} = \begin{cases} 1, \text{Travel from s to j} \\ 0, \text{other} \end{cases}. \tag{11}$$

Thus, the mathematical model of single-vehicle express logistics transportation scheduling problem can be obtained as follows:

$$Z_{\min} = \sum_{i=1}^{N}\sum_{j=1}^{N}\sum_{s=1}^{M} c_{ij}x_{ijs}, \tag{12}$$

$$\sum_{i=0}^{N} d_i y_{is} \le Q, \tag{13}$$

$$\sum_{s=0}^{M} y_{is} = \begin{cases} 1, i = 1, 2, \cdots N \\ M, i = 0 \end{cases}, \tag{14}$$

$$\sum_{i=0}^{N} x_{ijs=} y_{is}, j = 1, 2, \cdots N; s = 1, 2, \cdots, M, \tag{15}$$

$$\sum_{j=0}^{N} x_{ijs=} y_{is}, i = 1, 2, \cdots N; s = 1, 2, \cdots, M, \tag{16}$$

where $Z_{\min}$ represents the minimum length of single-vehicle express logistics transportation general scheduling route, and **Eq. 12** represents the minimization of single-vehicle express logistics transportation general scheduling route. **Eq. 13** indicates that the weight of the package at all distribution points in charge of each distribution vehicle does not exceed the maximum load value Q of the distribution vehicle. **Eqs. 14–16** represents that all tasks of the distribution center are jointly completed by m-quantity distribution vehicles, and it is necessary to ensure that the package distribution at each receiving point is completed by only one distribution vehicle. The aforementioned formula simulates the most common scenario of the logistics distribution center, and perfectly fits the process of formulating the scheduling scheme of the logistics distribution center through the common sense constraints (**Eq. 13**) and the theoretical constraints (**Eqs. 14–16**) considering the basic principle of maximizing enterprise profits. Therefore, the optimal solution in line with the aforementioned formula should also be the best scheduling scheme in practical problems.

DISCRETE DYNAMIC MODEL SIMULATION VERIFICATION

Simulation Preparation

In the past two years, the price war between express enterprises has become more and more intense, which also means that the development of the traditional profit theory by reducing labor cost and raw material cost is gradually narrow. More and more enterprises transfer the cost compression path to logistics transportation. According to the data of China Federation of Logistics and Purchasing, in 2018, the total consumption cost of Chinese citizens in the logistics industry reached 13.3 trillion yuan, accounting for 14.7% of the gross national product of that year, an increase of 9.8% compared with the total social logistics cost of 1.21 trillion yuan in 2018. In addition, the proportion of China's total logistics expenses in the gross national product in 2018 has decreased by three percentage points compared with six years ago, and its trend has shown a downward trend. However, the decline is slow, and the proportion is still three times higher than that in the United States. Figure 6 shows the volume of express business in China from 2010 to 2019. It can be seen that in 2019, the volume of express business in China has reached 63,520,000,000, representing an increase of twenty-five point three percent compared with 50,710,000,000 in 2018. The total amount of express business was 749.7 billion yuan, a year-on-year increase of 24.4%.

Previously, chaotic sequences were used to adjust heuristic optimization algorithms, such as genetic algorithm parameters, particle swarm optimization algorithms, harmony search, ant and bee swarm optimization, imperialist competitive algorithms, Firefly algorithm, simulated annealing. Such a combination of chaos and hyperheuristics has been shown. Some promise the correct use of a set of chaotic maps. It is not clear why an algorithm chaos replaces something. The use of parameters may change performance; however, empirical studies do show that chaos also has a high level of mixing. Therefore, it is to be expected that when a fixed parameter of the chaotic map is replaced, the resulting solution is possible. There will be high mobility and diversity. For this reason, it may have to be studied more by introduction chaos to other useful, especially new, heuristic algorithms.

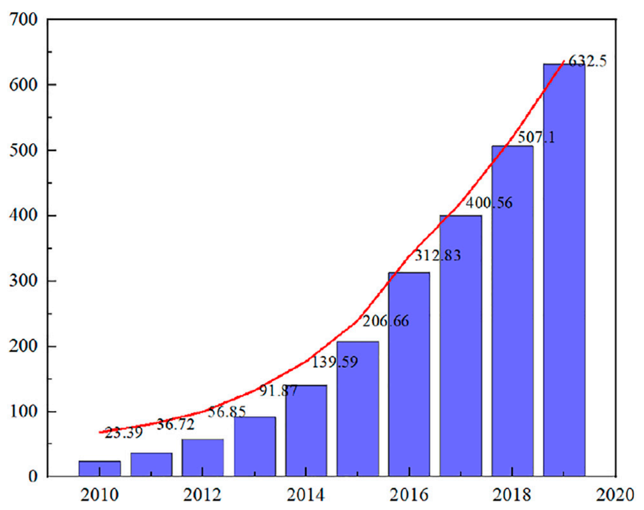

FIGURE 1 | Statistics of China's express business volume from 2010 to 2019.

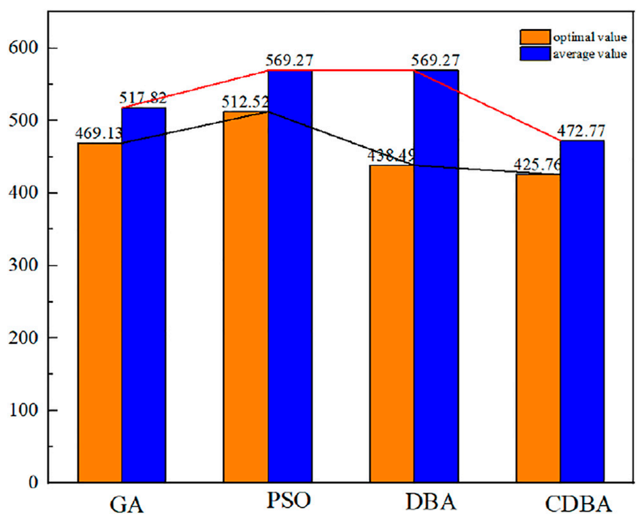

FIGURE 2 | Algorithm performance comparison experiments.

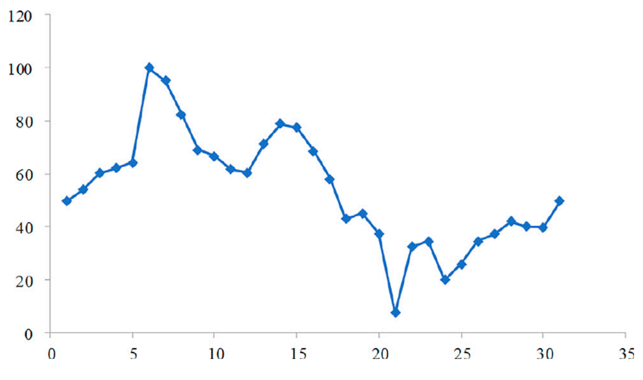

FIGURE 3 | CDBA solution for Oliver30.

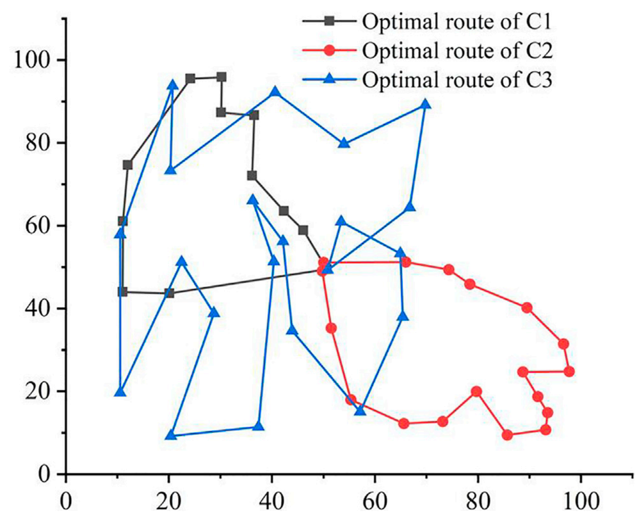

FIGURE 4 | Optimal route of C1~C3

Algorithm Performance Comparison

According to the aforementioned information, the optimized discrete dynamic algorithm is compared with the previous algorithm, and the results are shown in **Figure 1**.

As can be seen from **Figure 2**, the results of the discrete bat algorithm (DBA) in solving the logistics system scheduling problem with small data scale are due to genetic algorithm (GA) and particle swarm optimization (PSO) algorithm. However, with the gradual increase of solving data scale, its convergence decreases, and it is often unable to receive the same better value, which is more of the local optimal solution. The algorithm that adds the discrete dynamic algorithm to the previous algorithm and then carries out modeling analysis performs best in the process of solving the optimal solution, and it has a high improvement in the solution of the optimal value and the average value. It shows that adding the discrete dynamic algorithm to the original bat algorithm can effectively improve its convergence and global search ability. The specific path diagram is shown in **Figure 3**, it can be seen that as the number of abscissas increases, the solution process of the multi-model is more stable.

In order to ensure the accuracy of the solution ability of the optimized algorithm Vnqba, we use the optimized QBA algorithm and the optimized Vnqba algorithm for experimental comparison. The default initial bat population G is equal to 20; loudness attenuation coefficient of sound waves emitted by bats α is equal to 0.9, acoustic emission frequency enhancement coefficient γ equal to 0.9; the maximum number of iterations of bat population is 300. In order to control a single variable, the calculation CPU used in this experiment is Intel Core i5-3230 2.6GHz, the operating system is windows 10, the fixed running memory is 4GB, and the calculation software is MALTLAB 2014a. The results show that the optimized algorithm has the optimal solution of average timeout time in both BS and as situations, and FV is the fitness value of the optimal solution in both situations. In order to ensure the validity of the data, we take the measured values of 20 times in each group to calculate the average value. It can be concluded that both the Vnqba algorithm and QBA algorithm can obtain the optimal feasible solution under the load capacity of distribution vehicles not exceeding C1, C2, and C3. The optimized Vnqba algorithm based on the discrete dynamic analysis algorithm has obvious advantages in solving the large-scale single-vehicle express logistics transportation scheduling problem. The optimal solution obtained by the local search algorithm is obviously less than the QBA algorithm, which means that the path is the smallest when the Vnqba algorithm is used for logistics system transportation scheduling, and the quantum bat algorithm (QBA) will lead to distribution timeout when the data scale increases greatly. It can be concluded that the addition of discrete dynamic modeling analysis significantly improves the solvency of the bat algorithm. The optimal routes of C1, C2, and C3 are shown in **Figure 4**.

Result Discussion

Based on the aforementioned e-commerce industry needs, e-commerce logistics enterprises began to seek more efficient, fast, and low-cost logistics transportation operation methods on the premise of ensuring user service experience. First, this study decomposes the operation problem of e-commerce logistics system into a single distribution express logistics transportation scheduling problem. Based on the previous research on the bat algorithm, the bat algorithm is discretized and dynamically modeled and analyzed according to the full permutation theory and chaotic optimization strategy. Through the introduction of chaotic optimization and local segment counterclockwise search strategy, the bat algorithm based on discrete dynamic modeling analysis effectively improves the global search ability and the solution ability of local optimal solution. Finally, this optimized bat algorithm is called the chaotic discrete bat algorithm (CDBA). Experiments show that the chaotic discrete bat algorithm is more effective than the existing common algorithms in the single distribution express logistics transportation scheduling problem.

Second, this article continues to study the single-vehicle express logistics transportation scheduling problem. Compared with the single distribution express logistics transportation scheduling problem, the single-vehicle express logistics transportation problem has one more condition of distribution vehicles, which is more in line with the actual distribution situation in the logistics distribution of modern e-commerce enterprises. In this article, the local search ability is significantly improved by adding 2-opt strategy to the original bat algorithm. 2-opt strategy means that the bat algorithm changes the local search range by changing the neighborhood interval in the process of local search, so as to find the local optimal solution. Finally, in order to ensure the accuracy of the data, the experiment uses three cases with different distribution locations to simulate the pre optimization algorithm and the post optimization algorithm. The results show that the optimized Vnqba algorithm has stronger convergence ability than the optimized QBA algorithm, and performs better in local search.

CONCLUSION

Based on the application of the bat algorithm in the logistics and transportation scheduling of the e-commerce logistics system, this article optimizes the bat algorithm that has been less studied in the past, so as to be better applied to the operation of the e-commerce logistics system. By analyzing the actual demand of express logistics, a single-delivery express logistics transportation scheduling model is established. Based on chaotic optimization strategy and the discrete bat algorithm, a discrete dynamic chaotic bat algorithm is proposed. The experimental results show that the model algorithm can solve the optimal scheduling path more accurately than the commonly used intelligent algorithms, which proves that the algorithm is effective. At the same time, in view of the current situation of multi-vehicle distribution at the same time, a single-vehicle express logistics transportation scheduling model is established. Experimental results show that:

1) The algorithm has the highest accuracy in solving the optimal path scheduling scheme, which proves the effectiveness and feasibility of the algorithm
2) In this article, by adding the 2-opt strategy to the original bat algorithm, with the gradual increase of the scale of the data to be solved, the built model can effectively improve its convergence and global search ability
3) The optimized discrete dynamic algorithm is compared with the previous algorithm, and the performance is improved by about 20%

To sum up, this article has achieved some research results in the scheduling scheme of e-commerce logistics system, but the following improvements can be made in future research. For example, if the actual traffic conditions do not conform to straight-line transportation, traffic congestion may occur during peak hours. These important factors should be used as parameters affecting the discrete dynamic model, and we hope to continue to improve them in the future research process.

DATA AVAILABILITY STATEMENT

The raw data supporting the conclusion of this article will be made available by the author, without undue reservation.

AUTHOR CONTRIBUTIONS

GM independently completed all the content of the article.

REFERENCES

Asokan, A., Popescu, D. E., Jude, A., and Hemanth, J. (2020). Bat Algorithm Based Non-linear Contrast Stretching for Satellite Image Enhancement. *Geosciences* 10 (2), 45–50. doi:10.3390/geosciences10020078

Atefi, R., Salari, M., Coelho, L. C., and Renaud, J. (2018). The Open Vehicle Routing Problem with Decoupling Points. *Eur. J. Operat. Res.* 7 (4), 265. doi:10.1016/j.ejor.2017.07.033

Bayzid, M. S., and Warnow, T. (2018). Gene Tree Parsimony for Incomplete Gene Trees: Addressing True Biological Loss. *Algori. Mol. Biol.* 13 (8), 1–106. doi:10.1186/s13015-017-0120-1

Cai, X., Wang, L., Kang, Q., and Wu, Q. (2014). Bat Algorithm with Gaussian Walk. *Ijbic* 6 (3), 166–174. doi:10.1504/ijbic.2014.062637

Chen, H. (2019). The Promotion and Optimization of Big Data Analysis on E-Commerce Marketing. *Chin. Mark.* 1009 (18), 136–137.

Chen, R., Shen, Y-M., and Hong, W. (2019). Neural-like Encoding Particle Swarm Optimization for Periodic Vehicle Routing Problems. *Expert Syst. Appl.* 138, 112833. doi:10.1016/j.eswa.2019.112833

Dantzig, G., and Ramser, J. H. (2021). The Truck Dispatching Problem. *Manag. Sci.* 6 (1), 80–91. doi:10.1287/mnsc.6.1.80

Eligüzel, N., Çetinkaya, C., and Dereli, T. (2022). A Novel Approach for Text Categorization by Applying Hybrid Genetic Bat Algorithm through Feature Extraction and Feature Selection Methods. *Expert Syst. Appl.* 202, 117433.

Fachini, R., and Armentano, V. (2020). Exact and Heuristic Dynamic Programming Algorithms for the Traveling Salesman Problem with Flexible Time Windows. *Optim. Lett.* 14 (2), 99–105. doi:10.1007/s11590-018-1342-y

Fan, M. (2019). Research on the Optimization of Logistics Enterprises and Their Distribution under the Background of E-Commerce. *Logist. Eng. Manag.* 41 (04), 15–16.

Guo, D., and Lv, Y. (2015). Analysis and Optimization of Marketing Strategy of Membership System of E-Commerce Enterprise. *Bus. Econ. Res.* (19), 52–54.

Hafiz, T., Sumbal, M., Umar, S., Irfan, M. N., and Lali, I. (2020). Adaptive Inertia Weight Bat Algorithm with Sugeno-Function Fuzzy Search. *Appl. Soft Comput. J.* 90, 106159. doi:10.1016/j.asoc.2020.106159

He, M., Sun, L., Zeng, X., Liu, W., and Tao, S. (2020). Node Layout Plans for Urban Underground Logistics Systems Based on Heuristic Bat Algorithm. *Comput. Commun.* 154, 465–480. doi:10.1016/j.comcom.2020.02.075

Jin, H. (2017). Exploration of E-Commerce Marketing Channel Optimization under the Internet Environment. *Bus. Econ. Res.* 000 (022), 46–48.

Le, S., Wu, Y., Guo, Y., and Vecchio, C. D. (2021). Game Theoretic Approach for a Service Function Chain Routing in NFV with Coupled Constraints. *IEEE Trans. Circuits Syst. II* 68, 3557–3561. Published online. doi:10.1109/TCSII.2021.3070025

Li, H., Deng, J., Feng, P., Pu, C., Arachchige, D. D. K., and Cheng, Q. (2021). Short-Term Nacelle Orientation Forecasting Using Bilinear Transformation and ICEEMDAN Framework. *Front. Energy Res.* 9, 780928. doi:10.3389/fenrg.2021.780928

Li, H., Deng, J., Yuan, S., Feng, P., and Arachchige, D. D. K. (2021). Monitoring and Identifying Wind Turbine Generator Bearing Faults Using Deep Belief Network and EWMA Control Charts. *Front. Energy Res.* 9, 799039. doi:10.3389/fenrg.2021.799039

Li, H., Song, B., Tang, X., Xie, Y., and Zhou, X. (2021). A Multi-Objective Bat Algorithm with a Novel Competitive Mechanism and its Application in Controller Tuning. *Eng. Appl. Artif. Intell.* 106, 104453. doi:10.1016/j.engappai.2021.104453

Pan, H. (2018). Analyze the Impact of E-Commerce in Business Administration on Marketing and the Solutions. *Build. Mater. Decor.* 556 (47), 137–138.

Stodola, P. (2018). Using Metaheuristics on the Multi-Depot Vehicle Routing Problem with Modified Optimization Criterion. *Algorithms* 11 (5), 74–80. doi:10.3390/a11050074

Suganthi, J., and Malathi, V. (2017). Modified Bat Algorithm for Feature Selection with the Wisconsin Diagnosis Breast Cancer (WDBC) Dataset. *Asian Pac. J. cancer Prev. APJCP* 18 (5), 104–107. doi:10.22034/APJCP.2017.18.5.1257

Toyoda, M., and Wu, Y. (2021). Mayer-type Optimal Control of Probabilistic Boolean Control Network with Uncertain Selection Probabilities. *IEEE Trans. Cybern.* 51, 3079–3092. (Regular Paper). doi:10.1109/tcyb.2019.2954849

Wang, H. (2016). The Big Data Marketing Dilemma and Optimization Strategies of E-Commerce Companies. *Enterp. Technol. Dev. (second half)* 035 (015), 40–41.

Wang, Y., Li, K., Han, Y., Ge, F., Xu, W., and Liu, L. (2020). Tracking a Dynamic Invading Target by UAV in Oilfield Inspection via an Improved Bat Algorithm. *Appl. Soft Comput. J.* 90 (01), 22–27. doi:10.1016/j.asoc.2020.106150

Wu, Y., Guo, Y., and Toyoda, M. (2021). Policy Iteration Approach to the Infinite Horizon Average Optimal Control of Probabilistic Boolean Networks. *IEEE Trans. Neural Netw. Learn Syst.* 32 (6), 2910–2924. doi:10.1109/TNNLS.2020.3008960

Yong, J., He, F., Li, H., and Zhou, W. (2019). A Novel Bat Algorithm Based on Cross Boundary Learning and Uniform Explosion Strategy. *Appl. Math. A J. Chin. Univ.* 34 (04), 480–502. doi:10.1007/s11766-019-3714-1

Zhang, L. P., and Chai, Y. (2010). Improved Genetic Algorithm for Vehicle Routing Problem. *Comput. Eng. Appl.* 13 (13), 203–206.

Zhang, W., Hu, Y., He, H., Liu, Y., and Chen, A. (2019). Linear and Dynamic Programming Algorithms for Real-Time Task Scheduling with Task Duplication. *J. Supercomput.* 75 (2), 82–89. doi:10.1007/s11227-017-2076-9

Zhang, Y., Qian, T., and Tang, W. (2022). Buildings-to-distribution-network Integration Considering Power Transformer Loading Capability and Distribution Network Reconfiguration. *Energy* 244. Regular Paper. doi:10.1016/j.energy.2022.123104

Zheng, F., Pang, Y., Liu, M., and Xu, Y. (2020). Dynamic Programming Algorithms for the General Quay Crane Double-Cycling Problem with Internal-Reshuffles. *J. Comb. Optim.* 39 (3), 430–440. doi:10.1007/s10878-019-00508-9

Conflict of Interest: The author declares that the research was conducted in the absence of any commercial or financial relationships that could be construed as a potential conflict of interest.

frontiers | Frontiers in Energy Research

ORIGINAL RESEARCH
published: 26 September 2022
doi: 10.3389/fenrg.2022.927048

Study of Solar Combined Air Energy Greenhouse Heating System Model

Wang Hao[1,2], *Wei Jintao*[2], *Zhang Ruifeng*[1] *and Xu Zhenjun*[1]*

[1]*College of Civil Engineering and Architecture, Qingdao Agricultural University, Qingdao, China,* [2]*Qingdao Institute of Technology Mechanical and Electrical Engineering, Qingdao, China*

At present, it is difficult to bring centralized heating to rural areas owing to factors such as scattered distribution, distance from towns and cities, and difficulty in laying public pipes. According to research, most rural residents use inefficient household heating facilities, thereby resulting in serious environmental pollution and a decline in the quality of life of residents. In order to alleviate environmental pollution, the use of solar energy, air energy, and other renewable energy for rural heating of such decentralized buildings is of profound significance. This study analyzed the distribution characteristics of solar energy resources and solar combined air energy greenhouse heating system, established and solved a mathematical model of the solar combined air energy greenhouse heating system, calculated solar heat collection and solar heating energy consumption. From the data analysis, the relationship among heat gain power, heating power, and the water temperature of the water storage tank of the heat pump system was obtained. The mathematical model of the storage tank of the solar combined air energy greenhouse heating system was solved, and the operating conditions and volume of the storage tank of the solar combined air energy greenhouse heating system were determined. The study also analyzed the solar heat collection and solar heating energy consumption in Qingdao, thereby pointing out the advantages of the solar combined air energy greenhouse heating system, and finally obtained the best heating scheme.

Keywords: greenhouse, solar energy, air energy, COP, heating system

Edited by:
Yusen He,
The University of Iowa, United States

Reviewed by:
Hardeep Singh,
Sophia University, Japan
Sanjeev Kumar,
Lovely Professional University, India

***Correspondence:**
Xu Zhenjun
xuzhenjun@qau.edu.cn

Specialty section:
This article was submitted to Smart Grids, a section of the journal Frontiers in Energy Research.

Received: *23 April 2022*
Accepted: *13 May 2022*
Published: *26 September 2022*

Citation:
Hao W, Jintao W, Ruifeng Z and Zhenjun X (2022) Study of Solar Combined Air Energy Greenhouse Heating System Model. Front. Energy Res. 10:927048. doi: 10.3389/fenrg.2022.927048

INTRODUCTION

Greenhouses are an important infrastructure of modern agriculture. The development direction of modern greenhouse is large-scale, high-tech, factory, greenhouse product diversification, characteristic, low energy consumption and environmental protection (Wei, 1999). In the cold areas of north China, the energy consumption of the greenhouse heating load during winter is quite large, thereby accounting for 60–74% of the operating cost of greenhouses (Zhu, 2005). The average winter temperature in northern China is 5°C, and the negative accumulated temperature is 1–4 times higher than that in the same latitude around the world (Liao et al., 1998). Due to the high heat transfer coefficient of greenhouse covering materials and the inability of plants in the greenhouse to store a lot of heat, greenhouse heating is quite different from that of ordinary buildings. The most important characteristic of the greenhouse are the poor thermal inertia of the envelope and the huge temperature difference between day and night (Gao, 2012). These are the temperature regulation methods that are mainly followed for greenhouses in China (Zhou, 2003): (1) adding cover; (2) hot-water heating method; (3) wood heating method; (4) heating coal-fired hot blast stove temperature raising method; (5) electric heating; and (6) solar thermal storage pool, which is mainly used to collect and store solar energy. In recent years, solar energy technology has been widely applied at home and abroad (Ma, 2003). At the same time, as a type of green technology of energy saving, heat pumps are highly efficient, provide environmental protection, and have been increasingly applied in the field of facility agriculture (Mao et al., 2004).

There is a serious lack of energy in rural areas in China, remote and isolated areas are in urgent need of energy supply, and the use of solar energy is one of the main ways to solve the heating needs of greenhouses in these areas (Wang and Cheng, 2007). The use of solar energy for greenhouse heating, although energy saving and environmentally friendly, is subject to the weather and meets the needs of all-weather heating with difficulty (Zhang and Chen, 2008). With the rapid development of modern agriculture in China, energy saving, high efficiency, and environmental protection have become the development themes of facility agriculture, and greenhouse heating equipment and heating methods have also been developed in that direction (Liu et al., 2008). In recent years, solar energy technology has been widely used at home and abroad (Luo et al., 2007). Meanwhile, heat pumps, as an energy-saving, high-efficiency, and environmentally friendly green technology, are also being increasingly used in the field of facility agriculture (Luo et al., 2007; Fang et al., 2008). The traditional heating equipment relies on conventional energy to heat up during the day and most nights during winter, which can meet the heating requirements, but it produces problems, such as high heating cost, low efficiency, and environmental pollution. To improve the propane refrigeration system of the natural gas shallow cooling unit, the factors affecting the energy consumption of the propane compressor were analyzed, and it was found that reducing the condensing temperature of the propane at the outlet of the compressor could ensure that the grade and quantity of the cold quantity provided by the refrigeration system would not decrease and effectively reduce the energy consumption of the propane compressor (Fang and Zhuang, 2014). The cooling capacity of the cryogenic methane washing process is provided by a refrigeration cycle using the product gas CO as the working mass, which has high energy consumption (Li et al., 2013). The ternary hybrid refrigeration system provides the cooling capacity for the separation system to meet the heating demand of some low-temperature-distillation tower reboilers and effectively recovers the cooling capacity of the process logistics through precooling and subcooling of the refrigerant (Di, 2003). Process model of separation refrigeration system using demethanizer, Process simulation, parameter sensitivity analysis and process optimization of old refrigeration system in Yangzi ethylene plant (Xu and Gong, 2010).

PROCESS OF SOLAR AIR GREENHOUSE COMBINED HEATING SYSTEM

The refrigerant R134a is used in the solar air greenhouse combined heating system, and the compressor used is the Bizell piston compressor. The compressor compresses the refrigerant to high temperature pressure and transfers the refrigerant to a condensing coil, which then condenses it to a liquid state. The condensing coil is placed in the hot water storage bucket, and the water in the bucket is heated using the condensing coil. Liquid refrigerant passes through a liquid storage device, liquid mirror, and filter dryer, which is throttled by the expansion valve, becomes a low-pressure and low-temperature liquid refrigerant, and enters the solar plate collector to evaporate and absorb heat. The vaporized refrigerant is separated from the superheated gas by the gas–liquid separator into the low-pressure end of the compressor and compressed into a high-temperature and high-pressure liquid refrigerant. The hot water in the hot water storage tank is pumped into the fan coil unit in the greenhouse. The fan coil emits heat inside the greenhouse to maintain the temperature inside the greenhouse. The hot water is returned to the hot bucket to complete the hot water circulation. The solar plate collector in this system is processed from an aluminum plate, and its surface is painted black to absorb sunlight (Li, 2022a; Li, 2022b).

SYSTEM MATHEMATICAL MODEL

Heat Load Model

The greenhouse heating loss is mainly composed of heating loss of the envelope, cold air infiltration, and cold air invasion. The calculation formula of heat load (Zhang and Chen, 2011) is as follows:

$$Q = Q_1 + Q_2 + Q_3 \tag{1}$$

$$Q_1 = \sum K_n F_n (t_i - t_0) \tag{2}$$

$$Q_2 = 0.5 k_f V N (t_i - t_0) \tag{3}$$

$$Q_3 = \sum u_i A_i (t_i - t_0) \tag{4}$$

Here, Q_1 is the heat loss of the envelope structure; —Cold air permeates heat loss; —Ground heat loss; —Heat transfer coefficient of greenhouse envelope at n floor, W/(m^2·K), = 3 W/(m^2·K); —Surface area of the n greenhouse envelope, m^2; —Wind power factor, = 1; —Greenhouse air volume, m^3; —Number of chamber air changes, h-1, Greenhouse once/ 12 h; —Ground heat transfer coefficient in zone i, W/(m^2·K); —Area of block i, m^2; —The n greenhouse indoor heating design temperature, K = 18°C; —The n greenhouse outdoor heating design temperature, K. = 2°C.

Compressor Model

For small rolling-rotor compressors, the refrigerant flow rate and compressor power can be calculated using the following equation.

1 Refrigerant mass flow rate

$$m_r = \frac{n \lambda V_d}{60 v_i} \sum u_i A_i (t_i - t_0) \tag{5}$$

where v_i is the compressor suction specific volume expressed as m^3/kg; n is the heat loss of envelope structure, taking the value of 2880 r/min; C is compressor speed, taking the value of 0.91;

and V_d is the compressor theoretical discharge volume, taking the value of 13.40 cm^3/r.

2 Compressor power

The compressor input electrical power is:

$$W_{cm} = m_r \frac{P_e v_i}{\lambda_{cm}} \frac{k}{k-1}\left[\left(\frac{P_c}{P_e}\right)^{\frac{k}{k-1}} - 1\right] \tag{6}$$

where λ_{cm} is the total efficiency of the compressor; P_c is the evaporation pressure and condensation pressure, Pa; and k is the compression process multivariate index.

Solar Flat Plate Evaporator Model

Experimental study of direct expansion solar heat pump water heater.

Solar water supply systems require temperatures lower than 60°C and the use of collectors with glass cover. According to the energy balance can be obtained that as the design conditions under the pressure drop is small, you can ignore the pressure drop of the refrigerant in the tube.

1 Refrigerant side flow heat transfer equation (Chai et al., 2008; Chen et al., 2011; Kuang and Wang, 2005):

$$Q_r = m_r\left(h_{r2} - h_{r1}\right) = \alpha_i A_i\left(T_p - T_{rm}\right) \tag{7}$$

The formula, Q_r—Heat absorbed by Refrigerant, W; m_r—Refrigerant mass flow, kg/s; α_i—Convective heat transfer coefficient on refrigerant side surface, W/(m^2·K); A_i—Tube surface area, m^2; T_p—Tube wall temperature, K; T_{rm}—Average inlet and outlet temperature of refrigerant, K.

2 Compressor power

$$Q_d = A_d F'\left[S - U_{Lc}\left(T_{rm} - T_0\right)\right] \tag{8}$$

The formula, Q_d—Effective heat gain of heat collector plate, W; A_d—Micro-element length heat collection area on the upper surface of trace element heat collecting plate, m^2; S—The difference between absorbed and emitted radiation from the heat collector plate, W/m^2; U_{LC}—Total heat loss coefficient of heat collector plate, m^2, W/(m^2·K); —Heat collection efficiency factor of collector plate; T_0—Ambient temperature, K.

$$U_{1c} = \left(5.7 + V_W + 4\varepsilon\sigma T_0^3\right) \tag{9}$$

where ambient temperature is K, Boltzmann constant (blackbody radiation constant) is $5.67 \times 10 - 8$W/(m^2·K^4), the outdoor wind speed and the calculated outdoor wind speed in winter in the Chengyang area are taken in this paper, and T_0 is the ambient temperature, K, which is the unit of measurement of standard error in the total number.

Taking into account the installation angle and direct sunlight, sky radiation, and reflection of solar radiation from the ground, the total solar radiation is calculated as follows:

$$S = I_T\cos\theta_t + \left(\frac{1+\cos\beta}{2}\right)I_{dh} + \left(\frac{1-\cos\beta}{2}\right)I_t\rho_g \tag{10}$$

The formula, —Indicates the intensity of radiation projected on a horizontal surface; —Indicates the intensity of diffuse reflection projected on a horizontal surface; —Indicates the angle of projection of direct sunlight on inclined and horizontal surfaces; —Indicates the tilt angle of the collector plate installation; —Indicates the reflectivity of the ground to the total solar radiation, in engineering calculations, we usually take the average value as 0.2.

For an inclined surface facing due south, formula for calculating the .

For an inclined surface facing due south formula for calculating the formula, —Hour Angle; —Angle of incidence; —Local latitude; —Angle of declination; —inclination of collector surface (Duffie J.A. et al., 1991).

3 Heat balance equation inside and outside the tube:

$$Q_{cl} = \beta Q_r \tag{11}$$

Here, the coefficient introduced by considering impurities, such as oil, in the refrigerant takes a value of 0.9 in the model.

Mathematical Model of Condenser

Condenser (tank) uses immersion condensing spiral coil, and collectors are similar to the enthalpy difference in the direction of the length of the equal division of a number of microelements. When the enthalpy difference is small, the length of each microelement is also very small, which can be approximated by straight pipe section to deal with, and corrected using the spiral tube correction factor. For each microelement, the following control equation can be established.

1 Refrigerant side flow heat transfer equation:

$$Q_r = m_r\left(h_{r1} - h_{r2}\right) = \alpha_1 A_1\left(T_w - T_{rm}\right) \tag{12}$$

2 Water-side heat transfer equation:

$$Q_W = M_W C_{pW}\frac{dT_W}{dT_\tau} \tag{13}$$

where hot water heating power is expressed in W; total mass of water in the tank is expressed in kg; specific heat of water is expressed in kJ/(kgK); water temperature is expressed in K; and time is expressed in s.

3 Heat balance equation inside and outside the tube:

$$Q_W = Q_r \tag{14}$$

4 Microelement thermal conductivity equation:

$$Q_r = U_{cd} - A_{cd}\left(T_{rm} - T_{wm}\right) \tag{15}$$

The formula, —Heat transfer coefficient of overall on external surface area, W/(m^2·K); —Heat transfer area between condensing coil and water, here is the exterior area of the condensing coil, m^2; —Average temperature of water, K。

The heat transfer coefficient of the condensing coil to water can be calculated according to the formula:

$$U_{cd} = \frac{1}{\frac{A_{cd,0}}{aiA_{cd,i}} + \frac{\delta_m A_{cd,0}}{k_m A_{cd,m}} + \frac{1}{a_w}} \tag{16}$$

where metal tube wall thickness is m; thermal conductivity of metal pipe wall is expressed by W/(m^2·K); surface heat transfer coefficient of the refrigerant in the condensing coil is expressed by W/(m^2·K); water-side surface heat transfer coefficient is expressed by W/(m^2·K); inside and outside areas of condensing coils is expressed in m^2; and average surface area of condensing coils is expressed in m^2.

Thermal Expansion Valve Model

The thermal expansion valve model includes the following control equations:

Flow characteristic equation

The refrigerant flow rate through the thermal expansion valve can be calculated according to the following formula:

$$m_\tau = \left(0.2005\sqrt{\rho_1} + 0.634v_0\right)A_0\sqrt{2\rho_1\Delta p} \tag{17}$$

The formula, —Expansion valve inlet and outlet enthalpy, J/kg —Differential pressure before and after the valve hole, Pa —Flow coefficients, using empirical formulas from the literature —Minimum flow area of valve orifice, m^2—Inlet liquid refrigerant density, kg/m^3—Outlet refrigerant specific volume, m^3/kg.

Air Source Evaporator Model

On rainy days and at night, the evaporator gains heat from the surrounding air through the spiral finned tubes and collector plates, and the heat pump works as an air source:

$$Q_e = m_r\left(h_1 - h_4\right). \tag{18}$$

The formula—Refrigerant flow rate, —Refrigerant enthalpy at evaporator outlet; —The refrigerant enthalpy of the evaporator inlet.

Fan Coil Model

1 Chilled water heat balance equation

$$c_w = \frac{\partial t_w}{\partial \tau} - c_w u_w' \frac{\partial t_w}{\partial x} = \alpha_{bn} F_w\left(t_b - t_w\right) \tag{19}$$

2 Coil heat exchanger coil wall heat balance equation

$$\frac{\partial t_b}{\partial \tau} = \alpha_{bn} F_w\left(t_w - t_b\right) + a_{bw} F_a\left(t_a - t_b\right) \tag{20}$$

3 Air-side humidity equilibrium equation

$$\rho_a \frac{\partial d_a}{\partial \tau} + \rho_a u_a \frac{\partial d_a}{\partial x} = KF_a\left(d_g - d_a\right) \tag{21}$$

4 Energy equation

$$Q_0 = \rho_a U_a A\left(h_{a,i} - h_{a,o}\right) \tag{22}$$

The formula represents heat transfer coefficient, which is expressed as W/(m^2·K); cross-sectional area of air passing through the coil heat exchanger is expressed as m^2; specific heat capacity of guest product is expressed as J/(m^3·K); moisture content, based on 1 kg of dry air, is expressed as g/kg; heat transfer area per unit volume of fluid is expressed as m^2/m^3; enthalpy is expressed as J/kg; mass transfer coefficient between air and the outer surface of the coil is expressed as kg/(m^2·s); coil heat exchange is expressed as W; temperature is expressed as K; fluid flow rate is expressed as m/s; coefficient of heat transfer between air and the outer surface of the coil is expressed as kg/(m^2·s); fluid density is expressed as kg/m^3; and duration of a single stay is expressed as s.

Subscript, —Wet air; —Coil wall surface; —Between the chilled water and the inner surface of the coil; —Between the air flow and the outer surface of the coil; —Coil heat exchanger outer surface saturated with air; —Import; —The entire coil; —Export; —Frozen water.

Air-Side Heat Transfer Equation

Heat exchange of primary heat exchanger at dry working conditions.

The air on the outside of the evaporator tube in winter is an exothermic cooling process from the inlet to the outlet, and according to the state parameters of the air, its cooling process have three conditions: dry condition and wet condition.

The heat exchange volume in the dry condition is calculated by the following formula (Sun, 2008):

$$dQ_a = \alpha_a\left(\eta_f dA_f + dA_P\right)\left(t_a - t_w\right) \tag{23}$$

The formula, —Air-side heat transfer coefficient, W/(m^2·K); —Fin efficiency; —Fin area, m^2; —Base tube area, m^2; —Temperature, K.

Subscript, —Air; —Frosting; —Ribs; —Pipe Wall; —Base Management;

The fin efficiency is calculated using the following formula.

$$\eta_f = \frac{th(m \cdot l)}{m \cdot l} \tag{24}$$

The formula represents thermal conductivity of rib material, which is expressed as W/(m^2·K) and the average thickness of ribs is expressed as m.

$$l = \left(1.065R - r_0\right)\left[1 + 0.8051\lg\left(1.065R/r_0\right)\right] \tag{25}$$

The heat exchange coefficient on the air side was used from the literature (Kong et al., 2010).

The heat exchange volume at wet working conditions is calculated using the following equation (Hikari, 1983):

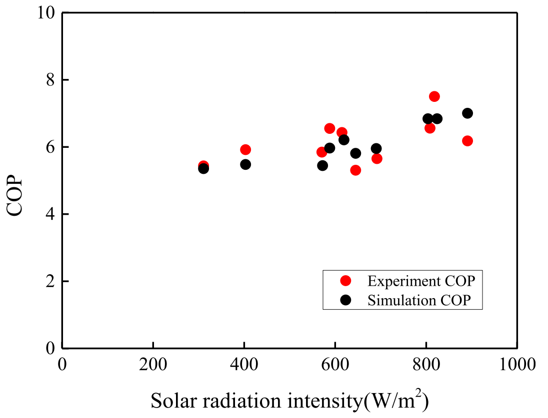

FIGURE 1 | Comparison of predicted and experimental values of COP and operation time.

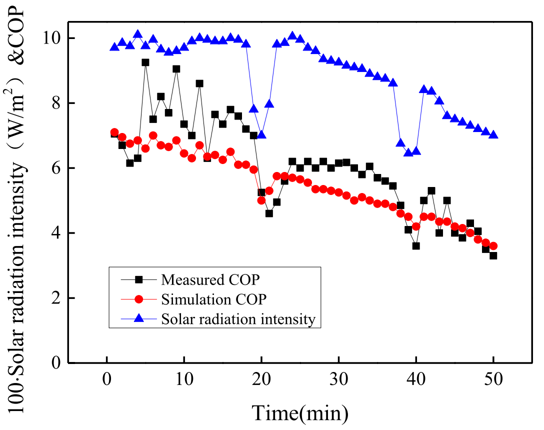

FIGURE 3 | Experimental simulation comparison of system COP transient values.

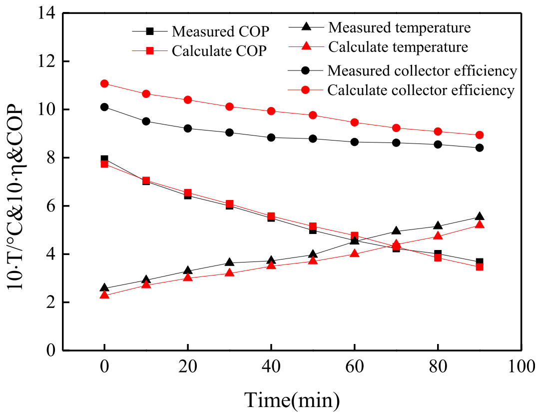

FIGURE 2 | Comparison of experimental and theoretical calculation of instantaneous values.

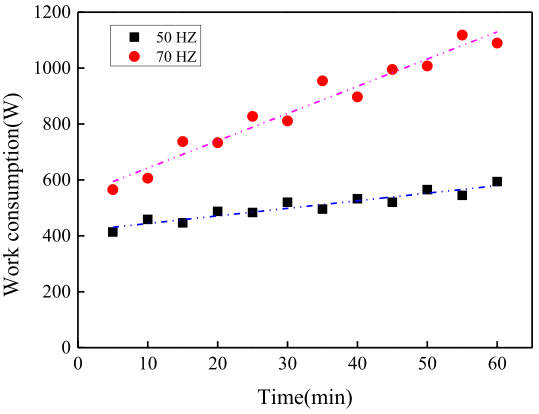

FIGURE 4 | Compressor power consumption curve.

$$dQ_a = \xi\alpha_a\left(\eta_{f\xi} dA_f + dA_p\right)(t_a - t_w) \tag{26}$$

The formula—Moisture dispersion coefficient —Fin efficiency under wet working conditions;

Moisture dispersion coefficient, the calculation of fin efficiency under wet working conditions is referred to literature 22.

Characteristic Analysis of Solar Air Energy Greenhouse Heating System

The project is located in Qingdao, Shandong province, the southern tip of Shandong Peninsula, at the longitude 119°30′E–121°00′E and latitude 35°35′N–37°09′ N. The terrain is high in the east and low in the west, uplifted on both sides of the north and south, and concave in the middle. Located in the warm temperature difference between day and night on January 28 sunrise at 7:03 and sunset at 17:20. Cloudy, RH 39%, no continuous wind direction and light breeze.

Figure 1 shows the COP variation with solar radiation intensity. As it can be seen from **Figure 2**, COP of the system increases with the solar radiation intensity. The solar combined air energy greenhouse heating system's biggest characteristic in solar panels is that the refrigerant directly absorbs heat from the environment and evaporation, the main source of energy is radiation from the sun, evaporation temperature increases with an increase in the radiation from the sun, and refrigerant phase-change heat absorption unit, which is the process of quality, is also increased. Thus, the system's COP also increases. By the same token, COP increases with ambient temperature. In the numerical simulation results, the maximum error of heating time is 11.02%, the average error is 5.43%, the maximum error of COP is 13.40%, and the average error is 4.12%. The error is acceptable in the engineering application range, and the simulation results are in good agreement with the test results.

Figure 3 shows the simulation comparison of the transient COP experiment of the system. As the temperature of condensed water increases, the COP of the system decreases due to the deterioration of condensation conditions. At the same time, solar radiation intensity changes due to cloud shielding when the system runs up to 16 min and 46 min, and the COP of the system also changes, which is consistent with the conclusion drawn in **Figure 3**. When the weather conditions change, in order to maintain a higher COP and a shorter system running time as much as possible, frequency conversion adjustment can be carried out on the heat pump system and the evaporation temperature can still be maintained in a reasonable range when solar radiation changes significantly. About the compressor running frequency effect on the COP of the system, the frequency and refrigerating capacity decrease, but the power reduction rate is greater than the heat; thus, the system COP in the reduced frequency is increased. Thus, we specially selected two days' climate conditions, which were close to the experimental data, to compare, and the final measurements for the two groups' experiment system' COP was 4.87 and 5.3.

Figure 4 shows the power consumption of the compressor in this group of experiments. The power consumption of the compressor at 70 Hz increases significantly faster than that of the compressor at 50Hz; thus, the COP of the latter is greater. In addition, when the solar radiation intensity decreases and the heating time is prolonged, the system operating at high frequencies will decline rapidly due to increased power consumption of the compressor. However, in contrast, it takes 52 min to heat the water in the water tank from 27 to 50°C at 70 Hz and 78 min at 50 Hz. Therefore, it can be considered appropriately to increase the frequency of the compressor when the hot water is expected to be heated quickly. The frequency of the compressor has an extremely important influence on COP and the speed of hot water. The frequency of the compressor should be adjusted according to the climatic conditions and user needs.

CONCLUSION

The centralized parameter model has satisfactory accuracy for the calculation of the transient process and the overall operation parameters of the solar air greenhouse combined heating system, and the calculation results have reference significance for guiding the experimental direction. It is evident that the COP increases with increasing ambient temperature. The results of the numerical simulation showed that the maximum error of heating time was 11.02% and the average error was 5.43%, whereas the maximum error of COP was 13.40% and the average error was 4.12%. The error is acceptable in the engineering application range, and the simulation results agree well with the test results.

DATA AVAILABILITY STATEMENT

The raw data supporting the conclusion of this article will be made available by the authors, without undue reservation.

AUTHOR CONTRIBUTIONS

WH conceived the idea and designed the experiments. The experiments were led by XZ, while WJ contributed to data analysis and interpretation along with writing paper. All authors read and approved the final manuscript.

REFERENCES

Chai, L., Ma, C., and Zhang, X. (2008). Experimental Research and Performance Analysis of Ground Source Heat Pump Greenhouse Cooling System. *J. Agric. Eng.* 24 (12), 150–154.

Chen, B., Luo, X., Bi, F., and Li, J. (2011). Experiment of Combined Solar and Air Source Heat Pump Heating System for Greenhouse. *China Agric. Sci. Technol. Her.* 13 (1), 55–59.

Di, X. (2013). Optimization of Combined Operation of De-ethanizer Tower and Refrigeration System in Ethylene Plant. *China Foreign Energy* 18 (10), 84–89.

Du, J., Wang, H., and YangDan, L. (2000). New Field of Heating Technology a Greenhouse Heating. *Energy Sav. Technol.* 18 (10), 22–23.

Duffie, J. A., and Beckman, W. A. (1991). *Solar Engineering of Thermal Processes*. Second Edition. New York: John Willy & Sons, Inc., 28–143.

Fang, X., and Zhuang, X. (2014). Application and Effect Analysis of Energy-Saving Technology for Propane Refrigeration System. *Petroleum Petrochem. Energy Conservation* 4 (08), 12–14.

Gao, L. (2012). *Analysis of Air-Source Heat Storage Soil-Source Heat Pump for Heating and Cooling of Sunlight Greenhouses in Severe Cold Areas, Master's Thesis*, 6. Harbin Institute of Technology.

Hikari .Q (Editor) (1983). *Cooling Technology for Air Conditioning* (China Construction Industry Press).

Hui, F., Yang, Q., and Sun, A. (2008). Application of Ground-Source Heat Pump-Floor Heat Dissipation System in Greenhouse Winter Heating. *J. Agric. Eng.* 24 (12), 145.

Jordan, R. C., and Priester, G. B. (1948). *Refrigeration and Air Conditioning*. New York: Prentic-Hall, Inc., 82–98.

Kong, X., Zhang, D., Ying, L., and Yang, Q. (2010). Simulation Study of Direct Expansion Solar Heat Pump Water Heater. *J. Sol. Energy* 12 (3112), 1574–1579.

Kuang, Y. H., and Wang, R. Z. (2005). Experimental Study of Direct Expansion Solar Heat Pump Water Heater. *J. Eng. Thermophys.* (3), 379–381.

Le, S., Wu, Y., Guo, Y., and Del Vecchio, C. (2021). *Game Theoretic Approach for a Service Function Chain Routing in NFV with Coupled Constraints*. IEEE Transactions on Circuits and Systems II. Published online.

Li, G., Zhang, X. W., Li, Y., and Guan, F. B. (2013). Design and Energy Saving Research of Refrigeration Cycle in Low Temperature Methane Washing Process. *Chem. Des. Commun.* 39 (06), 40–43.

Li, H., Deng, J., Feng, P., Pu, C., Arachchige, D. D. K., and Cheng, Q. (2021). Short-Term Nacelle Orientation Forecasting Using Bilinear Transformation and ICEEMDAN Framework. *Front. Energy Res.* 9, 780928–782021. doi:10.3389/fenrg.2021.780928

Li, H., Deng, J., Yuan, S., Feng, P., and Arachchige, D. D. K. (2021). Monitoring and Identifying Wind Turbine Generator Bearing Faults Using Deep Belief Network and EWMA Control Charts. *Front. Energy Res.* 9, 799039. doi:10.3389/fenrg.2021.799039

Li, H. (2022b). SCADA Data Based Wind Power Interval Prediction Using LUBE-Based Deep Residual Networks. *Front. Energy Res.* 10, 920837. doi:10.3389/fenrg.2022.920837

Li, H. (2022a). Short-term Wind Power Prediction via Spatial Temporal Analysis and Deep Residual Networks. *Front. Energy Res.* 10, 920407. doi:10.3389/fenrg.2022.920407

Liao, Y., Wang, L., and Wen, X. (1998). Facility Agriculture-An Important Way for Efficient Utilization of Agricultural Resources in China. *Resour. Sci.* 20 (3), 20–25.

Liu, S. Y., Zhang, J., and Zhang, B. L. (2008). Experimental Study of Solar Thermal Storage System to Increase the Ground Temperature of Greenhouse. *J. Sol. Energy* 3, 461–465.

Luo, Y., Jiang, L., and Xu, L. (2007). Research on the Application of Ground Source Heat Pump Greenhouse System. *Agric. Mech. Res.* 4, 59–61.

Ma, C. (2003). *Research on Active Greenhouse Solar Underground Heat Storage System*. Nanchang: Shanxi Agricultural University, 2–5.

Mao, H., Wang, X., and Wang, D. (2004). Design and Experimental Study of Greenhouse Solar Heating System. *J. Sol. Energy* 25 (3), 305–309.

Sun, Z. H. (2008). Performance Improvement and Experimental Study of Direct Expansion Solar Heat Pump Water Heater. *Master's thesis* 1, 41–42.

Toyoda, M., and Wu, Y. (2021). Mayer-type Optimal Control of Probabilistic Boolean Control Network with Uncertain Selection Probabilities. *IEEE Trans. Cybern.* 51, 3079–3092. doi:10.1109/tcyb.2019.2954849

Wang, S-S., and Cheng-wei, M. (2007). Experimental Study on Built-In Solar Thermal Collector and Thermoregulation Device for Solar Greenhouse. *Agric. Mech. Res.* 2, 130–133.

Wei, Q. (1999). The Development Status and Prospect of Factory Farming. *Rural. Pract. Eng. Technol.* (8), 2–3.

Wu, Y., Guo, Y., and Toyoda, M. (2021). Policy Iteration Approach to the Infinite Horizon Average Optimal Control of Probabilistic Boolean Networks. *IEEE Trans. Neural Netw. Learn Syst.* 32 (6), 2910–2924. doi:10.1109/TNNLS.2020.3008960

Xu, Y., and Gong, B. (2010). Simulation and Optimization of Ethylene Plant Refrigeration System. *Ethyl. Ind.* 22 (04), 3–9+25.

Zhang, X., and Chen, Q. (2008). Heating Effect of Ground Source Heat Pump Air Conditioning System in Solar Greenhouse. *J. Shanghai Jiaot. Univ.* 5, 436–439.

Zhang, X., and Chen, W. (2011). Energy Saving Analysis of Greenhouse Solar Thermal Storage Pool. *Agric. Mech. Res.* 8–8.

Zhou, C. (Editor) (2003). *Modern Greenhouse Engineering* (Beijing: Chemical Industryd Press), 2, 38–139.

Zhu, W. (2005). *CFD Simulation of Thermal Environment of Continuous Greenhouse at Night under Winter Heating Conditions*, 6. Dissertation, China Agricultural University.

Conflict of Interest: The authors declare that the research was conducted in the absence of any commercial or financial relationships that could be construed as a potential conflict of interest.

Frontiers in
Energy Research

Advances and innovation in sustainable, reliable and affordable energy

Explores sustainable and environmental developments in energy. It focuses on technological advances supporting Sustainable Development Goal 7: access to affordable, reliable, sustainable and modern energy for all.

Discover the latest Research Topics

See more →

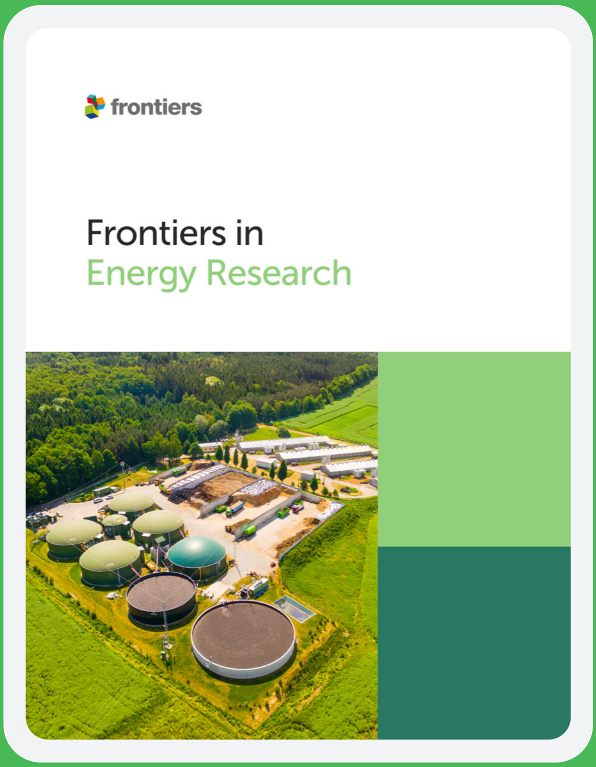

frontiers

Frontiers in
Energy Research

Frontiers

Avenue du Tribunal-Fédéral 34
1005 Lausanne, Switzerland
frontiersin.org

Contact us

+41 (0)21 510 17 00
frontiersin.org/about/contact